

Università degli Studi di Pavia
Dipartimento di Fisica

DOTTORATO DI RICERCA IN FISICA – XXXVII CICLO

Design, Implementation and Commissioning of an Ultrafast XUV Ptychography Beamline

Carmelo Grova

Submitted to the Graduate School of Physics
in partial fulfillment of the requirements for the degree of
DOTTORE DI RICERCA IN FISICA
DOCTOR OF PHILOSOPHY IN PHYSICS
at the
University of Pavia

Supervisor: Prof. Giulia Fulvia Mancini

Design, Implementation and Commissioning of an Ultrafast XUV Ptychography Beamline

Carmelo Grova

PhD thesis - University of Pavia

Pavia, Italy, July 2026

Ad Elisa,
la mia più grande tifosa,
la mia boccata d'aria nei momenti di apnea.

A mamma, papà, Desirée e alla nonna Anna,
che mi manca tanto.

Abstract

This thesis work focuses on the design, implementation and commissioning of a table-top beamline for Ultrafast Ptychography experiments using eXtreme UltraViolet (XUV) coherent light. Through High-Harmonic Generation (HHG), femtosecond pulses from a titanium-sapphire regenerative amplifier are coherently upconverted to produce two different harmonic combs, optimized for emission at $42.6eV$ and $96.5eV$. The generated radiation retains excellent spatial and temporal coherence, enabling the implementation of Ptychography, a computational microscopy technique based on Coherent Diffractive Imaging (CDI). In Ptychography, multiple diffraction patterns from overlapping fields of view are processed by iterative algorithms to separately reconstruct amplitude and phase images of the sample and the image forming beam with diffraction-limited resolution. The amplitude image of the specimen can exhibit quantitative sensitivity to material composition; the phase image is sensitive to both material composition and topography while the determination of the illumination function allows for monitoring aberrations and phase structures affecting the beam. The beamline is designed for combining ptychographic imaging with stroboscopic pump-probe techniques: the sample is driven out of equilibrium applying an external optical excitation pulse ("pump") followed by a sequence of XUV detection pulses ("probe") at variable time delays, allowing for the reconstruction of the sample's ultrafast dynamics at femtosecond time resolution. By integrating pump-probe capability with coherent XUV ptychography, this beamline represents a unique platform for quantitative microscopy study of ultrafast phenomena at the nanoscale.

The system targeted ptychographic reconstructions in transmission geometry with variable resolutions from $15nm$ to $233nm$, while its design was developed to also support operation in reflection mode. In order to simultaneously satisfy both the highest numerical aperture (N.A.) and achievable spatial resolution, and the Nyquist oversampling requirements at the detector's plane, accurate ray-tracing simulations were carried out using ShadowOui, an open-source software available through the OrAnge SYnchrotron Suite

(OASYS) for beamline design at large-scale facilities. The complete probe propagation path was then simulated, from the XUV source to the sample plane, finally addressing an off-axis z-fold configuration as the optimal high-demagnification ($\sim$ 10) focusing geometry scheme compared to ellipsoidal and toroidal mirrors working at grazing incidence angle. Critical operational parameters, including source size and divergence, distances, angles of incidence, mirror's offsets, and figure errors (quantified as 2D slope and shape errors), were explicitly considered, together with the potential impact of optical misalignments. The effects of surface roughness and spurious scattering effects along the beam path were also taken into account but assessed to be negligible. According to the ray-tracing and reflectivity analyses, the z-fold design employs one flat and one spherical multilayer mirror, optimized for robust operation at $42.6 \pm 0.3eV$ and $96.5eV \pm 0.3$ with a $3 \pm 0.3eV$ passband. Both mirrors work at a 2° angle of incidence, with offsets of $7mm$ and $9mm$ from their respective poles, and slope-error tolerances specified at $0.5\mu rad$ and $1\mu rad$ RMS, respectively. Once designed, the optics were commissioned to external suppliers for fabrication, and their compliance has been verified both at the supplier's premises and by independent metrology measurements at ELETTRA – Sincrotrone Trieste. Integrating the results of metrology inspections into the simulative environment, a faithful digital replica ("digital twin") of the XUV beamline in LUXEM was generated. The ultrafast XUV microscope is deployed in a rectangular experimental chamber for High-Vacuum (HV) operations, whose custom design was optimized in collaboration with the PI and the manufacturers. Internally, the chamber houses four motorized towers for optics and sample alignment, and two linear stages in cross-configuration to allow for direct beam imaging and adjusting the microscope's NA.

After design, the probe branch was implemented and tested: operating the amplifier at $788nm$ and the gas-filled waveguide with Ar at $40 - 80Torr$, we retrieved the HHG source parameters via M^2 measurements at $42.6eV$, namely the diameter ($3.5\mu m$) and the divergence ($0.8mrad$). The flux of the harmonic beam, measured with an in-line AXUV100G Si Photodiode, was correlated to the counts acquired by the XUV detector (AXIS-SXR from Axis Photonique Inc) to verify the efficiency of multilayer optics. At the sample plane, the detector measured $\sim 10^9\ ph/s$, approximately two orders of magnitude lower than the direct harmonic beam, in agreement with the mirror's reflectivity curves. In parallel, the design and implementation of the pump branch was carried out by combining three-dimensional modeling with geometric optics calculations. The configuration was defined through the detailed selection of optical components and ensures:

(i) a time delays span up to several hundred of picoseconds (ps), (ii) suppression of pulse broadening due to group-delay dispersion (GDD), (iii) tunable fluence in the range of $3.5 - 42.6 mJ/cm^2$, (iv) adjustable polarizations, and (v) few tens of femtoseconds (fs) time resolution. The deployed beamline thus fully supports ultrafast XUV ptychography with high throughput, based on optimized photon flux management and leveraging the sCMOS detector technology, which enables data collection at $24 fps$ and the reconstruction of a 100-frame nanoscale movie in 7 minutes, two orders of magnitude faster than previous demonstrations.

The thesis is organized into eight chapters. Chapter 1 introduces the context and motivation of this work, reviewing the development of microscopy and coherent radiation sources, with emphasis on XUV and soft X-ray imaging techniques, and concludes with the state of the art in XUV ptychography and the aims of the project. Chapter 2 presents the theoretical foundations of diffraction, from Maxwell's equations to scattering theory, providing the formalism necessary for Fourier optics and wave propagation. Chapter 3 is devoted to CDI and ptychography, describing the phase retrieval problem, the conditions for successful reconstruction, and the computational algorithms involved. Chapter 4 addresses the principles of time-resolved measurements and pump–probe methods, establishing the framework for ultrafast ptychography. Chapter 5 details the ultrafast light source, including the mode-locked oscillator and regenerative amplifier, and describes the diagnostics implemented for characterizing ultrashort pulses. Chapter 6 presents the design and implementation of the XUV ptychography beamline. It covers the HHG-based probe arm, the custom-designed pump branch and the procedure for time-zero retrieval. Chapter 7 constitutes the core of this thesis and describes the design of the microscope based on a set of detailed ray-tracing simulations, the metrological validation of the optics, and the realization of the experimental chamber. Finally, chapter 8 concludes the thesis by summarizing the main results and discussing possible upgrades of the beamline as well as its prospective applications.

The ultrafast XUV ptychography microscope thus commissioned represents an enabling tool for studies in materials science, nanotechnology, and biological imaging, with high lateral spatial resolution (nanometers), Angstrom-scale axial sensitivity, and few fs-temporal resolution in a compact laboratory environment. Ultimately, technical optimization and the use of the digital twin further enhance experimental throughput and minimize system downtime. This thesis work was supported by the European Union's Horizon 2020 Research and Innovation Program through the G.A. no. 851154 (ULTRA-

IMAGE).

Sommario

Questo lavoro di tesi è incentrato sulla progettazione, realizzazione e messa in servizio di una beamline da banco per esperimenti di Ptychography ultraveloce mediante luce coerente nell'estremo ultravioletto (XUV). Attraverso generazione di alte armoniche (HHG), impulsi al femtosecondo provenienti da un amplificatore rigenerativo al titanio-zaffiro vengono convertiti coerentemente per produrre due differenti pettini di armoniche, ottimizzati per l'emissione a $42.6eV$ e $96.5eV$. La radiazione generata mantiene un'eccellente coerenza spaziale e temporale, consentendo l'implementazione della Ptychography, una tecnica di microscopia computazionale basata sul Coherent Diffractive Imaging (CDI). Nella Ptychography, molteplici pattern di diffrazione ottenuti da campi di vista sovrapposti vengono elaborati da algoritmi iterativi al fine di ricostruire separatamente le immagini di ampiezza e fase del campione, nonché il fascio alla base della formazione dell'immagine, con risoluzione esclusivamente limitata dalla diffrazione. L'immagine di ampiezza del campione mostra sensibilità quantitativa alla composizione del materiale; l'immagine di fase è sensibile sia alla composizione sia alla topografia, mentre la determinazione della funzione di illuminazione permette di monitorare le aberrazioni e le deviazioni di fase del fascio ottico. La beamline è progettata per combinare l'imaging ptychografico con tecniche time-resolved: il campione viene portato fuori dall'equilibrio tramite l'applicazione di un impulso ottico esterno ("pump"), seguito da una sequenza di impulsi di rilevazione XUV ("probe") a ritardi temporali variabili, permettendo la ricostruzione delle dinamiche ultraveloci del campione con risoluzione temporale nell'ordine dei femtosecondi. Integrando la capacità pump-probe e la ptychography con XUV coerente, questa beamline rappresenta una piattaforma unica per studiare quantitativamente fenomeni ultraveloci su scala nanometrica.

Il sistema è stato sviluppato per ricostruzioni ptychografiche a risoluzioni variabili, da $15nm$ a $233nm$, sia in geometria di trasmissione che di riflessione. Per soddisfare simultaneamente la massima apertura numerica (N.A.) e la risoluzione spaziale raggiun-

gibile, nonché i requisiti di di campionamento di Nyquist al piano del rivelatore, sono state condotte simulazioni di ray-tracing con ShadowOui, un software open-source disponibile attraverso l'OrAnge SYnchrotron Suite (OASYS) ed usato nella progettazione di beamline in grandi impianti. È stato quindi simulato l'intero percorso di propagazione del probe, dalla sorgente XUV al piano campione, individuando infine lo z-fold fuori asse come la geometria ottimale per operare ad alta demagnificazione ($\sim$ 10), rispetto a specchi ellissoidali e toroidali operanti a incidenza radente. Parametri operativi critici — tra cui dimensione e divergenza della sorgente, distanze, angoli di incidenza, offset degli specchi ed errori di figura (quantificati come errori di pendenza e di forma in 2D) — sono stati esplicitamente considerati, insieme al potenziale impatto di disallineamenti ottici. Sono stati inoltre valutati gli effetti della rugosità superficiale e degli scattering spuri lungo il cammino del fascio e giudicati trascurabili. Seguendo le analisi di ray-tracing e di riflettività, lo z-fold utilizza uno specchio multilayer piano e uno sferico, ottimizzati per lavorare a $42.6 \pm 0.3eV$ e $96.5 \pm 0.3\ eV$, con banda passante di $3 \pm 0.3eV$. Entrambi gli specchi operano ad un angolo di incidenza di 2°, con offset rispettivamente di $7mm$ e $9mm$ dai propri poli, e tolleranze di slope-error di $0.5\mu rad$ e $1\mu rad$ RMS. Una volta progettati, gli elementi ottici sono stati commissionati a fornitori esterni per la fabbricazione, e la loro conformità è stata verificata sia presso i fornitori stessi sia tramite misure metrologiche indipendenti ad ELETTRA. Integrando i risultati delle ispezioni metrologiche nell'ambiente di simulazione, è stata generata una replica digitale fedele ("digital twin") della beamline XUV presso LUXEM. Il microscopio XUV ultraveloce è installato in una camera sperimentale rettangolare per operazioni in alto vuoto (HV), la cui progettazione è stata ottimizzata in collaborazione con il PI e i produttori. All'interno, la camera ospita quattro torri motorizzate per l'allineamento delle ottiche e del campione, e due stage lineari in configurazione incrociata per consentire l'imaging diretto del fascio e l'adattamento della N.A. del microscopio.

Dopo la fase di progettazione, il ramo di probe è stato implementato e testato: operando l'amplificatore a $788nm$ e riempiendo la guida d'onda del sistema di armoniche con Ar a $40 - 80Torr$, sono stati ricavate, tramite misure di M^2 a $42.6eV$, la dimensione ($3.5\mu m$ in unità σ) e la divergenza ($0.8mrad$ in unità σ) della sorgente HHG. Il flusso del fascio armonico, misurato con un AXUV100G Si Photodiode in linea, è stato correlato ai conteggi acquisiti dal rivelatore XUV (AXIS-SXR di Axis Photonique Inc) per verificare l'efficienza delle ottiche multilayer. Al piano del campione, il rivelatore ha mostrato un flusso di $\sim 10^9\ ph/s$, circa due ordini di grandezza inferiore rispetto al

fascio armonico diretto, in accordo con le curve di riflettività degli specchi. Parallelamente, il progetto e l'implementazione del ramo di pump sono stati realizzati combinando modellazione tridimensionale e calcoli di ottica geometrica. La configurazione è stata definita attraverso una selezione dettagliata dei componenti ottici e garantisce: (i) un intervallo di ritardi temporali fino a centinaia di picosecondi (ps), (ii) soppressione dell'allargamento dell'impulso dovuto alla Group-Delay Dispersion (GDD), (iii) fluenza regolabile nell'intervallo $3.5 - 42.6 mJ/cm^2$, (iv) polarizzazioni regolabili, e (v) risoluzione temporale di poche decine di femtosecondi (fs). La beamline realizzata supporta così pienamente la ptychography ultraveloce con elevata efficienza, grazie a un'ottimizzata gestione del flusso di fotoni e all'impiego della tecnologia sCMOS al detector, che consente una raccolta dati a $24 fps$ e la ricostruzione di un filmato a scala nanometrica di 100 frames in 7 minuti, due ordini di grandezza più veloce rispetto a precedenti dimostrazioni.

La tesi è organizzata in otto capitoli. Il Capitolo 1 introduce il contesto e la motivazione del lavoro, rivedendo lo sviluppo della microscopia e delle sorgenti di radiazione coerente, con particolare enfasi sulle tecniche di imaging XUV e soft X-ray, e si conclude con lo stato dell'arte della ptychography XUV e gli obiettivi del progetto. Il Capitolo 2 presenta i fondamenti teorici della diffrazione, dalle equazioni di Maxwell alla teoria dello scattering, fornendo il formalismo necessario tramite ottica di Fourier e propagazione ondulatoria. Il Capitolo 3 è dedicato alla CDI e alla ptychography, descrivendo il problema della fase, le condizioni per una ricostruzione di successo e gli algoritmi computazionali coinvolti. Il Capitolo 4 affronta i principi delle misure time-resolved e dei metodi pump-probe, stabilendo il quadro concettuale per la ptychography ultraveloce. Il Capitolo 5 descrive la sorgente di luce ultrarapida, includendo l'oscillatore mode-locked ed l'amplificatore rigenerativo, ed illustra i dispositivi di diagnostica implementati per la caratterizzazione degli impulsi ultracorti. Il Capitolo 6 presenta la progettazione e l'implementazione della beamline per la ptychography ultraveloce con radiazione XUV. Esso copre il ramo probe basato su HHG, il ramo pump e la procedura per l'individuazione del tempo-zero in un esperimento pump-probe. Il Capitolo 7 costituisce il cuore della tesi e descrive la progettazione del microscopio attraverso un dettagliato set di simulazioni ray-tracing, la validazione metrologica delle ottiche nonché la realizzazione della camera sperimentale. Infine, il Capitolo 8 conclude la tesi riassumendo i principali risultati e discutendo possibili aggiornamenti della beamline e le sue prospettive applicazioni. Il microscopio XUV per ptychography ultraveloce così realizzato rappresenta uno strumento abilitante per studi in

scienza dei materiali, nanotecnologia e biological imaging, con alta risoluzione spaziale (da Angström a nanometri) e risoluzione temporale di pochi fs in un ambiente compatto di laboratorio. In ultima analisi, l'ottimizzazione tecnica e l'uso del digital twin incrementano ulteriormente la produttività sperimentale e minimizzano i tempi di fermo del sistema.

Questo lavoro di tesi è stato supportato dal Programma di Ricerca e Innovazione Horizon 2020 dell'Unione Europea tramite il G.A. n. 851154 (ULTRAIMAGE).

List of Publications and Scientific Contributions

Research Articles

- S. Restelli, O. Cannelli, N. Colonna, **C. Grova**, *et Al.* "Ultrafast Formation of Jahn-Teller Polarons Revealed by State-Selective Excitation in Correlated Spinel Co3O4". In: *J Am Chem Soc.* (April 2026) DOI: doi:10.1021/jacs.5c23346.
- Mazzarone A, **Grova C** *et Al.* "Focusing Delivery Schemes: a Comparative Analysis for Extreme UltraViolet Ultrafast Tabletop Ptychography". Under review in: *Commun Phys*.

Conference Proceedings

- **C. Grova** *et Al.* "Ultrafast EUV microscopy of self-assembled nanomaterials". In: *Physical Chemistry of Semiconductor Materials and Interfaces XXIII*, SPIE, Vol. 13127, pp. 16–18 (2024). DOI: 10.1117/12.3027994.
- **C. Grova** *et Al.* "A Flexible Beamline for Ultrafast High-Throughput Microscopy with Extreme Ultraviolet Radiation". In: *CLEO 2024, Paper SM2H.5, Optica Publishing Group* (2024). DOI: 10.1364/CLEO_SI.2024.SM2H.5.
- **C. Grova** *et Al.* "Towards Real-Time Ultrafast Ptychography with Unsupervised Deep Learning". In: *2024 Conference on Lasers and Electro-Optics (CLEO)*, IEEE, pp. 1–2 (2024). URL: https://ieeexplore.ieee.org/document/10729002/.

- **C. Grova** *et Al.* "Unsupervised Deep Learning for Ptychography". In: *High-Brightness Sources and Light-Driven Interactions Congress, Paper JTu4A.26, Optica Publishing Group* (2024). DOI: 10.1364/EUVXRAY.2024.JTu4A.26.

- **C. Grova** *et Al.* "A Compact Beamline for High-Throughput, Multiscale, Ultrafast Extreme Ultraviolet Ptychography". In: *High-Brightness Sources and Light-Driven Interactions Congress, Paper HW3B.3, Optica Publishing Group* (2024). DOI: 10.1364/HILAS.2024.HW3B.3.

- C. S. Bevis, **C. Grova** *et Al.* "Multi-wavelength Ultrafast Ptychography: A Flexible Beamline with a Compact High Harmonic Source". In: *The International Conference on Ultrafast Phenomena (UP) 2022, Paper Th4A.41, Optica Publishing Group* (2022). DOI: 10.1364/UP.2022.Th4A.41.

Conference Presentations

Presenting Author

- **Oral Presentation:** *"A Compact Beamline for High-Throughput, Multiscale, Ultrafast Extreme Ultra-violet Ptychography"*, High-Intensity Lasers and High-Field Phenomena (HILAS), Vienna, Austria (12–14 March 2024).

- **Poster Presentation:** *"Unsupervised Deep Learning for Ptychography"*, High-Intensity Lasers and High-Field Phenomena (HILAS), Vienna, Austria (12–14 March 2024).

Contributions to International Conferences

Selection of abstracts authored/submitted by the candidate and presented by co-authors:

- **Oral Presentation:** *"Towards Real-Time Ultrafast Ptychography with Unsupervised Deep Learning"*, CLEO 2024, Charlotte, NC, USA (5–10 May 2024).

- **Oral Presentation:** *"High-Throughput, Tabletop, Ultrafast EUV Ptychography across Lengthscales"*, Ultrafast Phenomena (UP) 2024, Barcelona, Spain (14–19 July 2024).

- **Poster Presentation:** *"Enabling Real-Time Ultrafast Ptychographic Imaging through Unsupervised Deep Learning"*, Ultrafast Phenomena (UP) 2024, Barcelona, Spain (14–19 July 2024).
- **Poster Presentation:** *"A Flexible Beamline for Ultrafast High-Throughput Microscopy with Extreme Ultraviolet Radiation"*, CLEO 2024, Charlotte, NC, USA (5–10 May 2024).

Contents

1 Introduction **1**

1.1 Introduction to Microscopy 4
1.2 Coherent Radiation Sources 6
1.3 XUV and Soft X-Ray light manipulation 10
1.3.1 Refractive X-ray Optics 11
1.3.2 Diffractive X-ray Optics 12
1.3.3 Reflective X-ray Optics 14
1.4 STXM, CDI and Ptychography 17
1.5 State of the Art of XUV Ptychography 21
1.6 Scope of the Dissertation 25

2 Diffraction Theory **28**

2.1 Classical Electromagnetism and the Wave Equation 28
2.2 Scalar Theory and Helmholtz Equation 30
2.3 Propagation of Waves: the Angular Spectrum 31
2.4 Near-field Diffraction or Fresnel Approximation 33
2.5 Far-field Diffraction or Fraunhofer Approximation 35
2.6 The Fresnel Number 35
2.7 Scattering Theory 36
2.8 The Born Approximation 37
2.9 X-Ray-Matter Interaction: Atomic Scattering Factors and Contrast Generation in Imaging 38

3 Coherent Diffractive Imaging (CDI) and Ptychography **41**

3.1 The Phase Problem 41
3.2 CDI Requirements 42

3.3 Ptychography Requirements 44
3.4 Computational Phase Retrieval Algorithms 45

4 Time-resolved Measurements 52

5 The Ultrafast Laser Source 56
5.1 The Ultrafast Oscillator 56
5.1.1 Working Principle of Mode-Locked Oscillator 56
5.1.2 Optical Dispersion 60
5.1.3 Implementation of a Mode-Locked Oscillator 61
5.2 The Ultrafast Amplifier 64
5.2.1 Working Principle of a CPA-based Amplifier 64
5.2.2 Implementation of a CPA-based Amplifier 65
5.3 Ultrafast Pulse Duration Measurements 73
5.3.1 SHG-FROG and GRENOUILLE 75
5.3.2 The Diagnostic Branch 79

6 The Ultrafast XUV Ptychography Beamline 83
6.1 XUV Probe Branch 85
6.1.1 The High-Harmonic Generation Process 85
6.1.1.1 The Three-Step Model 86
6.1.1.2 Phase Matching 89
6.1.2 Implementation of HHG in a Laboratory 92
6.1.3 Driver Suppression with Rejector Mirrors 95
6.1.4 Thin Filters and Photodiode for XUV Flux Characterization . . . 99
6.1.5 Probe Delivery in the Experimental Chamber 102
6.2 Pump Branch 104
6.2.1 Requirements 104
6.2.2 Key Optical Elements and Pulse Duration Calculation 104
6.2.3 Fluence Calculations 107
6.2.4 Detailed Design of the Pump Arm 108
6.2.5 Qualitative and Quantitative Evaluation of Beam Polarizations . . 110
6.3 Time Zero 112

7 The XUV Microscope **116**
7.1 Constraints . . . 116
7.2 Ray Tracing with ShadowOui . . . 119
7.3 Reference Frame in ShadowOui . . . 123
7.4 Optical Fabrication Errors . . . 124
7.5 Ray Tracing Comparison of Multiple Focusing Delivery Schemes . . . 127
7.5.1 Distances . . . 129
7.5.2 Modeling the HHG Source . . . 131
7.5.3 Modeling the Rejectors and the Filters . . . 132
7.5.4 The Toroidal Focusing Scheme . . . 134
7.5.5 The Ellipsoidal Focusing Scheme . . . 137
7.5.6 The Off-axis Z-fold Focusing Scheme . . . 141
7.6 Comparative Simulation Results . . . 145
7.7 Improved Z-fold Design . . . 153
7.7.1 Source and Updated Distances . . . 153
7.7.2 Substrate Specifications of XUV Mirrors . . . 157
7.7.3 Multilayer Coating Specifications . . . 159
7.7.4 Representative Surface Error Profiles of XUV mirrors . . . 166
7.7.5 Real Mirror Profiles . . . 169
7.7.6 Future Perspectives of Ray Tracing Simulations . . . 177
7.8 Experimental Chamber Design . . . 180
7.9 Data Management System . . . 185
7.10 Preliminary Microscopy Reconstructions with Ray-traced Probes . . . 185

8 Conclusions and Future Perspectives **189**
8.1 Conclusions . . . 189
8.2 Future Perspectives . . . 194

List of Figures

1.1 Radiation emission. 8
1.2 Working principle of a FEL. 9
1.3 The electromagnetic spectrum. 10
1.4 Different XUV and X-ray optical elements. 14
1.5 Coherent and incoherent scattering. 19
1.6 Schematics of experimental CDI configurations. 20
1.7 Topographical maps of a nanostructure. 22
1.8 Ptychography applied to biology. 23
1.9 OAM beams generated via HHG. 25
1.10 Ptychographic reconstruction of acoustic dynamics in a tapered nanoantenna. 26

3.1 Concepts of spatial and temporal coherence. 43
3.2 Error Reduction Algorithm in CDI. 46
3.3 Working principle of Ptychography. 49
3.4 Quantitative full-field images of a periodic sample from XUV ptychography with MEP. 50

4.1 Pump-probe timing scheme. 54

5.1 Modes with random phases in a cavity. 57
5.2 Mode amplitudes versus frequency in a mode-locked laser. 58
5.3 Time behaviour of seven oscillating modes with locked phases in a cavity. 59
5.4 Pulse broadening in a dispersive medium of thickness L with positive dispersion. 61
5.5 Gain and losses in a laser resonator with output coupler. 62
5.6 Oscillator cavity and beam path. 64
5.7 Schematic of CPA. 66

5.8 Beam path inside the cavity with the Pockels cell in OFF state. 67
5.9 Pockels cell's operative times. 69
5.10 Beam trapping inside the cavity by turning the Pockels cell ON. 70
5.11 Amplified beam exits the cavity as PC is turned OFF. 71
5.12 Optical path outside the cavity when PC is turned ON. 72
5.13 SHG-FROG experimental layout. 76
5.14 Simulated SHG FROG traces. 77
5.15 Views of GRENOUILLE. 78
5.16 Diagnostic branch set for FROG measurements. 80
5.17 Retrieved trace from GRENOUILLE. 81
5.18 Diagnostic branch set for beam profiling. 82

6.1 Beam paths from RAEA. 84
6.2 The three-step model. 86
6.3 Distribution of harmonics in Ar atmosphere. 88
6.4 Generation of attosecond pulses. 89
6.5 Phase matching in a capillary waveguide. 91
6.6 XUUS^{TM} optical path sketch. 93
6.7 Use of the jig for beam mode diagnosis. 94
6.8 Driving laser wavelength out of the RAEA^{TM}. 95
6.9 XUUS^{TM} emission with Ar and He. 96
6.10 Rejectors in vertical configuration. 97
6.11 Power before the XUUS^{TM}. 98
6.12 Quantitative evaluation of the rejectors. 100
6.13 Beam path towards the experimental chamber. 101
6.14 Responsivity curve of the photodiode. 101
6.15 Beam path inside the chamber until the sample. 103
6.16 Reflectance and GDD curves of the ultrafast optics in the pump arm. . . . 105
6.17 Layout of the optical pump branch. 106
6.18 Length of the pump arm. 110
6.19 Quantitative evaluation of polarization out of RAEA^{TM} 111
6.20 Quantitative evaluation of polarization between WP1 and WP2 in the pump arm. 112
6.21 Quantitative evaluation of polarization in the final section of the beamline. 113

6.22 Scheme and practical result for SFG for time-zero retrieval. 114

7.1 Experimental geometry of a scattering experiment. 117
7.2 Isometric view of the AXIS-SXR detector. 119
7.3 Preliminary sketch of the focusing optics geometry. 120
7.4 ShadowOUI beamline example. 121
7.5 Coordinate system in ShadowOui. 123
7.6 Out-of-focus beams from an elliptical mirror with variable slope error. . . 125
7.7 Power Spectral Density. 126
7.8 View of the three simulated focusing cases. 128
7.9 ShadowOui implementation of the multiple focusing delivery schemes. . . 130
7.10 Input and output plane definition in ShadowOui. 133
7.11 Measured surface error profile of a representative rejector mirror. 134
7.12 Beam clipping from circular aperture in ShadowOui. 135
7.13 Toroidal illumination functions from ray tracing. 136
7.14 Circle of least confusion from a grazing incidence ellipsoid. 139
7.15 Multipanel figure showing the degrees of freedom of a mirror and its response as a function of misalignment and slope errors. 140
7.16 Sketch of the z-fold scheme implemented in ShadowOui. 142
7.17 Circle of least confusion attainable with an off-axis z-fold. 143
7.18 Slope error profile on the spherical mirror. 144
7.19 Ptychography results with different probes. 147
7.20 Realistic simulation of noise affecting the CMOS camera pixels. 149
7.21 Initial probe guesses for the ePIE reconstruction algorithm. 150
7.22 Reconstruction performances of multiple focusing schemes. 154
7.23 Beat at intermediate plane in ShadowOui simulation. 156
7.24 Focusing scheme of the Ultrafast XUV Ptychographic microscope. 157
7.25 Beam diameter as a function of FMM offset. 158
7.26 Maximum linear wavelength shifts of Ar-generated harmonics. 160
7.27 Spectral filtering from NTT mirrors at $42.6eV$. 162
7.28 [Spectral filtering from NTT mirrors at $96.5eV$. 163
7.29 [Spectral filtering from SESO mirrors at $29.1nm$. 164
7.30 [Spectral filtering from SESO mirrors at $12.9nm$. 165
7.31 Implemented figure and slope errors in the Digital Twin fo the beamline. . 167

7.32 Caustic curve and spot size as a function of the yaw angle. 168
7.33 Figure error profiles from metrology measurements carried out by NTT-AT and the LUXEM Group at ELETTRA – Sincrotrone Trieste. 170
7.34 Metrological investigation of the rejector's surface. 171
7.35 Multiple spot size intensity distributions. 172
7.36 Surface error profiles acquisition methods. 174
7.37 Figure error profiles of the SESO mirrors for 96.5eV XUV light. 175
7.38 Beam diameter dependence as a function z and yaw angle in different source conditions. 178
7.39 Figure error profiles of the SESO mirrors for 42.6eV XUV light. 179
7.40 Caustic scan from SESO mirrors operating at 29.1nm. 180
7.41 The experimental chamber. 181
7.42 Internal rendering of the experimental chamber. 183
7.43 Vertical positioning of the components inside the experimental chamber. . 184
7.44 Ptychography reconstruction of a Siemens star reconstructed with a ray-traced probe. 186
7.45 Reconstructed amplitude and phase images of monodispersed core-shell nanoparticles. 188

List of Tables

1.1 Comparative overview of coherent radiation sources. 7

6.1 HHG output in Ar atmosphere: conversion from measured photocurrent to photon flux. 102
6.2 Total GDD from transmissive elements in the pump branch. 107

7.1 Beam path in the z-fold delivery scheme simulated for the probe arm of the Ultrafast XUV beamline. 131
7.2 Beam path in the toroid/ellipsoid delivery scheme simulated for the probe arm of the Ultrafast XUV beamline. 131
7.3 Main parameters of each ptychographic simulation. 148
7.4 Computational demand for each probe under the three convergence criteria. 152
7.5 Beam path in the z-fold delivery scheme simulated for the probe arm of the Ultrafast XUV beamline. 155

Chapter 1

Introduction

Understanding how energy, charge, spin and structural degrees of freedom evolve in materials following ultrafast optical excitation represents a central challenge in modern condensed matter physics and nanotechnology. Many technologically relevant processes, including carrier relaxation in photovoltaic materials, ultrafast heat transport in nanostructures, strain generation and spin reconfiguration in magnetic devices, occur on characteristic spatial scales of tens of nanometers and temporal scales ranging from femtoseconds to picoseconds [1, 2]. Accessing these regimes experimentally is essential for establishing microscopic design rules for functional materials used in optoelectronics, spintronics, and energy conversion technologies [3, 4].

Despite major advances in ultrafast spectroscopy and nanoscale microscopy [5, 6], a significant experimental gap remains in the ability to directly observe such processes with simultaneous high spatial resolution, femtosecond temporal resolution, and quantitative material contrast. Techniques capable of resolving ultrafast dynamics are often rely on spatially averaged measurements, while high-resolution imaging methods typically require slow scanning approaches or are not easily compatible with pump–probe experiments [7]. Electron-based techniques can provide nanometer spatial resolution but are limited by space-charge effects that constrain the temporal compression of electron packets, while scanning probe methods offer extremely high spatial resolution at the expense of acquisition speed, making the observation of transient dynamics challenging [8]. Large-scale facilities such as synchrotrons and X-ray free-electron lasers enable powerful time-resolved experiments [9, 10], but their limited accessibility and the intrinsic complexity of pump–probe synchronization motivate the development of advanced laboratory-scale alternatives.

Coherent imaging techniques based on short-wavelength radiation offer a promising route to overcome these limitations. In particular, Ptychographic Coherent Diffractive Imaging (CDI) has emerged as a powerful lensless microscopy method capable of reconstructing both the amplitude and the phase of a specimen with nanometer-scale resolution [11–13]. When implemented with coherent eXtreme UltraViolet (XUV) radiation generated by High Harmonic Generation (HHG) sources, ptychography enables quantitative imaging with strong elemental sensitivity and Ångström-level sensitivity to structural variations. Combined with ultrafast pump–probe approaches, this technique provides a pathway to directly visualize the transient response of nanostructured materials to optical excitation [14–17].

Such capabilities open the possibility of addressing a wide range of scientific problems in nanoscale physics and materials science. One important class of investigations concerns photoinduced structural dynamics in functional nanomaterials, where ultrafast excitation can generate coherent lattice motion, thermal expansion, or strain waves in individual nanostructures [18]. The technique also enables the study of collective vibrational dynamics and electron–phonon coupling in nanoparticle superlattices, where optical excitation can trigger breathing modes and strain propagation across extended nanoscale assemblies. Multispectral XUV imaging further allows the selective probing of different elements within binary or hybrid nanostructured systems, enabling the investigation of band-gap modulation, strain redistribution, and energy transfer between distinct material components [14, 19, 20].

Another important application concerns the investigation of ultrafast magnetic phenomena. By exploiting the absorption edges of transition metals such as Fe, Co, and Ni in the XUV spectral region, it becomes possible to study element-specific magnetization dynamics and the evolution of complex spin textures, including magnetic domains and topological structures such as skyrmions or magnetic bubbles [21–23]. In addition, the penetration depth of XUV radiation enables the characterization of buried interfaces and multilayer nanostructures, allowing the study of processes such as interdiffusion, oxidation, and structural transformations occurring beneath the surface of functional devices [17].

To pursue these goals, I describe in this dissertation the design and development of a time-resolved microscope based on ptychography using XUV light from HHG sources. The ultrashort pulse duration and the high energy of the source, optimized either for $42.6eV$ (10^{12} ph/s) or $96.5eV$ (10^{10} ph/s) allow for fast changes to be recorded with

nanometer to angstrom (Å) spatial resolution, while providing low sample damage and quantitative elemental contrast in matter. A single XUV harmonic is selected with a set of multilayer mirrors, then focused, and overlapped with light pump pulses on the samples. The diffraction patterns from the sample, generated from multiple overlapping fields of view are collected directly on a pixelated detector to reconstruct the image of the sample using iterative algorithms avoiding image-forming optics. The delay between the IR pump photons and the probing XUV light is controlled by a motorized delay-line. With this method, the dynamic response of each sample is captured by collecting stroboscopic images as a function of time delay between pump and probe pulses. At each time delay, ptychography provides a complete description of the specimen in response to a laser-driven excitation, through an amplitude and a phase image. Due to the consistent amount of data to be acquired and analyzed, the throughput of the beamline has been maximized by an accurate probe design using Ray-tracing techniques. The position and the surface specifications of optical components have been tailored in order to optimize beamline efficiency and flexibility, also providing a solid basis for astigmatism correction in an original and unique way present in no other works.

The thesis is organized as follows. Chapter 1 introduces the context and motivation for the present work, providing a historical overview of microscopy developments and coherent radiation sources Furthermore, the chapter focuses on XUV and Soft X-ray imaging techniques such as STXM, CDI, and ptychography, emphasizing their respective strengths and limitations. It concludes with a detailed discussion on the state of the art in XUV ptychography and outlines the specific aims of this work. Chapter 2 presents the theoretical foundations of diffraction phenomena, with an emphasis on Fourier optics. Starting from Maxwell's equations, the scalar wave equation and the Helmholtz equation are derived, leading to the formalism of wave propagation via the angular spectrum, near-field (Fresnel) and far-field (Fraunhofer) diffraction approximations. Concepts such as the Fresnel number and the Born approximation are introduced within the framework of scattering theory to complement the chapter from a material science perspective. Chapter 3 focuses on the principles of CDI and ptychography. It describes the phase retrieval problem, the conditions required for successful image reconstruction, and the computational algorithms employed. The advantages of ptychography in terms of robustness, resolution, and simultaneous retrieval of the object and the illumination function are emphasized. Chapter 4 describes time-resolved measurements and the pump-probe approach, detailing the critical elements enabling the implementation of ultrafast ptychography and the potential for

real-time imaging of ultrafast dynamics at the nanoscale. Chapter 5 is dedicated to the theoretical analysis and experimental implementation of the ultrafast system, composed by a mode-locked oscillator and a regenerative amplifier, serving as the primary source of radiation for both pump and probe arms. The chapter concludes with a review of the methods employed for the determination of ultrashort pulses' duration, followed by the implementation of a diagnostic line dedicated to measuring the spatial, temporal and spectral properties of the optical beam. Chapter 6 represents the core of the dissertation, describing the design and implementation of the entire ultrafast XUV ptychography beamline. The discussion begins with the probe arm, introducing the High-Harmonic Generation (HHG) process, its realization on a laboratory scale, and its subsequent characterization. Then, attention turns to the pump arm, where the strategic selection of optical components, the three-dimensional modeling of the optical path, and the validation of the complete branch are presented. The central part of the chapter is devoted to the design of the microscope itself. Starting from practical implementation constraints, the optical layout was developed using ShadowOUI as a ray-tracing tool. A detailed geometrical and metrological analysis of the XUV mirrors employed to focus the beam onto the sample plane is provided, together with performance evaluation through ptychographic simulations. Finally, the chapter concludes with the technical implementation of the experimental chamber and a description of its internal components. Chapter 8 presents the conclusions, summarizing the work carried out in this thesis and outlining both the beamline's potential upgrades and its prospective applications, ranging from short- to long-term horizons.

1.1 Introduction to Microscopy

Microscopy is defined as the technique used to visualize objects and structures that cannot be directly observed with the naked eye. Its development has been primarily driven by the pursuit of ever higher spatial resolution, the ability to distinguish increasingly smaller details within a sample, which represented one of the central challenges in optics and engineering since the 17th century. More recently, as microscopy has expanded towards the study of transient physical phenomena, the attention has also turned on the complementary goal of achieving high temporal resolution, enabling the observation of fast dynamic processes in real time. The invention of microscopy is conventionally established in 1665 with the first scientific publication by Robert Hooke [24], which dramatically increased the human's understanding of the surrounding world, revolutionizing fields such as biology,

medicine, material science and physics [6, 25–27]. From that moment on, advancements in engineering and optics led to innovative design solutions by the scientific community, interested in increasing the level of details microscopy systems could reach. In 1873, the criterion expressing the fundamental resolution limit of a microscope was formulated by the German physicist Ernst Karl Abbe, which stated that, at best, the resolving power of a microscope is half of the illumination wavelength, and therefore no object smaller than $\sim 200nm$ could be resolved with visible light [28]. From Abbe's resolution criterion (eq. (1.1)), the minimum resolvable feature is directly proportional to the illumination wavelength and inversely proportional to the Numerical Aperture ($N.A.$). $N.A. = n \sin\theta$, where n is the refractive index of the medium in which light propagates and θ is the half-angle of the light collected by the imaging lens.

$$\Delta r = \frac{\lambda}{2n \sin\theta} = \frac{\lambda}{2N.A.} \tag{1.1}$$

To bypass this limit, scientist developed new methods to image the nanoscale. This includes multiphoton excitation techniques [29] and point-scanning methods such as Atomic Force Microscopy (AFM) [30] and Scanning Tunneling Microscopy (STM) [7]. These methods rely on different acquisition principles and therefore image formation does not require the satisfaction of the Abbe's law. However, these approaches come with the limitation of being typically invasive, relying either on fluorescent molecules or mechanical cantilevers, placed closely or in contact to the samples' surface.

An alternative approach to increasing the imaging resolution has been to decrease the illuminating wavelength. Exploiting de Broglie's hypothesis of wave-particle duality [31–33], Knoll and Ruska invented the first electron microscope in 1931 [34]. Although picometer scale resolution is theoretically possible by increasing the electrons' momentum by means of kV accelerating voltage, in practice the aberrations affecting electron lenses have been a limiting factor for decades. In recent years, however, new developments allowed for Å-resolution even though cost, sample preparation and data acquisition are still far to be perfected [35, 36].

Point scanning and electron microscopy can resolve objects on the nanoscale, but are to slow to observe ultrafast processes such as light-matter interaction (fs-to-ps scale). Recently, ultrafast electron microscopy has emerged as a powerful approach capable of combining fs-laser pulses and electron sources to guarantee both space and time requirements [37]. However, space charge effects pose an effective lower bound on the

dimensions of the electron packets to hundreds of femtoseconds, while also degrading the spatial resolution [38].

Following the same considerations that led to the use of electrons for high-resolution microscopy, coherent extreme ultraviolet (XUV) and X-ray radiation offer another relevant route for nanoscale imaging, possessing wavelengths between $100nm$ to 1Å. Discovered by chance by Wilhelm Rontgen in the late 19th century, X-rays have immediately raised interest in the scientific and medical community due to their property of producing shadowgrams of the objects within their path. The name of the rays is inherited from Rontgen's discovery, who did not identify their nature during its experiments [39]. In the next couple of months X-ray light was recognized as high energy electromagnetic radiation produced by deceleration of electrons and, in the 50 years which followed, their application in fields such as medicine and material science led to multiple discoveries and life-changing innovations [40].

1.2 Coherent Radiation Sources

Achieving high-resolution, time-resolved imaging requires powerful and coherent source of high-energy radiation. The availability of these source, particularly in the X-ray and XUV regime, has increased dramatically over the past few decades, thanks to the creation of synchrotron light sources, x-ray free electron lasers (XFELs) and high harmonic generation (HHG) sources. A qualitative comparison between these sources is resumed in table 1.1.

Synchrotron facilities are large-scale particle accelerators capable of producing high energy photons. They work by accelerating electrons to relativistic speeds and steering them through a curved path with powerful bending magnets [41, 42]. As the electrons are forced to change direction they emit synchrotron radiation. The power radiated per solid angle is determined by the following formula:

$$\frac{dP}{d\Omega} = \frac{e^2}{4\pi c^3}\frac{a^2}{(1-\beta\cos(\theta))^3}\left[1-\frac{\sin^2(\theta)\cos^2(\phi)}{\gamma^2(1-\beta\cos(\theta))^2}\right], \tag{1.2}$$

where e is the electron charge, c is the speed of light, a is the acceleration, θ is the polar angle between the particle's velocity $\mathbf{v}$ and the observation direction $\mathbf{n}$, ϕ is the azimuthal angle in the plane perpendicular to $\mathbf{v}$ with respect to the instantaneous direction of the acceleration, $\beta = v/c$ and $\gamma = (1-\beta^2)^{-0.5}$. When the velocity of charged particles approaches the speed of light, the power radiated per solid angle is altered by relativistic

Property	**Synchrotrons**	**Free-Electron Lasers (FELs)**	**High-Harmonic Generation (HHG)**
Scale	Large-scale (circular, $100m\text{-}km$)	Large-scale (linear, $100m\text{-}km$)	Laboratory-scale (tabletop, $1-5m$)
Mechanism	Relativistic e^- in undulators	SASE Micro-bunching	Strong-field non-linear interaction
Emission spectrum	Deep UV to hard X-rays	THz to hard X-rays	XUV to soft X-rays
Coherence	High (spatial), low (temporal)	High (spatial), moderate (temporal)	Very high (spatial), high (temporal)
Pulse Duration	tens of ps (10^{-12})	ps (10^{-15})	fs to as (10^{-15} – 10^{-18})
Peak Power	Medium	Extremely high (GWs)	Low to medium
Stability	High (steady-state)	Moderate (due to jitter)	Very high (phase locked to the IR driver)
Accessibility	Limited	Limited	High
Target Applications	Structural biology, static materials science	Non-linear X-ray physics, single-particle imaging	Ultrafast spectroscopy and imaging

Table 1.1: Comparative overview of coherent radiation sources.

effects and results in an emission peaked along the forward direction, with a divergence angle of approximately $1/\gamma$. Synchrotrons are therefore high brightness sources emitting pulsed radiation whose time duration, typically between $10-100ps$, is directly correlated to the spatial extent of the electron bunches traveling into the storage ring. Finally, as the emitted radiation covers a wide spectrum from deep UV to the hard X-rays, monochromator systems are typically used for filtering purposes before reaching the end stations, where the experiments take place.

X-ray Free Electron Lasers (XFELs) represent the next generation of large-scale coherent X-ray sources [44]. These facilities begins with a laser source that generates and accelerates an electron bunch that passes through a periodic arrangement of magnets,

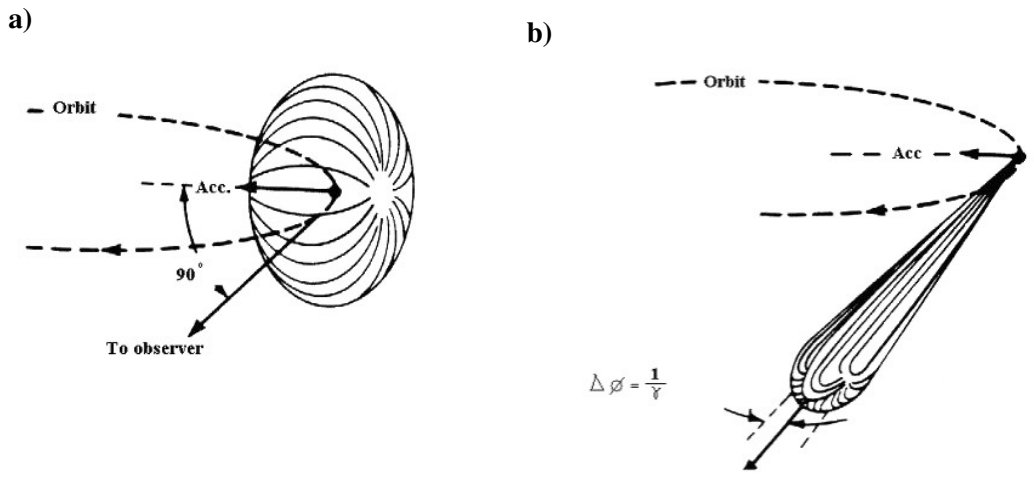


Figure 1.1: Radiation emitted from (a) non-relativistic and (b) relativistic electrons, adapted from [43].

alternating between negative and positive polarity. The purpose of this array is to generate a magnetic field causing the electrons to wiggle across the undulator axis and releasing photons due to their transverse acceleration. To produce bright pulses of spatially coherent X-rays, the undulators are long enough for Self-Amplified-Spontaneous Emission (SASE) to occur: initially, the uniform disposition of electrons radiates incoherently. The emitted field from the the wiggling electrons causes a periodic density modulation, or "micro-bunching", in the electron distribution. As the propagation inside the undulator occurs, the micro-bunches are separated in space by the distance of the radiation wavelength. (Fig. 1.2). The electrons start emitting light in phase and the process continues in a self-sustainable way, leading to the brightest X-ray pulses ever made [9, 10]. Compared to synchrotrons, FELs offer similar spatial coherence, higher temporal coherence, higher brightness and shorter pulses, with a narrower emission spectrum ranging from THz to hard X-rays typically filtered with a monochromator. This makes them more suitable for probing ultrafast dynamical response in materials and for experiments requiring high energy levels. However, due to their spontaneous build-up of radiation, XFELs typically suffer from high jitter, a critical drawback for experiments that demand high temporal precision, such as pump-probe experiments. In the last decades, recent advances like seeding techniques have emerged as a powerful way to drastically reduce jitter and increase temporal coherence [46].

Unlike the massive scale of synchrotrons and XFELs, High Harmonic Generation (HHG) provides a compact, tabletop solution for generating bright coherent X-rays [47,

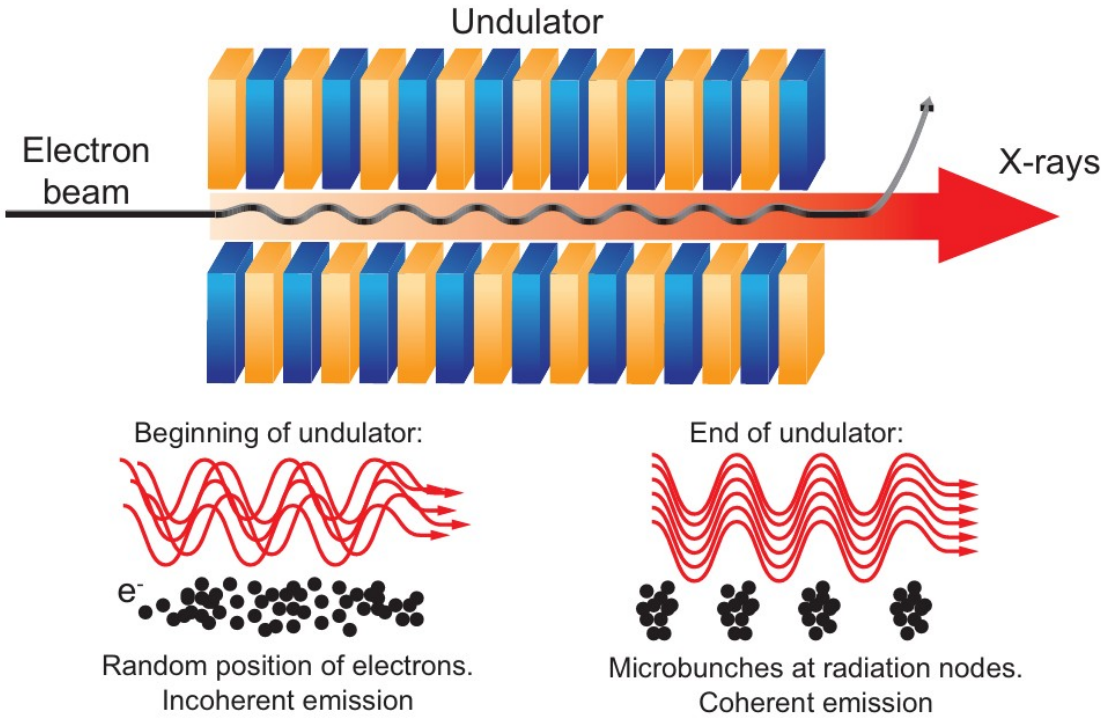


Figure 1.2: Depiction of the working principle of a free electron laser [45].

48]). This makes HHG sources uniquely accessible for small scale laboratories, universities, and industrial applications. From the '80s, when HHG was first demonstrated, sources have been constantly engineered and upgraded until becoming an almost turn-key solutions capable of reaching pulse durations in the order of the attosecond (as), making them unique tools for the study of ultrafast processes [49]. In this highly nonlinear process, an intense, ultrafast laser pulse, known as driver, is focused onto a target, typically a gas, solid or plasma which emits photons at integer multiples, or "harmonics", of the fundamental laser frequency [47]. The emitted HHG pulses range from fs-to-as in the time domain and cover a spectral region from the XUV to the soft X-rays (Fig. 1.3) with high flux when proper phase matching occurs [50]. The manipulation of the generated radiation requires high vacuum at the level of $10^{-7}\ mbar$, due to the high absorption in air, that approximately distinguishes the propagation of soft and hard X-rays. Indeed, the distinction between hard and soft X-rays is not marked by an abrupt change of properties and is often more operational than purely theoretical. As also shown in Fig. 1.3, Soft X-rays embrace a spectral range spanning approximately from hundreds of eV to few keV, while Hard X-rays extend at higher energies. Soft X-rays therefore cover the fundamental

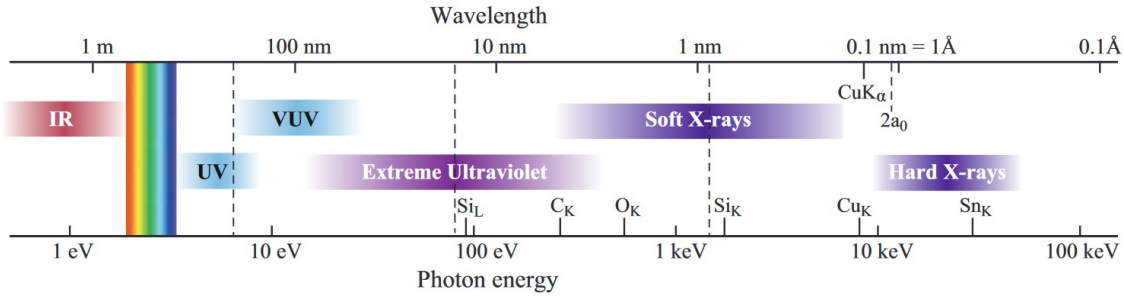


Figure 1.3: The electromagnetic spectrum from the infrared (IR) to the Hard X-rays region. The extreme ultraviolet region is highlighted in violet. The image shows the correspondence between wavelengths and energy, and highlights important absorption edges in materials of technological interest. From [52].

K-shell absorption edges of light elements (such as Carbon, Nitrogen, and Oxygen) and the L- and M-edges of many transition metals. In this regime, the radiation is characterized by a very large photoionization cross-section, which reduces the attenuation length in air to the order of tens of micrometers, thereby requiring high vacuum for its manipulation. The importance of HHG in attosecond physics was recognized by the 2023 Noble Prize in Physics, awarded to Agostini, Krausz and L'Huillier [51]. The coherent, short-wavelength radiation from HHG sources is perfectly suited for high-resolution microscopy as it satisfies the Abbe's criterion in eq. (1.1). Their ultrashort pulse duration provides the time resolution needed to study dynamic nanoscale phenomena. These advantages, including the proximity of the radiation energy to elemental absorption edges, which enhances contrast in imaging, as well as the increased penetration depth and reduced sample preparation demands compared to electron microscopy, represent non negligible factors that deserve to be highlighted in the current framework.

1.3 XUV and Soft X-Ray light manipulation

XUV and Soft X-ray sources present a major challenge for conventional optical systems due to the constraints imposed by the interaction between the high-energy photons and matter. Unlike the visible spectrum, where the refractive index of the common optical media is greater than unity, in the X-ray domain it is convenient to introduce the complex refractive index, expressed as

$$n(\omega) = 1 - \delta - i\beta. \tag{1.3}$$

Here δ and β respectively refer to the phase shift affecting the wave and the absorption of the medium. Both parameters are typically in the order of 10^{-3} to 10^{-5} and will be detailed in section 2.9. As a consequence, for XUV and X-ray light, the real part of $n(\omega)$ is slightly lower than unity, making it impractical for typical lens-based systems to deviate rays from their path [53] and employ them for focusing or image formation purposes. Furthermore, the proximity of the photon energies to the core-level electronic binding energies (K, L, and M absorption edges) results in extremely short attenuation lengths and dramatically reduced flux. Nevertheless, optical systems based on refractive optics exist despite the most widespread and robust solutions in X-ray microscopy rely on reflective and diffractive elements, that bypass these limitations by exploiting total external reflection at grazing angles or constructive interference in periodic structures.

1.3.1 Refractive X-ray Optics

Refractive optics, while standard for visible light, are the least common solution for manipulating XUV and soft X-ray light due to the absorption and the weak refractive power in this regions of the electromagnetic spectrum. Because the real part of the refractive index $(1 - \delta)$ is slightly less than unity, two phenomena occur:

- The phase velocity $v_{ph} = c/n$ of the X-rays propagating through the materials is higher than the speed of light in vacuum (c);
- The wave vector of the radiation entering the medium through vacuum bends away from the surface normal rather than towards it.

While the former observation is noteworthy, it lacks significant applicative impact, as the phase velocity does not carry information. Conversely, the second effect is of critical importance, as it dictates the refraction and reflection laws governing the X-ray regime. Indeed, the fact that $n < 1$ necessitates a radical departure from traditional lens design: while a convex lens converges visible light, to produce a convergent wavefront of X-rays a concave lens is required. Moreover, due to the extremely weak refractive power of a single interface, an individual lens with a reasonable radius of curvature would result in an impractically long focal length. To overcome this, a solution is the implementation of Compound Refractive Lenses (CRLs), which consist of a linear sequence of N concave elements stacked in series [54]. In practice, cylindrical or parabolical holes are carved in a single block of low-Z material (such as beryllium) to reduce the effect of absorption. The

cumulative effect results in a focal length equal to

$$f = \frac{R}{2N\delta}, \tag{1.4}$$

where R is the radius of curvature of the holes. With this approach, CRLs have been developed to achieve spot sizes as tight as $125nm$ [55]. Despite these notable results, refractive optics are a standard tool only for hard X-rays, where absorption β is relatively small. However, in the XUV and soft X-ray regimes they are extremely challenging due to the massive absorption caused by presence of K, L and M absorption peaks for all the relevant fabrication materials. Refractive optics are standard elements in synchrotrons operating at the hard X-ray regime ($> 5keV$). For imaging purposes, a notable example is the ID11 beamline at ESRF which employs a transfocator — a tunable X-ray focusing apparatus based on compound refractive lenses — to obtain focusing at different distances for different energies, up to $75keV$. Another trasfocator is used in the P06 beamline at PETRA III for energies up to $44keV$, where microscopy is carried out through a technique named Scanning Transmission X-Ray Microscopy (STXM), briefly explained in section 1.4.

1.3.2 Diffractive X-ray Optics

Diffractive optics manipulate the radiation by means of interference effects, providing high spatial and spectral resolution. A common type of diffractive optical element used in X-ray microscopy are Fresnel Zone Plates (FZPs) [56]. An FZP consists of a concentric pattern of transparent and opaque rings, known as Fresnel Zones, which are carefully designed to achieve a bright spot on a focal plane by constructive and destructive interference effects. The focusing properties of an FZP are dictated by the requirement that the optical path lengths from sequential transparent zones to the focal point must differ by integer multiples of the wavelength λ to ensure constructive interference. This means that, as shown in Fig. 1.4a, for a plane wave incident on the FZP, the radii of the zones r_n are defined such that the incremental path length to the focal point is $n\lambda/2$. Mathematically, this condition results in zonal radii defined by

$$r_n^2 = n\lambda f + \frac{n^2\lambda^2}{4}, \tag{1.5}$$

where f is the focal length of the first diffraction order. From this relation, defining N as the total number of rings and Δr as the width of the outermost ring, a series of relevant design parameters can be recovered:

- $D \simeq 4N\Delta r$ Zone plate's diameter; (1.6)
- $f \simeq \frac{D\Delta r}{\lambda}$ First order focal length; (1.7)
- $N.A. \simeq \lambda/(2\Delta r)$ Numerical Aperture. (1.8)

Following the mathematical calculation described in [52], applying the Rayleigh resolution criterion, the resolution of an FZP can be estimated as

$$\delta x \simeq 1.22\Delta r. \tag{1.9}$$

This result links the fabrication precision of the outermost zone to the achievable resolution, which nowadays, approaches the $10-30nm$ regime with the latest lithographic and etching techniques.

Even though FZPs have reached technological maturity, they have key limitations. First, the diffractive nature of the FZP introduces severe chromatic aberration and therefore, since $f \propto 1/\lambda$, the relative spectral bandwidth of the source must be strictly limited to $\Delta\lambda/\lambda \leq 1/N$ to maintain a near diffraction-limited focus. Second, they are inherently inefficient; the opaque rings absorb light, and the zone plate's structure directs light into multiple diffraction orders, distributing the incoming photons and reducing the flux available for image formation. This results in a typical photon efficiency of no more than 40% [52, 57]. Ultimately, their alignment in vacuum can be complex, leading to severe beam aberrations. Several beamlines at synchrotrons and XFELs employ FZPs for imaging and microscopy. An example is MISTRAL at the ALBA synchrotron facility, a full-field Transmission X-ray Microscopy (TXM) beamline operating at energies in the range $270eV - 1200eV$ and devoted to cryo nano-tomography in the water window for biological applications [58]. At ELETTRA – Sincrotrone Trieste, the TwinMic beamline exploits the properties of FZPs to operate in the range $400eV - 2200eV$ an obtain sub-$100nm$ spatial resolution [59].

Laue lenses in Fig. 1.4b share the same working principle with FZPs and can be considered as their one-dimensional approximation [60].Their vertical geometry allows to facilitate their fabrication, produce layers of finer thickness and therefore a tighter focus in

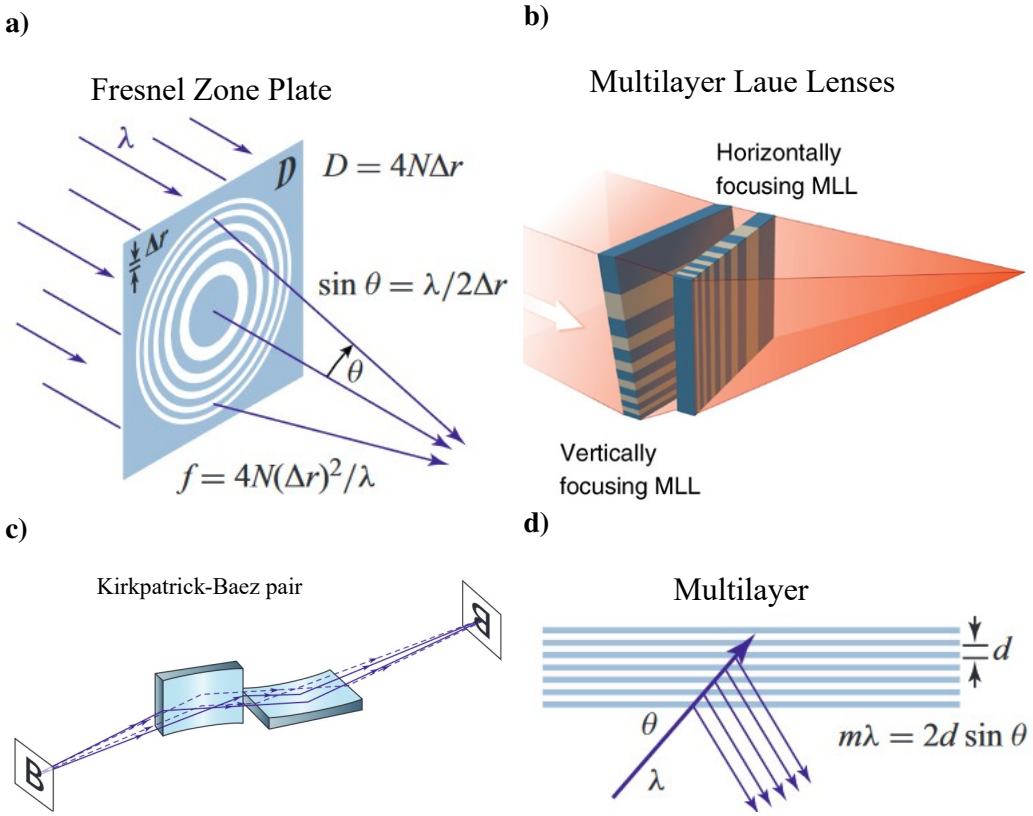


Figure 1.4: Different XUV and X-ray optical elements. (a) Fresnel Zone Plate: a diffractive element made of concentric rings of alternating opaque and transparent materials. Different variables are shown, such as the wavelength λ, the width of the outer zone Δr, the total number of zones N, the aperture diameter D, the first order diffraction angle $\theta$and the focal distance f of the FZP (b) Two orthogonal multilayer Laue lenses (MLL) used for two dimensional focusing (c) Kirkpatrick-Baez mirror pair, used to reflect light at grazing incidence allowing either for tight spot generation or for image formation (d) Bragg diffraction from multilayer mirror coatings, used for high reflectivity at normal and grazing incidence, as well as for bandpass. The figure shows the Bragg's law, with the multilayer period d and the diffraction order m. Panel adapted from [52].

a particular direction. Using two consecutive Laue lenses is a proper choice for creating a uniform tight focal spot.

1.3.3 Reflective X-ray Optics

For greater photon efficiency, reflective optics are often preferred due to their high flux efficiency and achromatic nature. As a consequence of the complex refractive index n, mirrors cannot be used at normal incidence. This is clear using the Fresnel Formula to

calculate the Reflectance R at normal incidence ($\theta = 0$) between vacuum ($n_1 = 1$) and a medium ($n_2 = 1 - \delta + i\beta$) in the XUV or soft X-ray regime:

$$R = \left|\frac{n_2 - n_1}{n_2 + n_1}\right|^2 \approx \left|\frac{\delta^2 + \beta^2}{4}\right|. \tag{1.10}$$

Since δ and β are in the order of $10^3 - 10^5$, extremely small values are obtained. However, since n is slightly smaller than unity, high reflectivity can be exploited through a phenomenon called Total External Reflection (TER), which occurs when the mirror's grazing incidence angle θ goes below the critical angle $\theta_c \approx \sqrt{2\delta}$. This angle is in the order of degrees or fractions of degrees and depends on the mirror's composition. The variable δ is indeed directly proportional to the atomic number Z, which is part of the atomic scattering factor $f_1(\lambda)$ in eq. (2.48). Therefore, mirrors are typically coated with high-Z materials to maximize the critical angle, optimize the collection of light and limit the tangential extent of mirrors which is needed to capture the entire beam diameter. On the other hand, when the critical angle is exceeded, a dramatic flux loss arises due to $\beta \propto Z^4$, and therefore elements such as gold, platinum or iridium are typically employed exclusively for gracing incidence mirrors. Values of δ and β are available from the website of the Center of X-Ray Optics (CXRO) [61].

Reflective optics are often shaped into specific aspheric geometries to achieve aberration-free imaging or focusing. Ellipsoidal mirrors (see section 7.5.5) provide ideal point-to-point focusing, while toroidal mirrors (see section 7.5.4) are utilized in unitary magnification schemes for stigmatic (i.e. perfect) focusing without coma. A particular arrangement is represented by Kirkpatrick-Baez (KB) systems (Fig. 1.4c). Here, two mirrors with extremely high surface quality are placed in a perpendicular configuration and operated at grazing incidence angles to guarantee high reflectivity values [62]. KBs allow for independent light focusing in both horizontal and vertical directions and have been used to achieve some of the tightest spots ever made [63]. However, they are complex and require extremely precise alignment to prevent aberrations. Additionally, grazing incidence reflective optics have achromatic nature, that is, the angle of reflection equals the angle of incidence for all wavelengths. This allows for focusing broadband pulses (such as coming from HHG sources or XFELs) without chromatic dispersion in a single point in space and time. Despite the advantages, the performance of these optical elements is limited by the optical surface quality needed for their effective operations, especially in the tangential beam propagation direction. This important point is covered in section 7.4.

To enable reflection at larger angles up to normal incidence, another widely adopted approach is using mirrors coated with multilayers. As sketched in Fig. 1.4d, multilayer coatings exploit the interference inside precisely fabricated periodic structures that guarantee the maximum reflectivity on a specific, narrow spectral region [64]. Typically, these materials alternate between a high atomic number (high-Z) absorber and a low atomic number (low-Z) spacer material to maximize the difference in electron density and, consequently, refractive index. The thickness of each layer is meticulously controlled, often within a few nanometers, to ensure that reflections from successive interfaces constructively interfere according to the principle of Bragg's Law:

$$m\lambda = 2d \sin\theta. \tag{1.11}$$

In eq. (1.11), λ is the wavelength, d is the bilayer period (the combined thickness of one high-Z and one low-Z layer), θ is the glancing angle of incidence and m is the diffraction order ($m = 1$ for the strongest diffraction order). For near-normal incidence, and hence for $\theta \approx 90°$, eq. (1.11) implies that the first order diffraction peak is maximized when the multilayer period d approaches half of the wavelength of the input light. As an example, Mo/Si mirrors consisting of 50 layer pairs have achieved, at near-normal incidence, a reflectivity as high as 70% [65]. However, while highly efficient within their designed range, this method sacrifices the broad tunability offered by grazing incidence mirrors. For this reason, even if possible with current deposition technologies, the fabrication of multilayer mirrors remains highly challenging and requires atomic-scale precision to produce thin layers with high quality along the interfaces, where roughness and interdiffusion phenomena can degrade the collective interference effect. In addition to this, as for grazing incidence optics, their performance is affected by the quality of the substrate due to fabrication errors.

Grazing incidence reflective optics remain the preferred choice for nanofocusing and imaging at facility scale and tabletop beamlines. Their achromatic nature and their geometrical properties allow for the smallest spots to be generated, despite requiring extreme surface quality and precise alignment. Multilayer mirrors are a compact solution, due to their near-incidence operation and are often associated to HHG sources to achieve spectral selection across the entire harmonic comb.

1.4 STXM, CDI and Ptychography

Some of the optical elements previously discussed have been used in various imaging configurations. For example, a conventional imaging system may be developed using highly coherent X-ray sources in combination with FZPs, which act as a typical lens. In a typical Scanning Transmission X-Ray Microscope (STXM), FZPs are combined with other optical elements with the final goal of producing a tight focus at a designed distance. In STXM, light is scanned point-by-point across the surface of a sample, and the transmitted light is collected in such a way to build an image pixel-by-pixel [66]. The resolution is directly determined by the size of the illuminated area, making the creation of nanometer-sized probes crucial.

An advanced imaging modality that overcomes the need of traditional image forming optics is Coherent Diffractive Imaging (CDI) [67]. In CDI, diffraction patterns generated by the interaction between a sample and coherent radiation are collected on a pixelated detector, with no need of intermediate optical elements. The principle at the basis of image formation in CDI is phase retrieval, a computational process by means of which the real space image of the sample is reconstructed through the recovery of phase information from a single scattered intensity pattern. This approach is required due to the so-called "phase problem": in any scattering experiment, detectors (such as CCDs or CMOS) are only sensitive to the intensity of the radiation, which is proportional to the square of the complex amplitude of the electromagnetic field ($I \propto |E|^2$). Consequently, information about the relative phase of the scattered waves is lost during the measurement process. Since the phase contains critical information about the relative positions of the features within the sample (also called "object"), its loss prevents a direct inverse Fourier transform to recover the sample's geometry. The phase problem will be described in other terms in section 3.1. Successful CDI reconstructions rely on the presence of a finite support for the object. When the object has a finite spatial extent, its diffraction pattern is effectively bandlimited, which allows the intensity distribution in the far-field to be Nyquist sampled by the detector. Under these conditions, the complex transmission function of the object can be reconstructed by intensity measurements. Because the detector samples the diffraction intensity rather than the complex field amplitude, the recovered object amplitude is effectively oversampled (typically by a factor of about two) relative to the Nyquist limit.

The solution to the phase problem was initially formulated by Sayre in 1952 [68],

who noted the potential application of Shannon's theory to sample diffraction patterns to determine crystallographic structures. Building upon this concept Gerchberg and Saxton developed a phase retrieval algorithm for electron microscopy [69], which was adapted in 1978 to optical problems by Fienup in early simulations [70]. Later, CDI was experimentally demonstrated with visible light [71, 72] and, at the end of 20th century, using x-rays [73]. In the x-ray regime, thanks to the absence of image forming optics, CDI is a highly photon-efficient technique. It offers both amplitude and phase contrast, enabling the study of a wide range of samples with theoretically diffraction limited resolution according to Abbe's formula (eq. (1.1)). This means the resolution is set by the system's geometry and the wavelength, with the practical limit often being the sample's ability to scatter light across the detector's full acceptance angle. The ability of CDI to reconstruct the image of a sample through iterative algorithms is based on the uniqueness of the diffraction patterns, which is a direct expression of the sample's specific microscopic arrangement in Fourier space. The fundamental requirement to obtain unique patterns is using coherent radiation. For example, consider a beam of light interacting with an inhomogeneous medium composed of nanoparticles, as seen Fig. 1.5. With incoherent illumination, the diffraction pattern observed in the far-field shows a maximum intensity at an angle $\sim \lambda/d$, where λ is the illumination wavelength and d is the interparticle distance. This result represents an average over the many different wavefront hitting the sample at the same time and can be conceptually thought also as an average over all the possible sample configurations. If instead a coherent beam of light is used, as in Fig. 1.5b, smaller features called speckle can be observed. These fine details are the effect of interference between coherent wavefronts, have a size of $\sim \lambda/a$, with a being the illuminated area, and their position is directly related to the particles' disposition within the illumination area.

The potential shown by CDI in its early development has led to the development of different specialized high-throughput and high-resolution configurations, partially shown in Fig. 1.6. Among these, ptychography has emerged as one of the most powerful imaging methods, offering significant improvements in robustness and resolution over conventional CDI. Unlike classical CDI, which uses a single diffraction pattern from an isolated sample, ptychography works by scanning a coherent probe beam across the sample while recording diffraction patterns at different positions with significant spatial overlap. This scanning procedure, combined with oversampling the diffraction patterns in reciprocal space, creates a highly redundant dataset, which in turn allows for the reconstruction of a wide field-of-view and provides strong constraints during phase retrieval. This makes the reconstruction

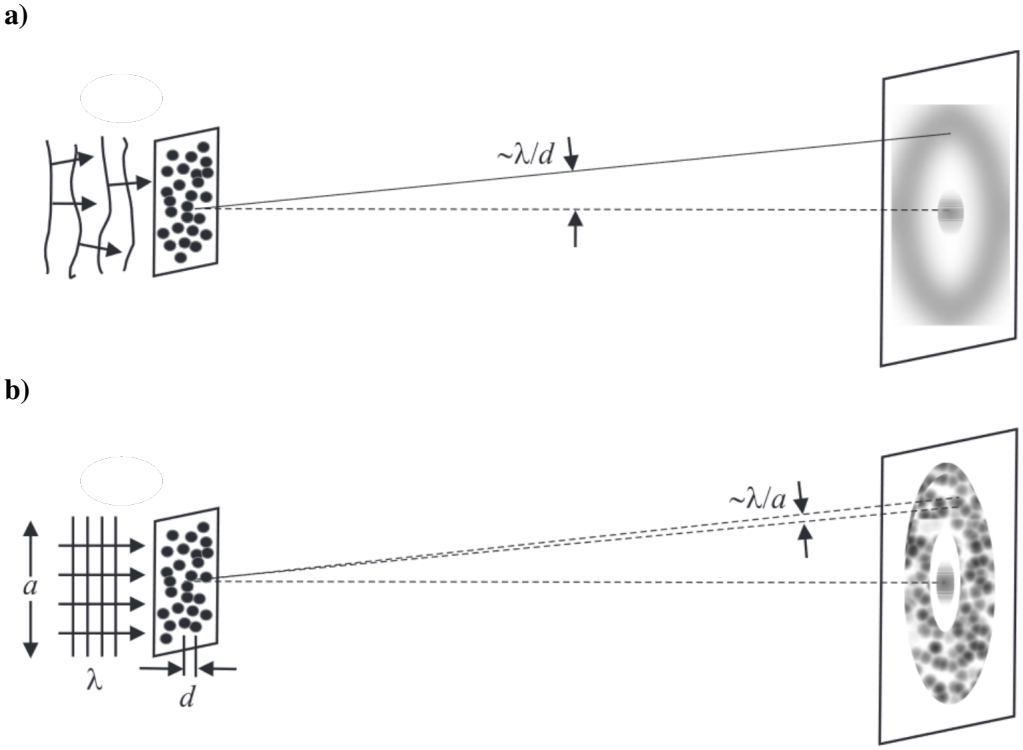


Figure 1.5: Difference between coherent and incoherent scattering. A set of nanoparticles with interparticle distance d dispersed on an area of lateral dimension $a$is illuminated with a wavelength λ. (a) With Incoherent illumination, a diffuse ring is observed (b) With coherent illumination, a specific speckle pattern is captured. Figure from [74].

process more stable and resilient against experimental imperfections such as positioning errors, partial coherence, and illumination fluctuations. Fundamentally, ptychography solves the "phase problem" using iterative algorithms to computationally reconstruct both the complex transmission function (amplitude and phase) of the object and of the complex profile of the illuminating probe beam itself. This yields quantitative, aberration-free images and, compared to STXM, decouples the resolution from the probe size, enabling resolution potentially much finer than the illumination spot.

As for classical CDI, the development of ptychography began in the context of electron microscopy. In their original work, Hegerl and Hoppe proposed the recording of relatively shifted electron diffraction patterns to overcome ambiguities in the phase retrieval of electron interference figures [75]. Ptychography's name, coined by its inventor Hoppe, comes from the Greek word "ptychē", meaning "to fold" or "convolution", a nod to the mathematical operation at its core. In its early times, ptychography variations making use of Wigner

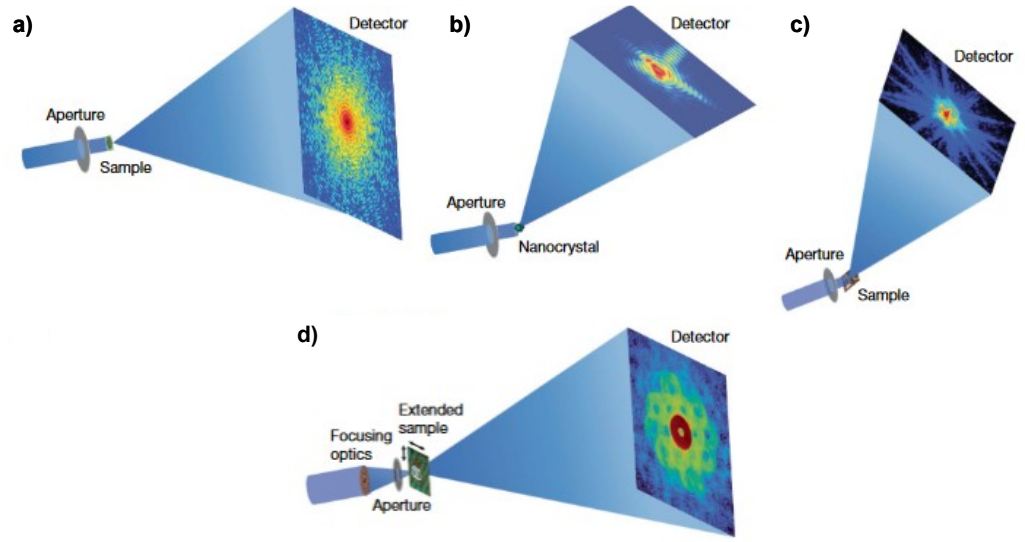


Figure 1.6: Schematics of experimental CDI configurations. (a) Conventional CDI: coherent plane waves illuminates a sample, the far-field diffraction pattern is sampled by the detector. (b) Bragg CDI: the diffraction pattern is acquired around specific Bragg peaks from a nanocrystal. (c) Reflection CDI: the diffraction pattern is obtained by the reflection of the coherent beam from the sample's surface. (d) Ptychography: a focused probe, in this case an X-ray beam, is focused and raster-scanned onto the surface of an extended sample for the detection and the phase retrieval of multiple diffraction patterns. Modified from [67].

distribution deconvolutions were developed for non-periodic objects and allowed to decouple effects from the illumination and the sample being studied [6, 76–78]. However, these techniques required a single deconvolution to be applied to the entire dataset and therefore demanded huge computational power, which limited the practical accessibility of ptychography. It remained largely theoretical until, in the early 2000s, the development of powerful iterative phase retrieval algorithms enabled its modern implementation [12, 79, 80]. These algorithms, operating by alternating between real and reciprocal space constraints, overcame the limitations of earlier methods. Further evolutions removed the need for "a priori" knowledge of the illumination function, making it possible to deconvolve the object and the probe simultaneously by exploiting the redundancy from the overlapping diffraction patterns acquired. This feature of the ptychographic engine enhances the range of applications of the technique, which is routinary used as an alternative to wavefront sensors for beam characterization [55, 81, 82].

1.5 State of the Art of XUV Ptychography

The application of ptychography in X-ray microscopy in the first decade of 21st century leveraged the coherent and stable beams available at synchrotron facilities. More recently the technique has been extended to Soft X-rays and XUV sources, including both large-scale facilities like XFELs [55, 83] and compact, lab based HHG sources [15–17, 84–86]. Tabletop HHG ptychography has been demonstrated using both reflective and diffractive optical elements for beam focusing, and XUV-sensitive Charge Coupled Devices (CCD) and scientific Complementary Metal-Oxide-Semiconductor (sCMOS) detectors for diffraction capture [87]. HHG ptychography is particularly well-suited for inspecting advanced nanostructures, as the high-energy photons are capable of penetrating hundreds of nanometers. For example, it has been used for actinic inspection of EUV lithography masks, a process that inspects masks using the same wavelength of light used for manufacturing. In a reflection-based setup using 13.5 nm radiation, Nagata et al. successfully obtained amplitude and phase images of mask structures and nanoscale defects [88]. Their illumination beam was a spectrally filtered HHG source using Mo/Si multilayer mirrors. Similarly, Shanblatt et al. demonstrated the extreme sensitivity of reflection-based XUV ptychography to the identification of oxidation layers and interdiffusion of materials at interfaces and boundaries in heterogeneous samples. By correlating the ptychography results with computational models and Auger electron spectroscopy, they were able to construct quantitative 3D maps of buried nanostructures, achieving performance comparable to that of AFM (see Fig. 1.7) [17].

HHG ptychography is an ideal tool for bio-imaging as it provides high contrast without the need for fluorescent labels or staining. Baksh at al. imaged fixed neuronal structures with an 80nm in-plane spatial resolution and sub-nanometer axial resolution using 29nm light [89]. Importantly, they observed no sample damage, a common issue with hard X-ray methods. A key advantage of ptychography over fluorescence microscopy is its ability to resolve fine structures that are too small to be targeted by fluorescent molecules (see Fig. 1.8a,b). For the upcoming years, using higher energies in the water window to image samples in aqueous environments would be of an important leap forward in the study of biological samples in a laboratory. However, this is still a challenge due to the insufficient flux available by HHG sources in this spectral region and the low scattering power of biological specimens. This is already possible in large scale facilities, where flux is not an issue [90, 91].

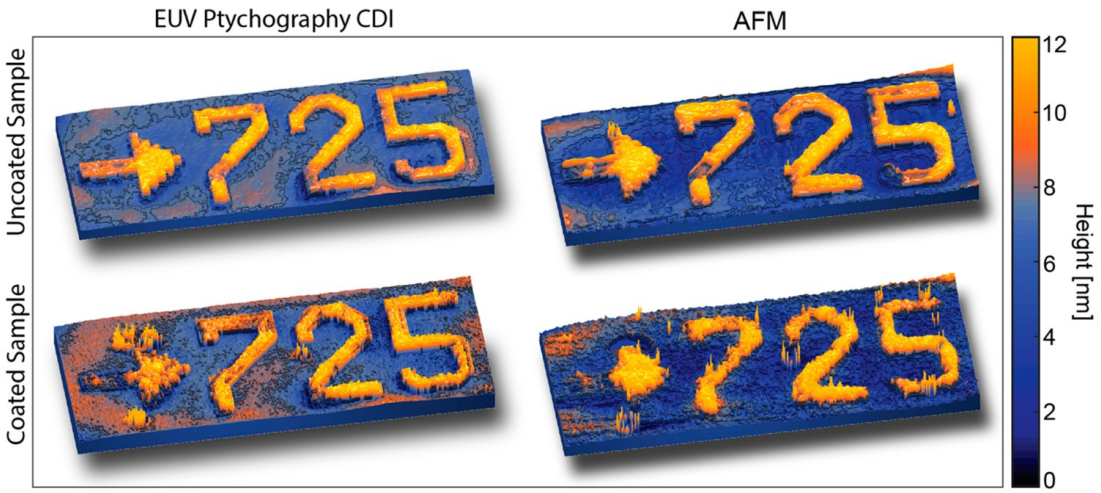


Figure 1.7: Topographical maps of a nanostructure before and after being coated with a 100*nm* thick Al film. The images obtained with AFM and ptychography in the extreme ultraviolet domain show similar features. From [17]

Ptychography is also capable of providing 3D reconstructions of samples using tomographic approaches. Ptychographic X-ray Computed Tomography (PXCT) [91–95] involves placing the sample on a rotation stage and taking a series of 2D ptychography scans at different angles. While widely used at the hard X-ray regime, it has not yet been demonstrated with XUV radiation due to high volumetric absorption and scattering effects. Multi-slice ptychography [13] in contrast is a well-established method for 3D imaging with visible light. Its functioning principle is based on considering the object as a series of slices, whose reconstruction can be obtained by computing the forward scattered fields at each slice but, as for PXCT, this method is not yet available for XUV light. The most promising technique for high-resolution 3D imaging with XUV is Ptychographic Optical Coherence Tomography (POCT). This method combines reflection-mode ptychography with a broadband source and a variable filter. Typical OCT acquisitions are made for each ptychography scan and each frequency in such a way to reconstruct the image of the object in depth [96].

Even though ptychography came up as an evolution of CDI, and therefore with the purpose of studying microscopic samples, one of its most widespread applications is wavefront sensing. The ptychographic algorithm's ability to simultaneously reconstruct the object and the illumination probe makes it a powerful tool for characterizing XUV beams, rivaling traditional methods like Hartmann [97] and interferometry [98]. The

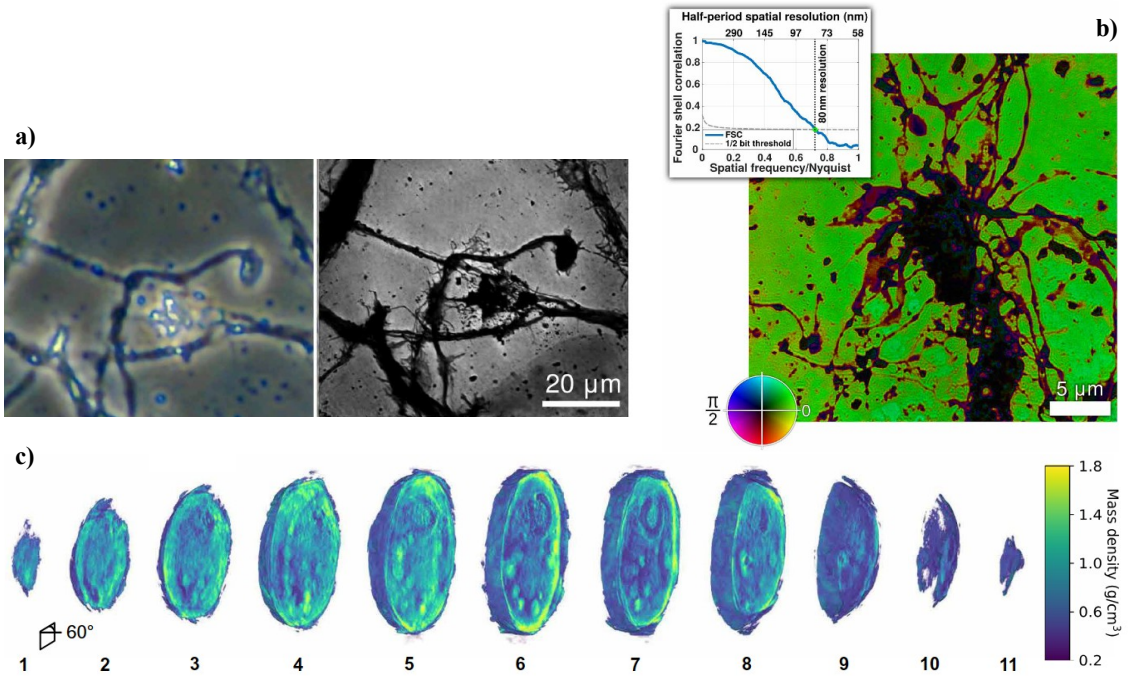


Figure 1.8: (a) Comparison between white-light phase contrast left) and $43eV$ intensity transmission ptychography (right) images of a $85\mu m$-wide area of a fixed mouse brain. An immediately visible higher level of details is captured with XUV ptychography. (b) Amplitude (image intensity) and phase (inset colour wheel) of a neuron sample and its Fourier Ring Correlation (FRC) to estimate an effective image resolution of $80nm$. (c) Ptychography combined with tomography on C. reinhardtii cells, with image intensity proportional to electron dense components. Each section is approximately $1\mu m$ wide and rotated by 60°. (a) and (b) are adapted from [89] while (c) from [91].

reconstruction of the illumination function is typically obtained by scanning the probe beam onto a known object, such as a siemens star, to provide the algorithm a close initial guess therefore improving its convergence. Test objects have also typically high scattering properties at higher diffraction angles, allowing to use most of the dynamic range of the detector and capture also faint speckle details. As for any ptychography scan, the probe's stability is fundamental for entire point-by-point acquisition process to succeed. During the years however, as the level of sophistication of the reconstruction codes increased, even this latter requirement has been relaxed [99]. Hence, ptychography has been used for the determination of aberrations and low-order Zernike polynomials in strongly focused probes, but also for studying structured and multi-wavelength beams.

In the XUV regime, Pelekanidis et al. utilized ptychography for exploring the generation dynamics of beams carrying orbital angular momentum (OAM) in a broad spectrum

from a HHG source [100]. They showed how the quality of the XUV beam is extremely sensitive to the driving laser's focus position into the gas jet, initial aberrations, and topological charge. Fig. 1.9 shows the propagation of XUV beams at different HHG wavelengths along the focal plane position, before and after the correction of astigmatism induced by the focusing optics. Via ptychographic wavefront sensing, the authors first quantified the degree of aberration of the HHG beam, and then the evolution of the rim thickness of the OAM beam as the focal position changes, cross checking the results with simulations. In this way, by characterizing the illumination functions, properties of the focusing optics as well as the optical setup alignment can be inferred and corrected in order to generate spatially controlled beams. Similar conclusions have been obtained, a few years earlier by Pancaldi et al. [83], which demonstrated in a first-time single shot ptychography experiment at an XFEL, that misalignment of K-B mirrors could drive distortions to the donut-like shape of OAM beams produced with a spiral zone plate. These results have particular relevance, since OAMs are gaining attention in multiple fields, in particular for studying chirally active materials, biomolecules and magnetic nanostructures [101]. In all these applications, the quality of the generated wavefront is crucial for obtaining highly accurate results. In the same study, Pancaldi at al. also demonstrated that images with better contrast and resolution could be reconstructed by imparting higher orbital angular momentum to the probe beam scanned during a ptychography acquisition, providing another knob to possibly push forward the resolution in XUV microscopy experiments.

The combination of ptychography's spatial resolution with the ultrashort pulse duration of HHG and XFEL sources is ideal for imaging dynamic nanoscale phenomena. So far, only a single example of time-resolved ptychography with XUV radiation has been reported in literature [15]. In this study, researchers used a pump-probe scheme to visualize the nanoscale thermal and acoustic dynamics in a tapered nanoantenna. The experiment achieved sub-100nm transverse and Angstrom-level axial resolution with a remarkable $10fs$ temporal resolution, as shown in Fig. 1.10. This work opens a new avenue for studying the complex light-activated dynamics of materials, from binary nanoparticles to core-shell structures, where simulations struggle.

This work opens a new avenue for the 3D characterization of spin, charge and lattice dynamics that characterize the light-activated functional response of highly heterogeneous materials such as, for example, binary and core-shell nanoparticles.

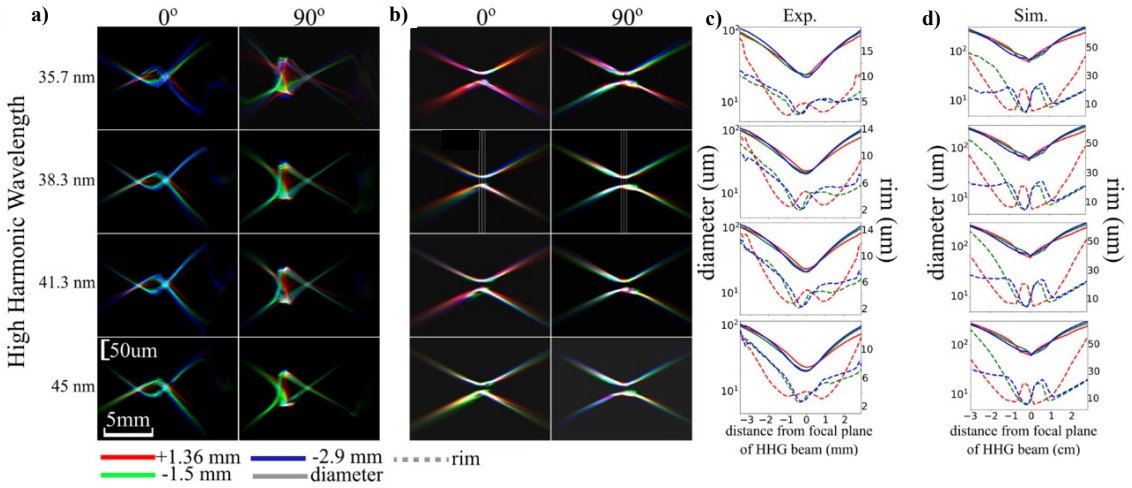


Figure 1.9: Propagation of multiple harmonics of a NIR laser with topological charge $l = 1$. The harmonic upconversion is generated through HHG. The images show the behavior of four harmonics along the focal plane, before and after refocusing, at different position of the laser focus. (a) 0° and 90° visual representation of specific astigmatic XUV wavelengths (35.7nm, 38.3nm, 41.3nm, and 45nm) generated at different focal position with respect to the gas jet source. (b) 0° and 90° visual representation of the same XUV beams with aberrations adjusted by multilayer mirrors after the HHG generation. Different position of the focus with respect of the gas jet are overlayed. (c) Experimentally measured dimensions of the beam's outer diameter and thickness of the corresponding harmonics (following the same line). (d) Simulated outer diameter and thickness profile at the same conditions explained in c. Adapted from [100].

1.6 Scope of the Dissertation

The understanding of fundamental mechanisms underpinning the functionality of materials at the nanoscale, as a response to an external stimulus such as ultrashort laser beam illumination, represents a crucial scientific challenge with deep technological implications. The study of these phenomena is particularly demanding, requiring experimental techniques with both nanometer spatial and femtosecond temporal resolution. Currently, there is a gap in our ability to observe these processes directly. Therefore, this dissertation presents the design, development, implementation, and early commissioning of an innovative XUV-based ultrafast tabletop ptychography microscope. This instrument is specifically designed to overcome the limitations of current state of the art technologies and allow the direct observation of photoinduced dynamics in complex nanostructured systems.

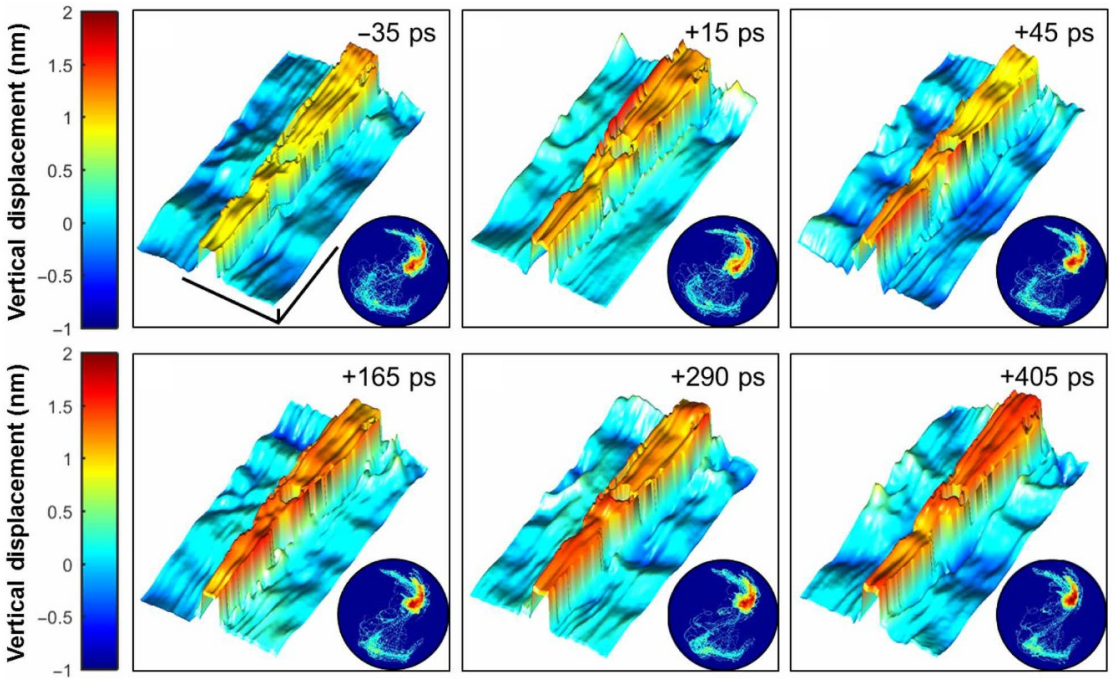


Figure 1.10: Acoustic dynamics of a Ni tapered nanoantenna on a Si substrate retrieved from pump-probe ptychography with 28.9nm XUV beam generated from HHG. All the panels show the reconstructed thermal expansion of acoustic waves propagating in the substrates at different pump-probe delays. The quantitative vertical displacement is common to all the images and reported in the color bars. Every panel also reports a 2D histogram of the real and imaginary part of the complex image, so that the dynamics of the nanoantenna (top area) and the substrate (bottom area) can be individually selected. From [15]

This research details the complete, green-field development of the experimental infrastructure, covering every aspect from the laser source to the final data analysis. We began by optimizing an ultrafast laser source, which serves a dual role: driving the generation of XUV pulses and initiating sample dynamics in pump-probe experiments. This involved rigorous characterization of its power, pointing stability, and spatial, temporal, and spectral profiles. We also carefully selected specific harmonics to generate coherent XUV pulses at wavelengths of 29.1nm (42.6eV) and 12.9nm (96.5eV) using metallic filters and custom multilayer mirrors, achieving photon fluxes of 10^{10} and 10^{12} photons/second, respectively. An extensive effort was dedicated to the detailed optical design of the entire XUV propagation path, from the source to the focusing optical elements, the sample and finally the detector. For the first time on a laboratory-scale setup, we employed advanced ray-tracing methods using the software ShadowOui, a tool typically reserved for large-

scale synchrotron facilities. ShadowOui is an open-source software available through the OrAnge SYnchrotron Suite (OASYS). Ray-tracing has been methodically applied for the definition of the most stringent requirement of the custom XUV multilayer mirrors used for focusing and monochromatizing the incident radiation to the sample plane, evaluating the effects of dimension and divergence of the HHG source, aberrations, slope errors, angles of incidence, demagnification and maximization of the output flux of the system. In parallel, the design of multilayer mirrors' passband requirements have been addressed by a close interaction with world-leading optical manufacturers such as SESO Thales and NTT-AT.

We designed, built, and validated an Ultra-High Vacuum (UHV) chamber to house all the microscopy components while maintaining mechanical stability, ideal flange positioning and magnetic compatibility. All internal components (including mounts for mirrors, sample and detector) were designed for remote actuation, maximizing operational flexibility and throughput. The system incorporates a high-speed CMOS detector for capturing XUV diffraction patterns. The detector-sample distance can be adjusted to vary the NA, allowing for a range of spatial resolutions from $15nm$ to $233nm$. Both the Near-Infrared (NIR) pump and XUV probe arms were designed using 3D CAD models to optimize space and calculate propagation distances. Through this approach, it has been possible to address the optimal position of optical elements for beam demagnification and focusing, as well as the location of the delay line for time-resolved experiments to guarantee sub-50fs resolution.

The overall goal of this work is to build a microscope able to perform full field ptychographic imaging at high spatial and temporal resolution with high throughput, allowing to "film" the ultrafast photoinduced dynamics in different materials. An important feature of this ultrafast microscope is the ability to provide quantitative information by reconstructing amplitude (related to composition) and phase (related to topography) of the sample and the beam. In summary, this thesis documents the complex and multidisciplinary effort required to conceive and realize a unique scientific instrument from the ground up. This work establishes the experimental and methodological foundation for future investigations into ultrafast nanoscale dynamical phenomena, paving the way for their real-time study.

Chapter 2

Diffraction Theory

To reconstruct high-resolution images using Coherent Diffractive Imaging (CDI) and Ptychography, the patterns that arise from a coherent light source interacting with a scattering object are recorded on a detector. The fundamental phenomenon behind this process is diffraction, which describes how light waves behave when they encounter an obstacle or an aperture. Understanding this concept is crucial for the framework of these imaging techniques. Consequently, this chapter provides an in-depth explanation of diffraction, with a specific focus on the principles of Fourier optics, which forms the basis for most of the mathematical modeling in CDI. Many of the derivations in this section are adapted from the work of Goodman [102].

2.1 Classical Electromagnetism and the Wave Equation

The propagation of light is fundamentally described by the classical theory of electromagnetism, articulated by Maxwell's Equations. In vacuum, with no free charge ρ and current density j, these four relations are:

$$\text{Gauss's Law for the electric field:} \quad \nabla \cdot \mathbf{D} = 0, \tag{2.1}$$

$$\text{Gauss's Law for the magnetic field:} \quad \nabla \cdot \mathbf{B} = 0, \tag{2.2}$$

$$\text{Faraday's Law:} \quad \nabla \times \mathbf{E} = -\frac{\partial \mathbf{B}}{\partial t}, \tag{2.3}$$

$$\text{Ampère-Maxwell's Law:} \quad \nabla \times \mathbf{H} = \frac{\partial \mathbf{D}}{\partial t}, \tag{2.4}$$

where ∇ is the gradient operator in three dimensions, $\mathbf{E}$ is the electric field, $\mathbf{H}$ is the magnetizing field, $\mathbf{D}$ is the electric displacement and $\mathbf{B}$ is the magnetic field. Assuming that the electric and magnetic fields are propagating inside a linear, isotropic and homogeneous dielectric medium, the following dependences, known as constitutive relations, hold:

$$\mathbf{D} = \epsilon\mathbf{E}, \tag{2.5}$$

$$\mathbf{B} = \mu\mathbf{H}, \tag{2.6}$$

in which ϵ is the electric permittivity and μ is the magnetic permeability inside the medium. Taking the curl of Faraday's law, eq. (2.3) looks like

$$\nabla \times (\nabla \times \mathbf{E}) = -\nabla \times \frac{\partial \mathbf{B}}{\partial t} = -\frac{\partial}{\partial t}(\nabla \times \mathbf{B}). \tag{2.7}$$

Combining eq. (2.1) with eqs. (2.4) to (2.7) and the vectorial relationship $\nabla \times (\nabla \times \mathbf{A}) = \nabla (\nabla \cdot \mathbf{A}) - \nabla^2\mathbf{A}$, it is possible to obtain the homogeneous wave equation:

$$\nabla^2\mathbf{E} - \mu\epsilon\frac{\partial^2\mathbf{E}}{\partial t^2} = 0. \tag{2.8}$$

Two relevant definitions are introduced which relate the properties of the propagating medium: the refractive index and speed of light. The refractive index in the medium is defined as

$$n = \sqrt{\frac{\mu\epsilon}{\mu_0\epsilon_0}}, \tag{2.9}$$

where μ_0 and ϵ_0 are the magnetic permeability and the electric permittivity in vacuum respectively. In vacuum the refractive index is unitary. The speed of light, c in vacuum is

$$c = \frac{1}{\sqrt{\mu_0\epsilon_0}} = 299\,792\,458\ m/s. \tag{2.10}$$

For eq. (2.8), it follows that:

$$\nabla^2\mathbf{E} - \frac{n^2}{c^2}\frac{\partial^2\mathbf{E}}{\partial t^2} = 0. \tag{2.11}$$

The ratio $c/n = v = \sqrt{\mu\epsilon}$ is interpreted as the speed of the electromagnetic wave inside the dielectric medium. Following similar steps but starting from eq. (2.4), the wave equation

referred to the magnetic field can be obtained as

$$\nabla^2 \mathbf{B} - \frac{n^2}{c^2}\frac{\partial^2 \mathbf{B}}{\partial t^2} = 0 \tag{2.12}$$

However, the following approximations and derivations are based solely on eq. (2.11), as the magnetic field amplitude is considerably smaller than that of the electric field in the propagation medium.

2.2 Scalar Theory and Helmholtz Equation

Altough light waves are vectorial entities, in many situations and especially when polarization is not of primary interest (or could be treated separately), physics problems may be simplified by using a scalar theory. This allows us to simplify the problem by using scalar electric field to find a solution to the wave equation, eq. (2.11). Let the scalar perturbation ψ be a generic solution such that

$$\nabla^2 \psi - \frac{n^2}{c^2}\frac{\partial^2 \psi}{\partial t^2} = 0. \tag{2.13}$$

ψ could, for example, be a field emerging from the iterations between light and matter.Assuming a monochromatic wave, i.e. with a singular angular frequency ω, the solution can be written as the product of two separate independent functions

$$\psi\left(\mathbf{r},\ t\right) = \psi\left(\mathbf{r}\right) e^{-i\omega t}. \tag{2.14}$$

$\psi(r)$ represents the complex amplitude of the perturbation describing the spatial distribution of the field. Substituting this form into eq. (2.13), and noting that $\partial_t^2 e^{-i\omega t} = -\omega^2 e^{-i\omega t}$, it is possible to obtain:

$$\nabla^2 \psi\left(\mathbf{r}\right) e^{-i\omega t} - \frac{n^2}{c^2}\left(-\omega^2\right)\psi(\mathbf{r}) e^{-i\omega t} = 0. \tag{2.15}$$

Simplifying the exponential factor and introducing the wavevector $k = \omega/c = 2\pi/\lambda$, where λ is the wavelength of the electromagnetic radiation, the Helmholtz equation is obtained:

$$(\nabla^2 + n^2 k^2)\psi(\mathbf{r}) = 0. \tag{2.16}$$

The Helmholtz equation describes the spatial distribution of a monochromatic wave in a homogeneous medium with refractive index n. For polychromatic waves, i.e. composed by multiple frequencies, it is possible to apply the Helmholtz equation to each spectral component independently, by expressing ψ as a Fourier decomposition with respect to time:

$$\psi\left(\mathbf{r},t\right)=\frac{1}{\sqrt{2\pi}}\int_{0}^{\infty}a(\omega)\psi(\mathbf{r})e^{-i\omega t}d\omega. \tag{2.17}$$

In eq. (2.17), $\psi(r)$ is the spatial component of a monochromatic wave and $a(\omega)$ is the spectral amplitude, a square integrable function that ensures the integral to converge. In this dissertation, the different wavelengths are treated as orthogonal modes, as any interaction between them lies beyond the temporal and spectral resolution of current detection systems. Conveniently we can define the complex wavefield $\psi(\mathbf{r})$ as composed by a real amplitude $A(\mathbf{r})$ and a phase $\phi(\mathbf{r})$:

$$\psi\left(\mathbf{r}\right)=A\left(\mathbf{r}\right)e^{i\phi(\mathbf{r})}. \tag{2.18}$$

The intensity measured at the detector is:

$$I\left(\mathbf{r}\right)=\left|\psi\left(\mathbf{r}\right)\right|^{2}=\ A\left(\mathbf{r}\right)^{2}. \tag{2.19}$$

Equation (2.19) highlights the phase problem: measuring the intensity of a wavefield only provides information about its amplitude, while the phase is inevitably lost. As a consequence, the phase loss prevents the direct reconstruction of the complex wavefield $\psi(\mathbf{r})$, and therefore of the object's structure responsible for its formation.

2.3 Propagation of Waves: the Angular Spectrum

A central problem in diffraction theory is calculating how a wavefield propagates from one plane to another. The angular spectrum approach provides an elegant and computationally efficient solution based on Fourier transform.

Let us start from a monochromatic field $\psi(x,y,z)$ satisfying the Helmholtz equation, and suppose we know its value at $z=0$. To calculate $\psi(x,y,z)$ at a distance $z>0$ from the known initial plane $\psi(x,y,0)$, the idea is to decompose $\psi(x,y,z)$ in elementary plane

waves through a 2D Fourier transform with respect to the transverse coordinates x and y:

$$\psi(x, y, z) = \iint_{-\infty}^{+\infty} \widetilde{\psi}\left(f_x, f_y, z\right) e^{i2\pi(f_x x + f_y y)} df_x df_y. \tag{2.20}$$

The term $\widetilde{\psi}(f_x, f_y, z)$ represents the angular spectrum at the plane z with f_x, f_y spatial frequencies. Each component $\widetilde{\psi}\left(f_x, f_y, z\right) e^{i2\pi(f_x x + f_y y)}$ represents a plane wave propagating towards a direction defined by the wavevector $\mathbf{k} = (k_x, k_y, k_z)$ where $k_x = 2\pi f_x$, $k_y = 2\pi f_y$ and k_z is determined by the relation $k_x^2 + k_y^2 + k_z^2 = k^2 = (2\pi/\lambda)^2$. Through these relations k_z is

$$k_z = \sqrt{k^2 - k_x^2 - k_y^2} = \frac{2\pi}{\lambda}\sqrt{1 - (\lambda f_x)^2 - \left(\lambda f_y\right)^2}. \tag{2.21}$$

Substituting eq. (2.20) in eq. (2.16) and assuming that the propagation takes place in vacuum (therefore the refractive index n becomes unitary), it is possible to obtain an ordinary differential equation that describes the evolution of each component of the angular spectrum along the propagation direction z. This function looks like

$$\frac{d^2\widetilde{\psi}\left(f_x, f_y, z\right)}{dz^2} + k_z^2\widetilde{\psi}(f_x, f_y, z) = 0, \tag{2.22}$$

and a solution, under the assumption of a homogeneous medium and considering only the forward-propagating components (neglecting back-reflections) along the propagation direction z, can be expressed as

$$\widetilde{\psi}\left(f_x, f_y, z\right) = \widetilde{\psi}\left(f_x, f_y, 0\right) e^{ik_z z} = \widetilde{\psi}\left(f_x, f_y, 0\right) e^{\frac{i2\pi z}{\lambda}\sqrt{1-(\lambda f_x)^2-\left(\lambda f_y\right)^2}}. \tag{2.23}$$

This equation shows that during the propagation, the angular spectrum of the initial field is multiplied by a phase term which depends on the individual spatial components. This factor is known as "Free space propagator" or "Free space transfer function" but can be generalized to homogeneous media with constant refractive index as

$$H\left(f_x, f_y, z\right) = e^{\frac{i2\pi n z}{\lambda}\sqrt{1-(\lambda f_x)^2-\left(\lambda f_y\right)^2}}. \tag{2.24}$$

The propagation can be written both in the spatial frequency domain,

$$\widetilde{\psi}\left(f_x, f_y, z\right) = \widetilde{\psi}\left(f_x, f_y, 0\right) H(f_x, f_y, z), \tag{2.25}$$

and in the real space by using the inverse Fourier transform:

$$\psi(x, y, z) = F^{-1}\{F\{\psi(x, y, 0)\} H\left(f_x, f_y, z\right)\}. \tag{2.26}$$

Here F and F^{-1} denote forward and inverse Fourier transforms with respect to the transverse coordinates x and y.

It is now worth examining the behaviour of H and, in particular, what happens when the value under the square root in eq. (2.24) is either positive or negative. In case $\lambda^2\left(f_x^2 + f_y^2\right) > 1$, the result of the square root becomes complex and $H = e^{-|k_z|z}$ corresponds to a rapidly decaying factor. This is why high spatial frequency components are attenuated in a short distance (a few wavelengths) and do not contribute to the far field distribution. These waves are called "Evanescent waves". On the other side, when $\lambda^2\left(f_x^2 + f_y^2\right) \leq 1$, the square root and k_z are real, and H is a phase factor with amplitude $|H| = 1$. In other words, the components of the lateral spectral decomposition of the wavefield continuously change their relative phases as an effect of propagation over a distance z, due to the oscillatory behaviour of the exponential function.

2.4 Near-field Diffraction or Fresnel Approximation

While the exact expression for retrieving the complex field distribution via the Angular Spectrum Method provides a rigorous description of wave propagation within the framework of scalar diffraction theory, its numerical implementation can be computationally demanding. Under specific conditions, however, physical approximations can be introduced to simplify the mathematical operations. Among these, the Fresnel approximation, also known as "Paraxial", "Near-field" or "Small-angle" approximation, is valid when the field has a small angular spread, meaning that its lateral extent is small compared to the distance separating the input and output planes over which the propagation occurs. In mathematical terms, this condition translates to

$$\lambda^2\left(f_x^2 + f_y^2\right) \ll 1. \tag{2.27}$$

Hence, it is possible to approximate the exponential of the transfer function H using the binomial expansion $\sqrt{1-\epsilon} \approx 1 - \epsilon/2$, being $\epsilon \ll 1$. It follows that

$$\sqrt{1 - \lambda^2 \left(f_x^2 + f_y^2\right)} \approx 1 - \frac{\lambda^2}{2}\left(f_x^2 + f_y^2\right). \tag{2.28}$$

Substituting this formula inside the exponential term of $H\left(f_x, f_y, z\right)$ in eq. (2.24), it is straightforward to obtain the Fresnel transfer function as

$$H_{fresnel}\left(f_x, f_y, z\right) = e^{i2\pi nz/\lambda} e^{-i\pi n\lambda z\left(f_x^2 + f_y^2\right)} \tag{2.29}$$

and, in the frequency domain, the output field on the plane at distance z as

$$\widetilde{\psi}\left(f_x, f_y, z\right) \approx \widetilde{\psi}\left(f_x, f_y, 0\right) e^{i2\pi nz/\lambda} e^{-i\pi n\lambda z\left(f_x^2 + f_y^2\right)}. \tag{2.30}$$

Going back to the spatial domain, this multiplication operation is equivalent to the convolution

$$\psi(x, y, z) \approx \psi(x, y, 0) * h_{fresnel}(x, y, z), \tag{2.31}$$

where the latter term $h_{fresnel}(x, y, z)$ is the impulsive Fresnel response given by the inverse Fourier transform of $H_{fresnel}$:

$$h_{fresnel}(x, y, z) = F^{-1}\left\{H_{fresnel}\right\} = \frac{e^{i2\pi nz/\lambda}}{i\lambda z} e^{-\frac{i\pi n\left(x^2+y^2\right)}{\lambda z}}. \tag{2.32}$$

This quadratic phase term is typical of propagation in the Fresnel regime (near-field). Now we have all the pieces to completely define the Fresnel diffraction integral in two alternative but equal forms:

$$\psi(x, y, z) = \frac{e^{i2\pi nz/\lambda}}{i\lambda z} \iint_{-\infty}^{+\infty} \psi(\xi, \eta, 0) e^{\frac{i\pi n}{\lambda z}\left[(x-\xi)^2 + (y-\eta)^2\right]} d\xi d\eta \tag{2.33}$$

$$\begin{aligned}\psi(x, y, z) = \frac{e^{\frac{i2\pi nz}{\lambda}}}{i\lambda z} e^{\frac{i\pi n}{\lambda z}\left(x^2+y^2\right)} \iint_{-\infty}^{+\infty} \left\{\psi(\xi, \eta, 0) e^{\frac{i\pi n}{\lambda z}\left(\xi^2+\eta^2\right)}\right\} e^{-\frac{i2\pi n}{\lambda z}(x\xi+y\eta)} d\xi d\eta = \\ = \frac{e^{i2\pi nz/\lambda}}{i\lambda z} e^{\frac{i\pi n}{\lambda z}(x^2+y^2)} F\{\psi(\xi, \eta, 0) e^{\frac{i\pi n}{\lambda z}\left(\xi^2+\eta^2\right)}\}\end{aligned} \tag{2.34}$$

Both expressions are equally valid: the first highlights the convolutional operation and is better suited for computation of propagating fields over small distances, while the latter is a relatively "simple" bidimensional Fourier transform with two conjugate variables (ξ, η) and $\left(\frac{x}{\lambda z}, \frac{y}{\lambda z}\right)$, typically employed for describing propagations over longer distances.

2.5 Far-field Diffraction or Fraunhofer Approximation

The Fraunhofer approximation is a limit case of Fresnel approximation. It is valid if the propagation distance is high enough to let the quadratic phase term $e^{\frac{i\pi n}{\lambda z}(\xi^2+\eta^2)}$ of eq. (2.34) become unitary on the entire region where $\psi(\xi, \eta, 0)$ is not null. Mathematically speaking, the formal condition is

$$z \gg \frac{i\pi n}{\lambda}\left(\xi^2 + \eta^2\right)_{\max} \tag{2.35}$$

In this case, the Fresnel diffraction integral further simplifies to

$$\psi(x, y, z) \approx \frac{e^{\frac{i2\pi nz}{\lambda}}}{i\lambda z} e^{\frac{i\pi n}{\lambda z}(x^2+y^2)} \iint_{-\infty}^{+\infty} \psi(\xi, \eta, 0) e^{-i2\pi\left(\frac{nx}{\lambda z}\xi + \frac{ny}{\lambda z}\eta\right)} d\xi d\eta \tag{2.36}$$

and recognizing the integral as the Fourier transform of the field $\psi(\xi, \eta, 0)$ evaluated on spatial frequencies $f_x = nx/\lambda z$ and $f_y = ny/\lambda z$, the Fraunhofer diffraction integral can be stated as:

$$\psi(x, y, z) \approx \frac{e^{\frac{i2\pi nz}{\lambda}}}{i\lambda z} e^{\frac{i\pi n}{\lambda z}(x^2+y^2)} \widetilde{\psi}\left(\frac{nx}{\lambda z}, \frac{ny}{\lambda z}, 0\right). \tag{2.37}$$

This result means that, besides a multiplicative phase factor (including a residual quadratic term) and an amplitude modulation term, the wavefield in Fraunhofer regime (or far-field) is directly proportional to the Fourier transform of the wavefield distribution on the initial plane. Often, only the intensity $|\psi(x, y, z)|^2$ of such a field is detected, therefore allowing to completely neglect the phase terms. In this case, the intensity of the far-field diffraction is proportional to the square modulus of the Fourier transform of the field distribution on the initial plane.

2.6 The Fresnel Number

To determine whether the Fresnel or the Fraunhofer diffraction regime is the most appropriate to describe an experimental configuration, a dimensionless quantity known as

"Fresnel number" is often used:

$$F_N = \frac{a^2}{\lambda z}, \tag{2.38}$$

in which a is a characteristic dimension of the aperture or the object present in the initial plane at $z = 0$. The three regimes so far described in terms of their propagator can be distinguished based on the value of F_N:

- $F_N \ll 1$: Fraunhofer regime
- $F_N \geq 1$: Fresnel regime
- $F_N \gg 1$: Angular spectrum method and geometrical optics.

Therefore, by using the Fresnel number, a general indication about the most appropriate propagation method is available.

2.7 Scattering Theory

We will now proceed in formulating the theory of diffraction using the formalism of scattering physics. A complete and exhaustive discussion is beyond the scope of this chapter and can be found in literature [103, 104].

The interaction between a wavefield $\psi(\mathbf{r})$ and an object can be described by extending the time-independent Helmholtz equation to include a source term. This term links the spatial variation of the wavefield to the local change of refractive index $n(\mathbf{r})$, relative to the surrounding environment. Therefore, we can reformulate eq. (2.16) to highlight such a source term and express the Helmholtz equation in its inhomogeneous form:

$$\left(\nabla^2 + k^2\right)\psi\left(\mathbf{r}\right) = -k^2\left(n^2\left(\mathbf{r}\right) - 1\right)\psi\left(\mathbf{r}\right) = -f\left(\mathbf{r}\right)\psi(\mathbf{r}) \tag{2.39}$$

Here k represents the wavevector in vacuum while the term $f\left(\mathbf{r}\right) = k^2(n^2\left(\mathbf{r}\right)-1)$ is defined as the "scattering potential". This function quantifies how strong the input wavefield is deviated from its propagation direction in free space when an object intercepts it (for $n = 1, f\left(\mathbf{r}\right)$ becomes equal to zero). In the XUV/Soft X-ray regime, the refractive index is close to unity and can be expressed as a continuous complex function of both space $\mathbf{r}$ and wavelength λ,

$$n\left(\mathbf{r}, \lambda\right) = 1 - \delta\left(\mathbf{r}, \lambda\right) + i\beta(\mathbf{r}, \lambda). \tag{2.40}$$

At the moment, it is sufficient to know that the real (δ) and imaginary (β) parts of the refractive index describe the dispersive and absorptive components of the interaction between the radiation and the object. Their meaning and their exact formula will be detailed in section 2.9. Now, for the sake of simplicity, we will neglect the dependence on the wavelength and work with $n(\mathbf{r})$. Since δ and β are much lower than unity, the quadratic products simplify and the optical properties of the material are linked to the scattering potential via

$$f(\mathbf{r}) = k^2\left(n^2(\mathbf{r}) - 1\right) \approx k^2(1 - 2\delta(\mathbf{r}) + 2i\beta(\mathbf{r}) - 1) \approx -2k^2(\delta(\mathbf{r}) - i\beta(\mathbf{r})). \quad (2.41)$$

The results show how scattering is guided by the capability of the sample's constitutive elements to change the phase and absorb the input light by means of δ and β. The general solution to eq. (2.39) can be through of as the sum of the unperturbed incident wave $\psi_i(r)$, which satisfies the homogeneous Helmholtz equation $\left(\nabla^2 + k^2\right)\psi_i(\mathbf{r}) = 0$, and a scattering wave $\psi_s(r)$ generated from the interaction with the $f(r)$ potential, through the equation

$$\left(\nabla^2 + k^2\right)\psi_s(\mathbf{r}) = -f(\mathbf{r})\,\psi(\mathbf{r}). \quad (2.42)$$

This inhomogeneous differential equation can be analytically solved by means of Green's functions, leading to an integral equation where the scattered beam $\psi_s(\mathbf{r})$ depends both on the scattering potential and on the total field inside the material, integrated over the entire object's volume:

$$\psi_s(\mathbf{r}) = \int f(\mathbf{r}')\,G(\mathbf{r},\mathbf{r}')\,\psi(\mathbf{r}')\,d^3\mathbf{r}'. \quad (2.43)$$

2.8 The Born Approximation

Solving the integral eq. (2.43) for $\psi_s(\mathbf{r})$ is not a straightforward operation, requiring the knowledge of the total field $\psi(\mathbf{r})$, which in turn depends on $\psi_s(\mathbf{r})$ itself. The Born approximation, or single-scattering approximation, drastically simplifies the problem by assuming that the amplitude of the scattered wave is much lower than the incident one ($|\psi_s| \ll |\psi_i|$). This practically means that the scattering inside the material is *weak*. This hypothesis allows substituting the total field $\psi(\mathbf{r}')$ inside the integral equation with the

known input field $\psi_i(\mathbf{r}') = e^{i\mathbf{k_0}\cdot\mathbf{r}}$. The scattered wave then becomes

$$\psi_s(\mathbf{r}) = \int f(\mathbf{r}') \frac{e^{ik|\mathbf{r}-\mathbf{r}'|}}{|\mathbf{r}-\mathbf{r}'|} e^{i\mathbf{k_0}\cdot\mathbf{r}'} d^3\mathbf{r}', \tag{2.44}$$

where Green's function has been introduced. Green's function represents a spherical wave propagating in free space from the scattering point $\mathbf{r}'$ to the observation point $\mathbf{r}$:

$$G(\mathbf{r},\mathbf{r}') = \frac{e^{ik|\mathbf{r}-\mathbf{r}'|}}{|\mathbf{r}-\mathbf{r}'|}. \tag{2.45}$$

When the observation point is far enough away that the size of the scatterer is negligible compared to the distance to the observation point, $|\mathbf{r}| \gg |\mathbf{r}'|$, $|\mathbf{r}-\mathbf{r}'| \approx \mathbf{r}$. With this approximation we can define $\mathbf{k} = k_0\widehat{\mathbf{r}}$ and the momentum transfer vector (or scattering vector) as:

$$\mathbf{q} = \mathbf{k} - \mathbf{k_0} \tag{2.46}$$

This allows us to simplify eq. (2.44), after some simple mathematical manipulation to:

$$\psi_s(\mathbf{r}) = \frac{e^{i\mathbf{k_0}\mathbf{r}}}{\mathbf{r}} \widetilde{f}(\mathbf{q}), \tag{2.47}$$

where the tridimensional Fourier transform of the scattering potential, $f(\mathbf{r}')$, is written as $\widetilde{f}(\mathbf{q}) = \int f(\mathbf{r}')\, e^{i\mathbf{q}\cdot\mathbf{r}'} d^3\mathbf{r}$. This result is of particular relevance: it states that the complex amplitude of the scattered wave in a certain direction (defined by the momentum transfer vector $\mathbf{q}$) is directly proportional to the Fourier transform of the object's scattering potential corresponding to that direction. This implies that, in a scattering experiment, the measured diffracted intensity as a function of the scattering angle provides access to the squared modulus of the Fourier transform of the object's scattering potential, from which the spatial distributions of $\delta(\mathbf{r})$ and $\beta(\mathbf{r})$ can be inferred.

2.9 X-Ray-Matter Interaction: Atomic Scattering Factors and Contrast Generation in Imaging

In the previous paragraphs we anticipated the existence of the complex refractive index $n(\mathbf{r},\lambda)$ (see eq. (2.40)), at the basis of the amplitude and phase modulation of light entering the object. Now, we go deeper into the details of δ and β,which are respectively

the functions responsible for the phase detuning and the attenuation. The macroscopic properties of δ and β depend on the interaction between the incoming radiation and the single atoms composing the material. This interaction is described by the atomic scattering factors, $f_1(\lambda)$ and $f_2(\lambda)$, which are the real and the imaginary part of a complex atomic form factor $f(\lambda) = f_1(\lambda) + i f_2(\lambda)$. In particular, the relationships are:

$$\delta(r, \lambda) = \frac{n_a(r) r_e \lambda^2}{2\pi} f_1(\lambda), \tag{2.48}$$

$$\beta(r, \lambda) = \frac{n_a(r) r_e \lambda^2}{2\pi} f_2(\lambda). \tag{2.49}$$

The $n_a(\mathbf{r})$ is the number of atoms per unit volume in a particular point $\mathbf{r}$ and $r_e \approx 2.818 \times 10^{-15}$ m is the classical radius of the electron. $f_1(\lambda)$ quantifies the capability of an atom to elastically scatter the radiation with the same phase as the input wave, providing a quantification of the dephasing δ. The variable $f_2(\lambda)$ is instead a measure of an atom's capability to absorb the input radiation (typically through the photoelectric effect for x-rays), therefore contributing to its attenuation β. It is fundamental to notice that both $f_1(\lambda)$ and $f_2(\lambda)$ strongly depend on the chemical elements composing the material or the energy of the incident photons. In particular, both functions present discontinuities when approaching the so-called "absorption edges". These edges are specific energies at which the excitation or ionization of core electrons occurs. The dependence of scattering factors in proximity to these specific energy regions stands at the basis of the exquisite elemental and chemical contrast of x-ray spectroscopy and imaging techniques. A region with high β value will be characterized by a higher level of absorption, resulting in a lack of signal and therefore a darker region, similarly to what happens in conventional radiography.

Phase contrast is instead generated by the dephasing

$$\phi(x, y) = -(2\pi/\lambda) \int \delta(x, y, x) dz \tag{2.50}$$

experienced by the wave passing through the sample. Since δ is related to the electronic density ρ_e though the formula $\delta = \frac{r_e \lambda^2}{2\pi} \rho_e$, the phase contrast is intrinsically sensitive to the density variations inside the material. Through this relation, CDI and Ptychography techniques can obtain, through iterative algorithms, quantitative maps of the projected electronic density inside the samples.

It is now possible to model the monochromatic wave $\psi(\mathbf{r})$ as the product of two

separate functions in the plane transverse to the propagation direction z, with $\mathbf{x} = [x, y]$:

$$\psi(\mathbf{x}) = O(\mathbf{x})P(\mathbf{x}). \tag{2.51}$$

From this moment on, $\psi(\mathbf{x})$ will be referenced as "exit surface wave", that is the wavefield directly behind the object, with $P(\mathbf{x})$ the incident wave in correspondence to the sample plane, and $O(\mathbf{x})$ the complex transmission function. This definition embeds both the information on phase shifting and absorption through the formula:

$$O(\mathbf{x}) = A(\mathbf{x})e^{i\phi(x)} \tag{2.52}$$

where

$$A(\mathbf{x}) = e^{-\frac{2\pi}{\lambda}\int_0^T \beta(\mathbf{x},z)dz} \tag{2.53}$$

$$\phi(\mathbf{x}) = \frac{2\pi}{\lambda}\int_0^T \delta(\mathbf{x}, z)dz \tag{2.54}$$

are the amplitude and phase contribution of an object with thickness T along the propagation direction of the wavefield. This formulation adds an additional level of detail compared to eq. (2.18) since the values of the exit surface wave are now linked to the properties of the object undergoing the interaction with the coherent light.

Chapter 3

Coherent Diffractive Imaging (CDI) and Ptychography

Coherent Diffractive Imaging techniques represent a lensless imaging modality capable of reconstructing the structure of an object from its diffraction pattern. As described in section 1.4, CDI is particularly relevant for XUV and soft X-ray light, due to the difficult manufacturing of lenses.

3.1 The Phase Problem

As briefly introduced in sections 1.4 and 2.2, when the exit surface wave ψ propagates to the far field (Fraunhofer regime),it undergoes a linear transformation, as expressed in eq. (2.36). The diffracted field $\widetilde{\psi}(\mathbf{f})$, apart from multiple phase factors, is equal to the Fourier transform of the field $\psi(x, y, z = 0)$, which appears inside the integral. When such a wavefield, mathematically expressed in complex notation as $\widetilde{\psi}(\mathbf{f}) = A(\mathbf{f})e^{i\phi(\mathbf{f})}$, is interjected by the detector, the device measures its intensity $I(\mathbf{f}) = \left|\widetilde{\psi}(\mathbf{f})\right|^2 = A(\mathbf{f})^2$. The amplitude can be calculated as the square root of the intensity, however this is not sufficient for calculating the initial field applying an inverse Fourier transform, since the information about the phase ϕ is still required. The Fourier transform is indeed a global operation and the phase at each point in the reciprocal space encodes the relative interference of all scattered waves from the sample. Hence, without the phase information, the inverse Fourier transform cannot be uniquely performed, preventing the reconstruction of the exit surface wave and, as a last step, the decoupling of the illumination $P(\mathbf{x})$ from the complex

transmission function of the object $O(\mathbf{x})$ (as defined in eq. (2.51)). The recovery of the phase from intensity data only is conventionally called "the phase problem" and is the central challenge that CDI techniques have been developed for.

3.2 CDI Requirements

The successful application of CDI relies on applying constraints to both the illumination function and the object during the iterative phase retrieval algorithm.

The first requirement of CDI is the use of coherent illumination light. Coherence is a measure of the correlation between the wave and itself in both space and time. Although perfectly coherent sources do not exist in practice, CDI requires illumination with a high degree of coherence to produce stable diffraction patterns that accurately encode the object's structural information in the far field. It is possible to distinguish spatial and temporal coherence (see Fig. 3.1. Spatial coherence is also known as transverse coherence and represents the area over which the illuminating wavefront (therefore transverse to the propagation direction of the beam) maintains a correlated phase. During a CDI experiment the illuminated region of the sample shall fall into an area of high spatial coherence, which can be quantified by using the horizontal and vertical transverse coherence length, respectively $L_h = \lambda R/a_h$ and $L_v = \lambda R/a_v$. These numbers denote the distance over which coherence is maintained in the two orthogonal directions on the wavefront, they are inversely proportional to the size of the source $a_{h,v}$ and directly proportional to both wavelength λ and the propagation distance from the source R. Therefore, having a sufficiently large coherence length is a critical parameter for beamline design. Temporal coherence instead is a measure of the phase correlation along the propagation direction (therefore the longitudinal one). This is intrinsically relating to the degree of monochromaticity of the illumination, which can be quantified by its spectral bandwidth $\Delta\lambda$, as shown in Fig. 3.1c and Fig. 3.1d. The temporal coherence length is approximately $L_l \approx \lambda^2/2\Delta\lambda$, here the exact prefactor changes in accordance with spectral density of the source. As seen in the definition, beams with a narrow bandwidth have longer coherence lengths. The attainable resolution in a CDI experiment is limited by the temporal coherence of the illumination. To ensure high-angle interference and prevent blurring of the diffraction pattern, the optical path length difference for waves scattered from opposite sides of the object must be smaller than the longitudinal coherence length. While conventionally CDI requires a high level of coherence, recent advancements such as multi-mode ptychography have

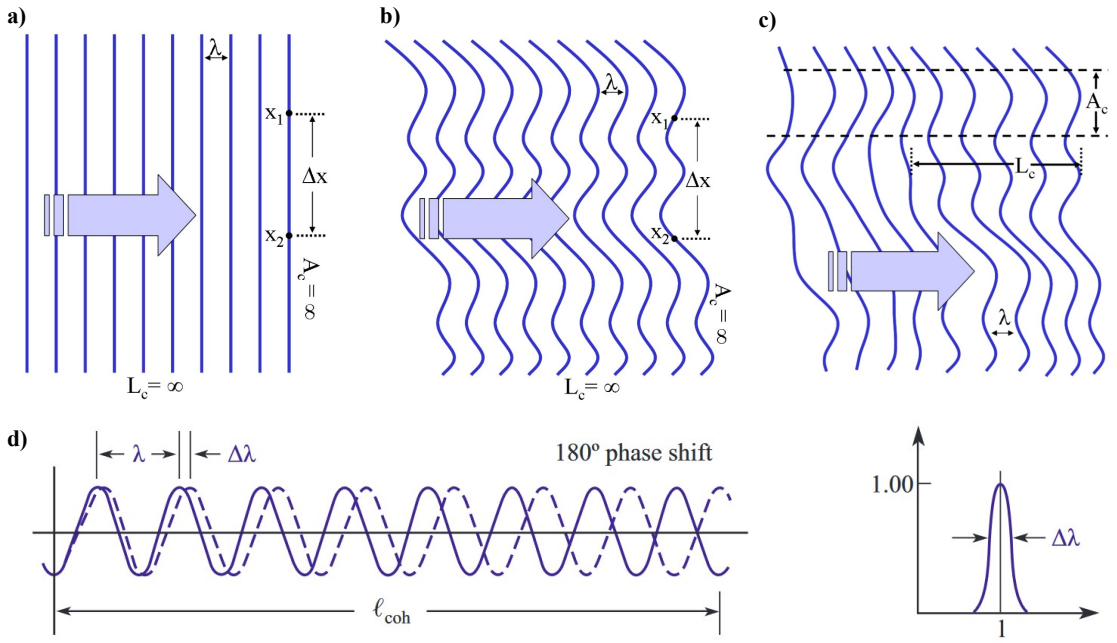


Figure 3.1: Spatial and temporal coherence concepts. (a) A beam with wavelength λ possessing an infinite coherence area and coherence length. Δx measures the distance between two arbitrary points on the same wavefront. (b) Partially coherent wave with infinite coherence length but finite coherence area, (c) A partially coherent wave with both finite coherence area and length. (d) Two waveforms possessing a slight $\Delta\lambda$ difference, the longitudinal coherence length marks the point of 180° phase shift. The spectral linewidth of the source is also shown. (a)-(c) adapted from [105]. (d) adapted from [52].

relaxed this requirement avoind the implementation of flux-reducing methods to improve the coherence of the sources (e.g. with apertures).

Beside coherence, overcoming the phase problem also requires the collection of a sufficient amount of information by sampling the diffracted intensity pattern. In conventional CDI where a single diffraction pattern from an isolated object is used, the principle of "oversampling" is applied. From Shannon's sampling theorem and Sayre's contribution, it is known that retrieving the phase becomes possible if the diffraction pattern is sampled at a rate higher than the Nyquist limit determined by the spatial extent of the illuminated object. In order to obtain sufficient information from a bidimensional object and avoid aliasing effects during reconstruction, its diffraction pattern shall be sampled in such a way that $\sigma \geq 2$ [73, 106, 107]. This requirement imposes several constraints when designing

an experimental geometry. The equation governing the oversampling is

$$\sigma = \frac{\lambda z}{pD}, \tag{3.1}$$

where λ is the wavelength, z the sample to detector distance, p the pixel size of the detector and D the probe's diameter. In practice, the quantity $\lambda z/D$ reflects the size of the smallest speckle grain at the detector distance z from the sample. By stating that $\sigma \geq 2$, the implicit requirement is that the detector's pixel must be able to sample the speckle at least twice. This relation is crucial since it allows to directly correlate the amount of information captured from a diffraction pattern to the experimental conditions and highlights the trade-offs to be faced during the design phase. For a given wavelength and detector, the only way to increase the oversampling is either increasing the sample-detector distance or reducing the object's size. On the other side, to to achieve $\sigma \geq 2$ when wavelength and detector distance are fixed parameters, the probe's diameter shall be

$$D \leq \frac{\lambda z}{2p}. \tag{3.2}$$

This sampling requirement also implies that, to reconstruct larger objects in CDI, a finer detector grid is needed. In practice, experimental CDI often need $\sigma \geq 4$ for an increase robustness of the phase retrieval process against noise and experimental imperfections.

3.3 Ptychography Requirements

Ptychography addresses the phase problem by scanning a localized illumination probe on sufficiently overlapped points across an extended sample, allowing for the acquisition of multiple diffraction patterns. While the oversampling requirement is still crucial, an additional parameter is the degree of overlap between consecutive probe positions. Sufficient overlap ensures that each point inside the specimen is illuminated multiple times, thereby generating a high redundancy of information for a robust phase retrieval. Compared to conventional CDI, the minimum sampling condition is not dictated by the sampling in reciprocal space, which in ptychography is determined by the probe size, being smaller than the object, but also by real-space sampling. In a simplified one-dimensional scenario, the minimum product of the real-space sampling interval ΔR and the reciprocal

space sampling interval Δu must satisfy the following equation [11, 108]:

$$\Delta R \Delta u = 2. \tag{3.3}$$

This relationship demonstrates flexible trade-off between sampling density in real space and Fourier space, allowing the same quantity of information to be preserved. Contrary to the requirement in CDI, it is possible to use a large probe that generates an under sampled diffraction pattern at the pixelated detector. This is possible as long as the real space sampling (the amount of spatial overlap between scans) is increased. However, a drawback of this approach is the potential for longer acquisition times, as a higher number of overlaps requires more time to cover the same Field Of View (FOV). This is a particularly important consideration for time-resolved experiments, where each dataset must be acquired at multiple time instances. In practice, however, ptychography experiments typically tend to collect significantly more data than the theoretical minimum, employing a high sampling rate at the detector and a 60%-70% overlap of the illumination function in real-space.

3.4 Computational Phase Retrieval Algorithms

The successful implementation of CDI relies critically on robust computational algorithms for phase retrieval. These algorithms are designed to recover, typically in an iterative way, the lost phase information from the measured intensity data by incorporating *a priori* constraints or known information about the experiment. Iterative methods, compared to non-iterative ones, are prevalent and cycle through estimation and refinement steps involving transformation between the real and reciprocal space representation of the wavefield. A common formulation involves the concept of constraint sets: the algorithm iteratively projects the current estimate of the wavefield between these sets, which represent the known information or the physical limitations in both the real and reciprocal space. The two constraints are:

- Reciprocal-space constraint (Fig. 3.2a): it is applied in the Fourier space (the diffraction plane), where the magnitude of the wavefield is known from the intensity measured by the detector. At each iteration, the magnitude of the computationally estimated wavefield in the reciprocal space is replaced by the square root of the measured intensity to ensure data consistency. Mathematically, the constraint enforces that $\left|\widetilde{\psi_{est}}\left(\mathbf{f}\right)\right| = \sqrt{I_{meas}\left(\mathbf{f}\right)}$, while keeping the the estimated phase. The reciprocal

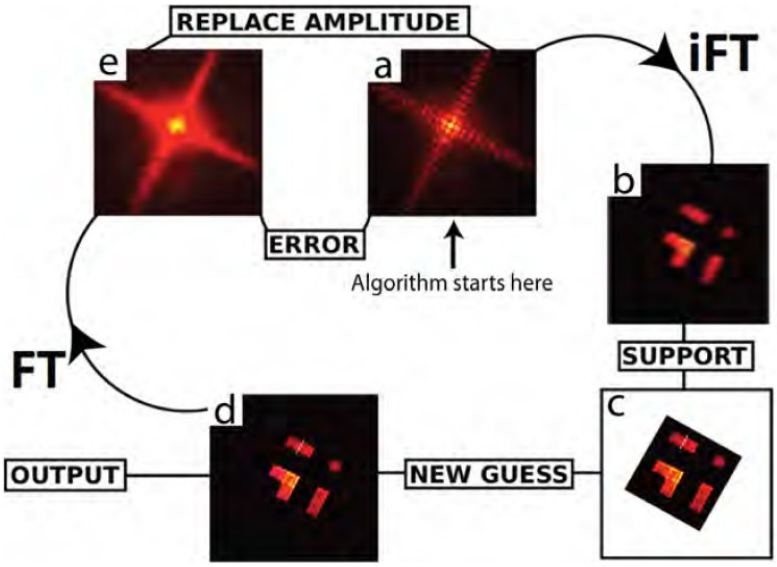


Figure 3.2: CDI with Error Reduction Algorithm. (a) The algorithm starts from the application of a random phase guess to the square root of the measured intensity diffraction pattern. (b) The diffraction gets projected into object space by means of an inverse Fourier transform. (c) The isolation constraint or support is applied, confining the object within specific boundaries. (d) Application of the support constraint yields a better guess of the object. (e) The better object guess is Fourier transformed back to frequency space. The phase is maintained and the amplitude replaced with the measured one. Convergence of the algorithm can be monitored by calculating the difference between (e) and (a). The algorithm continues the error below reach a predefined threshold. From [109].

space constraint is also known as the "amplitude constraint".

- Real-space constraint (Fig. 3.2c): it is applied in the real space domain and incorporates prior knowledge about the sample or the illumination function. A common constraint is the "support" or "isolation" constraint, which specifies the existence of the object only within a certain region, forcing the estimated wavefield to be null outside the specified boundaries. Other constraints can include the non-negativity of the pixels in the reconstructed image, or statistical properties of the pixel-value distribution, ensuring consistency with the material's physical properties and helping to exclude non-physical solutions. The Gerchberg-Saxton algorithm and its successors like the Error Reduction (Fig. 3.2) and the Hybrid Input-Output are early examples of algorithms relying on such constraints [69].

Similar to CDI, the algorithms used in ptychography typically iterate between real and reciprocal space applying appropriate constraints. However, the nature of the ptychographic dataset, with its high redundancy, necessitates a different algorithmic structure. At each scan position j, the exit surface wave $\psi_j(\mathbf{x})$ is given by

$$\psi_j(\mathbf{x}) = O(\mathbf{x})P(\mathbf{x} - \mathbf{x_j}), \tag{3.4}$$

with $O(\mathbf{x})$ and $P\left(\mathbf{x}-\mathbf{x_j}\right)$ being the object and the probe functions respectively. After propagation and detection, the measured diffraction intensity $I_j(\mathbf{f})$ is related to its Fourier transform in the following way:

$$I_j\left(\mathbf{f}\right) = \left|F\left\{\psi_j\left(\mathbf{x}\right)\right\}\right|^2. \tag{3.5}$$

The phase retrieval problem in ptychography then consists of recovering both $O(\mathbf{x})$ and $P\left(\mathbf{x}\right)$ from the set of measured diffraction patterns and the known scan positions $\mathbf{x_j}$. The earliest and most influential iterative algorithm addressing this problem is the Ptychographic Iterative Engine (PIE) [80]. In PIE the probe is known while the object is initially guessed. For a given scan position j, the exit surface wave is calculated and propagated to the Fourier space. The amplitude constraint is then applied to get an updated estimate of the function $\widetilde{\psi_j}(\mathbf{f})$ in such a way that

$$\widetilde{\psi_j'^i}\left(\mathbf{f}\right) = \sqrt{I_j}\frac{\widetilde{\psi_j^i}(\mathbf{f})}{\left|\widetilde{\psi_j^i}(\mathbf{f})\right|}. \tag{3.6}$$

Above, $\widetilde{\psi_j'^i}$ represents the updated function highlighted for the iteration number i. Equation (3.6) is then transformed back to real space to get

$$\psi_j'^i\left(\mathbf{x}\right) = F^{-1}\left\{\widetilde{\psi_j'^i}\left(\mathbf{f}\right)\right\} \tag{3.7}$$

that is used to update the object function through:

$$O^{i+1}\left(\mathbf{x}\right) = O^i\left(\mathbf{x}\right) + \frac{\left|P\left(\mathbf{x}-\mathbf{x_j}\right)\right|}{\left|P_{\max}\left(\mathbf{x}-\mathbf{x_j}\right)\right|}\frac{P^*\left(\mathbf{x}-\mathbf{x_j}\right)}{\left(\left|P\left(\mathbf{x}-\mathbf{x_j}\right)\right|^2+\beta\right)} * \alpha\left(\psi'^i\left(\mathbf{x}\right) - \psi^i(\mathbf{x})\right). \tag{3.8}$$

Here, α and β are appropriately chosen adimensional parameters and $\left|P_{\max}\left(\mathbf{x}-\mathbf{x_j}\right)\right|$ is the maximum value of the amplitude of the probe function. As observed, the standard PIE algorithm makes use of the normalized probe modulus and updates the object by correcting with a term expressing the local portion of the object exposed to the probe centered in $\mathbf{x_j}$. A significant improvement is the extended Ptychographic Iterative Engine (ePIE) algorithm [110], which allows for the retrieval of both object and probe simultaneously and *blindly*, i.e. without the need to know the probe function. Compared to PIE, the ePIE algorithm uses a different weighting factor based on the intensity of the probe, so that the β can be removed. In this case the object and the probe are both dynamically changed with the following update conditions:

$$O^{i+1}\left(\mathbf{x}\right) = O^{i}\left(\mathbf{x}\right) + \alpha \frac{P^{i*}\left(\mathbf{x}-\mathbf{x_j}\right)}{\left|P\left(\mathbf{x}-\mathbf{x_j}\right)\right|^2} * \left(\psi'^{i}\left(\mathbf{x}\right) - \psi^{i}(\mathbf{x})\right), \tag{3.9}$$

$$P^{i+1}\left(\mathbf{x}\right) = P^{i}\left(\mathbf{x}\right) + \alpha \frac{O^{i*}\left(\mathbf{x}+\mathbf{x_j}\right)}{\left|O\left(\mathbf{x}+\mathbf{x_j}\right)\right|^2} * \left(\psi'^{i}\left(\mathbf{x}\right) - \psi^{i}(\mathbf{x})\right). \tag{3.10}$$

The process is repeated position per position until completing one full update iteration for the entire scanned object area, as shown in Fig. 3.3. After finishing one iteration, the loop repeats until convergence is reached. To quantify and monitor the convergence of the algorithm, an error metric is defined and typically takes the form of a difference between the root mean squared value of the estimated diffraction amplitude with respect to the measured one:

$$\epsilon = \frac{\sum_j \left\| \left|\widetilde{\psi_j}\right| - \sqrt{I_j} \right\|^2}{\sum_j \left\| \sqrt{I_j} \right\|^2} \tag{3.11}$$

The methods so far described are typically referred to as "serial", being the object update carried out at each position. Other techniques instead have a batch-type approach, processing the update once the exit surface waves at each position have all been calculated. These methods are referred to as "parallel" and its most notable representatives are the Difference Map (DM) method [12] and the Relaxed Averaged Alternating Reflections (RAAR) [111]. Both approaches, serial and parallel, are equally valid and have been successfully implemented in many scenarios. In general, serial methods offer potentially faster convergence but may be more susceptible to stagnation in local minima, parallel methods instead can be more robust but require more computational resources since looking for a global solution

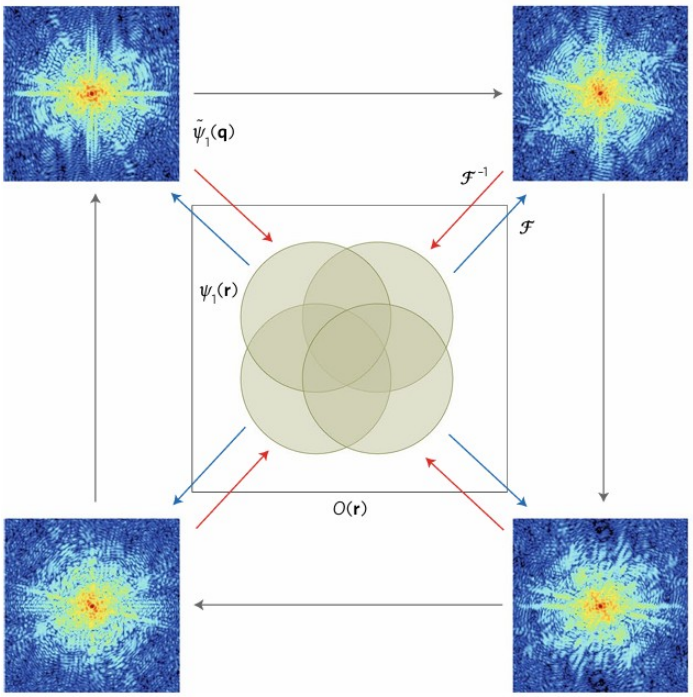


Figure 3.3: Ptychography working principle. The phase retrieval algorithm processes the first diffraction pattern position at position $j = 1$. A random phase guess is attached to its amplitude and the result is projected into the real space with an inverse Fourier transform (red arrow). Two object and probe guesses are updated with the results and then multiplied to get the new exit surface wave. The next portion of the object, that shares part of its values with the previous scan position, is Fourier transformed (blue arrow), then the amplitude constraint is applied, and finally inverse Fourier transformed. The brown area is updated, as well as the pixel shared with the previous position. The algorithm loops along the gray arrows until a global error metric reaches convergence. Adapted from [112].

Since its initial demonstration, ptychography has evolved tremendously, addressing more complex scenarios. Partial coherence of the illumination has been tackled by mode-decomposition methods [113] that, for instance, allows treating a partial coherent illumination by representing it as an incoherent sum of coherent modes that are reconstructed simultaneously. This approach allows handling both spatial partial coherences, but also temporal partial coherent illumination like the output of HHG sources. Algorithms have also been developed to increase robustness to noise (e.g. Poissonian) by incorporating noise models to improve the reconstruction quality, and have been upgraded to reconstruct 3D objects by developing approaches such as the multi-slice one [13].

A notable upgrade to classical ptychographic algorithms is the Modulus Enforced

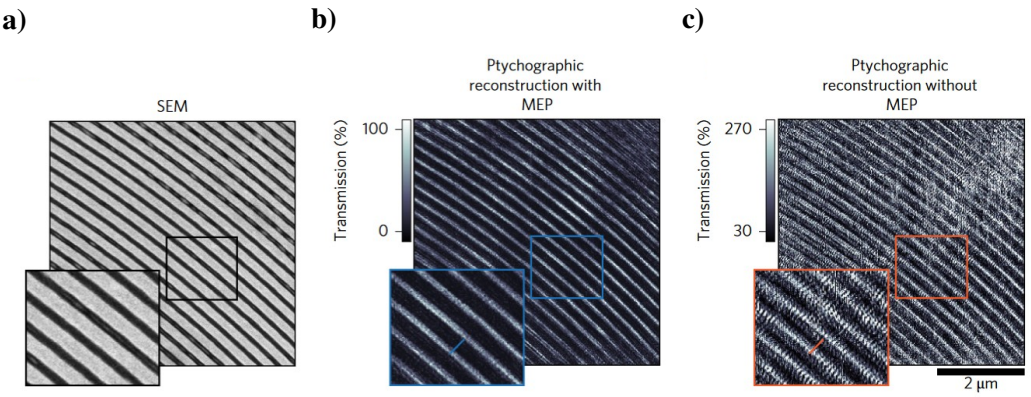


Figure 3.4: Quantitative full-field images of a periodic sample from XUV ptychography with MEP. (a) Reference SEM image of the rings of a Fresnel Zone Plate. (b) Ptychography reconstruction with MEP on the same area, with absolute transmissivity values provided by the knowledge of the probe's total power. (c) Ptychography reconstruction without MEP on the same area, with unphysical values of transmission. Adapted from [16].

Probe (MEP) [16], a sophisticated algorithmic constraint introduced to enhance the fidelity and the robustness of the reconstructions, particularly when dealing with challenging samples or non-ideal experimental conditions. The MEP constraint supplements the standard ptychography dataset with a direct recording of the undiffracted probe at the detector plane. This measurement is typically acquired immediately before or after the collection of diffraction patterns from the sample, by removing the sample from the beam path and exposing the detector to the beam alone. In this way, explicit information about the intensity of the probe at the detector plane is provided and it is possible to enforce the amplitude constraint to the probe. In fact, while methods like ePIE are designed to solve for the probe blindly, in particular conditions such as high noise levels or for particular samples, they can struggle and produce low quality reconstructions. The introduction of MEP has, for example, improved the reconstruction quality of periodic samples. Because of their regular arrangement, these samples produce diffraction patterns with limited diversity, making it difficult to decouple the object and probe contributions during reconstruction. A critical benefit of MEP is the ability to achieve quantitative reconstruction in the sample's transmission of reflectance functions, as shown in Fig. 3.4. In fact, in standard ptychography, although at convergence the form of the exit surface wave $\psi(\mathbf{x_j})$ is consistent with the measured diffracted intensity, the power within the algorithm can be arbitrary distributed among the probe $P\left(\mathbf{x}-\mathbf{x_j}\right)$ and the object $O\left(\mathbf{x}\right)$. While this can result in unphysical transmission or reflection values from the sample, enforcing the probe

power via MEP eliminates this ambiguity and generates quantitatively accurate phase and amplitude reconstructions. The additional information provided by MEP also allow for improved convergence rate and more tolerance to initial guesses. The MEP constraint has been successfully implemented in high-resolution coherent imaging using XUV light generated by HHG sources, filtered at a wavelength of $13.5nm$ to achieve sub-wavelength resolution in extended periodic samples. Moreover, three-dimensional topographical information was retrieved by converting the reconstructed phase into height, based on the known material properties

Chapter 4

Time-resolved Measurements

Ptychography can be extended beyond static imaging to investigate dynamic processes at characteristic length and time scales. This can be accomplished by integrating ptychography with pump-probe methodologies [8], a fundamental technique in ultrafast science for investigating transient phenomena occurring on timescales comparable to the duration of the probing pulses. The core principle uses two distinct signals: a "pump" that excites the specimen into a non-equilibrium state, and a subsequent "probe" that interrogates the sample's state at a precisely controlled time delay relative to the pump excitation.

While pulsed probes are essential for femtosecond-scale resolution, it is worth noting that CW sources can also be employed in pump-probe configurations by implementing external modulation, such as mechanical choppers or acousto-optic modulators (AOM). Such setups trade off temporal resolution (μs to ms timescales) for a significantly expanded temporal window, enabling the study of slower, long-lived dynamics that would be difficult to sample using standard optical delay lines. Conversely, by precisely controlling the temporal delay in pulsed configurations, sequential snapshots of the induced dynamics can be captured and stroboscopically reconstructed, provided the sample's response is reversible.

The typical experimental configuration for the investigation of ultrafast dynamics using pump-probe techniques originates from a single ultrafast pulsed laser source, such as a Ti:Sapphire laser. The output beam is split into two arms for the aforementioned delivery of pump and probe beams. In one of these arms, a variable optical delay line (e.g. a delay stage) is used for precisely adjusting the optical path length, therefore controlling the relative arrival time of pump and probe pulses at the sample plane. These systems can achieve high temporal resolution, as the synchronization of the beams is inherited from

their common source and pulse durations are on the order of tens of femtoseconds, which ultimately dictates the achievable temporal resolution. Furthermore, integrating systems based on HHG can enable probing material dynamics at even shorter timescales. The temporal relationship between pump and probe pulses is commonly categorized into three regimes, visualized in Fig. 4.1:

- Negative Times: the probe pulse arrives at the sample plane before the pump pulse. In this scenario, the specimen has not yet been excited by the pump, and therefore the probe measures the initial, unperturbed state of the system. The purpose of this measurement is to acquire the state of the sample before the perturbation induced by the pump beam occurs, thus providing a "baseline" configuration. Measurements at negative delay times can then help identifying several experimental issues; for example, they can be used to monitor the sample's initial state and verify that previous pump-probe cycles did not induce long term variations, or they can reveal the presence of instrumental drifts occurring at very low frequencies. Finally, and most importantly, the data acquired at negative times are often used for background subtraction or signal normalization, increasing the signal-to-noise ratio of pump-induced variations.

- Time-zero: the pump and probe pulses arrive at the sample simultaneously in time and space (spatio-temporal overlap). This marks the point where the specimen begins to interact with and respond to the pump excitation. Determining the "time zero" condition experimentally is a critical alignment step, often achieved by overlapping the pulses on a non-linear crystal and maximizing the generated signal by adjusting a motorized delay stage along the pump path. The incorrect collocation of time zero may lead to the misinterpretation of the data acquired by improperly flagging their time stamps.

- Positive times: the pump pulse arrives at the specimen before the probe pulse. The temporal delay between the pulses is positive, allowing the probe to interrogate the sample's state as it evolves in response to the pump excitation.

Integrating the pump-probe methodology with ptychography gives access to time-resolved imaging with quantitative phase information. This is especially useful when the probe beam is generated by HHG sources, as they provide high coherence, elemental selectivity, and ultrashort pulse durations. The pump beam, on the other hand, is typically

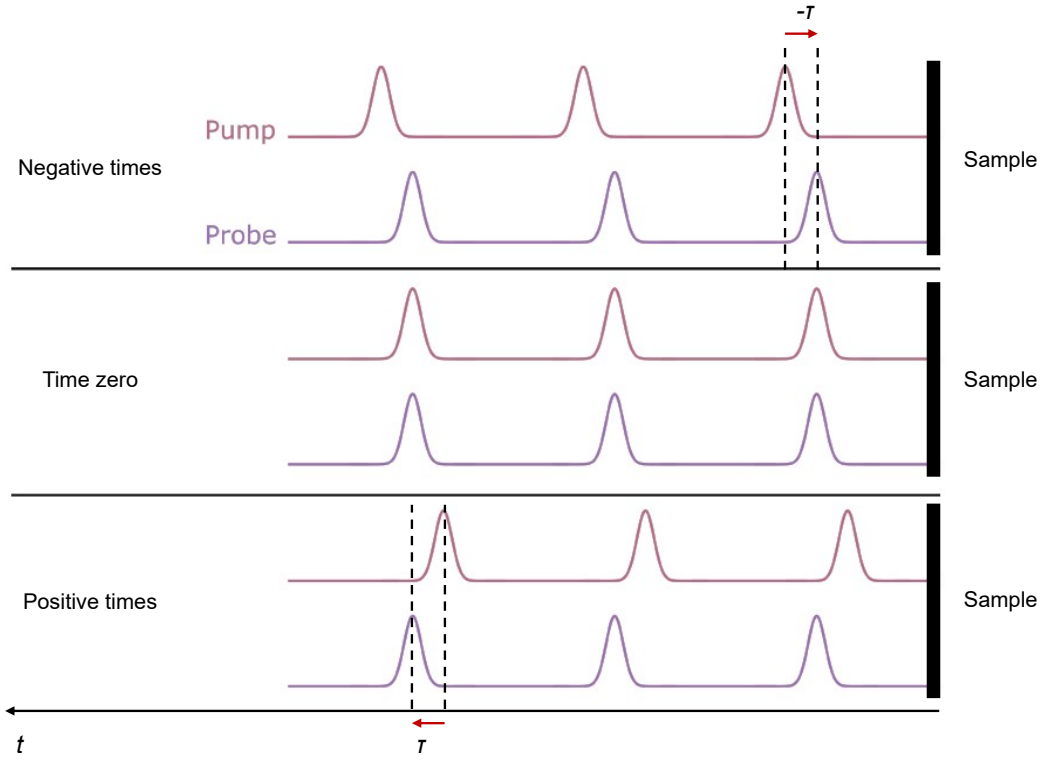


Figure 4.1: Pump-probe timing scheme. By means of delay lines, the arrival time of pump and probe beams on the sample is varied. During negative times, a baseline measurement is taken. At time zero instead, the pump and probe pulse trains arrive simultaneously. At positive times, each probe pulse captures the sample's dynamical response initiated by the pump. Adapted from [114].

the driving laser itself, used to initiate processes such as thermal excitation. In addition to a delay stage, the experimental setup for time-resolved ptychography with HHG requires an in-vacuum detector, CCD- or CMOS-based, and a set of stages to steer and focus both pump and probe beams onto the sample. The detector, used to record the diffraction patterns arising from the probe scattering from the sample, must be protected to prevent the much more intense pump light from saturating or damaging it. To do so, a metallic filter is typically placed in front of the chip to block the pump wavelength while transmitting the probe wavelength.

The data acquisition protocol for time-resolved ptychography with HHG involves performing a full ptychographic scan for each chosen pump-probe time delay. This means collecting multiple diffraction patterns at each overlapping position as the sample is moved through a grid. At each scan position, two separate diffraction patterns are recorded: one

"pump on", where the pump pulse is present, and another "pump-off", where it is blocked by an alternating shutter. The "pump-off" data at each point in the time series provides a crucial control measurement. This allows for the isolation of pump-induced changes from other sources of variation, such as experimental instabilities or irreversible modifications of the sample. After data collection, the ptychographic reconstruction algorithm is applied to the dataset at each individual pump-probe delay and, by comparing the reconstructed complex images across different delays, the transient dynamics initiated by the pump pulse can be directly visualized and quantitatively analyzed. Changes in reconstructed amplitude might indicate variations in absorption, while changes in phase can reveal alterations in the optical path length. These alterations correspond to changes in thickness, refractive index or physical displacement due, for example, to thermal expansion [15].

While a powerful technique, the combination of pump-probe and ptychography faces experimental and computational challenges. The volume of data collected across multiple delays and scan positions is substantial, and the total acquisition time can be significant, specifically when the camera redout time is long. This is even more critical when thinking about the beam delivery, which must be stable over extended periods of time. Additionally, the reconstruction task, while robust, remains computationally intensive for such large datasets. However, despite these challenges, this approach offers unique capabilities for spatially and temporally resolved quantitative imaging at the nanoscale.

Chapter 5

The Ultrafast Laser Source

Deploying ultrafast XUV ptychography in a laboratory requires an elaborated setup. In this chapter the details concerning the laser source for Ultrafast XUV Ptychographic Microscopy will be discussed. The description will be approached in a modular way. It starts from the generation of ultrashort laser beams in a mode-locked oscillator, followed by their amplification inside an optical amplifier and their upconversion to the XUV domain using an HHG source. Finally, the beam delivery inside the microscope chamber is described.

5.1 The Ultrafast Oscillator

The primary source of pulsed laser radiation is a mode-locked solid-state laser, a system capable of generating trains of ultrashort ($\sim 10^{-15}s$) optical pulses by imposing a definite phase relationship between the large number of longitudinal modes in its optical cavity. The mathematical formalism at the basis of its working principle and the technical implementation in LUXEM is described in the next sections.

5.1.1 Working Principle of Mode-Locked Oscillator

In a typical laser cavity, a high number of longitudinal modes can oscillate at the same time, separated in frequency by $\Delta\nu = c/2L$, where c is the speed of light and L is the cavity length. If these modes possess random phases, the output exhibit random but periodic fluctuations over time, similar to Fig. 5.1, where the time behavior of the squared amplitude of the electric field $|A(t)|^2$ is shown for 31 longitudinal modes with equal amplitude E_0.

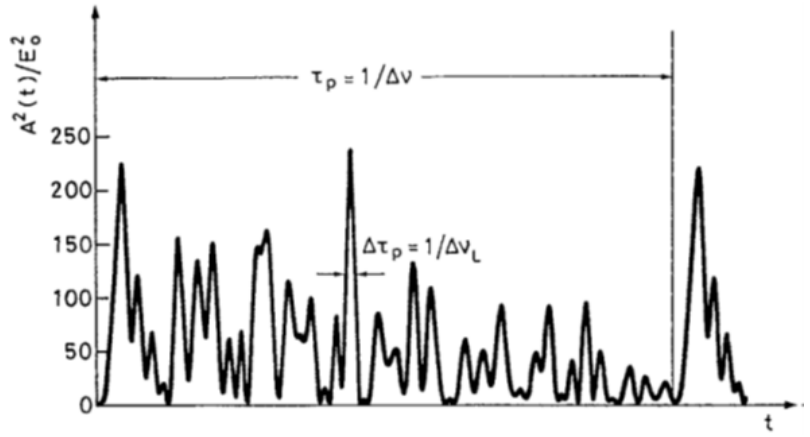


Figure 5.1: Time behaviour of the squared amplitude of the total electric field for 31 oscillating modes with equal amplitude E_0 but random phases. From [115].

Despite the random behavior, the waveform has the characteristic of a Fourier series and repeats itself with a period $\tau_p = 1/\Delta\nu$ (round-trip time), because the laser output is generated by a series of evenly spaced frequency components. The duration of each peak of the waveform is set by $\Delta\tau_p = 1/\Delta\nu_L$, where $\Delta\nu_L = N\Delta\nu$ is the total cavity bandwidth and ultimately set by the bandwidth of the gain medium, typically accommodating $10^3 - 10^4$ modes for solid state lasers. Mathematically, the period waveform can be described by

$$E(t) = \sum_{-n}^{n} E_{0,n} e^{i(\omega_0 + n\Delta\omega)t + i\phi_n(t)}, \tag{5.1}$$

where $2n + 1$ is the number of longitudinal modes in the cavity, $\phi_n(t)$ is a random time-dependent phase factor, ω_0 is the central mode frequency and $\Delta\omega = 2\pi\Delta\nu$ is the frequency distance between two separate modes. The purpose of mode-locking technique is to enforce a fixed phase relationship between longitudinal modes, leading to constructive interference only for short periods of time and causing the amplification of the generated pulses. This happens either when the phase term $\phi_n(t)$ is equal for each mode or if a definite phase relationship is established between them. To understand this let's consider the frequency domain picture of the cavity modes, in the simplified scenario depicted in Fig. 5.2, where $2n + 1$ longitudinal modes oscillate with the same intensity $|E_0|^2$. Assuming the following fixed phase relationship locking consecutive modes:

$$\phi_l - \phi_{l-1} = \phi, \tag{5.2}$$



Figure 5.2: Uniform mode amplitudes versus frequency for a mode-locked laser. Adapted from [115].

it is now possible to rewrite eq. (5.1) as

$$E(t) = \sum_{-n}^{n} E_{0,l} e^{i(\omega_0 + l\Delta\omega)t + il\phi} = \left(\sum_{-n}^{n} E_{0,l} e^{il\Delta\omega t + il\phi} \right) e^{i\omega_0 t} = A(t) e^{i\omega_0 t}. \tag{5.3}$$

The latter, more compact, form of the equation expresses the total electric field as a sinusoidal carrier wave with frequency ω_0 having a time-dependent amplitude. By changing the variable to $\Delta\omega t' = \Delta\omega t + \phi$, the amplitude can be rewritten as

$$A(t') = \sum_{-n}^{n} E_{0,l} e^{il\Delta\omega t'} = E_0 \frac{\sin\left[(2n+1)\Delta\omega t'/2\right]}{sin[\Delta\omega t'/2]}, \tag{5.4}$$

where the time dependent amplitude is expressed as a coherent sum of plane waves with locked phases, moving in the reference frame t'. The series can be furthermore recognized as a geometric progression, which clearly identifies the time dependent amplitude as a train of pulses repeating with the round-trip time $\tau_P = 1/\Delta\nu$ and possessing a Full Width Half Maximum (FWHM) equal to $\Delta\tau_P = 1/\Delta\nu_L$, as shown in the ideal case of Fig. 5.3. In other words, the pulsewidth is inversely proportional to the width of the laser spectrum and, in this case, is defined as transform-limited. In the realistic case where the amplitude of the modes follows a bell-shaped distribution, the pulse is modified to $\Delta\tau_P = 0.441/\Delta\nu_L$. A significant consequence of mode locking is the enhancement of the peak power of the emitted pulses. Compared to a non-mode-locked laser with the same number of oscillating modes and the same average power, the ratio between the peak pulse power in the mode-locked case and the average power is equal to the number of oscillating modes, which for solid state laser can lead to very high peak powers, due to the high number of modes. Mode-locking is therefore a valuable technique not only for producing pulses of very short duration, but also for achieving high peak power lasers.

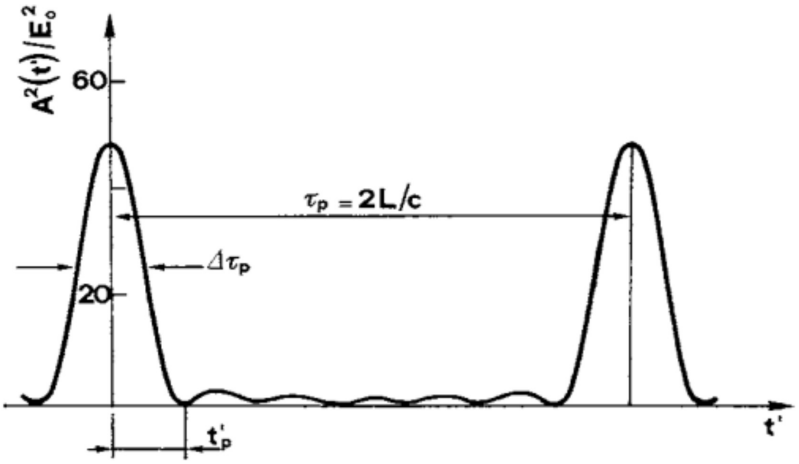


Figure 5.3: Time behaviour of the total electric field for seven oscillating modes with locked phases and equal amplitudes. Adapted from [115].

While an extensive explanation of mode-locking methods is beyond the scope of this dissertation and can be found in undergraduate textbooks [115, 116], the techniques employed to lock the phases of the modes can be broadly classified in two categories: active and passive mode-locking. Active mode-locking involves the introduction of an external optical element, such as an amplitude or a phase modulator, which operates at a harmonic frequency of the fundamental $\Delta\nu$ and modulates the modes inside the optical cavity. Passive mode-locking is instead based on an intracavity non-linear optical element, whose properties (typically absorption or refractive index) depend on the instantaneous intensity of light. This intensity dependence leads to self-amplitude or self-phase modulation that favors the formation and shortening of laser pulses. The oscillator described in this work is based on a passive mode-locking method called Kerr Lens Mode-Locking (KLM). This method exploits the optical Kerr effect, a nonlinear phenomenon in which the refractive index n of the gain medium is modulated by the intensity I of the circulating light, according to the formula

$$n = n_0 + n_2 I, \tag{5.5}$$

where n_0 is the linear refractive index and n_2 is the second-order nonlinear refractive index. This modulation can in turn induce self-focusing effects triggered by light intensity peaks. In the absence of physical apertures, this leads to a soft-aperture effect where the more tightly focused pulsed beam achieves a superior spatial overlap with the pump-induced gain volume within the medium compared to the lower intensity CW background. Consequently, the high-intensity peak experiences a higher extraction efficiency, while the

lower-intensity temporal tails are effectively penalized by receiving less gain per round-trip. This iterative discrimination continuously improves the stability and promotes the temporal shortening of the pulses. The final pulse duration is established as a dynamic equilibrium between nonlinear spectral broadening via SPM and the compensation of intracavity Group Delay Dispersion (GDD), eventually constrained by the finite gain bandwidth of the active medium. Another interesting property of KLM is its self-starting feature, meaning that the pulsed operation can take place spontaneously from intensity noise fluctuations.

5.1.2 Optical Dispersion

For the generation of very short pulses, particularly in the femtosecond regime, dispersion management is critical. Multiple dispersion effects can be analyzed by expanding in Taylor series the wavenumber $k(\omega)$ around the central frequency:

$$k(\omega) \approx k\left(\omega_0\right) + k'\left(\omega_0\right)\left(\omega - \omega_0\right) + \frac{1}{2}k''\left(\omega_0\right)\left(\omega - \omega_0\right)^2 + \frac{1}{6}k'''\left(\omega_0\right)\left(\omega - \omega_0\right)^3 \quad (5.6)$$

Each derivative of the wavenumber refers to a property of the pulse while propagating inside the medium. The first order term $k'\left(\omega_0\right) = \left(dk/d\omega\right)_{\omega_0} = 1/v_G$ is inversely proportional to the group velocity v_G, which represents the speed of the entire pulse envelope. In practice this means that the entire pulse propagates by keeping its shape, regardless of the phase velocity $v_{ph} = \omega/k$ of each frequency component. The second order term $k''\left(\omega_0\right) = \left(d^2k/d\omega^2\right)_{\omega_0}$ is termed Group Velocity Dispersion (GVD). It quantifies how v_G changes with frequency, causing the different spectral components of the pulse to travel at slightly different speeds. The practical consequences of GVD are pulse broadening and linear chirping, both being caused by the different spectral components spreading in space/time. From GVD it is possible to define the group delay dispersion $GDD = Lk''(\omega)$, that represents the different delays suffered by the multiple spectral components of the pulse while traveling into a dispersive medium of length L. GDD is measured in $\left[fs^2\right]$ and can be directly applied to assess the degree of temporal pulse dispersion in mirrors, prisms, gratings and other optical elements (see Fig. 5.4). Due to their short duration, fs-long pulses imply a spectral bandwidth so broad that Third Order Dispersion (TOD) $k'''\left(\omega_0\right) = \left(d^3k/d\omega^3\right)_{\omega_0}$ terms must be taken into account to accurately model the phase distortions across the pulse spectrum. They are particularly relevant for pulses close to $10fs$ and become the main limitation beyond that limit when

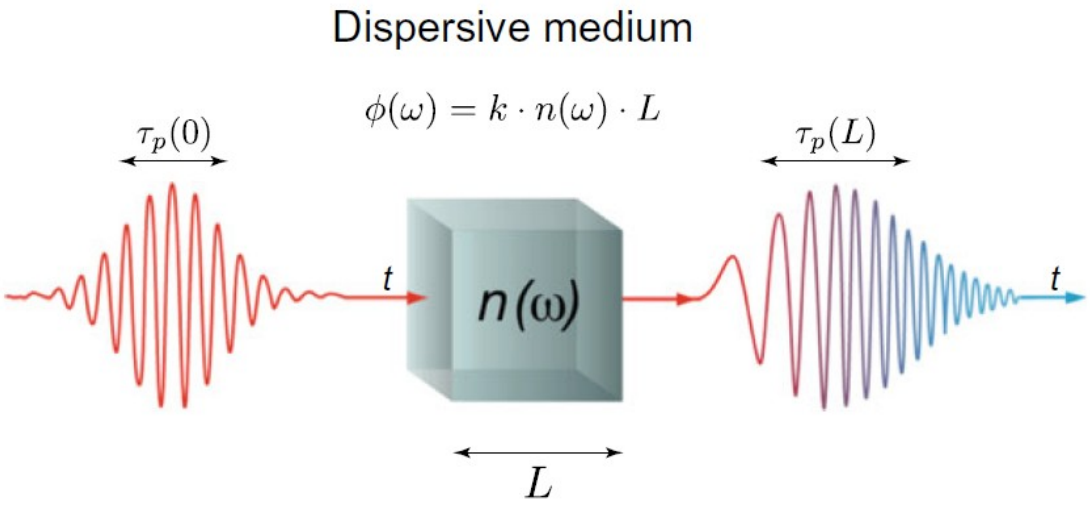


Figure 5.4: Pulse broadening in a dispersive medium of thickness L with positive dispersion. The horizontal axis of the electric field in this figure represents time. Therefore, the blue wavelengths of the pulse after the dispersive medium are in fact trailing the red wavelengths. From [116].

second order effects have already been compensated. The physical effects of third order dispersion (TOD) include an asymmetry in the temporal profile of the propagating pulse and a nonlinear temporal chirp, both resulting from the frequency dependence of the group delay dispersion. To counteract second order dispersion effects (and, to some extent, TOD), intracavity optical elements with negative GDD are required, such as prism pairs. These devices also compensate for another consequence of Kerr effect, that is self-phase modulation (SPM). In SPM, the leading and trailing edges of a pulse experience an instantaneous frequency shift due to the intensity-modulated refractive index, therefore chirping the pulse and broadening its spectral bandwidth. The interplay between SPM and negative GDD can lead to the formation of solitons, which are stable solitary pulses. Balancing dispersion effects and exploiting the huge gain bandwidth of Ti:Sapphire crystals, this method can lead to the generation of beams with time duration shorter than tens of fs.

5.1.3 Implementation of a Mode-Locked Oscillator

In the simplified picture shown in Fig. 5.5, the design of the passively mode-locked oscillator described in this thesis features the following components:

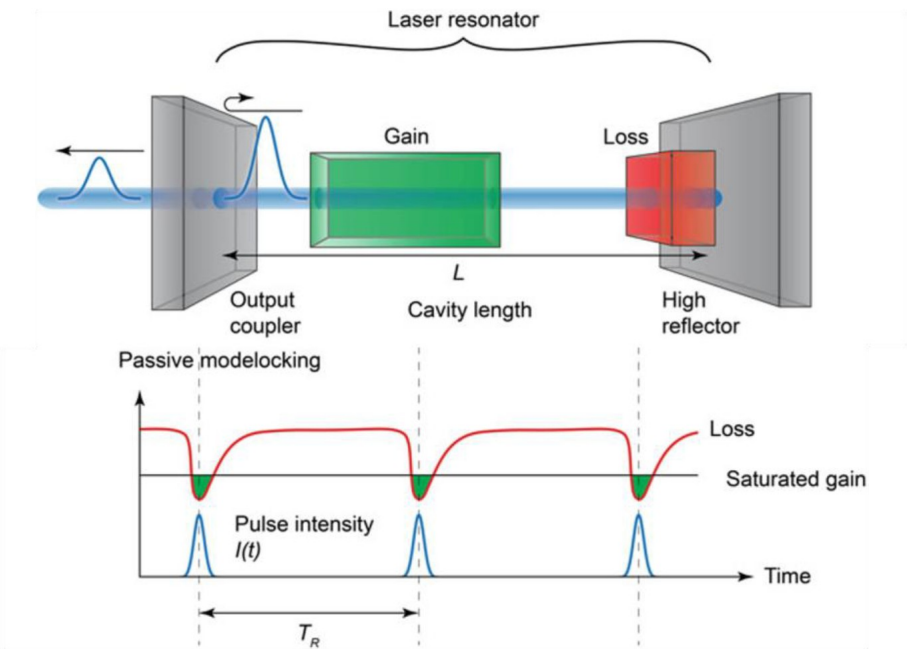


Figure 5.5: Schematic of the temporal behaviour of gain and losses in a laser resonator with output coupler. The laser cavity length L is defined by its end mirrors: the partially transmissive output coupler and the high reflector. Modified from [116].

- Ti:Sapphire crystal: this gain medium provides a large bandwidth for the amplification of a high number of longitudinal modes and shows optical Kerr effect when high intensity light passes through it.
- Output coupler: a partially reflective optical element used to extract a small portion of the laser light at low intensity while allowing the remaining power to circulate within the cavity. It acts as a fast saturable absorber when hit by high intensity laser light, leading to the generation of short pulses in output. It is one of the cavity end mirrors.
- High reflector: the second cavity end mirror.
- Prisms: although not shown in 5.5, they are often present and compensate for the positive GDD by delaying longer wavelengths relative to shorter ones, thus temporally re-aligning the spectral components.

In practice, however, such devices are complex and contain multiple optomechanical elements between the cavity end mirrors, making it nontrivial to understand their working principle.

The scheme of the oscillator (KMLabs Griffin^{TM}) used as a primary source of the Ultrafast XUV Ptychographic Microscope is shown in Fig. 5.6. The cavity is $\sim 1.8m$-long and is pumped with a $4.6W$ CW s-polarized laser (SPROUT-D) running at $532nm$ wavelength. The green laser light is directed towards a plano convex lens by means of two 45° steering mirrors (M1 and M2, not in the image). The lens focuses the input beam inside a Ti:Sapphire crystal, while passing through a curved mirror (CM1) transparent at this wavelength. The outcoming NIR radiation ($\sim 800nm$) is collected by a second curved mirror (CM2) which sends the beam to a third one (M3) and finally to the output coupler (OC). At the OC most of the radiation is sent back to the crystal while a small part is ejected from the cavity. In the first scenario the light travels back to CM1, which reflects it to the non-dispersed prism (NDP). The beam then reaches a cavity fold mirror (FM), the dispersed prism (DP) and the end cavity mirror or high reflector (HR). At this point the laser pulse is retroreflected to the crystal by following the exact same path in the opposite direction, it gets amplified and finally finishes the round trip by reaching OC again, where a small portion is transmitted through it. The purpose of DP and NDP are respectively to disperse the different spectral components of the pulse and subsequently recombining them during its last pass before traveling back to the OC. In this way a negative GDD can be imparted to the pulse, compensating for positive dispersion effects, for instance arising during the transmission through the Ti:Sapph crystal. In the second scenario, the leaking NIR beam bounces off a fourth mirror (M4) and on a thin beamsplitter placed immediately after it. Part of the beam is transmitted outside the cavity to be later amplified, while another portion travels to a photodiode and a spectrometer, used for diagnostic purposes. The stable and efficient mode-locked operation relies on the proper alignment of the oscillator cavity. Misalignments of its intracavity components can have several significant effects. They can directly affect the optical path length and the transverse mode profile into the cavity. The beam spot size and position on various optical elements, including the Ti:Sapphire crystal and the output coupler, are relevant for the efficient build-up of laser radiation and mode stability. The position of cavity mirrors and their distances, especially CM1 and CM2, have direct consequences on the Kerr lens mechanism of light inside the gain medium. Mechanical perturbations can therefore drastically change the degree of self-focusing and modify the phase locking between modes. Changes of the beam path can also affect the amount of dispersion accumulated per round trip if the prism pairs are traversed differently, leading to broader pulses or spectral distortions. Hence, to avoid these possibilities as much as possible, the components of the oscillator sit on high

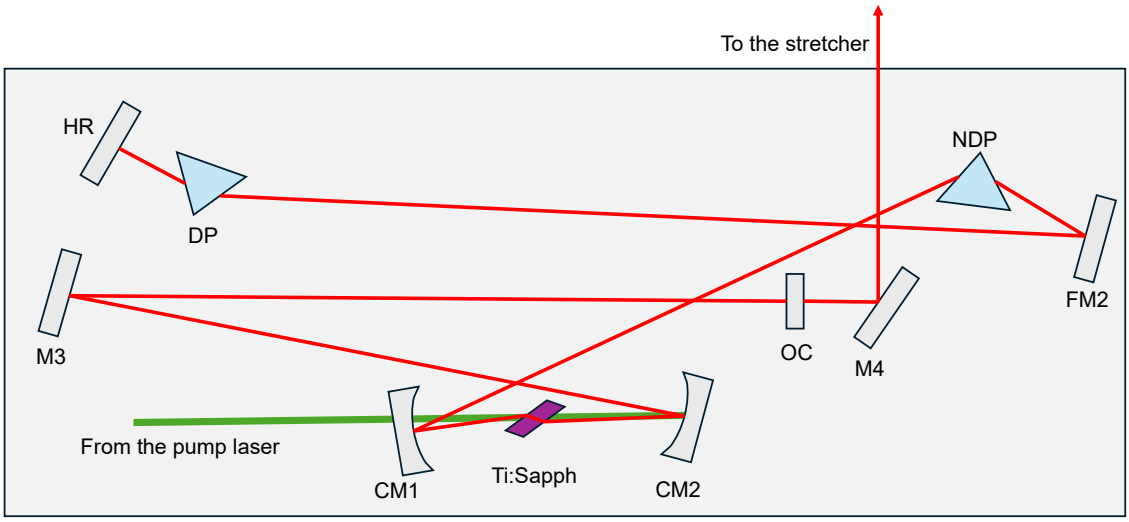


Figure 5.6: Oscillator cavity and beam path.

stability mounts and typically possess a high number of degrees of freedom to optimize the pulsed laser output. When properly aligned, the KMLabs Griffin^{TM} oscillator exhibits a contrast factor between the average power in pulsed and CW operations of ~ 1.5. During mode-locked operation the oscillator emits $7nJ$ p-polarized pulses at $81MHz$ repetition rate with duration $\Delta\tau_P = 10-15fs$, which, in the spectral domain, corresponds to a broad frequency comb with FWHM equal to $60-64nm$, centered around $\lambda_0 = 800nm$.

5.2 The Ultrafast Amplifier

By means of an anodized aluminum tube, the ultrafast oscillator is connected to a cryogenic laser amplifier system, whose purpose is to increase the energy of the seed by ~ 6 orders of magnitudes while retaining its temporal duration. This sophisticated system is based on the Chirped Pulse Amplification (CPA) technique [117, 118], a method used to circumvent the detrimental effects — such as self-focusing or multi-photon ionization — that arise from amplifying ultrashort pulses with high peak intensity. The theoretical and practical implementation of a CPA-based system is described in the following sections.

5.2.1 Working Principle of a CPA-based Amplifier

The core principle of CPA is illustrated in Fig. 5.7 and consists in reducing the peak intensity of the laser pulse while preserving its total energy. To do so, three main steps

are carried out:

- Stretching: the initial ultrashort beam is stretched out in time by passing through an optical system providing a large amount of positive GDD. The result is equivalent to Fig. 5.4, with lower frequencies (red) being slower than higher ones (blue). A common type of pulse stretcher is the Martinez design [119], composed by a set of antiparallel gratings separated by 1:1 telescope. This arrangement is configured in such a way that the multiple spectral components of a pulse propagate along optical paths of different lengths, in order to obtain a tunable high stretching factor $\left(\sim 10^3 - 10^4\right)$. Assuming negligible dispersion of the lenses composing the telescope and considering paraxial approximation to be valid, the GDD introduced by such a stretcher design is a function of the gratings period, their angles and the overall geometry.

- Amplification: after stretching, the pulse has a significantly lower peak power and intensity compared to its original shape. This power reduction $\left(\sim 10^{-3} - 10^{-4}\right)$ allows the amplification of the pulse to be carried out safely inside an optical cavity, without damaging the optics, the amplifying medium and limits unwanted non-linear effects potentially reducing the optical gain. A common amplification medium is a Ti:Sapphire crystal: this material is optically pumped at high power and placed inside an optical cavity, designed upon different operating principles depending on the requirements of the output pulse.

- Compression: after the amplification, the stretched pulse is recompressed back to its quasi-original duration. This is achieved by letting the pulse travel through another optical system designed to provide a negative GDD, reverting the effect of the stretcher and compensating for the dispersion of the amplification medium and other transmissive optical elements. Common compression schemes are the Treacy's design [120], based on a pair of parallel diffraction gratings, or sequence of prisms, or combination of both in order to partially counteract TOD as well.

5.2.2 Implementation of a CPA-based Amplifier

In this experimental work, the amplification of ultrashort pulses is performed by the RAEA^{TM} HP system from KMLabs. The design of the system follows the same principles

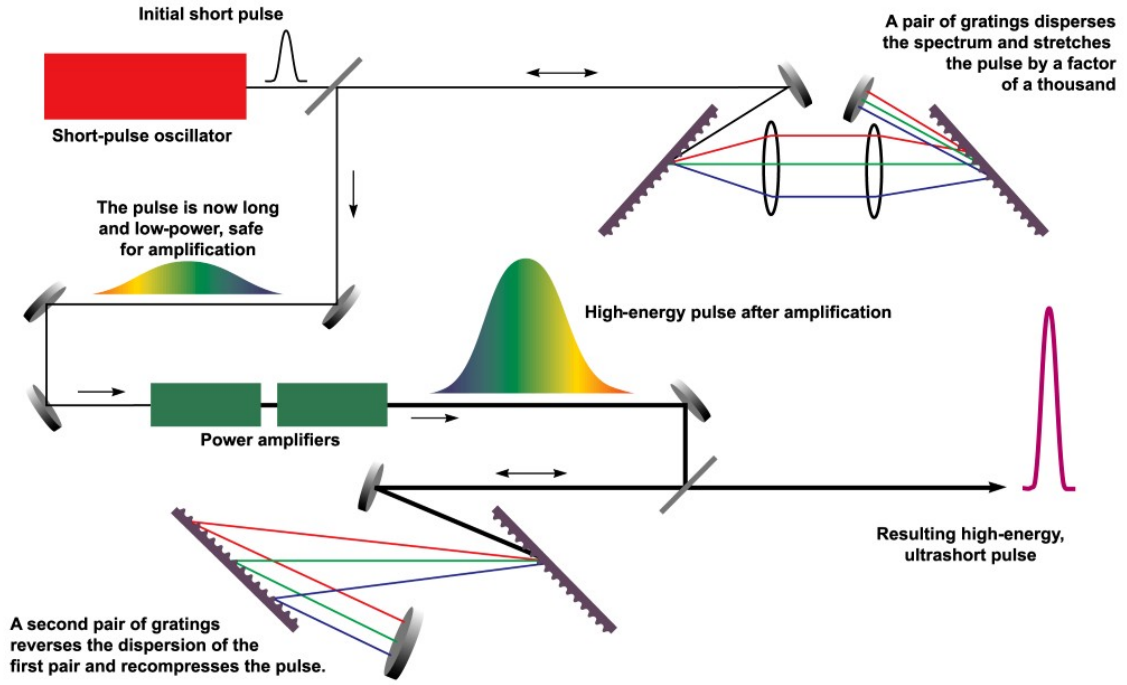


Figure 5.7: Schematic of CPA. The initial pulse is directed to a couple of gratings in antiparallel configuration, which disperse the spectrum and stretch the pulse. After retroreflection, the pulse is amplified and subsequently compressed by a pair of gratings parallelly oriented, resulting in an ultrashort pulse with high energy. From [121].

described so far and is therefore divided onto three separate subsystems: the stretcher, the amplification cavity and the compressor.

The designs of the stretcher and compressor differ from the Martinez and Treacy's ones: the former is based on a double transmission grating system inserted between two curved mirrors; the latter is a reflection-based device with a double-passing high-aperture gratings and a retroreflector. Despite the differences, their operation is based on the same principle of accurately tuning optical dispersion by spatially varying optical path lengths, before and after the amplification stage.

The RAEA^{TM} HP amplification cavity is based on a specific type of optical amplifier called "Regenerative amplifier". It consists of a folded resonator with multiple mirrors guiding the beam to an optically pumped cryo-cooled Ti:Sapphire crystal. This material is the most widespread solid-state amplifier medium thanks to its high thermal conductivity (46 W/mK at 300K and one order of magnitude higher when cooled), its broad absorption spectrum — making it suitable for frequency doubled Q-switched Nd:YAG laser pumping

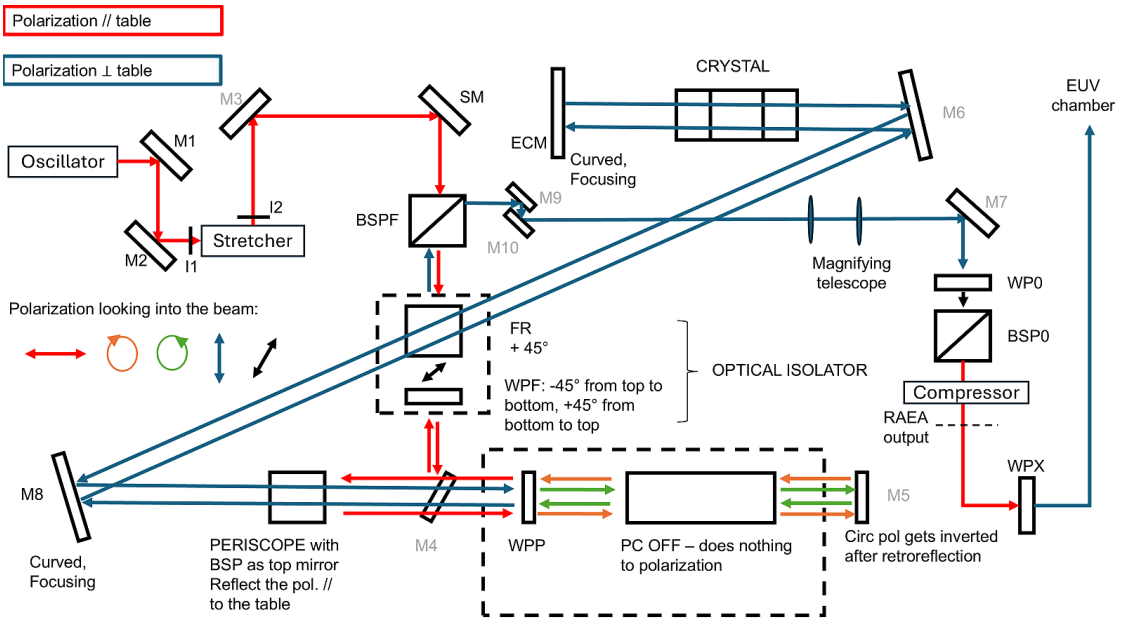


Figure 5.8: Beam path inside the cavity with the Pockels cell in OFF state.

— and large amplification bandwidth ($\approx 230nm$). The operation undergoing inside the amplifier cavity can be generally described by means of an injection, amplification and ejection sequence, where a key role is played by a Pockel cells (PC), an electro-optical device acting as an ultrafast optical switch and managing the entry and exit time of the pulse. The precise understanding of the operating principle of the amplifier is essential: the system is not conceived to be used as a black box but rather as a flexible device which can be adapted to operate in different regimes (output power, central frequency, bandwidth, beam size). Moreover, a deep understanding of the amplification cavity functioning is crucial for debugging and correct for any long-term deviations leading to suboptimal spatiotemporal characteristics of the laser pulses. Therefore, following Fig. 5.8, the structure and working conditions of the amplification cavity are described. First, the p-polarized (and parallel to the optical table) beam from the oscillator is manipulated by two 45° 1″ turning mirrors (M1 and M2), whose output is aligned with two irises (I1 and I2) placed before and after the stretcher. After suffering an increase in time duration up to hundreds of ps, the bean hits a third mirror (M3), placed on a high stability mount, and a steering mirror, which is used to regulate injection of the seed inside the cavity. The beam passes through a polarizing beamsplitter (BSPF) that transmits the horizontal polarization, while reflecting the vertical one, and reaches an optical isolator (OI) placed

immediately after. This device is internally composed by a combination of Faraday rotator and a $\lambda/2$ waveplate (WPF) and allows for the transmission of the optical radiation in a single direction. The polarization of the beam traversing the OI is initially rotated by 45° due to the Faraday effect and then restored to the initial polarization state by the WPF. In this way, the beam cannot back-propagate and any possible damage to the stretcher and to the components of the amplification cavity can be avoided. The beam continues its path to a fourth mirror (M4) oriented towards a periscope raising the height of the pulse up to the level of the PC. The periscope is composed of a mirror at the bottom and a polarizing beam splitter on the top part, oriented in order to reflect the beam when its polarization is parallel to the optical table. Afterwards, the pulse travels above M4 and passes through a $\lambda/4$ waveplate (WPP) just before entering the PC. The net effect of WPP is inducing a change of polarization from linear to circular, in the clockwise direction. The pulse now reaches the Pockel cell. This device exploits a voltage-induced birifrangence effect (Pockels effect) and acts as a fast switchable $\lambda/4$ waveplate. If the Pockel cell is in the OFF state (i.e. no voltage is applied) the beam passes through it without suffering any polarization changes. It ultimately hits a retroreflecting mirror (M5) which reverts the polarization to the anticlockwise direction, in such a way that when passing through WPP its polarization becomes vertical, and the beam is allowed to pass through the BSP inside the periscope. The pulse hits M8, a curved focusing mirror, then M6 and, after passing through the crystal at focus, it reaches the end mirror of the cavity (ECM). This optical element closes the cavity and sends collinearly the pulse back to complete the round trip. Hence the beam reaches WPP, its polarization gets rotated in the anticlockwise direction, passes through the PC, and is retroreflected by M5 which inverts also the helicity of the polarization. The pulse traverses the Pockel cell and WPP, leading to a polarization state equal to the horizontal initial condition. Therefore, the beam is reflected down by the BSP into the periscope, reaches M5 and finally comes back to the OI. Along this direction, the combined effect of FR and WPF is to rotate the linear polarization by 90°, which is the required condition for BSPF to reflect the beam and avoid any retropropagation to the stretcher. After being reflected by other two 1″ mirrors (M9 and M10), the beam passes through a magnifying telescope which increases its beam diameter by one order of magnitude (from $1mm$ to $10mm$ $1/e^2$). This is a particularly important step when the entire cavity is amplifying, since it allows to reduce the peak beam intensity (thereby the

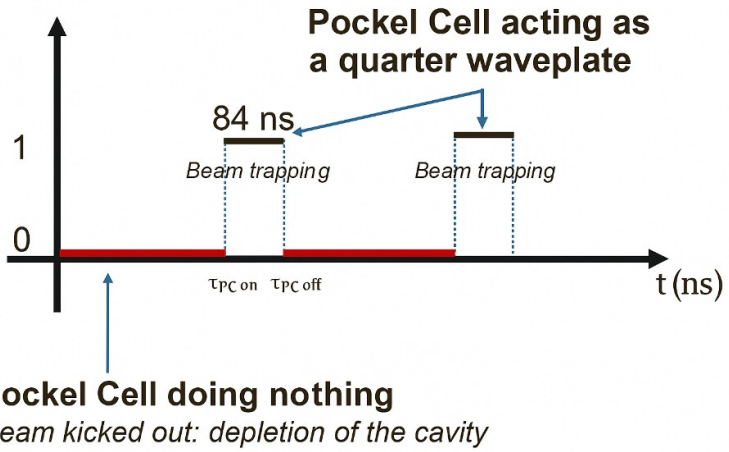


Figure 5.9: Pockels cell's operative times.

fluence) and consequently the B-integral. This is an adimensional quantity given by

$$B = \frac{2\pi}{\lambda} \int n_2 I(z) dz \tag{5.7}$$

and expresses the nonlinear phase shift accumulated by the pulse while propagating through a medium with intensity-dependent refractive index. If high values of the B integral are reached ($B > 3$), the optical components placed downstream could be damaged and, besides it, pulse breakups and strong degradation of the beam quality can occur. Moreover, the B-integral is basically a measurement of the total phase accumulated when the beam is undergoing SPM, which can induce a non-uniform variation of the pulse frequency content that can no longer be compensated by the compressor. After the telescope, the pulse reaches a 45° mirror (M7) which sends it through WP0, a remote controlled waveplate that, combined with a polarizing beamsplitter (BSP0), allows to regulate the power out of the amplifier cavity. When WP0 is set to 9°, the polarization gets perfectly horizontally oriented, and the power is maximized. When WP0 is instead rotated by 45° and therefore set to 54°, the output power reaches the minimum value (very close to zero). Before leaving the RAEA^{TM}, the pulse gets into the compressor which provides a negative GDD and compensates for the accumulated dispersion from the stretcher and the optics inside the amplification cavity. Inside the compressor, a polarization-neutral periscope raises the beam up to $114.3mm$.

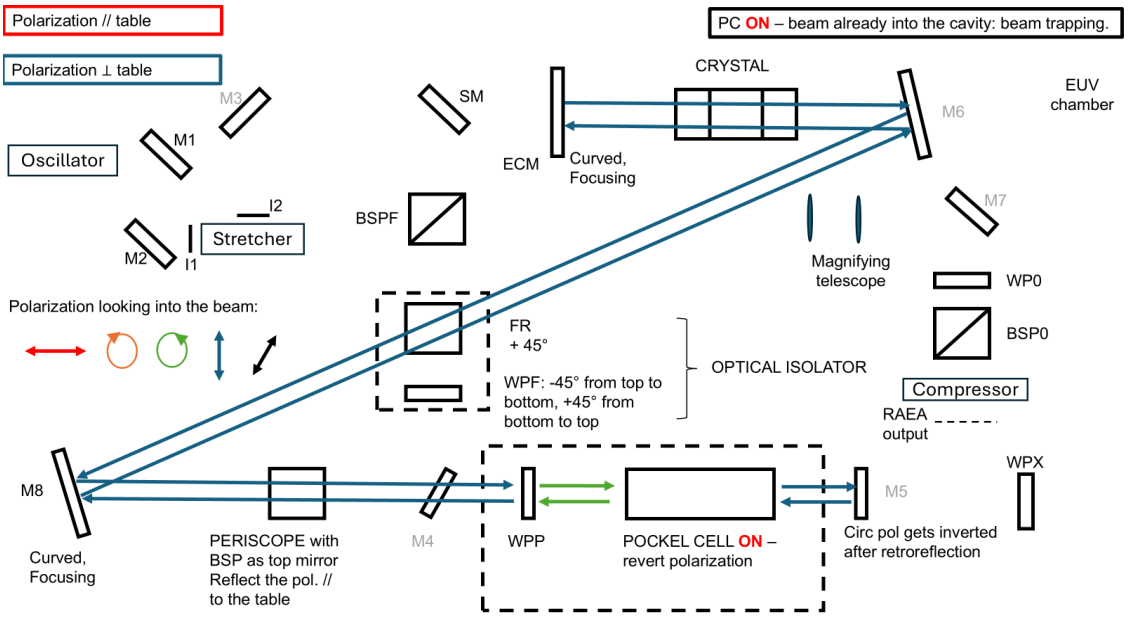


Figure 5.10: Beam trapping inside the cavity by turning the Pockels cell ON.

When voltage is applied to the PC, a change in the operating regime of the amplifier is induced. This can be directly set by the RAEA^{TM} software, which can be used to regulate the activation (PC ON) and deactivation (PC OFF) times while keeping a minimum delay of 70ns to avoid any damage to the PC itself. This is indeed the minimum switching time for the voltage driver to operate safely. A simple illustration of this working principle is shown in Fig. 5.9. Initially, when PC is OFF, the behavior of the pulse is as previously described; when PC turns ON instead, a beam already located into the cavity is trapped and the amplification process takes place by letting it circulate for a specific number of round trips. This number is proportional to the time delay between the activation time $\tau_{PC,ON}$ and deactivation time $\tau_{PC,OFF}$ of PC. After turning PC OFF, the cavity is depleted, and the amplified pulse finally exits the cavity. This open-close process happens at a specific frequency set by the 532nm Northrop-Grumman Q-switched laser (NG) used to pump the Ti:Sapphire crystal. Fig. 5.10 illustrates the beam trapping mechanism caused by the fast switch of the Pockels cell. A vertically polarized pulse already inside the cavity (delimited by M5 and ECM) and emerging from the crystal is transmitted by the BSP composing the periscope. When passing through WPP, it would experience a 90° phase shift on one component of the electric field, getting its polarization circulating in the anticlockwise direction. However, if PC is on, this effect is completely reverted and the beam, after

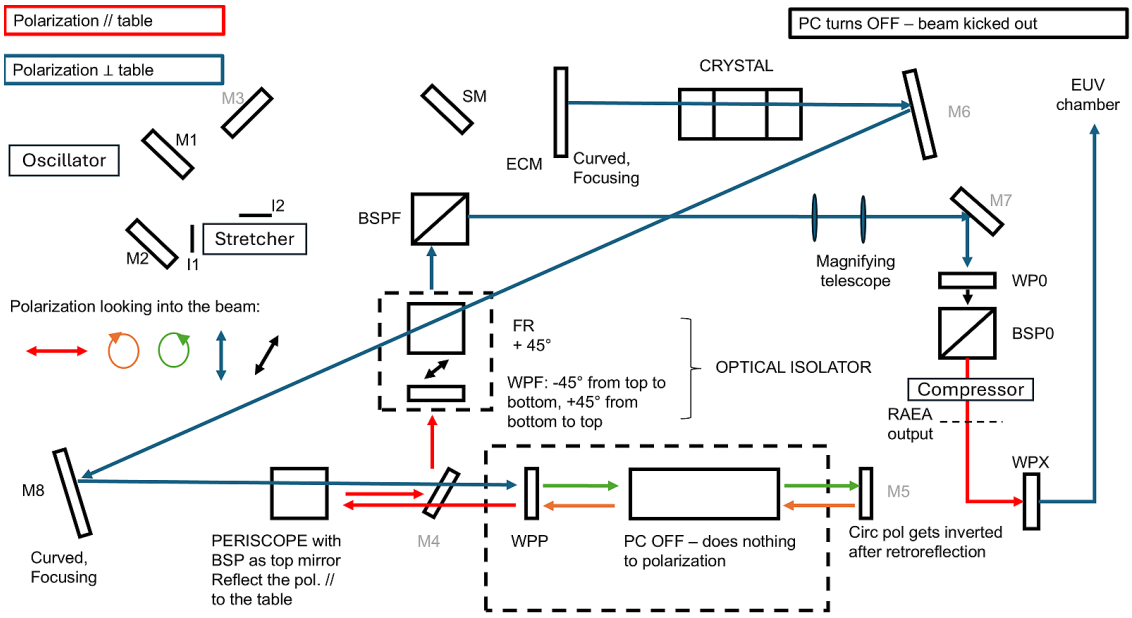


Figure 5.11: Amplified beam exits the cavity as PC is turned OFF.

hitting M5 and passing again inside the PC, gets out of WPP with the same polarization possessed previously. The pulse is therefore transmitted by the periscope's BSP and reaches the crystal again, building up its power in another amplification round. The process continues until PC is turned off (Fig. 5.11) and stops conditioning the polarization state of the beam after WPP. The polarization is instead reverted by M5 and, after transiting through WPP again, it gets horizontal. The BSP placed on top of the periscope reflects the beam to M4 and to the OI, which switches its polarization by 90° and allows the pulse to exit the system.

A different path in instead followed by the pulses outside the cavity when PC is switched on. As described in Fig. 5.12, the beam coming from the OI is horizontally polarized and, after bouncing on M4 and the periscope, reached WPP, where it becomes circularly (clockwise) polarized. The Pockels effect now restates the previous polarization state, meaning that when passing WPP again, the pulse is still p-polarized and therefore cannot be transmitted by the BSP placed on top of the periscope, leaving the system.

The RAEA^{TM} software allows for fine tuning the PC ON/OFF switches, which in our system are currently separated by $84ns$ ($\tau_{PC,ON} = 5006ns$ and $\tau_{PC,OFF} = 5090ns$, with respect to a common system clock). The arrival time of the 532nm pump pulse from the NG is also highly tunable parameter, allowing for the optimization of both the crystal-to-

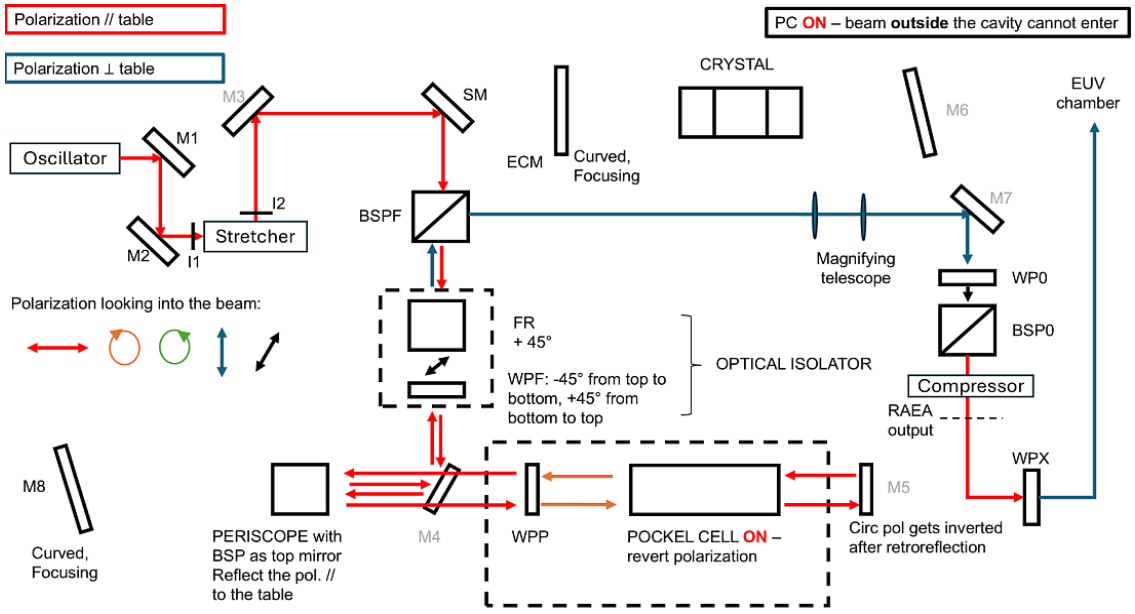


Figure 5.12: Path followed by the pulses outside the cavity when PC is turned ON.

seed stored energy transfer and for the entire repetition rate of the amplifier. The RAEA ™ is indeed capable to operate with variable repetition rates from $5KHz$ to $30KHz$ and different output powers and pulse energies. For the purpose of HHG, the current system is configured to generate 3mJ pulses at $5KHz$, corresponding to an average power of $15W$. Compared to the Griffin™ repetition rate of $81MHz$, the amplifier selects one pulse every 16000 pulses, therefore practically reducing the repetition rate of the system. However, it must be noted that the system simultaneously outputs both amplified and unamplified pulses, with the latter basically being a continuous background, having energies $6-7$ orders of magnitudes lower.

The software also admits piloting the stretcher and the compressor (using their stages) to optimize the temporal duration and the spectral phase of the pulse. In optimal conditions, the amplifier emits pulses of $26-28nm$ bandwidth, supporting $\sim 35fs$ beams. Compared to the oscillator output, the bandwidth is reduced, as expected, due to amplification gain narrowing process [118].

5.3 Ultrafast Pulse Duration Measurements

The precise characterization of ultrashort optical pulses generated by the RAEA^{TM} is crucial for ultrafast experiments and mandatory for time-resolved techniques employing HHG, where pulse durations can extend into the femtosecond and attosecond regimes. In addition to the requirements of high-peak power and fs pulse duration, which shall be accurately measured, the HHG process is profoundly sensitive to the electric field of the driving laser. Any phase distortion, such as chirp or higher-order dispersion, can significantly impact the trajectory of the electron and its probability of recombination with the parent ion, ultimately affecting the bandwidth of the produced harmonics (see the three-step in section 6.1.1.1).

The transient nature of the driving laser pulses, often comprising only a few optical cycles, necessitates sophisticated metrology techniques beyond the capability of conventional electronic devices. Commercial electronic systems, such as fast photodiodes combined with high-speed sampling oscilloscopes, are typically limited to time resolutions in the order of $1 - 10ps$. Also cables and connectors can introduce significant signal attenuation of RF frequencies and therefore their lengths should be kept as short as possible. Furthermore, electronic measurements primarily detect the pulse intensity and do not provide information on the phase, which is fundamental for the exact estimation of the shape and duration of the beam. Hence, a device or method capable of determining both the temporal amplitude and the spectral phase of the pulse is of critical importance, as these properties govern its spatiotemporal coherence and peak intensity, which are essential both for driving non-linear phenomena and achieving high-temporal resolution in pump-probe experiments.

The earliest methods providing a characterization of ultrashort pulses beyond the electronic limits are based on optical autocorrelation. These techniques rely on a nonlinear optical phenomenon, typically Second Harmonic Generation (SHG), to transduce a temporal delay into a measurable signal. Intensity autocorrelators [122] exploit the generation of a frequency doubled signal from the nonlinear interaction of two spatiotemporally focused ultrashort pulses on Beta-Barium Borate (BBO) crystals. By varying the delay τ, the intensity of the SHG signal $I_{2\omega}(\tau) \propto \int_{-\infty}^{+\infty} |E(t)E(t-\tau)|^2 \, dt$ can be measured. This operation is mathematically equivalent to an autocorrelation. Even though this operation can be used to infer the temporal intensity profile of the pulse, it does not include any detail about the spectral phase of the beam, being the phase factors lost in the modulus

squared operation. Another similar technique is Interferometric autocorrelation (IAC) [116]: this method uses SHG but instead of involving two separate beam paths, two pulse replicas are temporally delayed along the same direction, as in a Michelson interferometer, and focused on the nonlinear crystal. In this layout, the SHG signal encodes information about the coherent interaction between the two individual beams, providing a symmetric trace whose contrast and nodes are related to pulse chirp and phase distortions. Ultimately, despite providing more insights compared to intensity autocorrelations, IAC is not capable of providing the full spatio-spectral picture of ultrafast beams.

The loss of phase information in autocorrelation measurements leads to significant uncertainties in estimating the parameters of an ultrashort pulse, however, more recent and "complete" techniques are capable of simultaneously determining amplitude and phase of the pulse electric field. Spectral Phase Interferometry for Direct Electric-field Reconstruction (SPIDER) and Frequency-Resolved Optical Grating (FROG) represent the two most consolidated methods to obtain complete information on the temporal and spectral characteristics of such transient waveforms. SPIDER [123, 124] is based on the principle of self-referenced spectral interferometry. In this technique, two temporally delayed replicas of the pulse under investigation — each with a well-defined frequency offset $\delta\omega$ from the carrier — are generated through SFG with a third strongly chirped replica in a nonlinear crystal (e.g. a BBO). The resulting sum-frequency signals, each shifted in frequency, then interfere in the spectral domain, generating a 1D interferogram which encodes the differential spectral phase, subsequently retrieved using Fourier-based procedures such as the Takeda algorithm. Since the information are encoded directly into the interferogram, SPIDER is a highly robust method for pulses shorter than $10fs$, where fluctuations in the nonlinear conversion efficiency of the crystal may arise. On the other hand, it lacks flexibility: it is sensitive to pulses exhibiting very strong intensity modulation and cannot be arbitrarily used for pulses longer than a fixed duration, due to the intrinsic coupling between the time delayed replicas and the spectral shift introduced during the upconversion. This last consideration makes this tool inappropriate for the characterization of our amplifier. FROG [125–128] instead operates on the fundamental principle of spectrally resolving a non-linear optical signal generated by the interaction of the pulse under investigation and a variably delayed replica of itself. The end goal of FROG is basically the generation of a spectrogram of the pulse, which essentially addresses the time of arrival of each frequency constituting the pulse. This is achieved by gating the pulse $E(t)$ with a variably delayed gate function $g(t-\tau)$ generated from a shifted replica

of the pulse itself $E(t-\tau)$ within a nonlinear optical medium. The resultant nonlinear signal $E_{sig}(t,\tau)$ is then spectrally resolved as a function of the delay using a spectrometer and recorded by a detector (e.g. a CCD array) to produce a two-dimensional FROG trace, whose expression is

$$I_{FROG}(\omega,\tau) = \left| \int_{-\infty}^{\infty} E_{sig}(t,\tau) e^{-i\omega t} dt \right|^2 . \tag{5.8}$$

Like a musical score and in contrast to simpler intensity autocorrelation techniques, the FROG trace reveals the frequency content of the pulse versus time. This enables the characterization of complex pulse shapes, including those with linear chirp. The problem of retrieving the complex electric field $E(t)$ from its 2D Fourier transform is mathematically equivalent to a phase-retrieval problem [128], for which solutions exist despite certain ambiguities, such as the absolute phase, the pulse arrival time and the direction of time for certain FROG geometries such as SHG-FROG [129].

5.3.1 SHG-FROG and GRENOUILLE

Various nonlinear optical interactions can be used for FROG measurements, each defining a specific gate function $g(t-\tau)$ and resulting in different output signal fields [123]. Among these, SHG-FROG is probably the most widely used due to its high sensitivity, allowing measurements within the pJ regime, and excellent SNR. The experimental apparatus for SHG-FROG (see Fig. 5.13) is similar to an intensity autocorrelator: the pulse is firstly split into two identical replicas by a beamsplitter; one replica is subjected to a variable delay τ while the two pulses are overlapped spatially and temporally within a nonlinear optical crystal such as a BBO. The generated second harmonic signal is then spectrally resolved by a spectrometer and recorded by a camera as a function of the delay. The fundamental signal and any SHG from the individual beams (i.e. not generated by sum-frequency generation SFG) are typically blocked by apertures and/or filters. The primary challenge in FROG is to retrieve the electric field of the pulse from the measured intensity traces. This inversion problem can be solved by phase-retrieval algorithms, such as the generalized projection algorithm which offers robustness, speed and good convergence even with noise. The working principle is to alternate between two sets of constraints, in a similar fashion to what described in section 3.4 for CDI, but working in the temporal domain. Inside the first constraint set, represented by the physical constraint, all possible

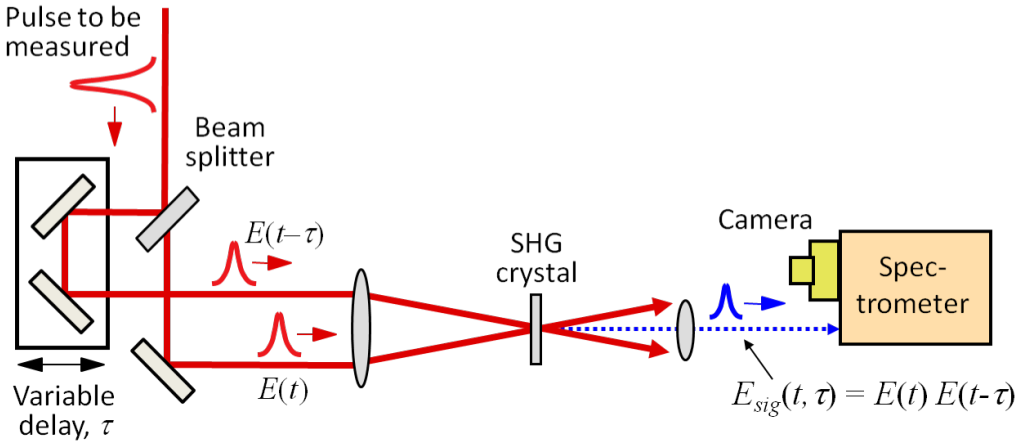


Figure 5.13: SHG-FROG experimental layout. Adapted from [130].

signals that satisfy the relation $E_{sig}(t,\tau) = E(t)E(t-\tau)$ are contained. The second domain instead comprises all complex functions whose magnitude squared matches the measured FROG trace $I_{FROG}(\omega,\tau)$. Starting from an initial guess (e.g. Gaussian beam with random phase distribution), the algorithm iteratively transforms the estimated field between time and frequency domains using a Fast Fourier Transform (FFT) and its inverse (iFFT), with the final purpose of minimizing the FROG error metric, which quantifies the difference between the measured and calculated FROG traces. In most cases, when the error reaches 1%, good agreement is reached and the complex electric field is estimated. However, a visual interpretation of FROG spectrogram can provide multiple qualitative information prior to the phase retrieval. One must first note that SHG-FROG traces are intrinsically symmetric with respect to the delay axis, therefore causing an ambiguity in the direction of time but also providing an indication on possible experimental issues (see Fig. 5.14). Transform-limited pulses would possess elliptical or round shape, with the extension on the temporal axis being linked to the pulse time duration while the vertical width is associated with the pulse's bandwidth (mostly constant along τ). For pulses suffering linear chirp, either positive or negative, the trace will be typically bigger both in τ and ω. This happens since chirped beams are longer than transform-limited ones and distribute their spectral components over time. Complex pulses possessing higher order dispersion terms will present more sophisticated structures. In our ultrafast XUV ptychography setup, a simplified FROG variant called GRENOUILLE is placed immediately after the amplifier, in order to monitor the quality of the beam to be used

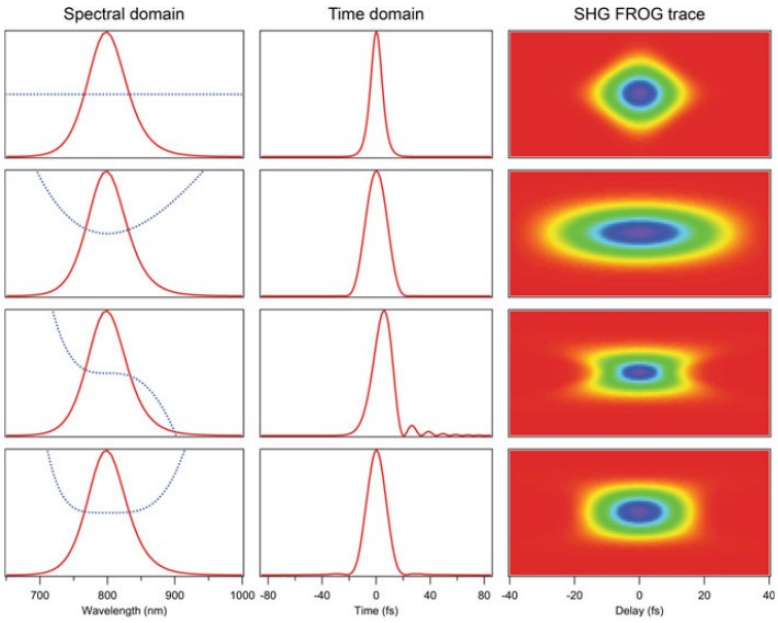


Figure 5.14: Simulated SHG FROG traces for $sech^2$ pulse shapes shown on the left. In the spectral domain, different orders of dispersions (from none to FOD) are added to the pulse.

for the HHG process. The GRENOULLE is designed to make the pulse measurement more practical and removes most of the alignment complexity. The device is compact and embeds multiple optical elements integrated inside a single case. The GRENOUILLE implements a Fresnel biprism to cross two replicas of the input pulse at a large angle, for accurately mapping their delays onto one axis of the detector. Moreover, instead of a thin crystal and a separate spectrometer, the GRENOUILLE employs a thick SHG crystal that simultaneously separates the different frequency components along the other transverse axis of the detector. In fact, when broadband light with a large convergence angle impinges on such a crystal, the phase-matching conditions become strongly angle-dependent. As a consequence, each spectral component of the pulse generates second-harmonic light at a different propagation angle. The angular spread of the SHG output decreases as the crystal thickness increases, providing sufficient angular discrimination to resolve the spectrum directly on the detector, without the need for a separate spectrometer. In order to operate properly, the crystal is accurately engineered to satisfy two key conditions: a large group velocity mismatch is required to ensure that the fundamental and the second harmonic beams cease to overlap by the end of the crystal and a small group velocity dispersion in order to avoid distorting the pulse itself. The GRENOUILLE 8-20-USB implemented

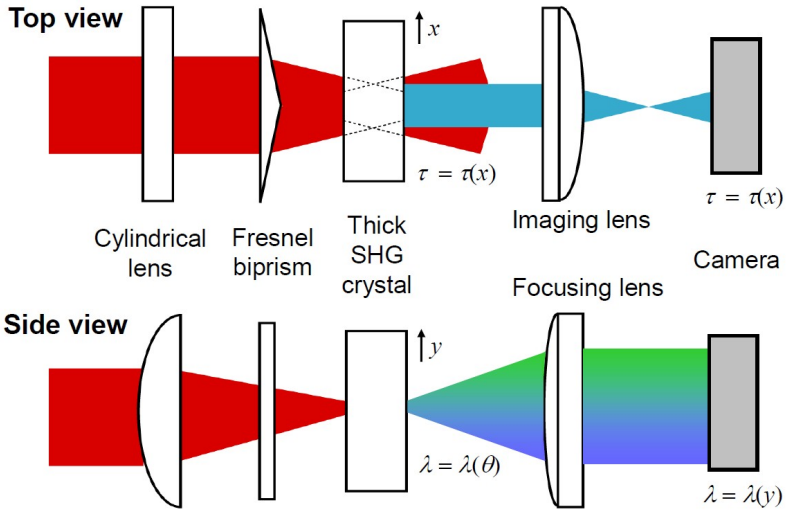


Figure 5.15: Top and side view of the GRENOUILLE. The Fresnel biprism maps the delay onto the horizontal transverse direction (top view) while the crystal spectrally resolves the SHG onto the vertical (side view) direction of the camera. From [131].

along the beam paths of our beamline is a simple and cost-effective solution for optimizing the output of the amplifier. It contains two cameras: one is devoted to the acquisition of the $\lambda - \tau$ traces discussed so far, the other allows for the visualization of the spatial beam profile. In this way, it is possible to completely determine the spatiotemporal picture of the pulse. Due to its compactness, it does not require significant space and it is robust to misalignments. However, certain beam conditions and setup procedures are nonetheless required for acquiring accurate data:

- Beam quality: the system operates best with a fairly smooth and collimated input beam, with deviations from ideality possibly compromising the measurement accuracy.

- Beam size: the diameter of the beam should be $> 2mm$ and $< 4mm$. An excessively small input beam would yield a reduced range of measurable delays and frequencies, while a particularly large beam would overfill the aperture and crop the wavefront, which would lead to inaccurate results.

- Polarization: the polarization of the input beam must be aligned to the double-headed arrow on the front aperture of the device. No trace will be visible if perpendicular to this direction.

- Input intensity: the intensity of laser radiation directed into the GRENOULLE must be adjusted to guarantee the detection of a signal while avoiding the saturation of the detector. To utilize the full dynamic range of the camera, the use of attenuators is recommended.

- Centering: the laser beam must be properly centered into the input iris of the GRENOUILLE. The system possesses a camera showing the spatial profile of the beam, which can be used as reference for the initial alignment. Non-circular input beams may indeed lead to measurement distortion.

- Time-duration: due to the inherent thickness of the crystal, the measurement is not suitable for pulses shorter than approximately $20 fs$.

Considering the above mentioned requirements and especially the beam size, the input intensity, and the laser alignment into the iris of the GRENOUILLE, the RAEA^{TM} output cannot be directly used as it leaves the compressor. The practical implementation of the FROG on the optical table will be discussed in the next paragraph.

5.3.2 The Diagnostic Branch

The diagnostic branch including the pulse measurement device is placed immediately after the ultrafast amplifier. After hitting three steering mirrors, 45° 2″ beamsplitter (BSP1 in Fig. 6.1) reflects 5% of the incident p-polarized light towards a dedicated optical path — the diagnostic branch — for pulse measurements. Such amount is sufficient to monitor the status of the amplifier and optimize its output. The specific purpose of this optical line is to characterize the pulse spatiotemporal characteristics both with a beam profiler (MKS Ophir SP90608), in order to address its astigmatism and potentially realign the telescope inside the cavity of the amplifier, and with the GRENOUILLE 8-20-USB, respecting the beam conditions described at the end of section 5.3.1. These two configurations are mutually exclusive. The diagnostic branch starts by attenuating the reflected laser from BSP1 by setting WP0 equal to 48° and using a single neutral density (ND) filter with optical density (OD) equal to 3. This leads to an estimated power of $0.65 mW$, which is sufficient to avoid saturation or damage to both downstream detectors. Afterwards, the beam is steered by a couple of 45° 1.5″ mirrors mounted on high stability mounts. At this point the FROG and beam profiling configurations diversify. The FROG one is represented in Fig. 5.16: the beam out of the RAEA^{TM} with diameter $D_{in,\ 1/e^2} = 10 mm$ is demagnified to

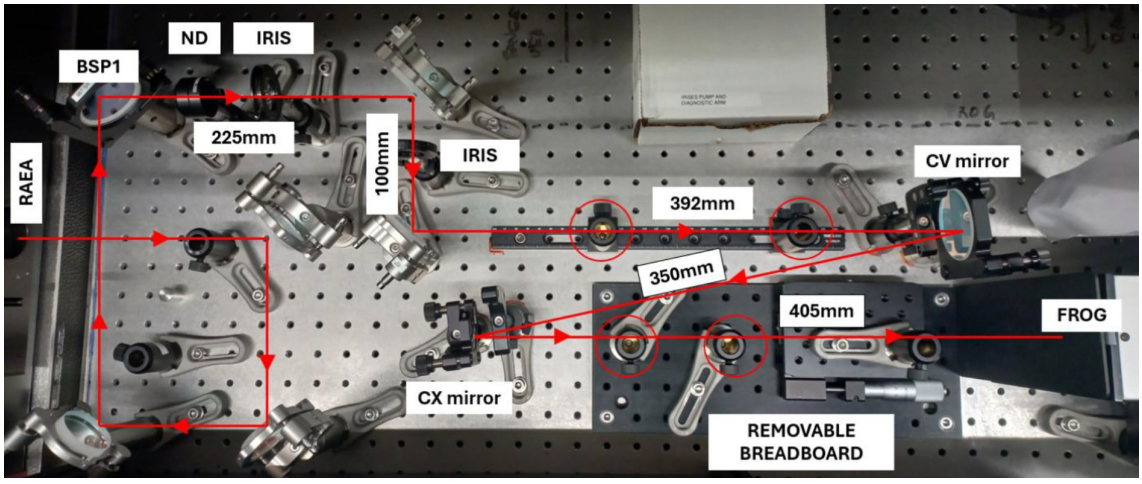


Figure 5.16: Diagnostic branch set for FROG measurements.

$D_{out,1/e^2} = 3mm$ using a reflecting telescope composed by a 2″ concave mirror (CV) with focal length $f = 500mm$ (Thorlabs CM508-500-E03) and a 1″ convex mirror (CX) with $f = -150mm$ (Edmund Optics #87-681), separated by a distance of $350mm$ in order to keep it collimated and avoid wavefront distortions. The telescope is composed of reflective optical elements instead of lenses in order to avoid the GDD induced by the passage through glass. Both CV and CX are moreover mounted on kinematic mounts in order to properly tune the alignment inside the input iris of the GRENOUILLE. Adopting this configuration, a typical result from pulse duration measurement is shown in Fig. 5.17. By imposing an input wavelength of $800nm$ (the output spectrum of the RAEA is often closer to $790nm$), the measurement highlights the retrieved pulse characteristics in the "Results Panel". Based on the successful convergence of the FROG retrieval algorithm, which reached an error of 0.0035, high reliability of the reconstructed pulse is achieved. The FROG analysis indicates that the investigated pulse is short, nearly transform-limited, and exhibits minimal phase distortions, suitable for high-precision ultrafast applications. The temporal intensity profile (red curve, center) exhibits a FWHM duration of $35.6fs$. The retrieved spectral intensity (green curve, right) shows a spectral FWHM of $25.5nm$. The resulting time-bandwidth product (TBP) is 0.416 (FWHM definition), close to 0.44, the Fourier limit value for a Gaussian pulse. This indicates near-transform-limited behavior. The retrieved temporal phase (blue curve) and spectral phase (magenta curve) display small deviations, with no significant higher-order distortions. The software shows other parameters relative to the acquisition process which can be considered non-relevant for the discussion.

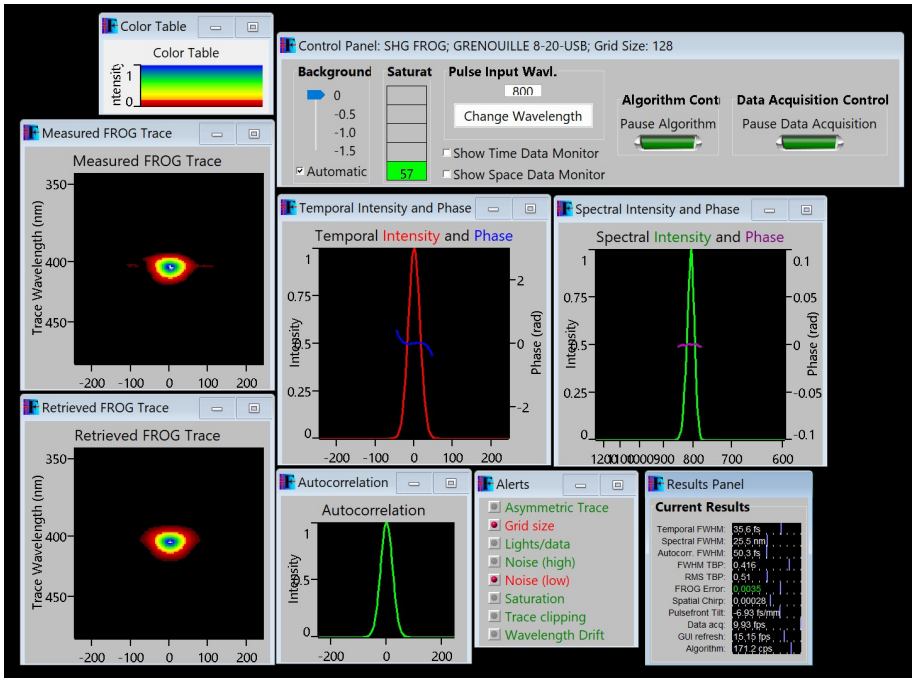


Figure 5.17: Retrieved trace from GRENOUILLE.

The second configuration of the diagnostic branch is shown in Fig. 5.18, which presents several additions: (i) two removable magnetic mirror mounts in front of CV and CX that allow an easy swapping to the FROG configuration; (ii) a focusing lens with $f = 752mm$, used to recreate the XUV generation conditions inside the HHG source; (iii) a beam profiler set at the lens focus through a linear translation stage. Moving the linear translation stage across the focal plane, possible beam astigmatism can be diagnosed and corrected. In both Fig. 5.16 and Fig. 5.18, multiple empty post holders are placed to facilitate an early alignment with irises.

Finally, two pre-alignment irises along the translation stage of the beam profiler are set on a removable breadboard, to allow quick disassembly during maintenance of the RAEA^{TM} cryocell.

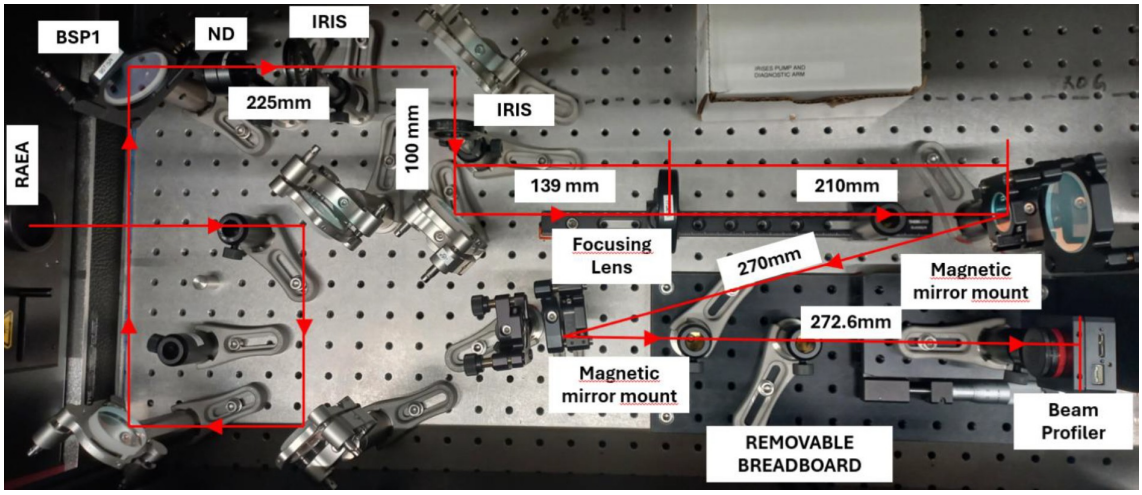


Figure 5.18: Diagnostic branch set for beam profiling.

Chapter 6

The Ultrafast XUV Ptychography Beamline

In this chapter, the design and the implementation of the entire Ultrafast XUV Ptychography Beamline – microscope excluded – is presented. The analysis starts from the output of the RAEA^{TM}, which is distributed to the diagnostic branch, to the Ultrafast Electron Diffraction setup (UED) and to both pump and probe branches of the ptychography beamline.

As shown in Fig. 6.1, immediately after the ultrafast amplifier, the p-polarized collimated laser beam is steered by three 45° 1.5″ mirrors mounted on high stability mounts, which serve to direct the beam in a long-lever arm. The mirrors have their poles centered at a height of 114.3mm from the optical table, equal to the height of the beam exiting the compressor. After leaving the third mirror, the beam follows a straight path intercepted by a series of three 45° 2″ BSPs used to split the beams onto three separate branches. The BSPs specifications have been carefully chosen in such a way that all three branches can run in parallel:

- The first beamsplitter (BSP1, Layertec 181216) transmits 95% of the incident power and reflects the remaining 5%, towards the diagnostic branch described in section 5.3.2.

- The second beamsplitter (BSP2, Layertec 181214) divides the two beamlines powered by the RAEA^{TM}: the Ultrafast Electron Diffraction setup (UED branch, out of the scope of this dissertation) and the Ultrafast XUV Ptychographic Microscope (EUV branch). To provide enough energy for both experiments to run in parallel,

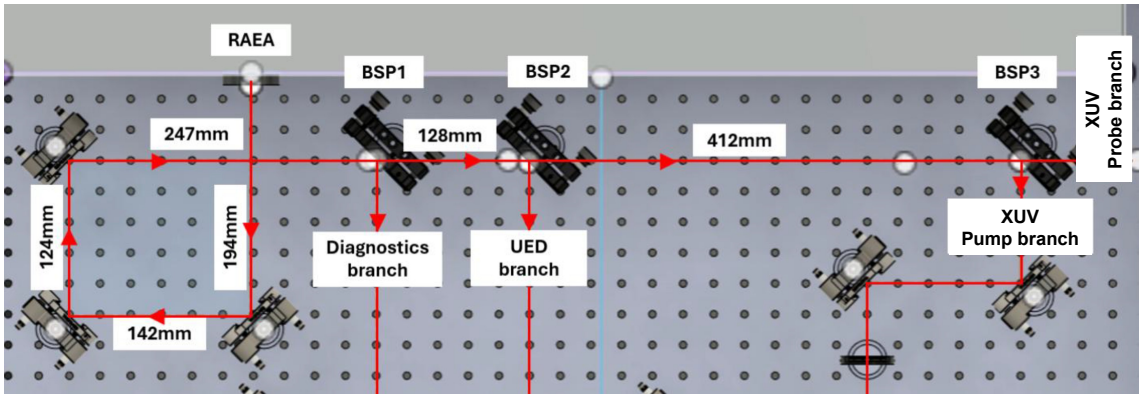


Figure 6.1: Detail of the beam path out of the RAEA and splitting into the three branches

BSP2 extracts 20% (2.85W) of the input radiation for the UED setup and transmits 80% (11.4W) for the XUV beamline.

- The third beamsplitter (BSP3, Layertec 107612) is used to divide the XUV pump (10% reflection, 1.14W) and probe (90% transmission, 10.26W) branches as required for time-resolved experiments.

All the BSPs inside the beamline possess low GDD to minimize stretching and chirping of the pulse. Each optical element is indeed constituted by a substrate in UV fused silica (UVFS) with thickness $L = 3.05mm$ and a GVD of $36fs^2/mm$. When the transmitted beam is analyzed, the pulse-broadening effect provided by the first beamsplitter, assuming a gaussian-like profile of the laser pulse out of the amplifier can be estimated in [116]

$$\tau_P(L) = \frac{\sqrt{\tau_P^4(0) + (4\ln 2 * GVD * L)^2}}{\tau_P(0)} = 36fs. \tag{6.1}$$

The result is obtained with an initial pulse duration of $\tau_P(0) = 35fs$ and shows a $\sim 3\%$ increase of the pulse duration compared to the initial condition. As the pulse passes through BSP2 and BSP3, the effect of GDD to the pulsewidth reduces. After BSP3, a time duration of $\tau_P \approx 37.8fs$ is obtained by the application in series of eq. (6.1). The three beamsplitters have their front surfaces coated with highly reflective materials for 45° incidence of p-polarized laser pulses with bandwidth inside the $750-850nm$ range. These coatings are designed to provide a guaranteed $GDD < 20fs^2$ across the entire spectral range, both in transmission and reflection, with values approximately equal to zero at $800nm$. The rear surface of each optical element is covered with an anti-reflective coating

with reflectance < 0.2%, therefore, negligible pulse modifications are expected from it.

Laser induced damage threshold (LIDT) has been also considered. According to the supplier, the UVFS substrate possess a $LIDT \sim 0.4 J/cm^2$ for lasers operating in proximity of $800nm$ and fs-long pulse duration. This value is substantially higher than the maximum fluence from the RAEA^{TM}, which is

$$\mathcal{F} = \frac{E}{A} = \frac{4P f_{rep}}{\pi D^2} \approx 3.82 mJ/cm^2, \tag{6.2}$$

considering a maximum power equal to $P = 15W$, a repetition rate of $f_{rep} = 5KHz$ and a gaussian-like pulse with diameter $D = 1cm\ 1/e^2$.

This first common section is therefore fully compatible with the operative conditions of the laser source. It allows an effective distribution of the optical radiation to the diagnostic branch and to the UED and XUV beamlines, with limited effects on the pulse spatiotemporal characteristics, particularly relevant to the harmonic upconversion process. In the next sections, the probe and pump branches are discussed in detail.

6.1 XUV Probe Branch

The probe branch of the Ultrafast XUV Ptychographic Microscope is dedicated to the generation of XUV radiation through a process known as High-Harmonic Generation (HHG), briefly mentioned in section 1.2 during the introduction of coherent radiation sources. In the following paragraphs the fundamental principles of HHG are discussed as well as their practical implementation in the laboratory.

6.1.1 The High-Harmonic Generation Process

The High-Harmonic Generation process is a sophisticated nonlinear optical process that efficiently converts intense, ultrafast driving laser pulses (typically in the IR or visible spectrum) into coherent radiation at much shorter wavelengths, specifically in the XUV or the soft X-ray regions. Over the past three decades, the development of HHG has matured significantly, almost transforming it into a “turn-key” solution for high-energy coherent light emission in a laboratory. This technique is particularly valuable because preserves the coherent properties of the input light while guaranteeing access to the more energetic and shorter pulse durations.

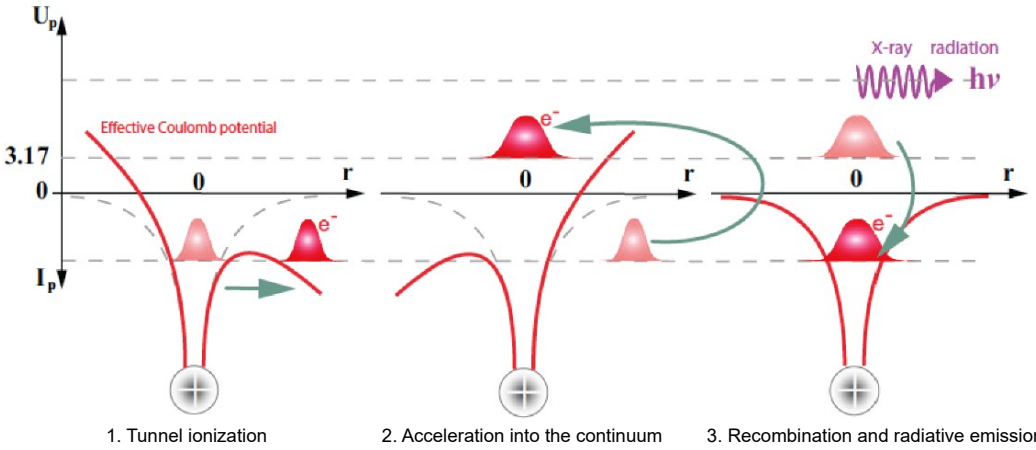


Figure 6.2: The three-step model of High Harmonic Generation. Adapted from [132].

6.1.1.1 The Three-Step Model

The underlying physical mechanism of HHG at the single-atom level is elegantly described by the semi-classical "three-step model", which, despite its simplifications, intuitively predicts several important features of the process [133–135]. This is shown in Fig. 6.2 and described as follows:

1. Tunnel Ionization: the process begins when an intense IR laser pulse — typically focused to reach intensities of the order of 10^{14} – 10^{15} W/cm^2 — interacts with a noble gas atom, such as He, Ne, Ar, Kr or Xe. The strong electric field of the driving pulse significantly distorts and lowers the binding potential of the atom, allowing a bound electron at the ground state to tunnel through the energy barrier and reach the continuum. The tunneling probability follows an exponential trend and depends on the atomic ionization potential I_p and the strength of the laser electric field E_0. The tunneling regime is typically governed by the Keldysh parameter $\gamma_K = \sqrt{I_p/2U_p}$, where U_p is the ponderomotive energy, that is, the mean kinetic energy of the electron quivering in the laser field. The Keldysh parameter expresses the type of ionization process taking place at the single atom, with HHG typically occurring at values of $\gamma_K \leq 1$. In this step the "slow-field approximation" is assumed, which means that the duration of a half-cycle of the laser field is considerably longer than the characteristic tunneling time of the electron, with the consequence of the electric field being treated as a static entity.

2. Acceleration into the continuum: once freed, the electron is assumed to possess zero

kinetic energy and therefore becomes accelerated by the oscillating electric field of the intense laser pulse. The electron travels inside the continuum and gains kinetic energy according to its emission time with respect to the phase of the cycling electric field. When the laser reverses its direction, the electron is slowed and reverses its trajectory, traveling back to the parent ion. Depending on the phase of the electric field when tunneling occurs, the electron experiences different trajectories, leading to an accumulated kinetic energy in the range $20 - 200eV$.

3. Recombination and radiative emission: the third step involves the finite probability that the returning electron recombines with the parent ion, releasing, in the form of a highly energetic photon, the acquired kinetic energy plus the atomic ionization energy. The maximum value of the emission is marked by a cutoff at

$$h\omega = 3.17U_P + I_P \tag{6.3}$$

where the 3.17 factor can be calculated by solving the equation of motion of a charged particle oscillating in an electric field and finding the trajectory maximizing the kinetic energy [133]. The probability of radiative recombination is relatively small due to several factors, including that no photoelectrons emitted before the peak of the pulse return to the parent ion and that the electron's wavepacket diverges during propagation in the 3D space, further reducing the probability of recombination.

The three-step model culminates with the generation of a comb of intense, polarized and coherent odd-order harmonics of the fundamental driving laser frequency up to the XUV/Soft X-ray domain. The produced spectrum is typically centered on specific harmonic orders and follows the peculiar shape indicated in Fig. 6.3, with an intensity decrease for the first orders, a plateau and a sharp cutoff approximately at the energy indicated in eq. (6.3). The pondermotive energy can be derived as a function of the properties of the electron (mass m and charge e), the electric field amplitude E and the oscillation frequency ω_0 as

$$U_P = \frac{e^2E^2}{4m\omega_0} \approx I_L\lambda_L^2. \tag{6.4}$$

The result approximately depends on the intensity I_L and wavelength λ_L of the driver. The equation reveals that longer driving laser wavelengths can produce higher energy photons [135] and access the water window, where biological samples can be studied [136–138]. This comes however at the expense of HHG flux, as probability of radiative recombination

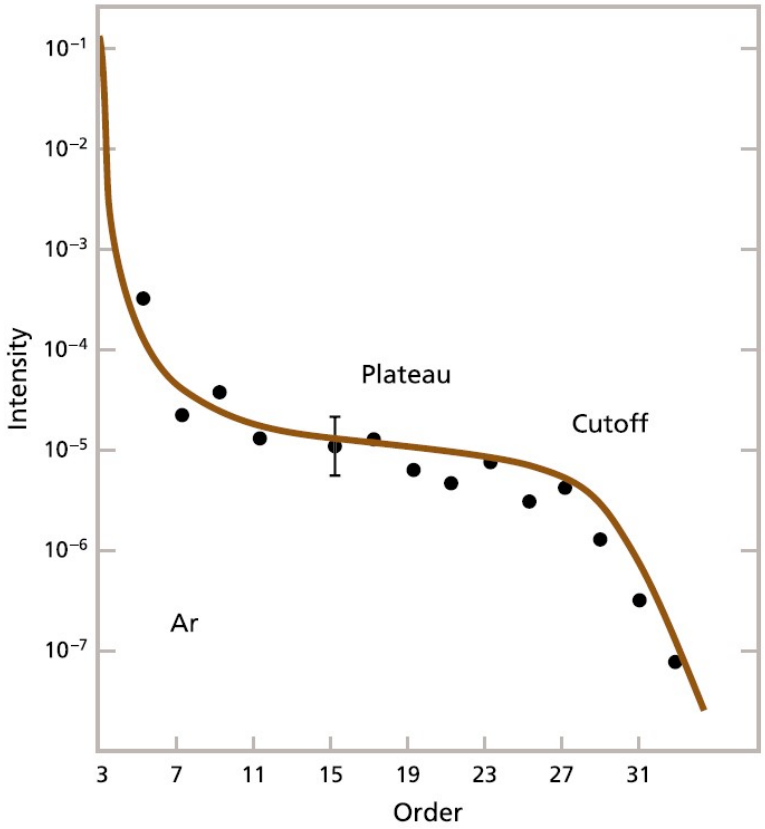


Figure 6.3: Distribution of harmonics in Ar atmosphere. From [136].

is reduced and the conversion efficiency significantly decreases approximately as $1/\lambda^4$ to $1/\lambda^6$ [52].

The nonlinear nature of HHG confines the ionization and recombination processes to a very short temporal window within the driving laser pulse, typically less than 10% of the oscillation period [139]. As a consequence, the generated high-harmonic radiation can reach the attosecond limit and, for multi-cycle driving beams, it can result in a continuous burst of pulses in the time domain. The generation of isolated attosecond pulses is however possible by combining near single-cycle IR driving laser pulses or advanced gating techniques such as polarization gating, to restrict the emission of the electron to a single half-cycle.

A significant advantage of HHG radiation is its high degree of spatial coherence, which is largely imprinted from the input laser wavefront. Each participating atom experiences a well-defined phase of the driving field at its local position, leading to emission with a fixed phase relation across the transverse wavefront. As a consequence, the spatial

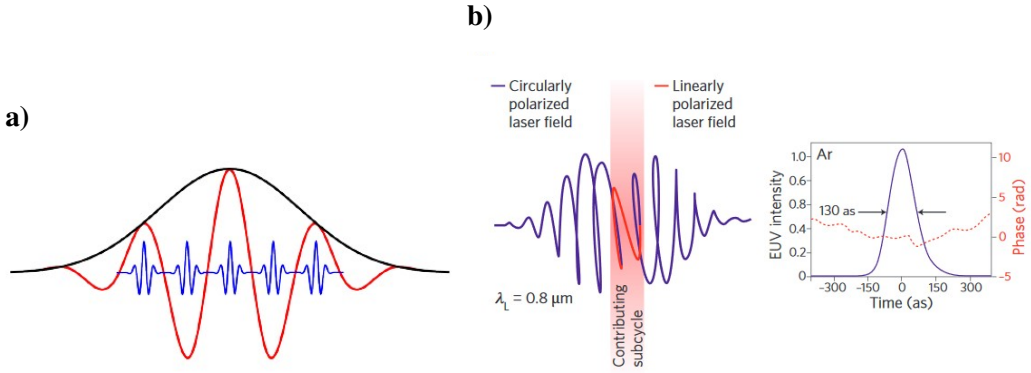


Figure 6.4: Generation of attosecond pulses. (a) Continuous burst of pulses generated from multi-cycle beams. (b) Polarization gating technique leading to the generation of a single as-long pulse, shown on the right. Adapted from [134].

coherence and beam quality of the harmonic radiation are strongly determined by the spatial uniformity of the driving laser. Any distortion in the input beam wavefront or intensity profile may degrade the transverse coherence and focusability of the generated harmonics, therefore an accurate diagnostic system is required to assess the quality of the driving laser beam.

While these considerations are true at the single emitter level, achieving bright coherent beams of XUV light requires the coherent summation of the emissions from different atoms over the entire interaction length. This is achieved by satisfying a condition called phase matching.

6.1.1.2 Phase Matching

Phase matching refers to the condition leading to a macroscopic build-up of harmonic intensity from the constructive interference of harmonic waves emitted from different positions along the interaction length. Without this collective interference, light emitted from multiple atoms would be out of phase, resulting in destructive interference and a substantial reduction of the overall intensity of the XUV beam. The necessity for phase matching comes from the inherent dispersion mismatch between the fundamental IR driving laser field and the generated XUV light as they propagate through the nonlinear medium. This mismatch arises due to the difference in their phase velocity $v_{ph} = \omega/k$, whose primary cause is the frequency-dependent refractive index of the plasma generated during the laser-matter interaction. The ideal phase matching condition for a q-th harmonic

order with wavenumber $k_{q\omega}$ driven by a laser with wavenumber k_ω can be expressed by

$$\Delta k = k_{q\omega} - q k_\omega = 0, \tag{6.5}$$

with Δk being the total phase mismatch. This value is provided by the combination of four main physical effects influencing the propagation of both the fundamental and the harmonic fields within the medium such as:

- Δk_{atom}: an effect originating from the neutral atoms and the non-linear refractive index of the medium that, being wavelength-dependent, contributes to the dephasing between the fundamental and the XUV light;
- Δk_{plasma}: a critical factor originating by the ionization of the gaseous medium in a plasma by the intense IR pulse;
- Δk_{geom}: a geometrical factor;
- $\Delta k_{AD_{phase}}$: a dipole-phase mismatch arising from the longitudinal gradient of the intensity-dependent atomic dipole phase accumulated during the excursion of the electrons in the continuum.

An effective phase matching can be established in a gas jet or, as in our implementation, in a hollow waveguide, where the dispersion mismatch, under the assumption of single mode propagation inside the capillary, low ionization fraction and slowly varying intensity, can be written as [140]

$$\Delta k \approx q\frac{\mu_{11}^2 \lambda_L}{4\pi a^2} - q\frac{2\pi P(1-\eta)}{\lambda_L}(\Delta\delta + n_2) + qP\eta N_a r_e \lambda_L. \tag{6.6}$$

The first positive contribution is the geometric term, arising from the modal dispersion in the capillary waveguide. The quantity μ_{11} is an adimensional factor of the fundamental mode TM_{00} propagating inside the waveguide. The dispersion increases with the laser wavelength λ_L, the harmonic order q, and is inversely proportional to the square of the waveguide radius a. The second term accounts for the contribution of the neutral atoms inside the gas medium. Here, P is the gas pressure, η the ionization fraction, and $\Delta\delta = \delta(\omega_L) - \delta(q\omega_L)$ is the difference in the refractive index experienced by the fundamental and harmonic frequencies in the medium. An additional intensity-dependent phase shift is embedded in n_2, which emerges from the nonlinear interaction between the

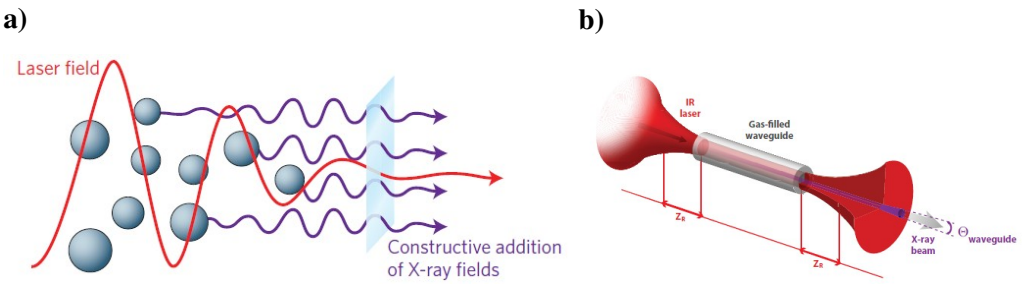


Figure 6.5: Phase matching in a capillary waveguide. (a) Intuitive depiction phase-matching with coherent addiction of XUV beams generated by an intense laser field. (b) Phase-matching implementation in a gas-filled waveguide, where the intense laser pulse is loosely focused and guided. The propagation of the x-ray/XUV beam takes place collinearly to the IR beam with, however, smaller divergence. Adapted from [134].

laser and the medium. This contribution is typically negative and helps to compensate for the first term. The last contribution models the effect of the free electron plasma generated by the strong-field ionization of the gas. Here $N_a$is the atomic density at ambient pressure and r_e is the classical radius of the electron. The contribution of the plasma is positive and increases with both pressure and degree of ionization, with a total effect of disfavoring the phase matching process. In practice, for waveguides of a given radius, adjusting parameters such as gas pressure, the laser wavelength and the pulse energy, is a suitable strategy for fine tuning the ionization level η and achieving high-energy phase-matched emission.

Ultrafast XUV Ptychography greatly benefits from HHG in capillary waveguides when compared to other widely diffused geometries, such as gas jets. First, they enable the propagation of the laser pulse over an extended interaction length while maintaining intensity and beam quality. In this way, the constructing interference region is extended beyond the typical dephasing distance of a few mm, leading to significantly brighter and more coherent XUV build-up [141]. The second motivation relies on the high spatial coherence exhibited by phase-matched generated harmonics, occurring at a very specific fundamental mode of the waveguide. In this way, every atom across the uniform NIR wavefront emits radiation in the forward direction and collinearly with the driving laser. As a consequence, coherent beams with low divergence can be obtained, which is dramatically important when designing an illumination function meters away from the generation point. Considering the alignment complexity and coupling, which sometimes can be difficult, typical conversion efficiencies in waveguides can reach the order of 10^{-6},

leading to more than 10^9 photons per second per 1% bandwidth.

In the following section, effective implementation of HHG in the probe branch of the beamline will be discussed.

6.1.2 Implementation of HHG in a Laboratory

The probe arm of the Ultrafast XUV Ptychography Beamline originates from BSP3 Fig. 6.1. Two high-stability 45° 1.5″ mirrors guide approximately $10.26W$ of intense IR laser radiation towards a 1.5″ piezo-actuated mirror. This is considered the first component of the XUUS^{TM} system of KMLabs, the coherent XUV light source based on HHG. Indeed, this last optical element, combined with another in-vacuum controlled mirror inside the XUUS^{TM}, allows the stabilization of the driver via point-locking onto two cameras, while producing the harmonics. Before entering the system, the beam passes through a $\lambda/2$ waveplate (WPX), a key component used to switch from the original p-polarization state to a s-polarized condition. As long as the polarization is linear, the HHG process remains uneffected by the value of WPX. However, the reflectivity of the optical elements placed downstream the generation point changes. By setting WPX to 17°, the transmission of the IR beam is maximized, which is used during the alignment procedures of the probe arm. On the other hand, by setting the waveplate to 62°, the polarization is oriented in such a way that the flux of XUV radiation is favored and the driver laser is minimized.

The XUUS^{TM} is composed by three chambers: two operate out of vacuum, can be opened during the HHG process and are indicated by the red color of their lids. The central chamber is vacuum-pumped and indicated by a lid colored in grey. The XUUS^{TM} was originally conceived to be directly connected to the RAEA^{TM} and, in this configuration, the first red section was devoted to accommodate the first piezo-actuated mirror. However, in our laboratory, the RAEA^{TM} is used to power two separate beamlines and the XUUS^{TM} is placed at a different location on the optical table. Therefore, the mirror has been moved outside, leaving the first chamber empty. The purpose of the second section is to focus the beam inside the capillary waveguide (hereafter called “cartridge”) and to monitor the beam shift and tilt by means of two point-lock cameras. This section is directly connected to the cartridge, it works under vacuum and therefore cannot be accessed during operations. The third section is accessible, contains the cartridge for the generation of XUV light, and is vacuum-sealed to the previous chamber by a swagelok connector. This section is

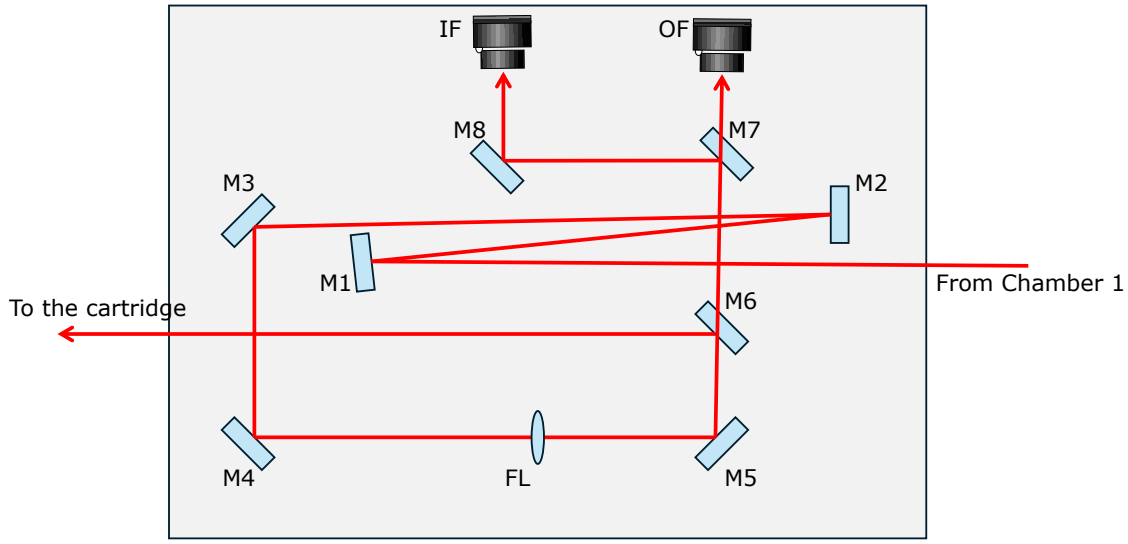


Figure 6.6: Sketch of the optical path occurring inside the second chamber of the XUUS^{TM}.

accessed to replace the cartridge and is often used for accurately beam-profiling the mode coupled inside it before starting the HHG process. After getting inside the first section of the XUUS^{TM}, the beam directly reaches the second section passing through a sapphire window capable of sustaining high laser powers. Under vacuum, the driver follows the path indicated in Fig. 6.6: the beam firstly gets steered by four mirrors, two 1″ mirrors at near-zero angle of incidence (M1 and M2) and a second pair of 45° 1″ mirrors (M3 and M4). Due to the delicate coupling to be achieved inside the cartridge, the mirrors and the other optical elements inside the cavity are placed on monolithic mounts. The beam gets thus directed to a plano-convex lens (FL) with a long focal length $f = 750mm$. The lens is mounted in such a way to allow tip and tilt for astigmatism compensation and, moreover, is placed along a rail to guarantee a precise fine tuning of the focus inside the capillary waveguide. Before reaching the focal point, the beam is steered by the second 1.5″ piezo-actuated mirror (M5) for point-lock stabilization and is later intercepted by a 1.5″ dielectric mirror (M6), which leaks a small portion of the optical radiation for the point-lock cameras. The transmitted component is immediately split again by another 45° dielectric mirror (M7), which makes it pass part of the incident radiation to the out-of-focus camera (OF), while the remaining part bounces on another mirror to goes to the in-focus camera (IF). By means of a control loop, the OF camera is used alongside the first piezo-mirror to stabilize the beam pointing before focus or, in other words, to avoid

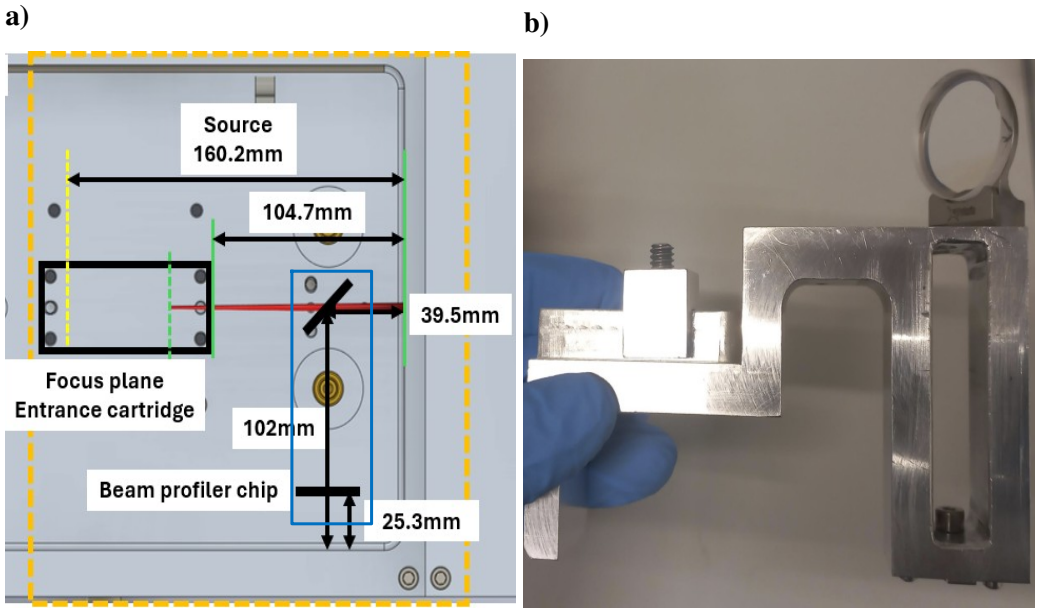


Figure 6.7: Use of the jig. (a) Beam profiling scheme inside before the cartridge, the blue line represent the area where the jig must be placed. Distances relative to the cartridge entrance point and the XUV emission source are referentiated to the chamber's wall and highlighted in green and yellow respectively (b) Custom jig to be placed inside the XUUS^{TM}.

major shifts of the illumination. The IF camera is instead employed for the stabilization of the beam at the focal point, in a way that any tilt of the beam is compensated by the second piezo-mirror. The reflected component out of M6 directly continues towards the cartridge and later proceeds to the following section. To get a proper coupling in the cartridge, the alignment of all mirrors in the previous chamber must be accomplished. To this purpose, along the optical path, custom made irises are strategically placed, in order to keep the beam at a constant height of $19mm$ with respect to the XUUS^{TM} base. Moreover, two irises on both sides of the rail create a reference for accurately set the tip, tilt and position of the lens, and achieve a symmetric focus at the required position along the cartridge. If the alignment has been performed effectively, the beam passes through the third chamber, which is the section accommodating the gas-filled waveguide for the HHG process. Operatively, in order to optimize the upconversion process, the quality of the beam mode across the focus must be checked. We have therefore designed a jig for beam profiling (Fig. 6.7b). The jig is meant to be used only during alignment at low power and accommodates a 1″ beamsplitter and a flexible rail for an Ophir Spiricon SP90549

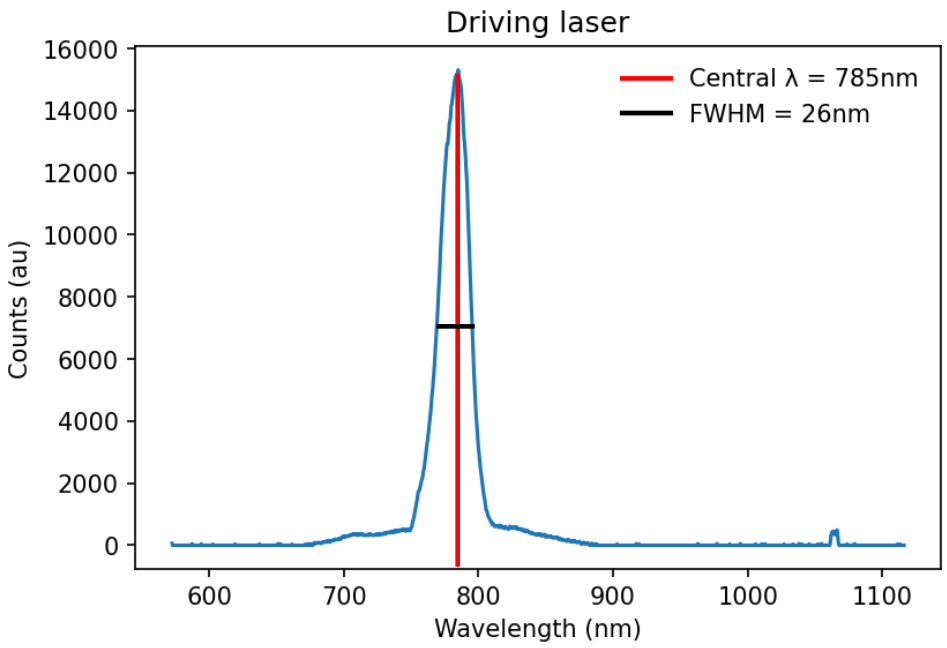


Figure 6.8: Driving laser wavelength out of the RAEA^{TM}.

beam profiler. Another jig, supplied directly by KMLabs is instead compatible with a WinCamD-LCM-NE DataRay. In this way, the chip position of both beam profilers can be set at a distance of $768.2mm$ from FL, identical to the separation length between FL and the insertion focusing point at the entrance of the cartridge, as sketched in Fig. 6.7a. Using a $785nm$ driver with FWHM of $26nm$ — typical values out of the RAEA^{TM} (see Fig. 6.8) — , and filling the cartridge with Ar or He, two different combs with outputs of 10^{12} ph/s and 10^{10} ph/s, respectively, can be generated (see Fig. 6.9). Injecting Argon at 37% in fractional volume, a $3.1eV$ equally spaced comb that maximizes the emission of the 27th harmonic at $42.6eV$ can be obtained. Using Helium at 10.6% in fractional volume instead, the emission consists of a $3.04eV$-spaced comb with maximum output energy at $96.5eV$. At waist, the diameter of the XUV beam is estimated to be approximately $30-50\mu m$ with a divergence of $0.5-2mrad$. According to previous tests and analysis from the supplier, average values are $1.2mrad$ and $1.4mrad$ for Ar and He, respectively.

6.1.3 Driver Suppression with Rejector Mirrors

Following the XUUS^{TM} system, the XUV radiation generated via HHG co-propagates with the residual fundamental beam. Both beams traverse a gate valve and subsequently

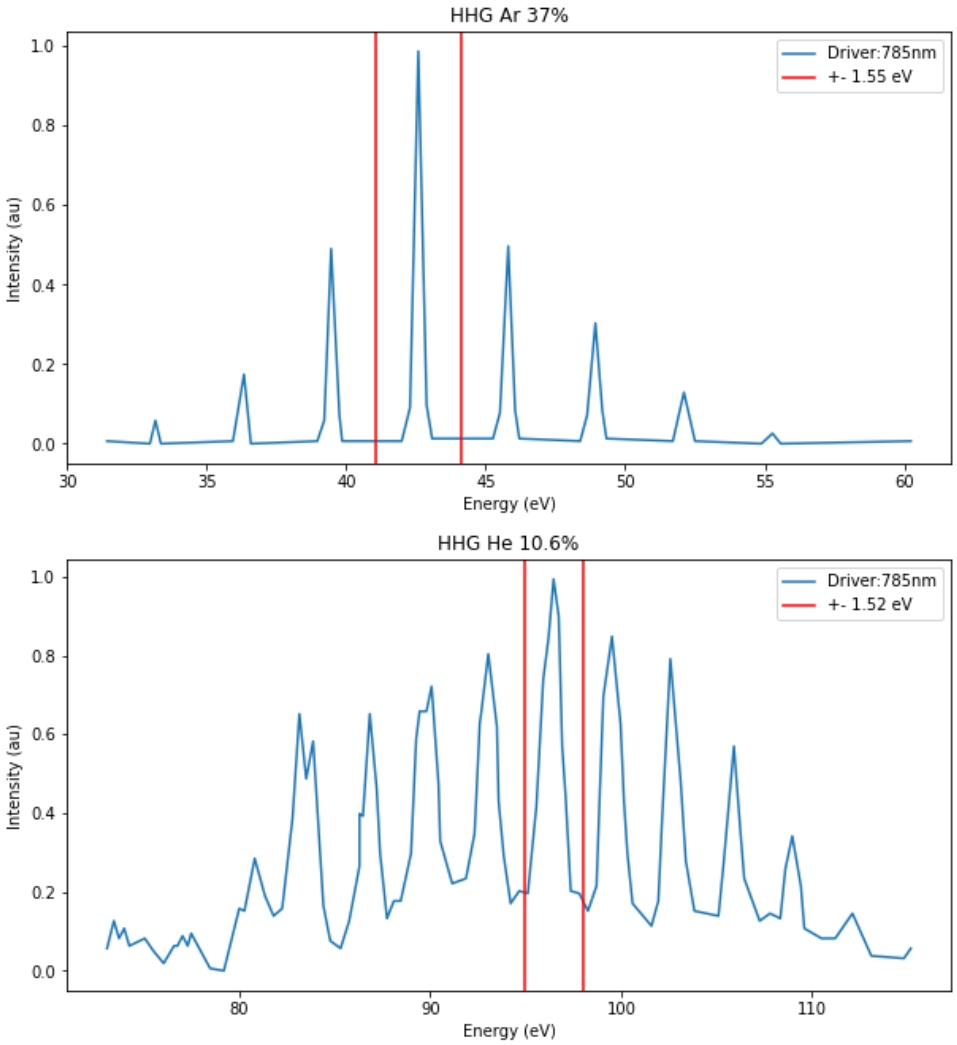


Figure 6.9: XUUS^{TM} emission with Ar and He.

go on a pair of reflective optics, referred to as rejectors, whose primary function is to reflect the XUV component while suppressing the fundamental field. Each rejector consists of a plane mirror with dimensions $65mm \times 12.5mm \times 12.5mm$, made of a fused silica substrate coated with a $13nm$-thick layer of Ruthenium. These mirrors operates at a grazing incidence angle of 6°, which corresponds to the Brewster angle for p-polarized fundamental light, thus minimizing the reflectivity for the driver and maximizing that of the XUV. In the original configuration provided by KMLabs, the rejector enclosures — the vacuum housings containing the optics — were mounted horizontally, with the normal of each mirror parallel to the optical table and their poles spaced approximately

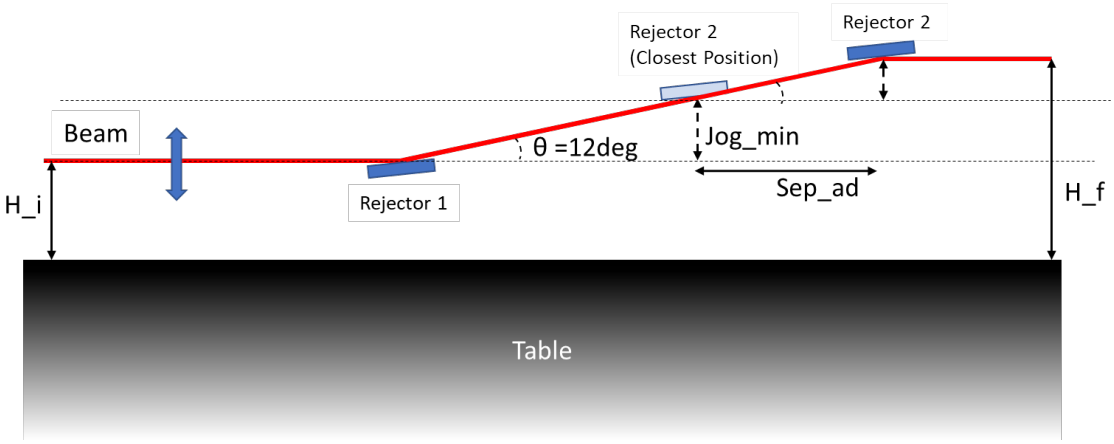


Figure 6.10: Rejectors in vertical configuration.

200mm apart. However, in order to achieve the beam height required by the downstream experimental chamber (as detailed in section 7.8), the system was reconfigured such that the rejectors are mounted vertically. This adjustment allows the beam to reach a final height of $H_f = 201.5mm$, eliminating the need for an in-vacuum periscope. The new configuration is schematically illustrated in Fig. 6.10. The initial beam, at height H_i, is deflected by an angle $\theta = 12°$ by the first rejector. The second rejector, which is longitudinally displaced by 214.7mm and has a vertical offset of $jog_{\min} = 41.58mm$ from the first, introduces a cumulative beam path displacement of 219.6mm. A vacuum bellow mechanically couples the two rejector chambers, maintaining the vacuum continuity. This vertical arrangement has a significant impact on the required polarization state of the incident light. In the original horizontal configuration, the laser pulses from the amplifier were p-polarized with respect to the mirror plane, thus optimizing the suppression of the fundamental beam. Upon vertical rotation of the mirrors by 90°, however, the polarization of the incident light becomes s-polarized relative to the new plane of incidence. To restore the desired p-polarization, the beam polarization is adjusted upstream the XUUS^{TM} by rotating WPX to 62°. While this modification does not affect the HHG process itself, it is critical for determining the polarization-dependent performance specifications of the optical components placed downstream in the experimental chamber. Moreover, becasue of the rotation of the rejector boxes, water-cooled lines used for heat dissipation in the first rejector have been modified by redesigning the flange and the housing of the mirror. In addition, also the flange on which the second rejector sits has been remanufactured to allow for the in-vacuum alignment of the mirror with three knobs

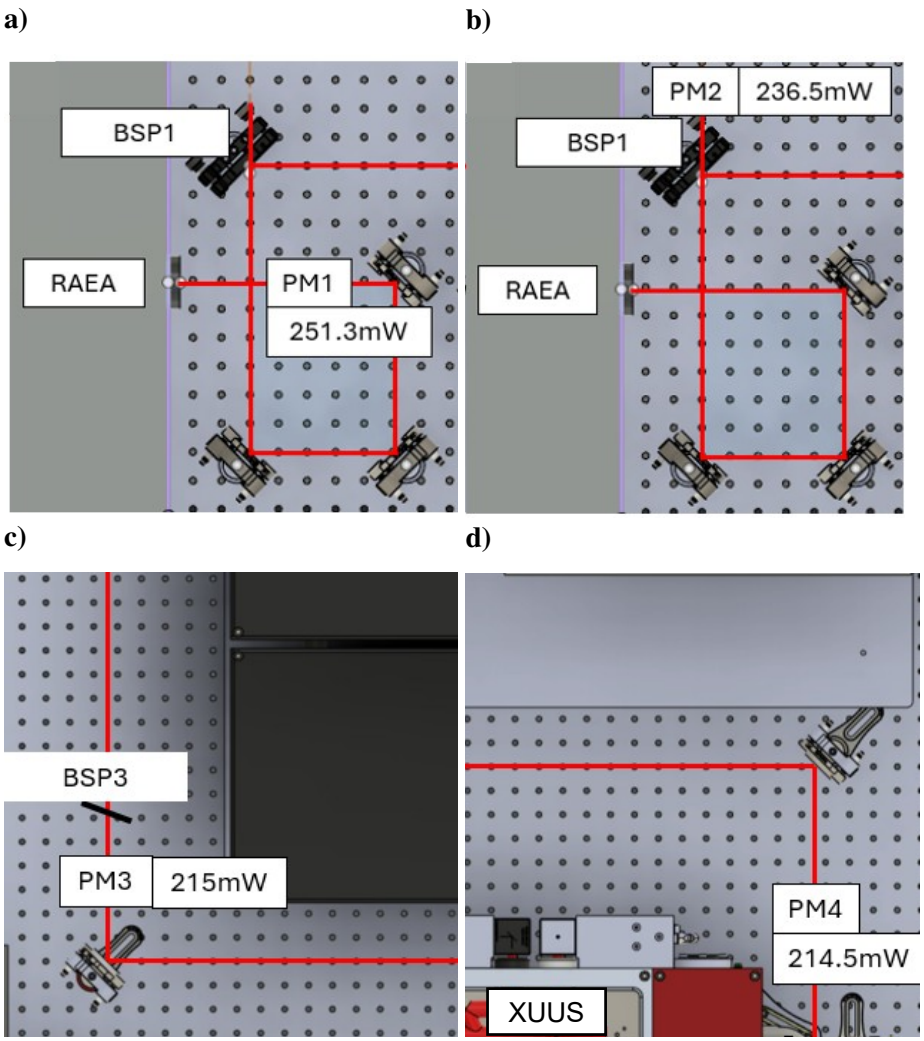


Figure 6.11: Evaluation of the power before the XUUS^{TM}. Panels (a)-(d) show the beam as it propagates to the HHG source and the positions of the powermeter sensor.

To validate the effective filtering of the rejectors and the polarization status of the driver, qualitative and quantitative checks have been carried out. The first qualitative test has been performed with the minimum power out from the RAEA^{TM} (WP0 set to 54°). The evaluation started with WPX set to 17° (fast/slow axis parallel to the optical table) and a linear polarizer placed after the second rejector. When the axis of the linear polarizer was set perpendicular to the optical table surface, no visible output was observed on a beam block positioned afterwards. On the other hand, by rotating the polarizer, the most intense beam was observed corresponding to the axis of the polarizer being parallel to the optical table, confirming that the rejectors do not filter horizontally polarized light. The

second, quantitative, test has been carried out by accurately measuring the laser power with a S350C thermal power sensor combined with a PM100D powermeter from Thorlabs. Following Fig. 6.11, when the waveplate inside the RAEA^{TM} was initially set to 51°, it provided a stable reference power of $251.3mW$ (PM1). Afterwards, the beam power was measured after BSP1 (PM2) and BSP3 (PM3), validating their respective transmission coefficients of 95% and 90% (BSP2 was not placed). The power has then been recorded before the XUUS (PM4) after the second rejector (PM5) in two conditions, depending on the orientation of WPX :

- with WPX set to 17°, $P_{out} = 92mW$, which corresponds to $\sim$ 42% of PM4;
- with WPX set to 62°, $P_{out} = 6.5mW$, which corresponds to $\sim$ 3% of PM4.

By maintaining WPX at 17°, a linear polarizer (LP) has been placed before the powermeter in front of the second rejector. The results show that

- when LP is set at 330°, with polarization axis parallel to the surface of the optical table, $P_{out} = 77.5mW$, corresponding to $\sim$ 84% of PM5, with the decreasing power due to the dispersion by the glass of the linear polarizer;
- when LP is set at 60°, with polarization axis perpendicular to the surface of the optical table, $P_{out} = 1.5mW$, which corresponds to $\sim$ 2% of PM5.

Setting finally WPX to 62°, and rotating LP in the same configuration mentioned above, no power output was ever observed. This confirms the proper alignment of the rejectors and their ability to remove the IR beam when vertically polarized. Representative schemes are shown in Fig. 6.12.

6.1.4 Thin Filters and Photodiode for XUV Flux Characterization

After the rejectors, the residual driver is filtered off by $10mm$-wide Lebow Al (for Argon) and Zr (for Helium) metallic filters. The filters have thickness spanning from $0.2\mu m$ to $1\mu m$ and are placed inside a vacuum-compatible wheel, which allows their mutual combination. As a drawback, the filters absorb part of the harmonic flux and, since are porous, can cause the partial leaking of the fundamental light when used singularly. Therefore, in standard operation the filters are always employed in couples.

Following the beam path in Fig. 6.13, the HHG comb can be intercepted by a mechanically-switched AXUV100G Si Photodiode in connection with a Keithley 6485

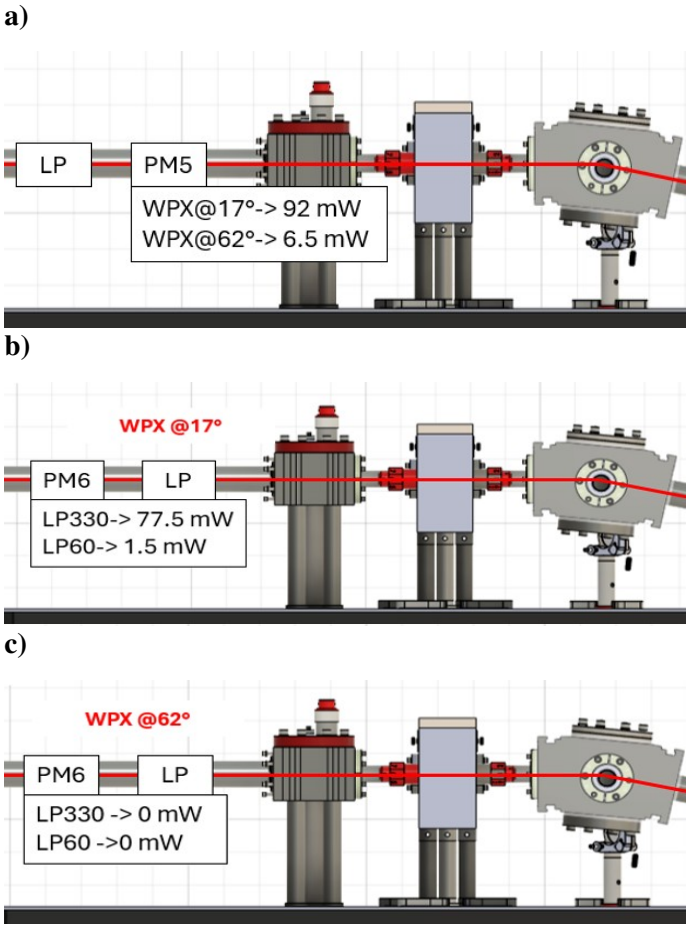


Figure 6.12: Quantitative evaluation of the functioning principle of the rejectors. (a) Power measured directly after the rejectors for different WPX values. Most of the power is provided when WPX equals 17°, that is the horizontal polarization. (b) Power measured by interposing a linear polarizer before the powermeter head and mantaining WPX equal to 17°. By setting LP with polarization axis parallel (330°) and perpendicular (60°) to the optical table, we verify the radiation is horizontally oriented with a the vertical component provided by noise fluctuatons. (c) Same as (b) but WPX equal to 62: the polarizer basically block the light, meaning that the rejectors filter light when vertically polarized, that is p-polarization for each rejector.

Picoammeter before reaching the experimental chamber. This system is used to measure the current generated by the harmonics and consequently characterize the flux of the source. The XUV power in Ar atmosphere has been estimated in multiple experimental campaigns by dividing the current I $[A]$ by the responsivity function R $[A/W]$ of the photodiode (see Fig. 6.14). The calculated value was converted to eV and divided by the energy of the most intense comb tooth hv. Table 6.1 presents, for each filter combination,

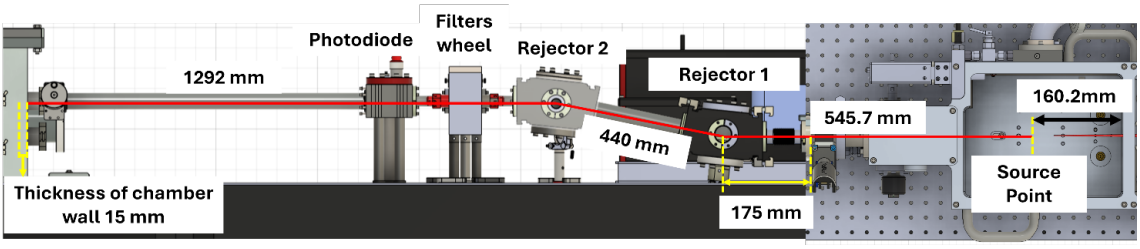


Figure 6.13: Beam path between gate valve of the XUUS and the one of the experimental chamber, with distances highlighted. The image is composed by two sections: the one on the left is lateral while the one on the right, where the source is located, is observed from the top.

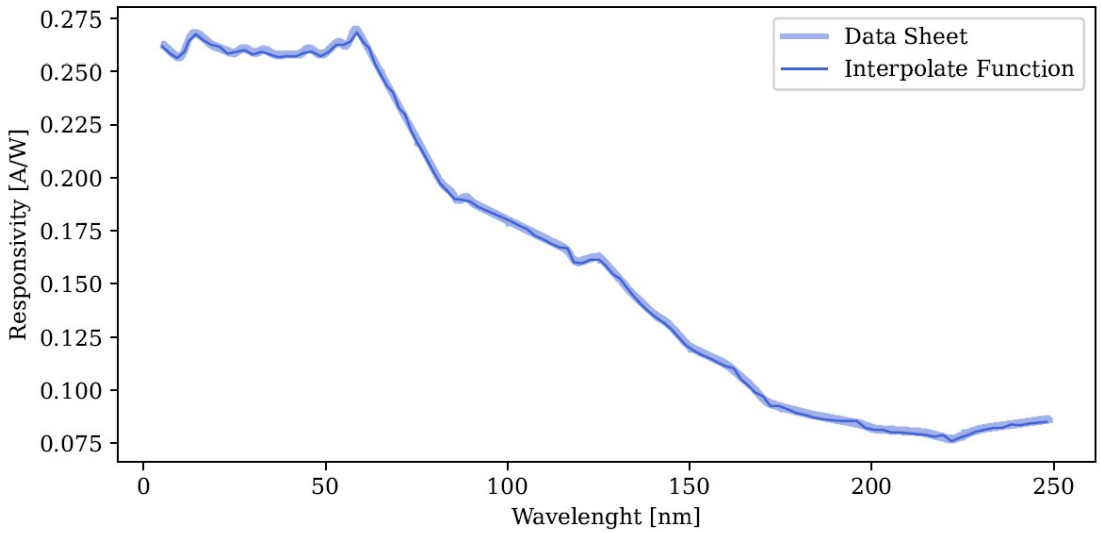


Figure 6.14: Photodiode responsivity curves from data sheet

the conversion factors from average photocurrent to photon flux (photons per second) at the source in an argon atmosphere of $74 Torr$. The experiment was conducted in January 2025 and employed a $790 nm$ driving laser with a spectral bandwidth of $26.5 nm$, corresponding to a pulse duration of $34 fs$. The average power of the fundamental beam was set to $2.48 W$ by adjusting the waveplate of the RAEA^{TM}, and a coupling efficiency into the hollow-core waveguide of approximately 67% was inferred from measurements of the transmitted power. The first column of the table reports the couple of filters employed during the measurements. The codename reflects their thicknesses and position on the filter wheel, while "_N" represents the specific round number. The second column instead shows the total thickness of the combined filters, in μm. The third column reports the

Filter	Thickness [μm]	Current [pA]	$\Upsilon_\eta \times 10^{10}$ [ph/s]	$\Upsilon_f \times 10^{10}$ [ph/s]	$\Upsilon_{r2} \times 10^{10}$ [ph/s]	$\Upsilon_{r1} \times 10^{10}$ [ph/s]
A0B6C0D6_1	1.0	1397.5	0.081 300	0.809 607	2.284 418	0.644 580
A0B6C0D6_2	1.0	1282.0	0.074 581	0.742 695	2.095 616	0.591 307
A6B6C0D0_1	1.5	224.0	0.013 031	0.409 505	1.155 474	0.326 033
A6B6C0D0_2	1.5	203.5	0.011 839	0.372 028	1.049 727	0.296 195
A6B0C0D6_1	1.5	290.0	0.016 871	0.530 162	1.495 926	0.422 096
A6B0C0D6_2	1.5	292.5	0.017 016	0.534 732	1.508 822	0.425 735

Table 6.1: HHG output in Ar atmosphere: conversion from measured photocurrent to photon flux.

average current values (in pA) obtained by averaging the high and low readings of the Keithley.

The column denoted by Υ_η corresponds to the photon flux obtained after correcting the measured current for the quantum efficiency of the photodiode. The subsequent column Υ_f, accounts for the transmission of the aluminum filter, which depends on the specific thickness used for the in each configuration. The columns Υ_{r1} and Υ_{r2} incorporate the reflectivity correction due to the rejector mirrors, evaluated at a wavelength of $30nm$, with a nominal reflectivity of 0.354404 according to the data provided by the Center for X-Ray Optics (CXRO). The last value therefore represents the estimated photon flux at the source taking into account the sequential attenuation and reflection losses in the detection path. The average value of $\sim 10^{11}$ photons/s is an in-field validation of the estimated values from the supplier.

6.1.5 Probe Delivery in the Experimental Chamber

When the photodiode is removed from the optical path, the HHG comb, filtered from the driver, travels along a $1292mm$-long custom bellow and reaches a gate valve at the entrance of the experimental chamber (see Fig. 6.13). The purpose of the gate valve is to allow the high volume of the experimental chamber to be pumped independently from the remaining part of the beamline. The valve is opened once the differential pressure between both sides is a fraction of $10^{-7}mbar$, a value sufficient to avoid damaging the thin and fragile metallic filters. Once this condition is met, the XUV beam enters the experimental chamber. Although a complete description of the vacuum layout, structural design, and internal diagnostics of the chamber lies beyond the scope of this section (see section 7.8 for a detailed discussion), it is instructive to follow the beam propagation up to the sample plane, to complete the description of the probe arm. Once inside, the XUV probe is monochromatized, focused and spatiotemporally overlapped at the sample plane

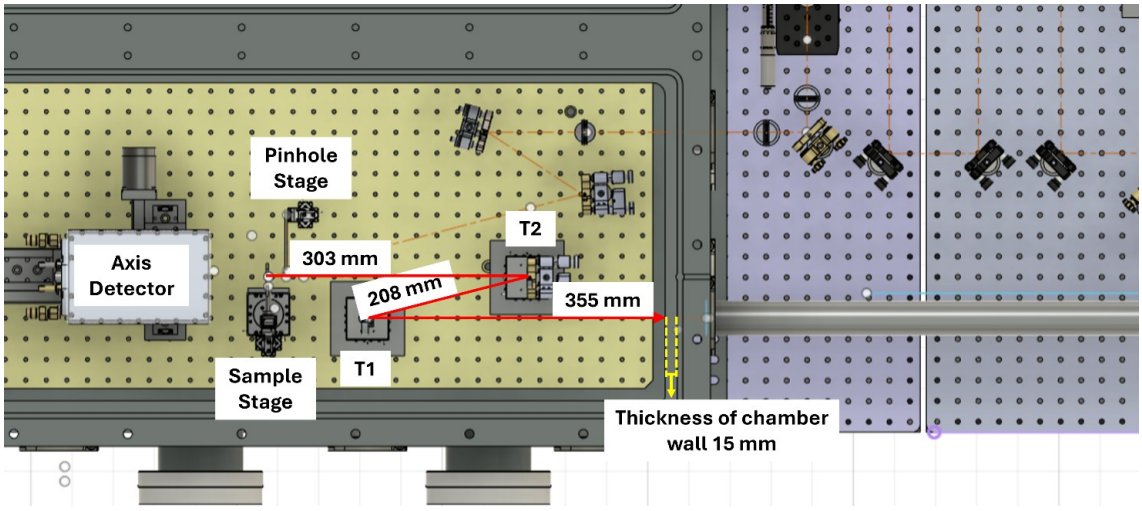


Figure 6.15: Beam path inside the chamber until the sample.

with the pump beam, for time resolved experiments. Specifically, the focusing is achieved with an off-axis z-fold system producing a slightly aberrated probe, which comprises a flat and a spherical mirror. The same optical elements are coated with multilayers specifically designed for each HHG comb, respectively optimized for $\sim 13nm$ and $\sim 30nm$ outputs. Notably, the mirrors partially reflect also the IR beam and can work with any input linear polarization, therefore their prealignement can be executed with visible light. The focusing geometry was preferred to other types of systems given a tradeoff between ease of alignment, fabrication quality and size of the illumination function at the image plane (see section 7.5 for an extensive discussion on the topic). The mirrors are mounted on top of two towers — T1 and T2 in Fig. 6.15 — made by a vertical stack of piezo-actuated Smaract stage with five degrees of freedom (X, Y, Rotation, Swivel on X, Swivel on Y). The spherical mirror on T2 features an additional tip-tilt motion imparted by a piezo actuated mount (Newport 8821-L-UHV) to provide more flexibility during the alignment in vacuum. The alignment is flexible and admits the fine tuning of the illumination function in terms of size and position. In the case shown in Fig. 6.15, which is a realistic operating condition, the location of the mirrors provide an additional beam path of $833mm$ inside the experimental chamber before the position of the sample. In this case, the total length measured from BSP3 is $8269.9mm$, a distance that shall be matched by the pump beam to ensure the spatiotemporal overlap on the sample.

6.2 Pump Branch

In time-resolved experiments, the pump beam has the fundamental role of initiating the dynamics in the sample under investigation. In this section, the pump branch of the Ultrafast XUV Ptychography Beamline is detailed in terms of beam path length, time-delays and beam requirements such as size, fluence and polarization.

6.2.1 Requirements

The design of the pump arm was guided by a set of fundamental criteria, each addressing specific experimental constraints associated with pump-probe measurements. First, the preservation of the spatiotemporal quality of the laser pulse throughout the propagation was a critical constraint. Particular attention was devoted to the choice of optical elements with low GDD, in order to minimize beam chirping and broadening during multiple transmission and reflection events. Second, the beamline had to support operation over a broad range of fluence regimes. This capability is essential because enables systematic investigations of excitation processes in matter by tuning the intensity of the pump beam and exploring both linear and nonlinear regimes of light-matter interaction. Third, it was necessary to ensure that the optical path lengths of the pump and probe arms were matched to achieve temporal and spatial overlap at the sample plane. To this end, the propagation distance of both the pump and probe beams from the reference point BSP3 to the sample position was measured using both a detailed CAD model of the beamline and a measuring tape. These independent approaches yielded a propagation length of $8269.9mm$, with limited uncertainty The beam path was designed to take into account accessibility, ease of alignment in a robust optical layout. Ultimately, the design was conceived to be flexible in order to accommodate a range of experimental configurations and excitation conditions through the delivery of different polarization states of light. In the following sections, each key requirement is addressed.

6.2.2 Key Optical Elements and Pulse Duration Calculation

To preserve the temporal and spectral shape of the laser pulses in the entire beam path, the beamline accommodates custom flat $1''$ and $1.5''$ ultrafast mirrors working either at $0°$ or $45°$ AOI, produced by OPTILAB Ltd. The mirror substrate possesses high flatness ($\lambda/10$ planarity) and is made by N-BK7, a ceramic material that guarantees a $LIDT > 1J/cm^2$.

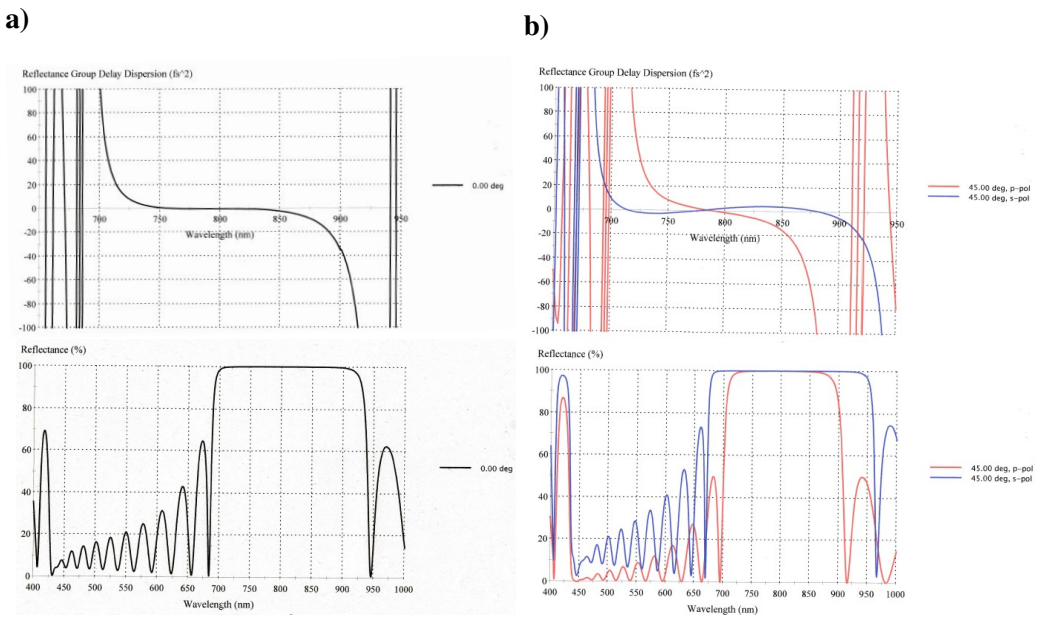


Figure 6.16: Reflectance and GDD curves of the ultrafast optics in the pump arm. (a) Mirrors working with a near 0° AOI: top row showing the GDD and bottom row the reflectance value across the designed spectral region. Here the mirror shows no difference for s- or p-polarized light (b) Mirrors working at 45° AOI: top row showing the GDD in reflection while bottom row the reflectance value. The plot shows that s-polarized light works slightly better when considering the entire spectrum.

As later discussed in section 6.2.3, the maximum fluence exerted on the last mirror of the pump branch does not exceed $0.13 mJ/cm^2$, making the mirrors compatible with the design. The surfaces are coated with a low GDD and highly reflective coating, covering the emission spectrum of the amplifier ($760 - 810nm$), for both s- and p-polarizations. The reflectance and GDD curves of these mirrors are plotted in Fig. 6.16, for 45° and at near-zero incidence angles.

The pump arm of the optical setup in Fig. 6.17 includes a hollow retroreflector (OW-25-1PS from PLX) on a delay stage (DS), a precision alignment-insensitive device designed to reflect the incident light back towards its source with minimal beam deviations. The device is provided with a protected silver coating with 96% mean reflectance from $450nm$ to $10000nm$. Unlike retroreflector prisms, the hollow design eliminates material dispersion and bulk absorption, and is especially appropriate for pump-probe experiments with ultrafast laser pulses.

Along the pump beam path, polarizers (POL) and half-waveplates (WP1 and WP2) are inserted for polarization conversion and power tuning. In particular, a broadband

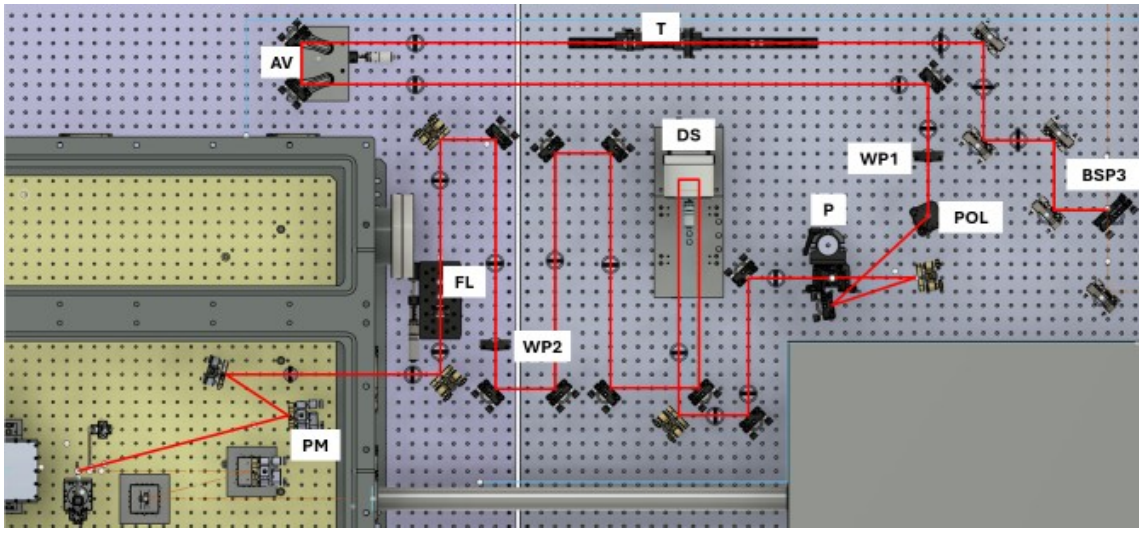


Figure 6.17: Layout of the pump branch. T: telescope, AV: manual retroreflector, POL: polarizer, WP1: first half-waveplate, P: periscope, DS: delay stage, WP2: second half-waveplate, FL: focusing lens, PM: piezo-actuated mirror.

thin film laser polarizer (Model 420-1696BBi70 from EKSMA) is employed to spatially separate the s- and p-polarized components of the beam at $AOI = 70°$. This optical device is optimized for high-energy femtosecond pulses and features high polarization-dependent efficiency ($Rs > 99.5\%$, $Tp > 95.0\%$) within the $750 - 850nm$ spectral range. Its geometry ($20 \times 60mm \times 4mm$) and coating make it suitable for high peak power operation while maintaining minimal pulse distortion. The polarization state of the pump beam is controlled via zero-order, air-spaced half-waveplates specifically engineered for high-power femtosecond applications (Mod. 464-4220 from EKSMA). The waveplates are made of single-crystal quartz and provide a retardation of $\lambda/2$ over a spectral range of $740 - 820nm$. They feature a clear aperture of $17mm$ within a $25.4mm$ diameter mount and possess an anti-reflection coating to minimize losses and back-reflections. The zero-order design ensures high temporal and spatial fidelity of the transmitted pulse, with negligible dispersion and excellent thermal stability, making it well suited for intensity tuning in combination with the polarizer, as well as for experiments requiring controlled linear polarization states.

Transmissive optical elements are also implemented in the beamline, although limited to a couple of convex-concave lenses for telescoping (T) the beam (Thorlabs LA1256-B, Edmund Optics 21058) and a focusing lens (FL, Thorlabs LA1464-B) to provide a tunable illumination function at the sample plane. These elements are made of N-BK7

Item	Substrate material	Thickness [mm]	GVD [fs^2/mm]	GDD [fs^2]
Thorlabs LA1256-B	N-BK7	5.0	44.65	$5.0 \times 44.65 = 223.25$
Edmund Optics 21058	Fused Silica (UVFS)	2.5	36.20	$2.5 \times 36.20 = 90.50$
EKSMA 464-4220 waveplate	Single Crystal Quartz	1.5	35.80	$1.5 \times 35.80 = 53.70$
Thorlabs LA1464-B	N-BK7	2.2	44.65	$2.2 \times 44.65 = 98.23$
Total				**519.38**

Table 6.2: Total GDD from transmissive elements in the pump branch.

and UVFS, have LIDT well above our operating values and are the major contribution to pulse broadening. Using eq. (6.1), and considering the spectrum of the amplifier centered approximately at $800nm$, the cumulative effect of optical dispersion in terms of pulse broadening is estimated to

$$\tau_P(L) = \frac{\sqrt{\tau_P^4(0) + (4ln2 * GDD_{tot})^2}}{\tau_P(0)} \approx 54fs. \tag{6.7}$$

Here $\tau_P(0) = 37.8fs$, as calculated after BSP3 at the beginning of chapter 6, while the total GDD is derived from table 6.2.

6.2.3 Fluence Calculations

To accurately control the excitation conditions at the sample plane, a quantitative analysis of the pump beam fluence was performed along the pump branch. The RAEA^{TM} typically delivers an average power of approximately $15W$ at a $5KHz$ repetition rate, corresponding to a pulse energy of $3mJ$. After the application of BSP1, BSP2 and BSP3 (see details in chapter 6), the probe branch is powered by $11.4W$ while the power allocated to the pump arm is $P_{XUV,\ pump} = 1.14W$, or $E_{XUV,pump} = 0.228mJ$ per pulse.

The beam entering the pump path has an initial $1/e^2$ diameter of $D_{in} = 1cm$ but, for an easier management in the alignment, it is reduced down to $D_{out} = 0.7cm$ using a demagnifying telescope. Under these circumstances, the expected fluence is

$$\mathcal{F}_{avg} = \frac{4E_{XUV,\ pump}}{\pi D_{out}^2} \approx 0.59mJ/cm^2. \tag{6.8}$$

Assuming 1% optical losses due to coatings, waveplates and imperfections in the alignment, the fluence at the plane of the focusing lens is estimated to $\sim 0.58mJ/cm^2$. This level of fluence is below the LIDT values for the optical components in the beamline and

ensures safe operations.

The plano-convex focusing lens with $f = 1000mm$, mounted on a linear translation stage (Thorlabs XR25C/M), allows for control over both the waist position and the beam diameter at the position of the specimen. Under the assumption of ideal Gaussian propagation ($M^2 = 1$) and using a central wavelength of $\lambda = 785nm$, the expected beam waist at the focus is $\sim 145\mu m$, with a depth of focus approximately equal to $40.8mm$. Translating the lens, the spot size can be continuously varied up to $500\mu m$, and can be used to excite a wider sample area. Therefore, a high level of flexibility in the available fluence values can be achieved by simply moving the lens stage by $6.8mm$. For simplicity, the fluence values at minimum, maximum and at $250\mu m$ spot size are reported below:

$$\mathcal{F}_{\max} \approx 1419mJ/cm^2,\ \mathcal{F}_{250\mu m} \approx 464mJ/cm^2,\ \mathcal{F}_{\min} \approx 116mJ/cm^2. \tag{6.9}$$

These values, while theoretically accessible, are well above the desired operating regime and may damage the sample rather than exciting it. We therefore decided to insert multiple neutral density (ND) filters before the focusing lens. For instance, an $OD = 1.5$ filter, which corresponds to a transmission of approximately 3% of the incident energy, lowers the fluence to

$$\mathcal{F}_{\max} \approx 42.6mJ/cm^2,\ \mathcal{F}_{250\mu m} \approx 13.9mJ/cm^2,\ \mathcal{F}_{\min} \approx 3.5mJ/cm^2, \tag{6.10}$$

which are values within the optimal range for safe nonlinear excitation studies.

6.2.4 Detailed Design of the Pump Arm

The layout of the pump beam path is illustrated in Fig. 6.17. Approximately 10% of the laser power is extracted from the main beam after BSP3 and directed into the pump arm. The beam first reflects off four ultrafast 1.5″ dielectric mirrors (45°, s-pol optimized), mounted on high-stability kinematic holders, and then passes through a Galilean telescope (T) composed of a 2″ plano-convex lens (Thorlabs LA1256-B, $f = 300mm$) and a 1″ plano-concave lens (Edmund Optics 21058, $f = -200mm$). This configuration reduces the beam diameter from $D_{in,1/e^2} = 10mm$ to $D_{out,1/e^2} = 7mm$. Each lens is mounted on five-axis stages from Thorlabs (K5X1 and K5X2), allowing for precise alignment and astigmatism compensation. A manual retroreflector (AV) is placed after the telescope on a manual linear translation stage, enabling fine adjustment of the optical path length to

match the pump probe arm lengths. The beam is then reflected by a 1″ mirror at 45°, and directed onto a half-waveplate (WP1, EKSMA 464-4220) followed by a broadband ultrafast polarizer (POL, EKSMA 420-1696BBi70, AOI = 70°), optimized for high-power femtosecond pulses. WP1 is typically set to 50°, maximizing the s-polarization of the beam and thus the reflectivity of the polarizer and subsequent mirrors. This arrangement serves as a tunable attenuator for controlling the pump power. Following the polarization control stage, two near-0° mirrors redirect the beam into a vertical periscope (P), which raises the optical height from $114.3mm$ to $201.5mm$, that is the level required for injection into the experimental chamber. The elevated beam then reflects off three additional 45° mirrors, the last of which is mounted on a high-stability holder, before reaching a hollow retroreflector (PLX OW-25-1PS) mounted on a motorized linear stage (DS, Newport GTS150). This delay stage allows for precise tuning of the optical path length and relative arrival time of the pump pulse with respect to the probe. To match the full propagation length of the probe arm, the beam is further reflected by six 1″ dielectric mirrors (45°), after which it passes through a second half-waveplate (WP2) for final polarization tuning. In standard conditions, WP2 is set to 314°, restoring the p-polarization of the beam at the sample plane. The beam is then focused by a plano-convex lens (FL, Thorlabs LA1464-B, $f = 1000mm$), mounted on a precision translation stage (Thorlabs XR25C/M), which allows the adjustment of the spot size, and thus fluence, at the target. The final redirection into the experimental chamber is achieved via a 45° ultrafast mirror and a z-fold configuration using two near-0° dielectric mirrors. The last mirror is mounted on a piezo-actuated tip-tilt stage (PM, Newport 8821-L-UHV), enabling remote alignment in vacuum. This mirror is the final optical element before the sample and sustains the highest fluence in the pump path. Considering a lens-to-sample distance of $625mm$ and the final beam attenuation explained in the previous section, the expected fluence on this optic is approximately $0.13mJ/cm^2$, well below its LIDT values.

In Fig. 6.18, the relevant distances within the pump arm, obtained by CAD and cross-checked using the measuring tape are shown. The delay stage is set to a negative position of $-55mm$, a value which allow additional $20mm$ of negative time delays ($\sim 67ps$), while the remaining $130mm$ ($\sim 433ps$) can be used for positive times.In the condition described currently, the total optical path from BSP3 to the sample amounts to $8271mm$, within $1.1mm$ of the probe arm length, well within the compensation range of the delay stage.

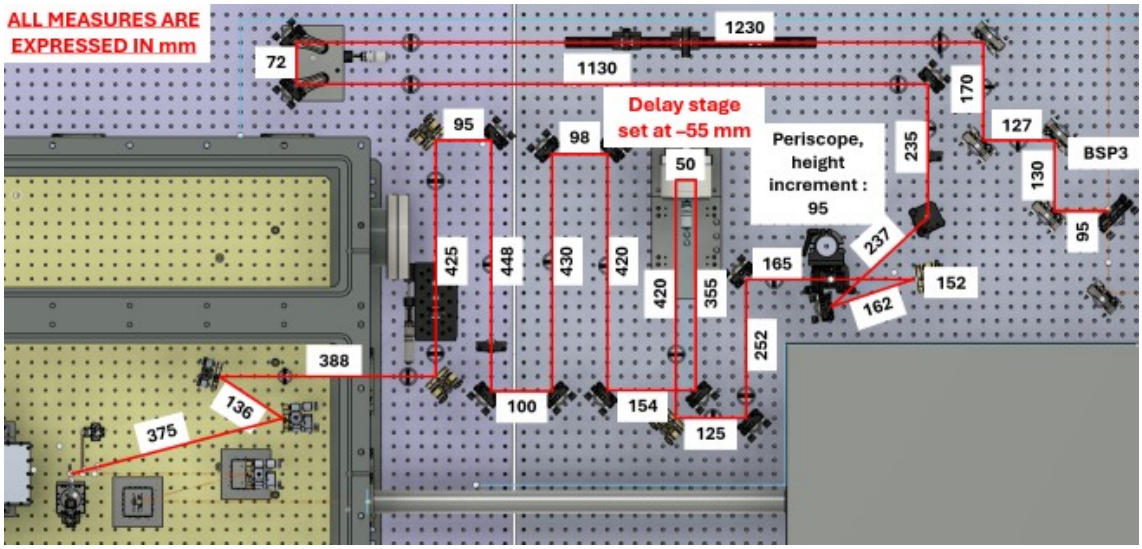


Figure 6.18: Length of the pump arm expressed in mm. The delay stage is set at $-55mm$ position, nominally the time-zero condition.

6.2.5 Qualitative and Quantitative Evaluation of Beam Polarizations

The polarization state along the pump beamline was verified both qualitatively and quantitatively.

Qualitative checks were performed with a reference linear polarizer (LP) inserted at three positions along the pump arm: (i) after the telescope (T), (ii) after WP1 and POL but before the delay stage (DS), and (iii) after WP2, upstream of the focusing optics (FL). The source waveplate WP0 was initially set to 54°, corresponding to a predominantly horizontal (p) polarization at the compressor output. Adjusting WP1 to 50° rotated the beam to the vertical (s) state with respect to the table. Visual inspection confirmed correct orientation of the polarization elements: for example, with the LP placed after WP2 and its transmission axis set to 150° (parallel to the table), transmission was extinguished. However, a transmitted beam was observed when WP2 restored the p-state (WP2 $\approx$ 314°).

Quantitative characterization employed a powermeter (PM_n) combined with the LP. Measurements were collected at the locations indicated in Figs. 6.19 to 6.21. With WP0 at 54° the total power measured immediately after the compressor was $14.06mW$; transmission through the LP aligned at 330° (horizontal) accounted for most of the power, whereas the orthogonal LP orientation transmitted only a few hundred μW, confirming a strong p-polarization. Subsequent measurements confirmed the expected performance of BSP1 and BSP3 (95T/5R and 90T/10R), with values measured at PM3, PM4, PM5, and

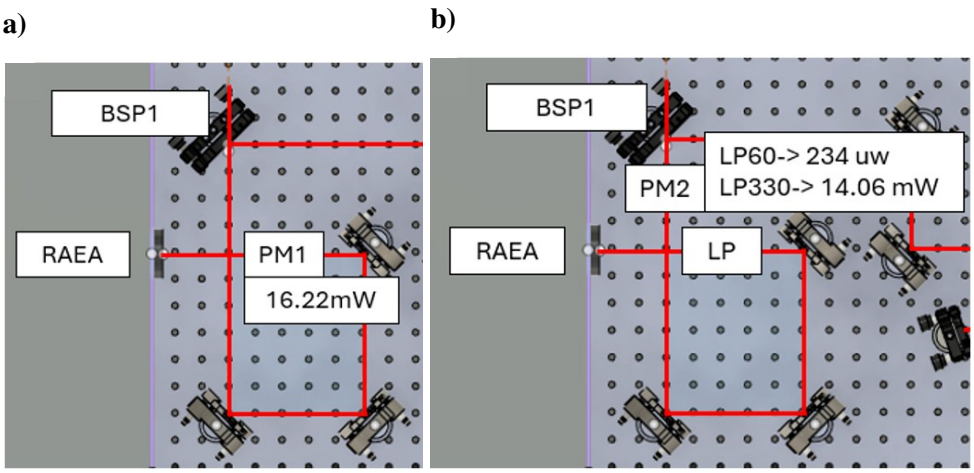


Figure 6.19: Quantitative evaluation of polarization out of RAEA^{TM} when running at minimum power out

PM6 in agreement with manufacturer specifications and consistent with p-polarized light behavior.

After WP1 was set to 50° the polarization rotated to the s-state. Measurements at PM7 and PM8 (before and after POL) gave $1.68mW$ and $1.66mW$, respectively, corresponding to transmission losses $< 1.2\%$ and consistent with the specified reflectance of the polarizer to s-polarized beams (Rs $\approx 99.5\%$). This configuration allows the POL and the ultrafast optics to operate at maximum efficiency both in terms of reflectance and GDD.

In the last section of the pump arm, the polarization of the beam can be set either in the s- or p- configuration by operating WP2 respectively at 359° or 314°. Further measurements at downstream positions (PM9–PM11) verify the action of WP2: with the LP at 60° the transmitted power at PM9 was $\sim 1.5mW$, while with the LP at 330° only a few μW were recorded, indicating near-complete extinction of the p-component. After setting WP2 to restore the p-polarization (WP2 $\approx$ 314°), PM10 and PM11 measured $1.64mW$ and $1.48mW$, respectively, in agreement with the expected behavior. The final part of the pump arm and the power measurements are displayed in Fig. 6.21. With this assessment, the beamline pump path has been validated in a modular and complete fashion against the designed principles.

By taking power measurements along the pump path (including after BSP3 and at the final element), the total power decrease over the $(8216mm \pm 75mm$ propagation length was estimated as $\approx 21\%$ (from $1.9mW$ to $1.5mW$). These values are consistent with the element specifications and confirm the modular performance of the pump arm.

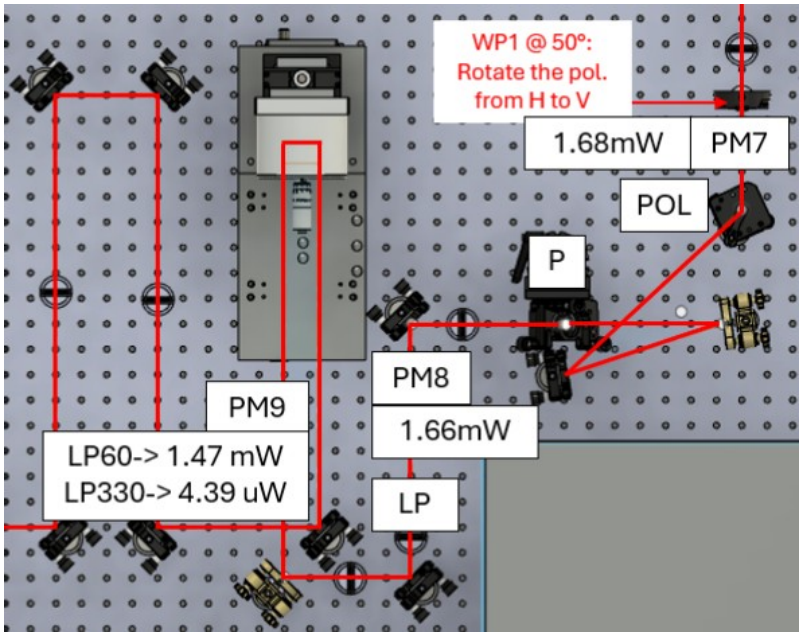


Figure 6.20: Quantitative evaluation of polarization in the pump arm between WP1 and WP2 in the section where the ultrafast polarizer is employed.

6.3 Time Zero

After characterizing the pump and probe branches separately, a critical step to initiate pump and probe experiments is the identification of time-zero (t_0), that is, the spatiotemporal overlap of pump and probe pulses at the sample plane. A precise determination of t_0 is fundamental to reconstruct the transient dynamics with femtosecond temporal resolution and to generate a common time axis for all measurements.

In our experimental setup, t_0 is determined with the IR beam by exploiting second-order nonlinear optical phenomena: SHG and SFG. SFG is based on the mixing of two input photons at frequencies f_1 and f_2 to generate a third photon at frequency $f_3 = f_1 + f_2$. Like others χ^2 optical phenomena in nonlinear optics, this process can only occur if light is interacting with matter and possesses a very high intensity for which nonlinear contributions become relevant. Efficient SFG must not only satisfy the conservation of energy, but also wavevector. This means obeying the phase matching condition

$$\mathbf{k}_{f_3} = \mathbf{k}_{f_1} + \mathbf{k}_{f_2}, \tag{6.11}$$

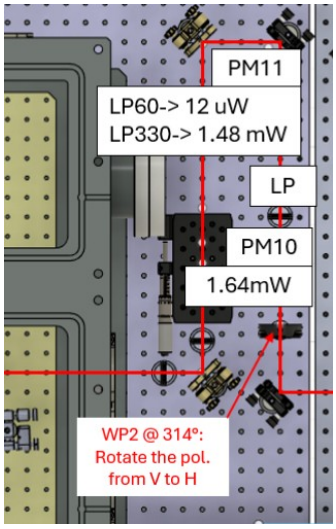


Figure 6.21: Quantitative evaluation of polarization in the final section of the beamline close to the experimental chamber.

with

$$\Delta\mathbf{k} = |\mathbf{k}_{f_3} - (\mathbf{k}_{f_1} + \mathbf{k}_{f_2})| = 0. \tag{6.12}$$

In this way, constructive interference of the generated wave over the interaction length is obtained by ensuring that both waves remain in phase as they propagate, maximizing energy transfer [142]. SHG is a particular case of SFG in which $f_1$and f_2 are equal in energy and share the same wavevector. Therefore, the generated photons will be centered at frequency $f_3 = 2f_1 = 2f_2$ and will co-propagate along the same line of the driver. To find t_0 in our experiment, we employ a Type I BBO crystal (EKSMA BBO-1003H) placed at the sample position. When pump and probe beams independently reach the BBO, new photons at $2f_1$and $2f_2$ are observed in the same direction as the incoming beams, due to SHG occurring between pump-pump and probe-probe photons. This results in two bright purple spots generated by the visual superposition of the IR driver with the $\sim 400nm$ second harmonic beam. When the delay line is adjusted, the two pulses overlap within the BBO, and if phase matching condition is fulfilled, a third central blue spot from SFG can be observed (see Fig. 6.22). Before inserting the BBO, the procedure to determine t_0 requires a spatial overlap between pump and probe beams at low power. This is obtained by actuating the piezo-mirror of the pump arm inside the experimental chamber and visualizing its overlapping with the visible probe beam on the MKS Ophir SP90608 beam profiler placed at the position of the BBO (that is, the future sample plane).

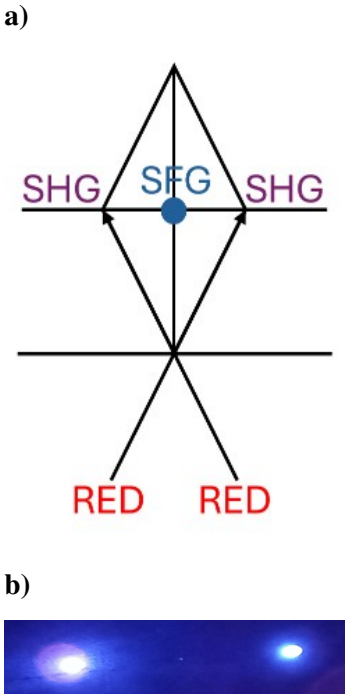


Figure 6.22: Scheme and practical result for SFG for time-zero retrieval. (a) Simplified scheme of SFG with two IR beams spatiotemporally overlapped at the BBO, the crystal is assumed to be oriented at an angle ϕ for phase matching. (b) SFG on the BBO before the optimization of the spatiotemporally overlap of pump and probe, with a faint SFG beam visible at the center.

To facilitate alignment and reduce aberrations caused by beam overfilling, the probe beam is spatially filtered by closing an upstream iris, producing an Airy pattern whose central lobe better mimics the high-harmonic beam size. In this configuration, the pump is, by design, approximately four times larger than the probe, since it shall uniformly illuminate a wider sample region during ptychography scan. The BBO is then inserted and the temporal alignment between both beams can be refined. Initially, p-polarization on both arms must be ensured, as required for χ^2-phase matching condition in the BBO [142]. The proper combination of half-waveplate angles in both pump (WP1 at 50° and WP2 at 314°) and probe (WPX at 17°) indeed serves to this purpose. Afterwards, the temporal optimization is carried out. It is achieved first by coarsely matching the pump and probe path using the manual retroreflector in the pump arm, which possesses a $\sim 1cm$ range from the central position. Fine adjustments are instead executed by actuating the Newport GTS150 delay line in the pump branch. This motorized linear stage has $150mm$ travel range and a minimum incremental motion of $100nm$, with submicrometer accuracy and

repeatability, which allows for the precise determination of t_0 in a consistent way. The optimization with the delay line is alternated with the refinement of the spatial overlap between the beams. The position at which the SFG signal reaches the maximum intensity, determined by the brightest and most stable blue spot, is identified as t_0. In our setup this was experimentally found at $53.7mm \pm 1mm$ relative to the central position of the delay stage , corresponding to a pump arm matching the probe arm ($8269mm$) with $\pm 1mm$ uncertainty. This relative uncertainty arises due to the extended interaction length into the BBO. To optimize the localization of t_0, a coarse alignment procedure with chirped pulses is followed by a final fine-tuning with compressed, unchirped pulses. In fact, when operating with chirped pulses (e.g. $\sim 175fs$), the SFG signal persists over a longer range of delay positions ($0.3465mm$ corresponding to $\sim 1156fs$), easing the initial identification of the t_0 region. However, due to the reduced temporal intensity and lower peak power, the nonlinear signal intensity is significantly diminished. In contrast, using transform-limited pulses (e.g. $40fs$ at the FROG position) results in stronger nonlinear signals and a sharper window ($0.13975mm$ corresponding to $\sim 466fs$), which allows a more precise localization of t_0. This sequential approach ensures both practical visibility of the SFG and sub-$100fs$ accuracy in t_0 determination.

Chapter 7

The XUV Microscope

The core of the Ultrafast XUV Ptychography Beamline is the experimental chamber containing the lensless microscope. The design philosophy of the microscope revolved around three primary constraints that set the parameter space for potential geometries: the physical spatial envelope available on the optical table, the properties of the detector and the required spot size for ptychography. Rather than a linear progression, the development process evolved through successive refinements, with the physical constraints of the chamber and optomechanical components informing optical parameters and vice versa. This methodology ensured that practical limitations such as the detector positioning and the spatial footprint of other components were conciliated with optical performance requirements to realize a robust and flexible experimental setup.

7.1 Constraints

The available space for the deployment of the microscope and the experimental chamber constituted a significant design constraint. The entire breadboard consists of two separate Newport optical tables (M-RS4000-1500x3000x457 and M-RS4000-1500x2600x457), forming an L-shaped surface. Along the direction of the XUV beam propagation, the total length of the optical table is $4.5m$ $(3m + 1.5m)$, of which approximately $2.2m$ are occupied by the HHG source, the filter wheel, and the photodiode. In the early design phases, $0.8m$ of the first $3m$-long table section were allocated for the installation of an in-line spectrometer, intended to spectrally resolve the HHG emission and enable I_0 normalization for quantitative ptychographic reconstructions. Consequently, the available space for the mi-

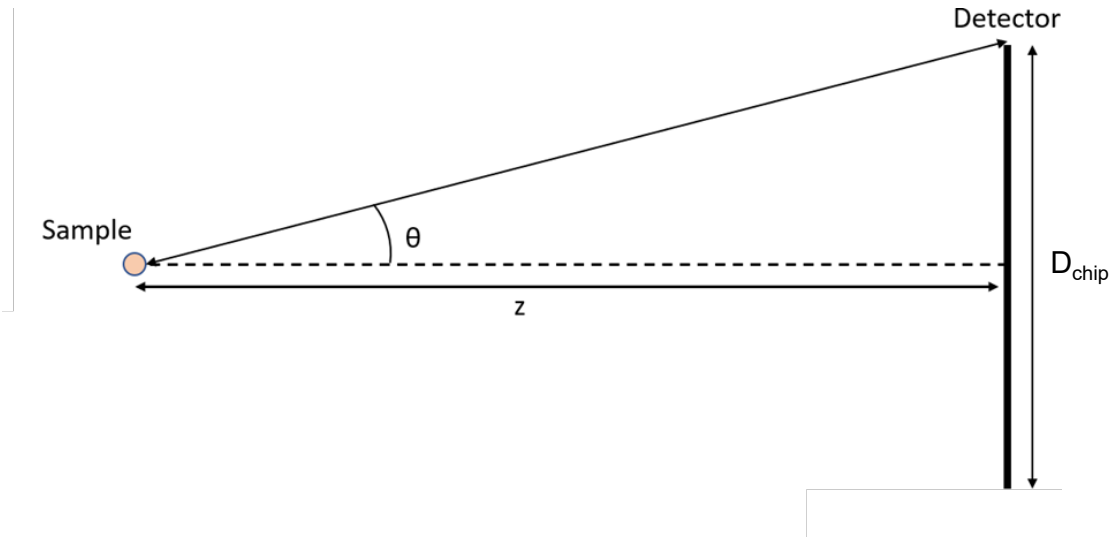


Figure 7.1: Experimental geometry of a scattering experiment. The detector possesses a chip size D_{chip} and is located at a distance z from the object to be imaged. The semi angular aperture is indicated as θ.

croscope and experimental chamber was constrained to the remaining $1.5m$ section at the end of the optical path. This limitation had important implications for the optical design of the microscope, as the spatial divergence of the XUV beam exiting the source cartridge leads to a significant increase in beam diameter along propagation, an effect that must be counteracted by the focusing geometry within the experimental chamber. The design of the microscope is critically and directly influenced by the characteristics of the detector system employed. This intrinsic relationship arises from its role in capturing the diffraction patterns leading to the reconstruction of the image using ptychographic algorithms. The interplay between detector specifications and fundamental optical principles dictates the attainable spatial resolution and thus the overall physical layout of the experimental apparatus. The properties of the detector are integrated into the core relationships governing CDI, specifically the diffraction-limited resolution and the oversampling condition. Considering the simple experimental geometry shown in Fig. 7.1, the theoretical limit of spatial resolution can be stated in 1D by approximating eq. (1.1) to

$$\Delta r = \frac{\lambda}{2NA} = \frac{\lambda}{2nsin\theta} \approx \frac{\lambda z}{D_{chip}}, \tag{7.1}$$

where λ is the wavelength, z is the sample-to-detector distance and D_{chip} represents the size of the detector chip. Since the chip size can be defined as $D_{chip} = Np$ (where N is

the number of pixels and p is the pixel pitch), it directly set the achievable resolution of the system. A larger chip correlates with a higher numerical aperture and, consequently, improved resolution. However, a smaller pixel size allows for finer sampling (see eq. (3.1)), enabling the camera to be positioned closer to the sample, thus increasing the numerical aperture. In other words, the ideal detector combines a very large sensor and infinitesimally small pixels. Our system design targets a minimum resolution of $\approx \lambda$ and a maximum resolution of $\approx 100nm$ with $13nm$ XUV light, which is the most demanding wavelength in terms of oversampling.

Recalling section 3.2, the oversampling requirement for CDI and Ptychography is stated as

$$\sigma = \frac{\lambda z}{p D_{probe}} > 2. \tag{7.2}$$

This means establishing a direct link between the size of the detector pixel p, the sample-to-detector distance z, and the properties of the beam: wavelength λ and $1/e^2$ diameter D_{probe}. This last point is especially relevant since, neglecting diffraction effects, the probe size is geometrically determined by the magnification imparted by the focusing geometry of the system. This can be expressed both as a function of the source S and image s sizes, but also as a function of the distance from the image plane r' and the object plane r:

$$M = s'/s, \tag{7.3}$$

$$M = r'/r. \tag{7.4}$$

In addition to these fundamental optical constraints, other practical characteristics, such as the high-vacuum compatibility and the sCMOS sensor type, led to the choice of the AXIS-SXR from Axis Photonique Inc., rendered in Fig. 7.2. This is a 4-megapixel back-illuminated scientific CMOS (BSI-sCMOS) camera optimized for XUV applications. The sensor features a 2048×2048 pixel array with $11\mu m$ pixel pitch and offers full-frame acquisition at $24Hz$. The camera ($11.4cm \times 10cm \times 21.5cm$) is moreover designed for compatibility with high-vacuum environments ($\leq 5 \times 10^{-7} mbar$), operates with active water cooling, low dark current ($< 0.5\ e^-/pix/s$ at $-25°C$) and provides both a high dynamic range (via dual-gain HDR readout) and low readout noise ($< 2\ e^-\ RMS$). The specifications of AXIS-SXR potentially allow for the acquisition a large dataset composed by $30k$ diffraction patterns in $21mins$, a particular relevant value for pump-probe ptychographic experiments which are inherently data intensive. By setting a sample-to-

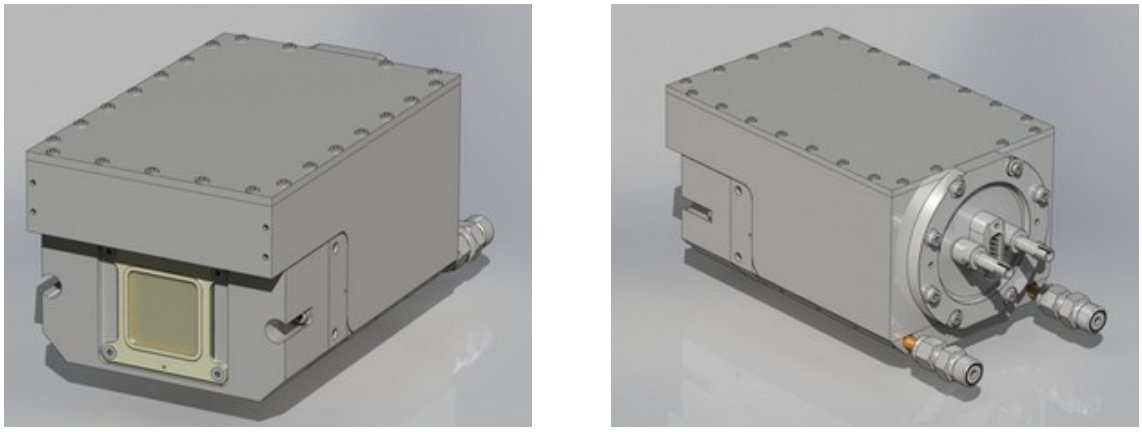


Figure 7.2: Isometric view of the AXIS-SXR detector.

detector distance to $z = 26mm$, this detector also allows for a resolution of $15nm$, which is our target. This comes with significant constraints on the working distance of the optics composing the microscope and their mechanical layout. For easier reconstruction tasks we initially aimed for oversampling values higher than 2 and $D_{probe} \approx 5\mu m$ which, considering a HHG source size of $D_{source} = 50\mu m$ (in the worst case scenario) and using eq. (7.3), imposes a required demagnification of ~ 10, a value particularly challenging for the realization of a non-aberrated illumination profile. Additionally, as shown in Fig. 7.3, through eq. (7.4) and considering a distance of $r \approx 3m$ from the XUUS^{TM} cartridge, the microscope needs a image plane located $300mm$ away from the focusing optics, which implies a particularly shallow focal length. The methodology used to carry out the design of the microscope and the optical elements therein is discussed in the next section.

7.2 Ray Tracing with ShadowOui

To properly synthetize the $5\mu m$ probe to fulfill the ptychography oversampling requirement under the constraints described insection 7.1, ray tracing has been used. In the context of X-Rays and XUV beamline design, this constitutes a fundamental computational methodology to simulate the propagation of photons in complex optical systems and optimize the design for an efficient light delivery [143–146]. This approach models the beam as a collection of discrete, monochromatic rays, each treated as traveling along a straight line according to geometrical optics, where the wavelength is much smaller than the characteristic dimensions of the optical elements and their surface irregularities. The

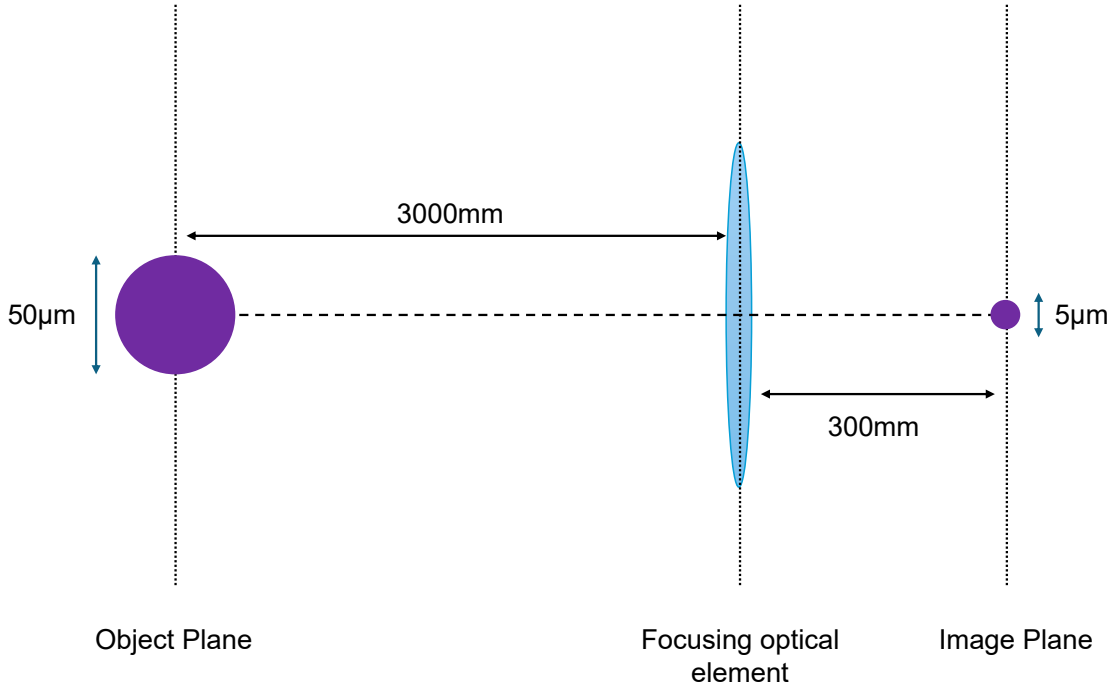


Figure 7.3: Preliminary sketch of the focusing optics geometry where parameters $s = 50\mu m$, $s' = 5\mu m$, $r = 3000mm$, $r' = 300mm$ and a focal length $f = 250mm$. The focusing element is depicted as a thin lens for the visualization purposes

essence of ray tracing in our case lies in its ability to facilitate the design, the optimization and, in future, the characterization of the optical setup.

Ray tracing does not account for diffraction, interference, or wavefront distortion effects, which are significant in coherent regimes such as HHG and are particularly relevant for ptychography. Nevertheless, in the regime of large optics, characterized by the absence of beam clipping, moderate-to-small figure errors, and moderate focusing conditions, diffraction effects are not dominant. Under these circumstances, ray tracing remains highly representative of the actual beamline performance and stands as a valuable tool in the early design phase, where a robust initial optical layout must be established. Specifically, ray tracing enables the precise determination of the positions, orientations, and apertures of all optical components (e.g., mirrors, gratings, and slits), ensuring maximum photon flux throughput while avoiding aberrations. In this way, during the implementation phase, it is possible to correctly guide the beam to the sample plane with the desired demagnification.

The design of the beamline is carried out on a python-based ray tracing platform called SHADOW3 through its Graphical User Interface (GUI) named ShadowOui, embedded

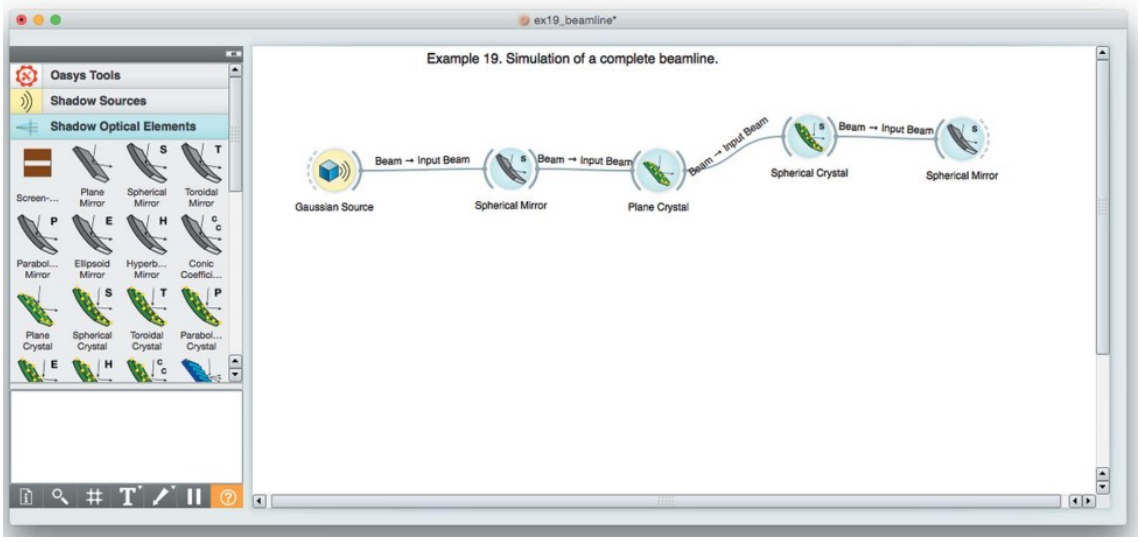


Figure 7.4: The ShadowOui application showing the OASYS canvas, the ShadowOui menus and an example beamline. From [145].

within the OrAnge SYnchrotron Suite (OASYS). Historically, the SHADOW code, developed in the 1980s by Professor F. Cerrina, emerged as a seminal and widely adopted ray-tracing tool specifically tailored for synchrotron radiation applications [147]. Today, its status as a benchmark and widely adopted tool within the synchrotron radiation and FEL communities makes it a standard for preliminary design and optimization tasks. The emerging design thus represents a solid and optimized foundation upon which subsequent, more computationally intensive wavefront propagation simulations can be built to accurately model the coherence properties of the beam and the diffraction-limited spot profile at the position of the sample. The ShadowOui interface, illustrated in Fig. 7.4, is structured around a modular and interactive computational environment. Its central component is the "Canvas", a graphical workspace that enables the construction of optical systems by assembling individual functional units called widgets. Each widget represents a discrete computational block, associated with a specific role in the simulation workflow, and is characterized by a defined set of input parameters that govern either physical properties or the flow of data between components. Widgets are organized in the "ToolBox" and span a wide range of functionalities. They include models of photon sources, optical elements (e.g. mirrors, gratings, crystals), compound optical assemblies (e.g. Kirkpatrick–Baez mirror systems), and various diagnostic tools (e.g., slits, screens, and virtual detectors). These elements can be combined to form arbitrarily complex beamlines, enabling the user

to define the sequence of interactions that photons undergo as they propagate through the optical system. Communication between widgets is established via logical connections, visualized as directional lines on the canvas. These connections function as channels through which the simulation transmits the evolving state of the photon beam from the generation at the source to the detection plane. This architecture supports a transparent and hierarchical representation of the beamline, where each stage of the optical path is explicitly defined, facilitating both iterative design and reproducible simulations.

An important feature of ShadowOui is the "Hybrid Screen" widget, which computes diffraction effects produced by beam clipping at apertures or mirror edges and includes the contribution of mirror figure errors [148]. The "Hybrid Screen" proved to be helpful in many cases for evaluating the performances of focusing mirrors, especially for the design of diffraction–limited focusing beamlines. However, in the specific case of our Ultrafast XUV Ptychography Beamline, for a preliminary estimation of the output, the "Hybrid" method has been avoided due to its computational cost and the absence of strong focusing conditions. In particular, the design constraints of the setup impose a relatively large focal spot ($\sim 5\mu m$) compared to the working wavelength ($\sim 13 - 30nm$), resulting in a regime where the geometrical approximation remains valid. In fact, recalling eq. (2.38) and considering $a \sim mm$ as the footprint of the beam on the optical elements in the beamline, the Fresnel Number during the beam propagation is several orders of magnitude higher than unity, both for $13nm$ and $30nm$ light. Moreover, the HHG source, despite exhibiting a high degree of spatial coherence, emits in a discrete comb of harmonics with partial temporal coherence, which reduces the physical interpretation of full-wave propagation. Under these conditions, the use of standard ray tracing is sufficient to evaluate the beam footprint, estimate optical losses, and optimize the positioning and curvature of the focusing optics. Inclusion of diffraction corrections, although feasible, is therefore not required in this phase of the design. Hence pure ray tracing via ShadowOui has ultimately been used for the first order approximation of multiple focusing schemes, with a clear scope of guiding the design of the microscope towards cost-effective, flexible and robust focusing solutions capable of satisfying the ptychography requirements. These multiple scenarios are illustrated in section 7.5.

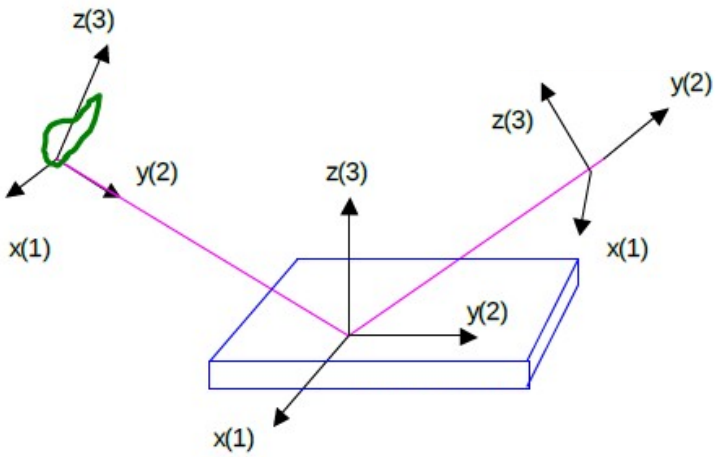


Figure 7.5: Coordinate system in ShadowOui, from [144]

.

7.3 Reference Frame in ShadowOui

In the ShadowOui environment, the beam propagation and the placement of optical elements are based on a dynamically updated local coordinate system, inherited from the SHADOW3 engine. Each optical element is defined with respect to a local frame that adapts to the direction of beam propagation. As depicted in Fig. 7.5, the $y(2)$ axis always aligns with the local beam direction, while the transverse axes $x(1)$ and $z(3)$ define the sagittal and meridional directions, respectively. This convention ensures that each optical element is described in a frame of reference that is rotated and translated relative to the preceding element, maintaining consistent internal geometry regardless of global orientation. Importantly, when an optical element is rotated (e.g., via the orientation angle parameter), the entire coordinate system is correspondingly re-aligned. This feature allows for complex beamline geometries to be modeled with precision, as every position, tilt, and alignment is always defined relative to the previous component in the optical path. Understanding this reference frame is crucial for the correct orientation of the optical elements in the beamline.

A particularly critical parameter is the orientation angle, which defines a rotation of the optical element around the local beam axis $y(2)$. This angle determines how the sagittal and meridional directions $x(1)$ and $z(3)$ are oriented relative to the physical surface of the optical element. This rotation does not affect the angle of incidence but is essential to correctly describe the tilt of the optical surface and the direction of figure and slope

errors (described in section 7.4). As such, incorrect specification of this parameter can lead to non-physical beam paths or improper modeling of surface deformations and optical aberrations.

7.4 Optical Fabrication Errors

At X-ray and XUV wavelengths, the fidelity of optical components is essential to achieve diffraction-limited performance. However, optical surfaces are far from ideal and fabrication errors (also known as form errors) fundamentally constrain the quality of the illumination function. In cases like CDI and ptychography, it can affect the image formation process. These errors are typically categorized into figure errors and slope errors, with surface roughness often considered a distinct, yet related, type of imperfection.

Figure errors represent macroscopic deviations of an optical surface from its ideal, prescribed geometric form. These imperfections are typically considered low-spatial frequency errors due to their characteristic relatively large spatial periods, often comparable to or larger than approximately one-tenth of the aperture diameter ($D/10$), extending up to the full size of the optical element. The presence of figure errors directly translates into aberrations, distorting the phase and intensity distribution of the reflected light. They affect the focusing properties of the optical element and degrade the focal spot. Figure errors directly contribute to the RMS wave phase error ϕ of the aberrated beam, which, in turn, dictates the Strehl Ratio S. The Strehl ratio espresses the ratio between the peak intensity I of the focal spot in a real optical system and the peak intensity of the focal spot I_0 generated by a perfect, ideal optical system. The Strehl ratio is defined by

$$S = \frac{I}{I_0} \approx e^{-(2\pi\phi)^2}, \tag{7.5}$$

where ϕ is related to the RMS figure error δh and the grazing angle of incidence θ_g according to

$$\phi = \frac{2\delta h \sin\theta_g}{\lambda}. \tag{7.6}$$

Figure errors can arise from various sources such as mechanical strain during the mounting of the optics, thermal effects induced by the absorbed input power or, as typically happens, manufacturing limitations. In this case, the combination of advanced techniques such as Elastic Emission Machining (EEM), Computer-Aided Polishing (CAP), Ion Beam Figuring

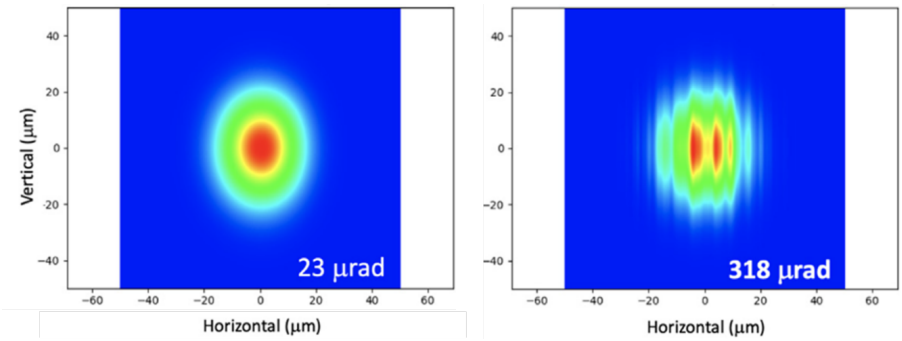


Figure 7.6: Out-of-focus simulated beam obtained for an elliptical mirror with identical Strehl ratio and 1nm RMS figure errors and increasing RMS slope errors Adapted from [149].

(IBF), or Magnetorheological Finishing (MRF) can allow sub-nanometer shape precision.

Slope errors quantify the rate of change of the deviation of the optical surface from its ideal shape and, mathematically, a slope profile is the first derivative of the height profile of the optical surface. Typically, when specifying the slope error of an optical element, the length over which the measurement occurs and the corresponding sampling rate shall be taken into account. Slope errors are often associated with Mid-Spatial-Frequency (MSF) surface deviations, typically spanning spatial periods from sub-millimeter scales up to several millimeters or centimeters. Slope errors have an important impact on the optical performances of coherent beams. This happens primarily when the transverse coherence length of the beam is smaller than the aperture of the mirrors and when the beam is used out of focus. Indeed, as plotted in Fig. 7.6, simulations have shown that for the same peak intensity at focus, implementing a higher slope error may considerably degrade the beam profile out of focus.

Another relevant surface irregularity is roughness, which describes the microscopic High-Spatial-Frequency (HSF) deviations from the nominal surface profile. In contrast to figure and slope errors, roughness originates from imperfections at the nanometric or sub-nanometric scale, typically with spatial periods below 1mm. Unlike figure errors, which primarily affect the geometric wavefront propagation, and slope errors, that have a mixed nature, surface roughness mainly determines the scattering properties of the optical element. In the XUV and soft X-ray regimes, where the wavelength becomes comparable to the typical surface roughness scale, even sub-nanometer roughness values can lead to significant scattering, resulting in a diffuse background at the image plane. Thus, compared to a smooth surface, roughness provides a reduction of the specular reflectivity

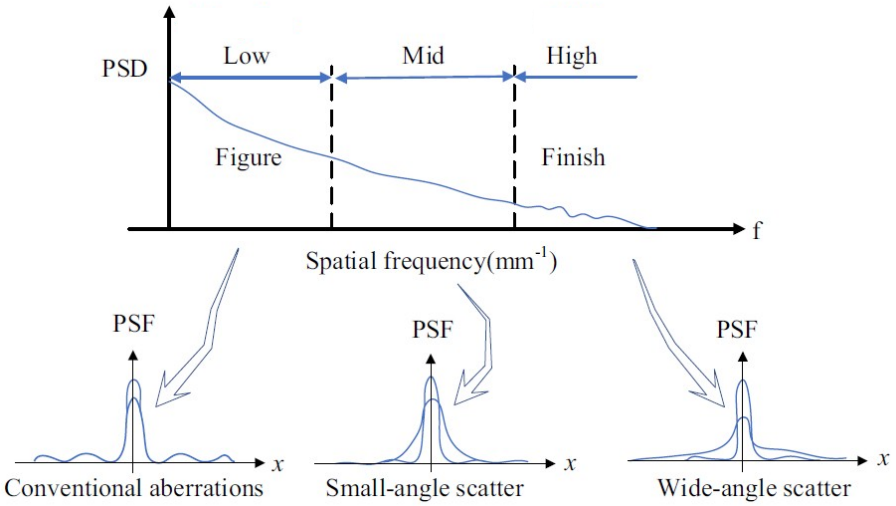


Figure 7.7: Power Spectral Density as a representation of different optical fabrication error regimes. Adapted from [150].

R that can be computed using the formula [146]:

$$\frac{R}{R_0} = \exp\left[-\left(\frac{4\pi\sigma\cos\theta}{\lambda}\right)^2\right], \tag{7.7}$$

where σ is the RMS roughness and θ is the incidence angle measured from the surface normal, λ is the wavelength of the incident light and R_0 is the reflectivity of a smooth surface. An international standard used to characterize surface topography errors is the Power Spectral Density (PSD). This metric provides a comprehensive decomposition of these errors across the entire spectrum of spatial frequencies. A depiction of PSD is shown in Fig. 7.7, where the low, mid and high spatial frequency regions correspond to figure errors, slope errors and roughness. Because figure and slope errors can directly distort the Point Spread Function (PSF) incident on the sample, significant deviations of the probe from the assumed shape can adversely affect both the convergence rate and the reconstruction quality in CDI and ptychography. Moreover, in extreme but relatively common cases, the beam can spread out and meeting the oversampling requirement in eq. (3.1) can become a challenge. In these cases, a pinhole shall be applied to confine the illumination function. Excessive roughness can on the other hand produce diffuse scattering, reducing the intensity of the beam and the signal-to-noise ratio at high diffraction angles that carry the high-resolution information.

Surface and slope error profiles of the reflective optical elements in the beamline can be simulated and/or imported in ShadowOui. Different widgets serve to this purpose but the more advanced is the "Height Error Profile", where both real and synthetic metrology data are available through the DABAM (DAtaBAse for Metrology) [151] . In order to carry out realistic simulations of multiple beam focusing schemes, slope errors have been considered, and their effect on the final performance of the microscope have been accounted for. In the following analysis, roughness has not been considered since related to the coherence properties of the radiation, which is neglected in the geometrical approximation.

7.5 Ray Tracing Comparison of Multiple Focusing Delivery Schemes

Ptychography and CDI are lensless imaging methods and the key elements composing the "microscope" are essentially limited to the detector and the focusing optics. These are devoted to the demagnification of the beam in order to suffice the oversampling requirement. Notably, ptychography poses significant demands in terms of photon flux, especially to resolve the fine speckle structures at high detection angles, which embed the highest frequency components and enable maximum resolution. For this reason, the following analysis is limited to reflective optical systems rather than transmissive or diffractive elements such as Fresnel Zone Plates. Each solution is conceived to be cost-effective and deployable, with minimal alignment complexity, in a few meters from the HHG source. Stemming from these considerations, three astigmatic-free focusing schemes have been simulated for the XUV microscope:

1. an off-axis z-fold composed of a flat and a spherical mirror at quasi normal AOI,
2. two 45° flat mirrors and a grazing incidence toroidal mirror (with and without pinhole),
3. two 45° flat mirrors and a grazing incidence ellipsoidal mirror.

The three cases are illustrated in Fig. 7.8. and are identical in the section preceding the microscope. The simulations start at location of the HHG source, named source plane (SP). The beam propagates into the beamline till reaching the rejectors (R1 and R2) and the filter (F) placed immediately after. The XUV comb finally reach the experimental

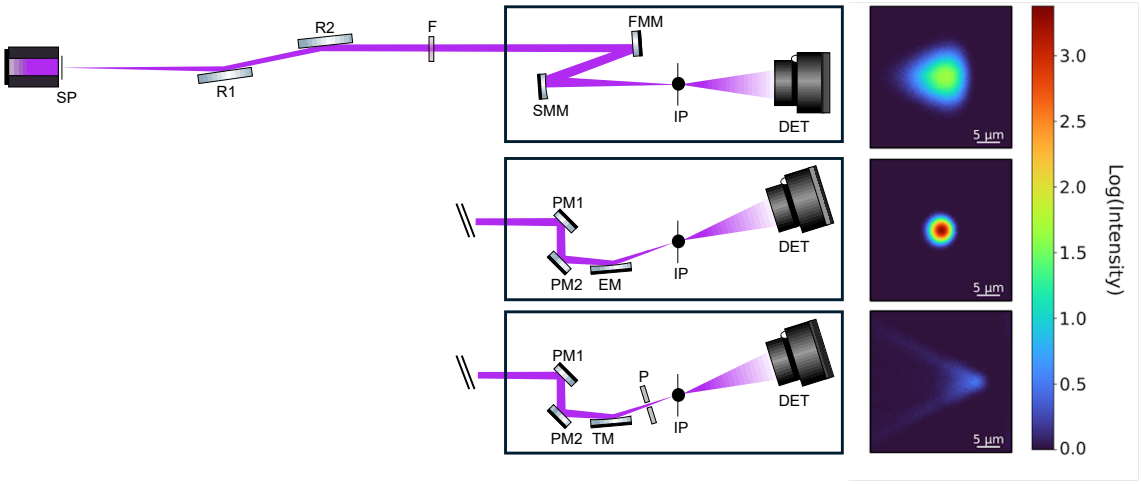


Figure 7.8: View of the three simulated cases. From the source plane the beam propagates down to the experimental chamber after bouncing off the rejectors (R1 and R2) and being filtered by the thin metallic filter (F). On top, the off-axis z-fold design, in the middle section the grazing ellipsoid (EM) case and at the bottom section the toroidal mirror (TM) focusing system including a pinhole (P). The three configurations are designed to have the same distance ($2800mm$) from the source plane (SP) to the surface of the focusing optical element. The position of the image plane (IP) is chosen to achieve a demagnification factor close to 10. Common elements in both simulations are rejector mirrors working at Brewster angle and a thin metallic filter. The z-fold employ a single flat mirror (FMM) working at quasi-normal AOI while the toroidal and ellipsoidal cases make use of a couple of them (PM1 and PM2) working at 45°. On the side, the spot size at the image plane of the three focusing cases with a $5\mu m$ scalebar for reference.

chamber, where the microscope geometry differs between the z-fold and the cases where the grazing incidence optical element is employed. Light is focused at the image plane (IP) and the emerging diffraction patterns are captured by a pixelated detector. In ShadowOui, a unique workspace, shown in Fig. 7.9, has been implemented to simulate the results of the multiple delivery schemes simultaneously. The three cases are highlighted by the red arrows and in principle originate from the HHG source modeled with the "Geometrical Source" widget. The widget specifies the properties of the output beam at a specific plane position, which is used as the input information delivered to the next widget, that is the first rejector (R1) and, later, the second rejector (R2). Both mirrors are modeled using the "Plane Mirror" widget. To conclude the common section of the probe branch, the "Screen-Slit" widget is used to model the aperture of a thin metallic filter (F) in the filter wheel. At this point the output plane of the filter widget serves as an input plane of all three cases. In the z-fold case, this information is processed by another "Plane Mirror" widget

representing a Flat Multilayer Mirror (FMM), with different specifications compared to R1 and R2. The output finally reaches the "Spherical Mirror" widget, which mimics the presence of a Spherical Multilayer Mirror (SMM) and acts as a focusing device for the beam, which is visualized using the "Plot XY" widget. The simulation also includes the "Hybrid Screen" widget to account for diffraction effects. This is however rarely used due to the motivations provided in section 7.2. From the output of the filter, another line guides the beam to a second branch, which accommodates two "Spherical Mirror" widgets (PM1 and PM2) with infinite beam radius. Their implementation is identical to the "Plane Mirror" widgets but allow to change the radius of curvature (ROC) if needed during troubleshooting. After PM2, three cases emerge: two of them are referring to the toroidal focusing configuration, which have been explored using either the "Toroidal Mirror" widget or in combination with another "Screen-Slits" widget, used as a pinhole to confine the illumination function at the image plane. The ultimate branch presents an "Ellipsoidal Mirror" widget, to simulate the focusing geometry employing a single ellipsoid mirror for focusing. The simulation is also supported by other widgets: the "Scanning Loop Variable Point" allows to perform loops on a particular configuration parameter of the optical element, whose effect can be monitored and recorder with the "Plot XY" widget at the image plane. "FocNew" is a quick tool to record caustic scans and to find the circle of least confusion of a given focusing optical element. In our simulation is typically attached to the last widget before plotting the spot size at the image plane. The Beamline Renderer is used for a rapid visualization of the beamline structure, in order to verify the correct implementation of incident angles, optical element orientation and distances. Finally, the "Info" widget provides crucial information about the entire simulation. In the next section, the beam propagation will be described step by step by illustrating the actual parameters implemented into the ShadowOui canvas.

7.5.1 Distances

For a fair comparison, all light delivery schemes were designed with identical propagation distances, demagnification factors, and detector resolution. The entrance arm is approximately estimating the distances in the probe arm, considering the beam propagation from the HHG downstream, towards the location of the experimental chamber. At the first design stages, the precise knowledge of the optical elements was not available, therefore the values were approximated. The exit arm was instead chosen to produce the same

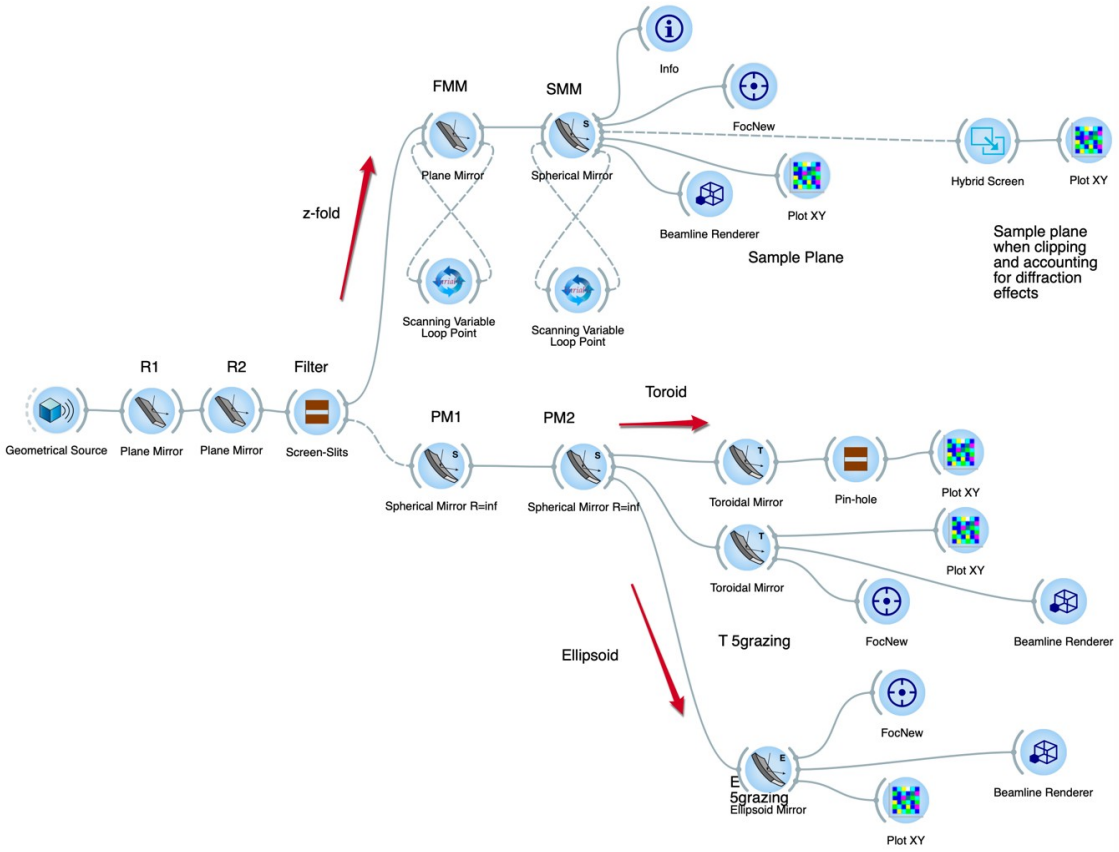


Figure 7.9: ShadowOui implementation of the multiple focusing delivery schemes.

demagnification factor despite different elements were used. In ShadowOui, the distances are defined as the separation between an output (q) and an input (p) plane, with the widget performing a certain transformation between the two. These distances are inherited from the lens equation

$$\frac{1}{f} = \frac{1}{p} + \frac{1}{q}, \tag{7.8}$$

which establishes a precise mathematical relationship between the object distance, image distance, and the focal length of an optical element. For non-focusing optical elements the nomenclature remains the same, even though the focal length is considered infinite. In the simulations, p and q are set at the intermediate positions between consecutive optical elements, in order to monitor the intensity figure variation when configuration parameters of the widgets are changed. This is schematically shown in Fig. 7.10. Table 7.1 summarizes the propagation distances in the simulates z-fold case, while table 7.2 is referred for the ellipsoidal/toroidal one. In all of them, the entrance arm is 2800mm long while the exit

Optical Element 1	Optical Element 2	Distance [mm]
Source Plane	Rej 1	600.0
Rej 1	Rej 2	400.0
Rej 2	Filter	200.0
Filter	Flat	1400.0
Flat	Spherical	200.0
Spherical	Image Plane	274.5

Table 7.1: Beam path in the z-fold delivery scheme simulated for the probe arm of the Ultrafast XUV beamline.

Optical Element 1	Optical Element 2	Distance [mm]
Source	Rej 1	600.0
Rej 1	Rej 2	400.0
Rej 2	Filter	200.0
Filter	Flat 1	1200.0
Flat 1	Flat 2	200.0
Flat 2	Toroidal / Ellipsoidal	200.0
Toroidal / Ellipsoidal	Image Plane	274.5

Table 7.2: Beam path in the toroid/ellipsoid delivery scheme simulated for the probe arm of the Ultrafast XUV beamline.

arm is ($274.5mm$) to maintain an equal demagnification factor of 10.2. Compared to the first case, toroidal and ellipsoidal configurations present an additional plane mirror before the focusing optics, as commonly done in practice for easier alignment. As a consequence, the distances between the optical element is different. In the next sections the three configurations are individually presented and later compared in order to find the most appropriate microscope design. To do so, the simulative framework in ShadowOui is presented.

7.5.2 Modeling the HHG Source

The first element implemented in the ShadowOui environment is the HHG source, which is defined by its size, divergence, photon energy and flux. According to the supplier, at the generation point the source size is in the range $30-50\mu m$ $1/e^2$ of intensity diameter. The exact value depends on the generation condition, with the average being $\sim 40\mu m$. The typical divergence ranges between $0.5mrad$ and $2mrad$ $FWHM$, with the most frequent

values of $1.2mrad$ and $1.4mrad$ for Ar and He combs respectively. The XUV combs generated from the XUUS are optimized for $\sim 13nm$ ($95eV$) and $\sim 30nm$ ($42eV$) energy emission, with a respective flux of 10^{10} ph/s and 10^{12} ph/s according to the supplier's datasheet.

In ShadowOui the HHG source can be modeled with the "Geometric Source" widget. ShadowOui requires the definition of an initial number of rays, since the flux cannot be input directly. The number of rays can be monitored after each widget during propagation. The spatial and angular distribution of rays is statistically but deterministically determined by a Monte-Carlo generation process. Therefore, the source has been initialized using $1M$ rays with a gaussian profile and a gaussian angular distribution, with size and divergence of ($S_{1/e^2} = 40\mu m$ and $Div_{FWHM} = 1.4mrad$). These values are converted using

$$Div_{\sigma} = \frac{Div_{FWHM}}{2.355} = 0.594mrad \tag{7.9}$$

and

$$S_{\sigma} = \frac{(S_{1/e^2}/1.699)}{2.355} = 10\mu m, \tag{7.10}$$

because ShadowOui only admits sigma-values.

The design has been carried out using the divergence of the He generated beam, since the oversampling requirement more challenging at shorter wavelengths. For simplicity, the energy distribution of the beam is approximated to a single line at $13nm$, since the exact energy content of the probe is not relevant at this stage where diffraction effects are neglected.

7.5.3 Modeling the Rejectors and the Filters

Following the source, the beam is directed towards the rejector mirrors, which are implemented using the "Plane Mirror" widget within the ShadowOui environment. Each mirror is defined as a flat rectangular optical element with dimensions $8mm \times 56mm$ (the surface portion which has been metrologically investigated), positioned at a grazing incidence angle of 6°, in agreement with the optical layout specifications provided by KMLabs. R1 is placed such that its source plane distance is $600mm$, corresponding to the distance from the HHG source. Its image plane is set to $200mm$, corresponding to the intermediate plane between R1 and R2. The second rejector is modelled identically in terms of shape and incidence angle, but has a source plane distance of $200mm$ and an image plane distance

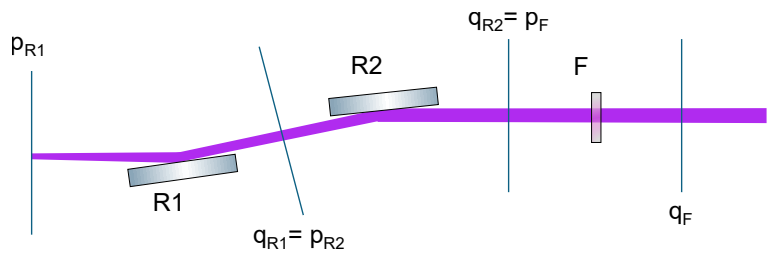


Figure 7.10: Input and output plane definition in ShadowOui. R1 processes the information from its input plane and provides a new intensity figure of the beam at its output plane. The output plane is made coincident with the input plane of the following optical element. The process continues until the last optical element.

of $100mm$ as sketched in Fig. 7.10.

The two mirrors possess different orientation angles. The orientation angle of R1 is set to 0°, meaning that its local reference frame aligns directly with the global coordinate system defined from the source. The orientation angle of R2 is instead set to 180°, which corresponds to a mechanical rotation of the mirror along its longitudinal axis. This configuration ensures that the reflective surfaces of the two mirrors "face each other" and are correctly aligned to achieve the required beam rejection geometry. Each mirror is equipped with the figure error shown in Fig. 7.11, composed by an array of 226×34 squared pixels with side length of $247.57\mu m$. The profile has been acquired by the supplier using an interferometer and is representative of the effective mirrors in the beamline. The SHADOW3 engine directly provides a calculation of $\sim 2\mu rad$ 1D RMS slope error along both tangential and sagittal direction. These values are not critical and do not affect the shape of the spot size at the image plane of the beamline.

The "Screen Slit" is placed afterwards to simulate the presence of a filter. This element is modeled as a simple circular aperture with $5mm$ diameter, as the size of the real filter in the beamline. Since the simulation is independent from the spectral characteristics of the emitted light, no transmission curve is attached to the widget. The input plane is set to $100\mu m$ and the output one is set to be 700mm after the filter itself, with no other parameters defined. Visualizing the beam statistics at this position, it emerges that only 0.21% of the initial rays are lost due to clipping, as shown in Fig. 7.12. Most of the beam instead passes through the aperture and continues its path towards the multiple microscope layouts.

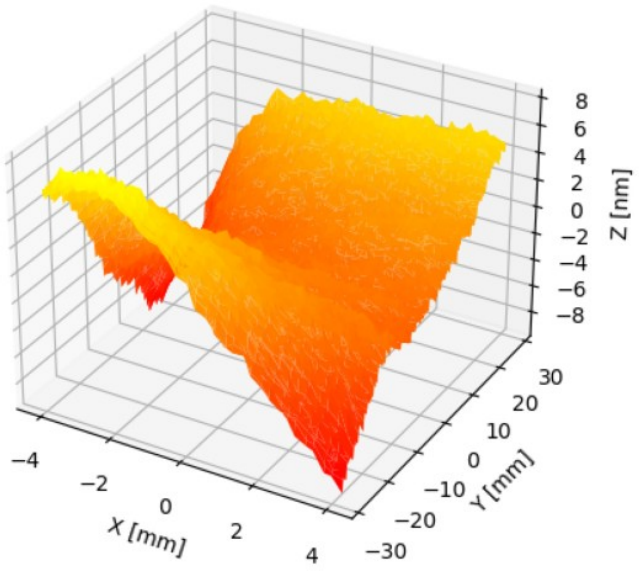


Figure 7.11: Measured surface error profile of a rejector mirror similar to the ones implemented in the beamline.

7.5.4 The Toroidal Focusing Scheme

The toroidal focusing scheme employs three optical elements. Initially two flat mirrors are modeled with the "Plane Mirror" widgets as circular optical elements with $1''$ diameter. The first mirror is located $1200mm$ downstream the Screen Slit, has an $AOI = 45°$ and reflects the beam towards the second identical mirror. The orientation angles of these reflective optical elements is 90° and 180°, respectively, such that the beam continues its propagation along the initial direction with a lateral displacement of $\sim 83mm$. Located $200mm$ after the last 45° mirror, the toroidal mirror intercepts the beam. This optical element is simulated via the "Toroidal Mirror" widget and is configured to have a footprint of $200mm \times 25.4mm$ and a realistic grazing angle of incidence of 5°. A toroidal mirror is geometrically defined by two different radii of curvature: a tangential radius R and a sagittal radius ρ. To achieve a point-to-point image at grazing incidence, the astigmatism must be compensated by matching the tangential and sagittal focal lengths. This requirement leads to the stigmatic focusing condition

$$\rho/R = \cos^2 \alpha, \tag{7.11}$$

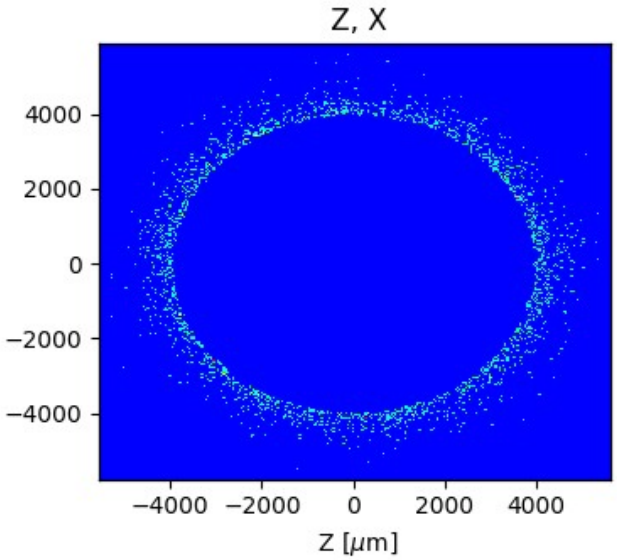


Figure 7.12: Lost rays due to beam clipping 700mm away from the circular aperture modeling the beamline's filters. The image 2D plot is directly obtained in ShadowOui by placing a 256×256 screen at the image plane.

where α is the angle of incidence measured from the surface normal. In the current layout, α is equal to 85° and the radii are respectively $R = 5736.67mm$ and $\rho = 43.5765mm$. These values are accurately chosen to set the image plane at $274.5mm$, obtain a demagnification factor of 10.2 and satisfy eq. (7.11). At the image plane, which corresponds to the future location of the sample plane, the "Plot XY" widget is used to evaluate the spot size characteristics. The widget is configured to be consistent with the FOV and the resolution of the AXIS-SXR detector when placed $26mm$ away from the sample. For a wavelength $\lambda = 12.9nm$ (see section 7.7.3 and a detector chip of linear size $D_{chip} = 22.5mm$, the projected pixel size on the sample plane is

$$\Delta r = \frac{\lambda z}{D_{chip}} = 14.88nm, \tag{7.12}$$

resulting in an effective field of view of

$$FOV = \Delta r \times 2048 = 30.5\mu m. \tag{7.13}$$

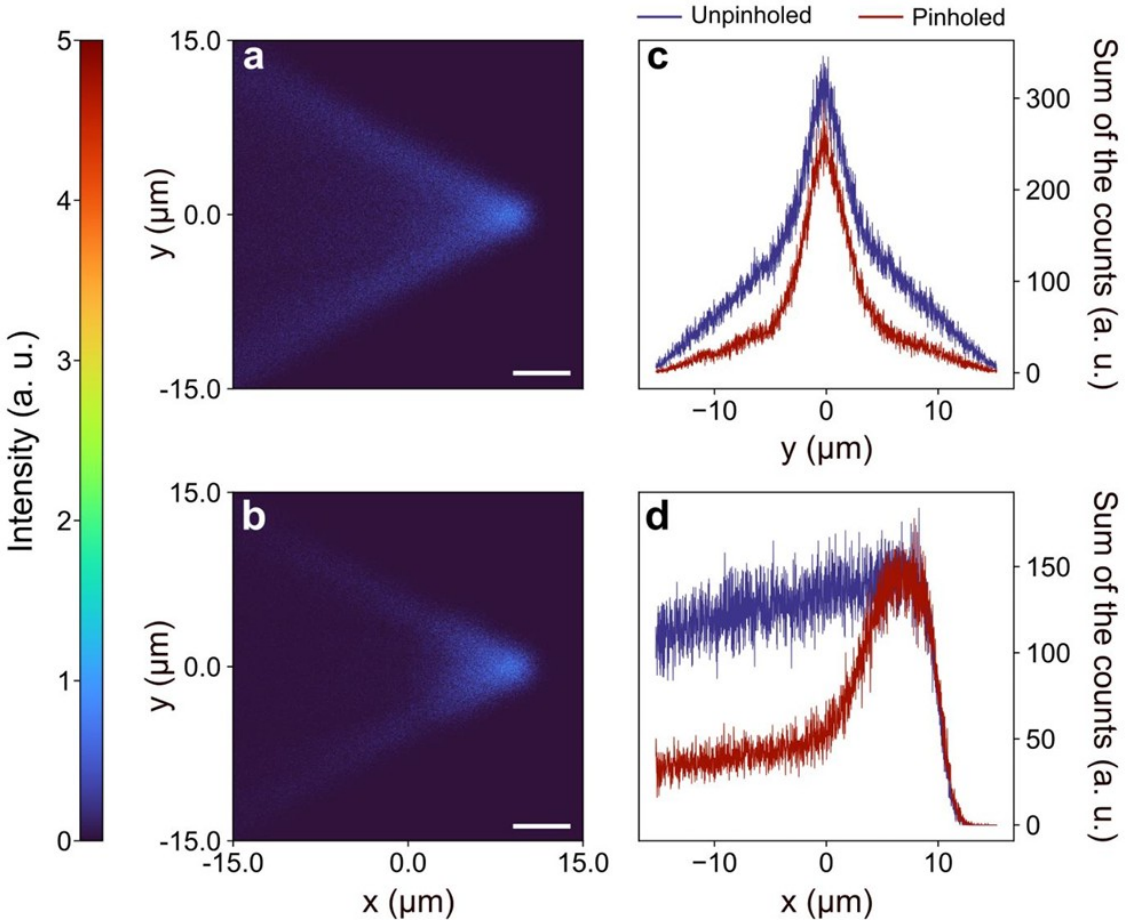


Figure 7.13: Toroidal illumination functions from ray tracing. a) Without and b) with confinement through a pinhole with a diameter of $60\mu m$ placed $10mm$ before the image plane. Total flux at the image plane obtained by integrating all pixel counts along the c) x, and d) y axis. Scale bar is $5\mu m$.

Operatively, the widget allows to directly set the FOV and the number of bins of the screen, thereby automatically determining the resolution of the screen. The higher the number of bins, the more granular the image is, since each bin becomes smaller and collects a lower number of rays. With the "Plot XY" widget, the position of the image plane can be either locked to its geometrically defined location or manually retraced to find the circle of least confusion. This is particularly relevant because enable to follow the image plane when a certain parameter is varied. Despite the fulfillment of eq. (7.11), in the studied configuration, the toroidal mirror produces a highly aberrated spot. This is expected for single toroids, since stigmatic focusing is typically achieved with unity magnification within a Rowland mounting configuration, where coma aberration is minimized [152].

Coma is the limiting factor of this configuration and manifests as a degradation of the image quality where rays originating from off-axis points in the object plane are focused into a "triangular" shape rather than a sharp point. This results in a degradation of the spot size, reaching a diameter of $65.7\mu m$ $1/e^2$ ($\sigma = 0.5$), which is too large to meet the oversampling requirements for high-resolution ptychography. While a structured, non-isotropic probe can sometimes be beneficial for ptychographic reconstructions, the aberrations produced by the toroidal mirror are too significant to be of practical use. This effect is shown in Fig. 7.13a).

To mitigate the severe aberrations, an alternative setup was simulated. The "Screen Slits" widget was used to model a $60\mu m$ diameter pinhole placed $10mm$ upstream the sample. This spatial filter effectively "cleans up" the beam, drastically reducing the spot size at the sample plane to $10.7\mu m$ $1/e^2$) ($\sigma = 2.85$) as shown in Fig. 7.13b). This value is comparable to that achieved with the z-fold configuration (see section 7.5.6), however, it comes with significant drawbacks. The first is flux reduction: the pinhole allows for smaller spot size by blocking a significant portion of the rays. The simulations in Fig. 7.13b) and Fig. 7.13c) show that the intensity at the sample substantially drops, with only 21.6% of the photons from the toroidal mirror reaching the sample plane. For an intrinsically photon-demanding technique like ptychography, such loss of flux would lead to unacceptably long exposure times. The second relevant consideration regards the practical complexity of such configuration. From an experimental standpoint, implementing a pinhole very close to the sample can be extremely challenging because complicates the integration of other components, such as in-vacuum motion stages, or can block the optical path for the pump laser in time-resolved experiments. Given these critical disadvantages, in particular the severe loss of flux, the toroidal mirror configuration was, in principle, deemed unsuitable for the beamline. As such, no further simulations in ShadowOui have been carried out using surface error profiles and misalignments.

7.5.5 The Ellipsoidal Focusing Scheme

The second focusing scheme investigated is based on a single ellipsoidal mirror, which is by design capable of perfect, aberration-free focusing for a point source. The layout in the experimental chamber is similar to the toroidal mirror setup and is composed by two 45° plane mirrors that direct the beam towards the focusing element at $\theta_g = 5°$ grazing incidence angle. The choice of the grazing incidence angle comes from previous

experience within the group, however ellipsoidal mirrors may be used at shallower grazing angles with consequences on the required mirror's length, reflectivity and tolerances. The ellipsoidal mirror in ShadowOui is modelled using the dedicated "Ellipsoid Mirror" widget, in which a major semi-axis $a = 1537.25mm$ and a minor semi-axis $b = 73.41mm$ are accurately selected to satisfy the conditions [151]

$$a = \frac{1}{2}(p + q) \tag{7.14}$$

and

$$b = \sqrt{pq}\sin\theta_g. \tag{7.15}$$

The fulfillment of these equations is required to focus the light originating from one conjugate focal point to another, thereby producing an "aberration-free" image on axis. Here, the object p and image distances q were kept identical to the other configurations ($2800mm$ and $274.5mm$) for an equivalent comparison. As expected, the simulation for an ideal ellipsoidal mirror without misalignments or surface errors shows superior performance compared to the single toroid. It delivers a clean, symmetric, Gaussian-shaped probe to the image plane with a $1/e^2$ diameter of just $4\mu m$ as shown in Fig. 7.14, which is significantly smaller than that produced by all the other geometries and enables diffraction pattern binning. This tight focus translates to a very high oversampling parameter of 7.6, far exceeding the threshold for ptychography.

Despite its excellent performance in the ideal case, a relevant drawback of the ellipsoidal mirror configuration is its extreme sensitivity to misalignments. Since a stigmatic condition is guaranteed only when the source is located exactly at this first focus, any shift immediately breaks the point-to-point focusing condition of the elliptical surface and leads to rapid broadening of the probe size. To quantify this effect, the percentage of relative increase ($RI\%$) of the spot diameter at the image plane is computed, according to the following formula:

$$RI\% = \frac{S_f - S_i}{S_f} \times 100, \tag{7.16}$$

Where S_f is the final spot size and S_i an initial reference value equal to $4\mu m$, which corresponds to the aberration-free case. Misalignments are depicted in Fig. 7.15a and can be divided into translational and rotational categories. A translational misalignment consists of a shift of the optical surface in any spatial direction; a rotational misalignment consists of any angular deviation from the normal operative condition of the optical

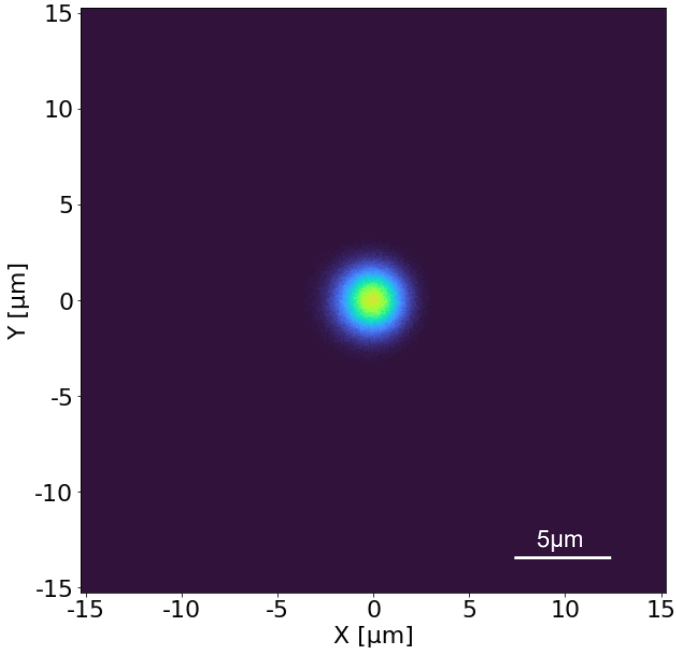


Figure 7.14: Circle of least confusion attainable with a pair of 45° flat mirrors and a single ellipsoid working at grazing incidence. The $1/e^2$ diameter is estimated to be $4\mu m$, leading to an oversampling of 7.6.

element, and can be expressed as a roll, pitch and yaw angle. The grazing incidence geometry makes the system highly sensitive to rotational errors. An angular offset of just a few hundredths of a degree in pitch or yaw and can cause the beam diameter to increase by more than three times, severely degrading the probe quality. Fig. 7.15e explores the effect of pitch misalignment in the range ±0.03° using steps of 0.01°. The image shows a linear increase in the spot size from $4\mu m$ to $25\mu m$ $1/e^2$ ($RI\% = 84\%$) beam diameter, violating the limit for oversampling at the image plane (grey area) even with deviations of ±0.01°. The ellipsoidal mirror is therefore 100 times more sensitive compared to the z-fold described in section 7.5.6. The effect of roll on the spot is less severe: varying the misalignment angle by 0.1° in a range of ±0.3°, the spot size increases from $4\mu m$ to $37.5 \pm 0.2\mu m$ $1/e^2$, with ($RI\% = 89.3\%$). However, the beam retains a Gaussian-like profile which can be compensated by adjusting the sample position. The configuration is also sensitive to translational shifts: a displacement of $3mm$ in any direction can broaden the beam up to $88.2 \pm 0.4\mu m$, when the oversampling requirement is completely violated. Although small, the shift amounts to the 35% of the clear aperture, calculated considering the grazing incidence angle of 5° and half of the longitudinal mirror length $200mm$.

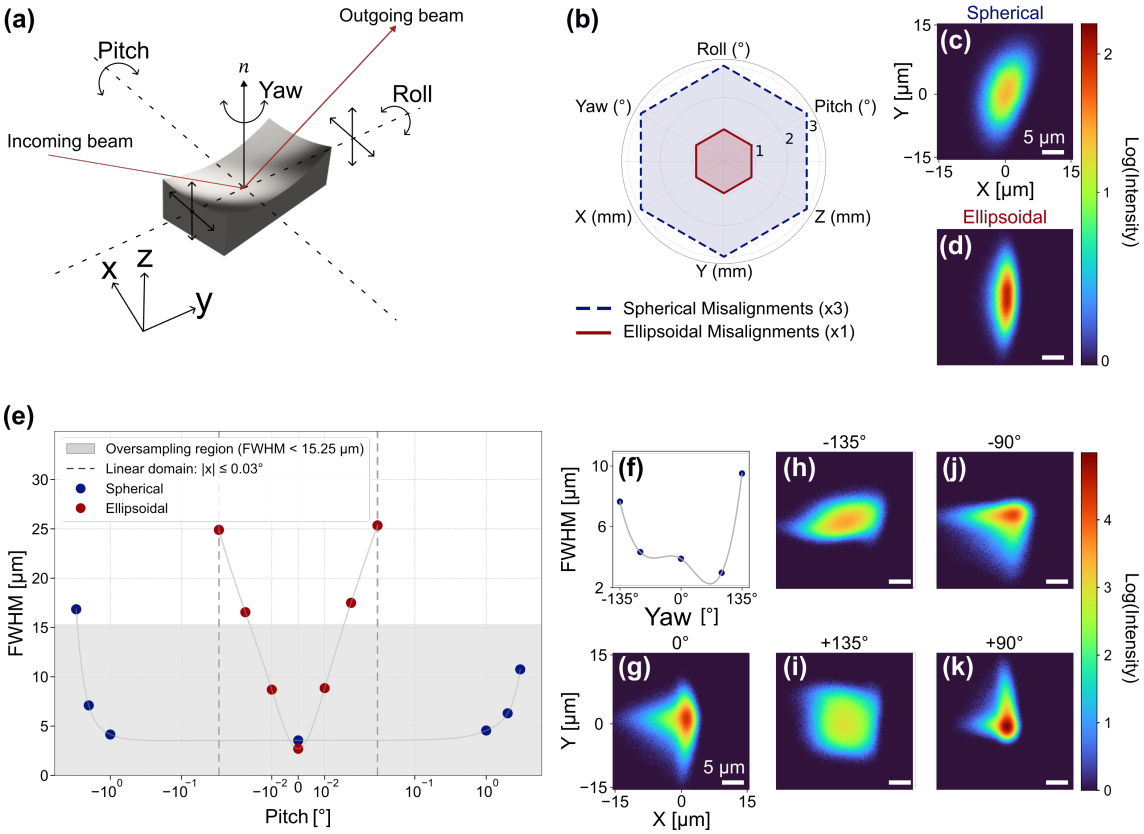


Figure 7.15: (a) Translational and rotational degrees of freedom on an optical mirror. (b) Misalignments applied to the ellipsoidal and the spherical mirror of the z-fold. Despite the different magnitudes, comparable results are obtained as shown in (c) and (d). (e) Effect of pitch misalignment on both the ellipsoid-based and the z-fold focusing configurations. The spot size produced by the ellipsoid suffers $RI\%$ up to 84% in a the range $\pm 0.03°$. A 100 times higher misalignment on the spherical mirror of the z-fold does not provide important variations in spot size. The region for oversampling $\sigma > 2$ is highlighted in grey. (f) Spot size variation in FWHM units obtained by exploiting the yaw angle of a spherical mirror with $5\mu rad$ RMS slope error, hit $5mm$-away from the pole. The 2D spot size is shown in (h)-(k) at specific positive and negative angles.

Unlike the z-fold scheme, where some misalignments can be compensated by adjusting the sample position, this corrective action is only effective for the ellipsoidal mirror when the shift occurs along the tangential direction. This high sensitivity requires using very high-precision and stable in-vacuum actuation stages, increasing both cost and complexity. Interestingly, the ellipsoidal configuration showed a relatively low sensitivity to surface slope errors in the range ($2.5 - 10 \mu rad$ RMS, in both the sagittal and tangential directions. Introducing these realistic surface imperfections results in an increase of the spot size up to $1 \mu m$, inside the range $4.6 - 5.4 \mu m$ compared to the ideal case. This robustness is attributed to the implemented design, which does not use extremely shallow grazing incidence angles. This indicates that in this geometry, while the alignment of the mirror is critical, the specifications for the mirror's surface finish are less demanding.

7.5.6 The Off-axis Z-fold Focusing Scheme

This microscope focusing scheme is sketched in Fig. 7.16 and is made of two mirrors, a plane and a spherical one, composing a z-fold configuration. To keep the layout compact and experimentally compatible with the presence of actuation stages, the two mirrors are separated by a distance of $\sim 200mm$, with the beam hitting their surface with a tangential (along y in Fig. 7.15a) offset from the pole. The flat mirror, the first of the z-fold couple, is placed $1400mm$ away from the Screen Slit and is modeled with a "Plane Mirror" widget. The mirror is circular with a $1''$ diameter and operates at $AOI = 2.5°$, with the beam hitting into a position $5mm$ away from the mirror's center. The orientation angle is set to 90°, which allows to reflect the beam backwards towards the source.

The focusing optics is a curved mirror modeled using a "Spherical Mirror" widget with a Radius of Curvature (ROC) of $500mm$. The choice of this value is based on two reasons: first, it allows to obtain an image plane at $274.5mm$ away from its surface, which guarantees a beam demagnification of 10.2; second, it is a standard value typically available from suppliers without customization.

The mirror possesses an orientation angle of 180° and the angle of incidence of 2.5° with respect to the pole, with an identical offset of $5mm$ as for the flat mirror. In this way, the beam exits the z-fold parallel to the incoming direction. The z-fold scheme guarantees no lost rays, an input beam of $\sim 3.5mm$ FWHM wwhen hitting the surface of the flat mirror and a $\sim 8mm$ jog to avoid clipping at the edge of the spherical mirror.

Compared to the grazing incidence optical elements presented before, to properly

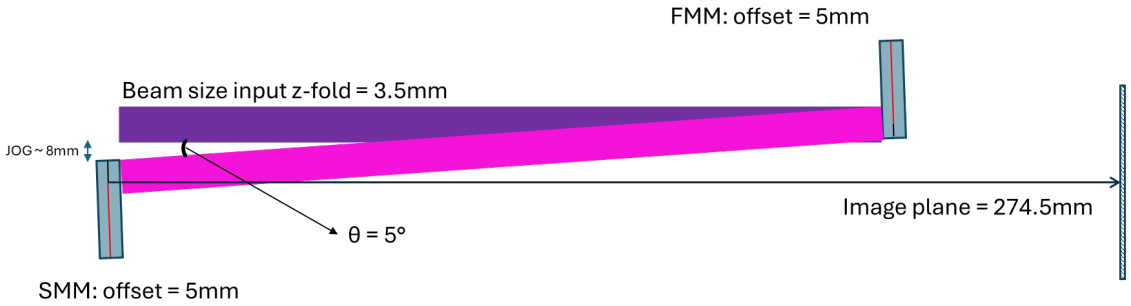


Figure 7.16: Sketch of the z-fold scheme implemented in ShadowOui. For visualization purposes the spherical mirror is approximated as a flat one.

operate in the XUV regime at near normal incidence, the z-fold mirrors shall be coated with multilayers. The coating allows to overcome the issue of low refractive index in this region of the electromagnetic spectrum, and to direct XUV light towards the sample. Although the reflectivity can reach values up to 70% (e.g. for Mo/Si at 13.5nm), unlike achromatic grazing incidence mirrors, multilayer mirrors are inherently narrowband, reflecting only a specific spectral window defined by the layer composition, the periodicity and the angle of incidence of the input light. However, since the current analysis targets the geometrical robustness of the focusing optics, the presence of multilayers has minor importance and can be neglected.

To comprehensively evaluate the performance and robustness of the z-fold configuration, the analysis was carried out in four stages: an ideal case, the introduction of misalignments, the inclusion of surface slope errors, and finally a combined simulation with both misalignments and slope errors. In this phase, slope errors were applied exclusively to the focusing optics. In its ideal configuration, without any misalignments or surface errors, the simulation shows that the off-axis z-fold produces a slightly aberrated probe (see Fig. 7.17) at the image plane. As expected from the geometry, a clear coma aberration is present due to the 5mm offset from the mirror's pole. Nevertheless, the resulting spot at the circle of least confusion is well-defined, with a $1/e^2$ diameter of approximately 10.7μm. This focused spot size is within the requirements for robust ptychographic reconstruction, yielding an oversampling parameter of 2.85 calculated through eq. (3.1). The second phase of the analysis introduced translational and rotational misalignments to the spherical mirror to assess the stability of the system under realistic and operative conditions. The configuration demonstrated considerable tolerance to translational misalignments. Shifts parallel to the mirror's surface in the sagittal direction

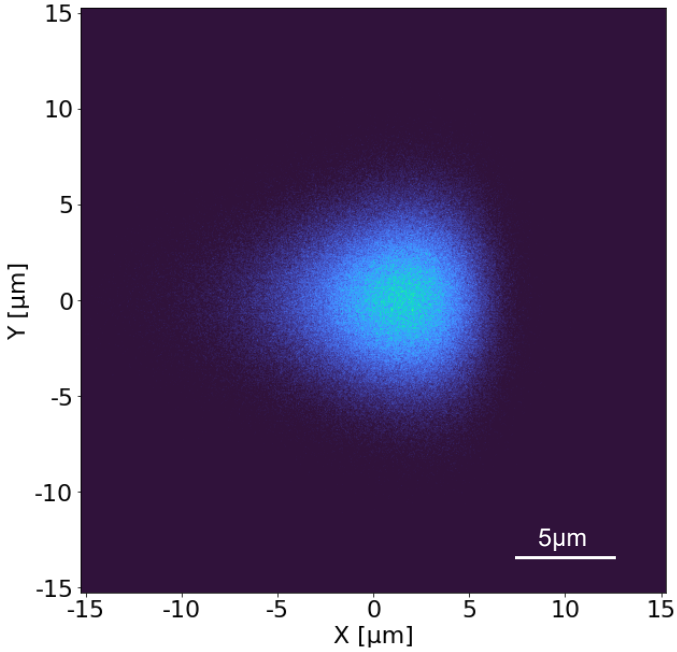


Figure 7.17: Circle of least confusion attainable by means of an off-axis z-fold composed by a plane and a spherical mirror. The $1/e^2$ diameter is estimated to be $10.7\mu m$, leading to an oversampling of 2.85.

(x-translation) have a minimal impact on the beam size at the focus. For instance, the beam retains a size of $10.7 \pm 0.3mm$ upon the application of a translation equal to 12% of the mirror's clear aperture. Shifts in the tangential direction (y-translation) have instead a slightly larger effect on the spot size, due to the inherent asymmetry of the off-axis design, but the system remains robust for small adjustments. In general, shifts parallel to the mirror's surface do not induce significant beam broadening unless they exceed several millimeters, at which point beam clipping can occur. Offsets perpendicular to the mirror surface (z-translations) primarily shift the position of the focal plane along the optical axis, which can be visualized by moving the plane imaged by the "Plot XY" widget. This effect is not critical: the diameter of the beam can expand up to 70.1% and enhance astigmatism, but can be completely recovered by shifting the position of the image plane by an amount proportional to the shift applied. The system is instead more sensitive to angular errors. The blue curve in Fig. 7.15e shows the effect of pitch misalignment in the range $\pm 3°$ with by steps equal to $1°$. The beam suffers beam broadening and astigmatism as the effective angle of incidence changes. The results however show, especially compared to the ellipsoidal configuration (red curve) that, despite the sensitivity, the spot

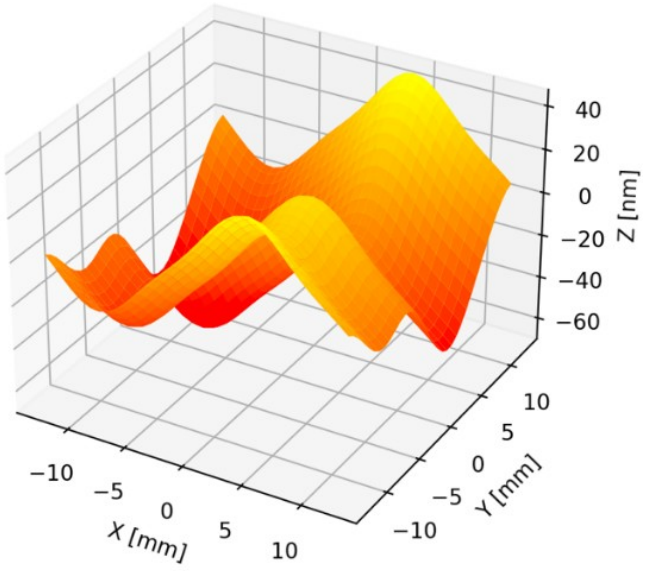


Figure 7.18: Slope error profile on the spherical mirror.

size almost never falls outside the acceptance value for oversampling at the image plane. Actually this sensitivity can be exploited in practice during alignment by monitoring the reflectivity curve of multilayer coatings, which are designed for a specific angle. Roll errors also have a relevant effect on the determination of the spot size. Introducing in the simulation a ±3° misalignment, the beam diameter at the image plane can increase up to 42.7 ± 0.3μm ($RI\%$ = 74.8%) with severe aberrations. However, this effect can be partially compensated by shifting the position of the spherical mirror — and therefore the image plane — by 0.01%. This allows the fulfillment of the oversampling criterion up to ±2° deviations where the beam reaches a uniform intensity distribution across a 15.1μm diameter. Ultimately, thanks to the rotational symmetry of the ideal spherical surface, yaw misalignments are mere rotations and have no effect on the focused spot size. In this sense, the possibility to follow the image plane in a realistic experiment, through the adoption of appropriate in-vacuum automated systems, can turn turning misalignments into degrees of freedom that help optimizing the experimental conditions.

To simulate a more realistic optical element, the analysis was repeated with surface slope errors introduced on the spherical mirror, while keeping the alignment ideal. A profile with an RMS slope error of 5μrad in both the tangential and sagittal directions was chosen, as represents a reasonable value for commercially available optics. The profile,

displayed in Fig. 7.18 was synthesized using the "Height Profile Simulator" widget in ShadowOui: it has a 1″ lateral dimension and $0.75mm$ squared pixels. To obtain a realistic profile, a correlation length, which practically determines how "large" a local peak or valley is defined. Values of $4.5mm$ and $5.5mm$ were arbitrarily chosen in the tangential and sagittal direction respectively. Including surface imperfections, the yaw angle becomes a critical yet useful degree of freedom. As shown in Fig. 7.15f to Fig. 7.15k, rotating the mirror around its normal can be exploited to alter the focusing properties of the optics. The incoming beam indeed interacts with different portions of the imperfect surface containing local "bumps" or "depressions". This allows yaw to be used as an effective fine-tuning tool to optimize the shape and size of the illumination probe. The z-fold provides an average spot size of $11\mu m$ $1/e^2$, achieving spots as small as $6.3\mu m$ $1/e^2$ as in Fig. 7.15k, where the yaw angle is set at 90° compared to the initial condition.

The z-fold is finally simulated to simultaneously include both realistic misalignments and the $5\mu rad$ 2D slope error profile. To rigorously test the robustness of the z-fold, the spherical mirror is subjected to translational and rotational misalignments three times larger than those applied to an ellipsoidal mirror as sketched in Fig. 7.15b. Specifically, the misalignments are: 0.015° for pitch/yaw, 0.15° for roll, and up to 2.3% of the mirror's diameter for translation. The results, shown in Fig. 7.15c and Fig. 7.15d, demonstrate the exceptional stability of the z-fold scheme. Even when subjected to three times more severe errors compared to the ellipsoidal configuration, the system produces a final focused spot with $11\mu m$ $1/e^2$ diameter, comparable to the ellipsoid in terms of size and quality of the beam profile ($13.9\mu m$ $1/e^2$). This is obtained also exploiting the translation of the image plane position by $56mm$ (0.2% with respect to the nominal value), which allows to compensate for beam broadening while retaining highly structured intensity distributions. Taking into account misalignments, yaw and image plane shifting, the z-fold configuration can be considered a highly robust, flexible, and practical solution for a compact XUV ptychography beamline.

7.6 Comparative Simulation Results

To finalize the comparison of the different focusing schemes beyond their geometric robustness, their performances in terms of ptychographic reconstruction speed and image fidelity are also addressed. Four cases are simulated and analyzed:

1. a perfectly aligned ellipsoid with $5\mu rad$ RMS tangential and sagittal slope error. This probe has a $4.6\mu m$ $1/e^2$ mean spot size at the image plane, and it allows to investigate a regime of short exposure times and nearly isotropic illumination characterized by a modest degree of diversity;

2. a misaligned z-fold with $5\mu rad$ RMS slope error on the spherical mirror surface and realistic misalignments applied consistently with the tolerance analysis in section 7.5.6: $x = 0.6mm$, $y = 0.3mm$, $z = 0.3mm$, $pitch = 0.015°$, $roll = 0.15°$, $yaw = 45°$. This probe is obtained by following the shifted image plane from $274.5mm$ to $275.06mm$, obtaining a mean spot size of $11\mu m$ $1/e^2$ ($\sigma = 2.77$) . This probe profile also represents multiple cases where the z-fold alignment and surface imperfections of the optics concur to generate an inhomogeneous beam which still fulfills the oversampling condition;

3. the same z-fold with 90° yaw angle applied, which allows to address a condition where a sufficiently small ($6.3\mu m$ $1/e^2$) yet structured illumination function is present;

4. a perfectly aligned toroidal mirror with $5\mu rad$ RMS tangential and sagittal slope error, including a pinhole to confine the intensity distribution at the image plane. This solution, which possesses a diameter of $10.7\mu m$ $1/e^2$ is a particular instructive case of low flux and aberrated, structured, probe delivery at the image plane.

The comparative ptychographic reconstructions follow a rigorous simulation pipeline, specifically designed to emulate realistic experimental conditions while enabling a consistent and quantitative comparison across the different illumination geometries. First, although the "Plot XY" widget in ShadowOui successfully captures the intensity distribution of the ray-traced probes, the appearance of the spot is granular due to the finite number of rays employed. The spot sometimes results decentered, due to an imperfect alignment onto the detection window and necessitates further preprocessing. To reduce the high-frequency artifacts and simulate a realistic scenario, a Gaussian blurring filter is applied. Subsequently, rigid spatial shifts are introduced in order to center the illumination and mitigate reconstruction artifacts due to proximity to the window's edge.

Since ray tracing does not account for coherence and diffractive effects, the phase of the probes is estimated using the Gerchberg-Saxton algorithm [69] at multiple planes during the propagation from the focusing optics, as displayed in Fig. 7.19a. This analysis

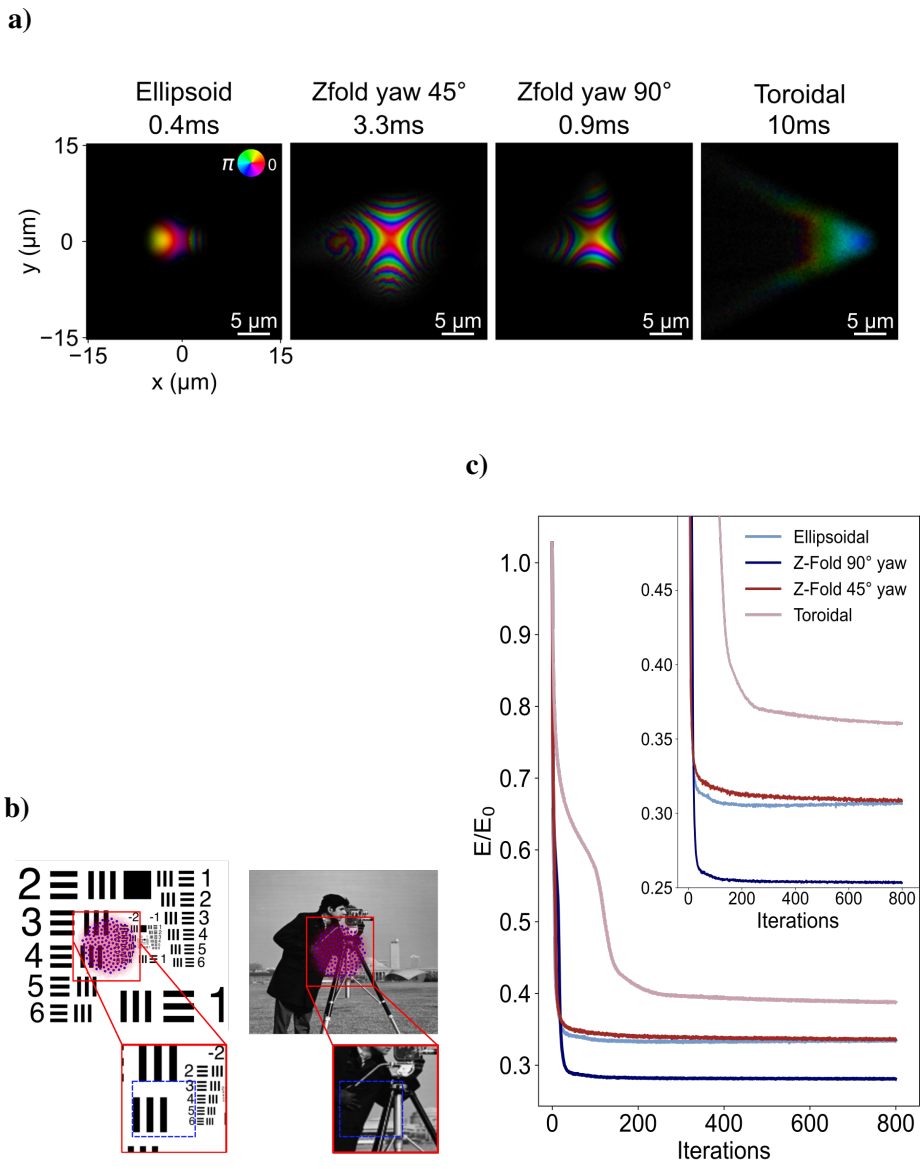


Figure 7.19: (a) Ground truth of the different probes used for the ptychography simulation. The phase of each probe is obtained through the Gerchberg-Saxton algorithm. (b) Ground truth of the object, in amplitude and phase, with the scanning grid following a Fermat spiral. (c) Normalized DRMS error minimization for each focusing scheme.

revealed that the aberrated and astigmatic z-fold beam presents a quadratic phase at the circle of least confusion, which is relevant for reconstruction starting guesses. The object used in the simulation is the synthetic image shown in Fig. 7.19b, composed by the 1951-USAF test pattern served as the amplitude map and the well-known “cameramen” image

Probe	Beam Diameter	Points	Exp. Time	Probe Phase Guess
Ellipse	$4.6\mu m$	280	$0.4ms$	Gaussian
z-fold +45°	$11\mu m$	49	$3.3ms$	Astigmatic
z-fold +90°	$6.3\mu m$	149	$0.9ms$	Astigmatic
Pinholed Toroid	$10.7\mu m$	52	$10ms$	Flattop

Table 7.3: Main parameters of each ptychographic simulation.

to define the phase profile. For all the simulations, the object is defined over a 5096×5096 pixel grid,with no padding. Scanning positions are generated following a Fermat spiral distribution with 70% overlap between adjacent probe positions, ensuring translational symmetry breaking and uniform sampling while minimizing periodic artifacts. A fixed circular scan region with a diameter of $23\mu m$ is maintained across all simulations; however, the number of scan points varies in accordance with the spatial extent of the probe. The number of positions captured in summarized in table 7.3.

The simulated experimental setup is modeled using a custom MATLAB code executing a version of the ePIE. This choice ensures that the conclusions of this analysis remain general and directly applicable to any user approaching ptychography for the first time. It also allows the comparison across focusing geometries, rather than algorithm-specific optimizations. Each probe is scanned across the sample, generating as many diffraction patterns as the number of points in the scanning grid. The virtual detection system acquiring the diffraction patterns accurately matches the specification of the AXIS detector. It mimics a 2048×2048 chip with $11\mu m$ square pixels, positioned $26mm$ away from the sample plane. These parameters yield a numerical aperture of 0.4, enabling a theoretical in-plane resolution of approximately $15nm$ when operating at a photon energy of $96.5eV$ (corresponding to $12.9nm$). A comprehensive noise model, shown in Fig. 7.20, is then applied to simulate realistic conditions of the detectior during experiments. This model includes several components: Poisson-distributed shot noise (with average μ_p and variance σ_p^2), camera's quantum efficiency ($\eta = 0.99$), and a composite dark noise (σ_d) derived from both the readout noise ($1.5e^-$) and dark current ($2.17e^-/s/pix$ at $-10°C$) from the manufacturer, modeled using Gaussian statistics. Fixed-pattern noise, pixel non-uniformities, and hot pixels are added using an experimentally measured AXIS detector background data. The analog-to-digital unit (ADU) conversion is simulated using a sensitivity factor $K = 2.18ADU/e^-$, and quantization noise from the 16-bit digitization process is also included. ADU values are clipped at 65536 to reflect saturation limits.

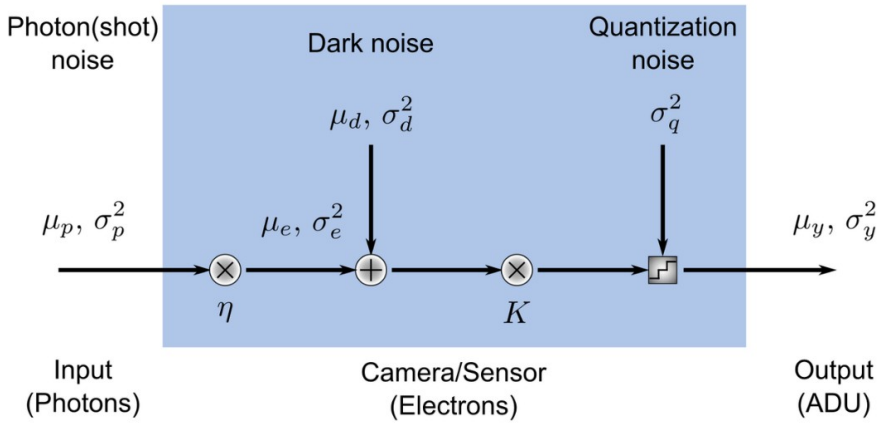


Figure 7.20: Realistic implementation of the CMOS camera pixel, affected by multiple noise sources. The camera takes a given number of photons, with mean μ_p and variance σ_p^2. The quantum efficiency η is used to convert the photon distribution to an electron distribution with characteristic values μ_e and σ_e^2, upon which a normally distributed dark noise is added. The number of electron is then converted to digital units by means of the camera's sensitivity K and the uncertainty based on the bit depth is added as quantization noise σ_q^2. The output in digital unit is ultimately obtained, with mean values μ_y and variance σ_y^2.

The exposure time of the camera is chosen to be probe-dependent, in order to allow all the illumination functions to achieve comparable signal-to-noise ratios (SNR) and to properly fill the entire dynamic range of the detector. This resulted in the exposure times in table 7.3. Finally, prior to being processed by the reconstruction algorithm, all simulated datasets undergo identical background subtraction and noise thresholding procedures to standardize the input conditions. The ePIE is initialized with the probe guesses shown in Fig. 7.21. To avoid any favouring or penalization between the different probes, the phase profile of each guess is chosen to be close to the ground truth (Fig. 7.19b) used to simulate the diffraction patterns. The algorithm later follows the established workflow described in 3.4 but makes use of two different update parameters for object and probe, respectively $\alpha = 0.9$ and $\beta = 0.7$.

The convergence and reconstruction fidelity of the algorithm is monitored using the Diffraction Root Mean Square (DRMS) error, which provides a measure of the reconstruction fidelity for each probe and is computed at each iteration. Fig. 7.19c reports the evolution of the normalized error metric E/E_0, defined as the average squared norm of the update factor over all diffraction patterns and normalized to its initial value, as a function

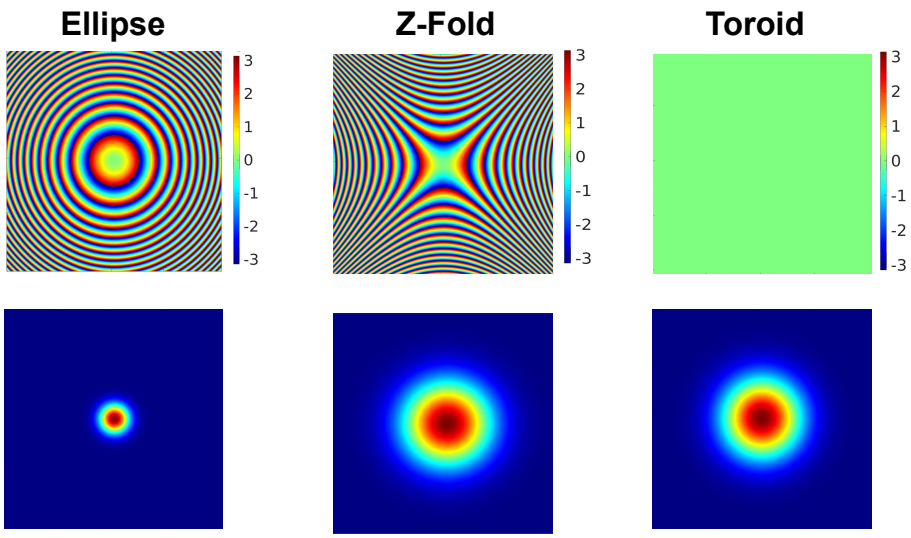


Figure 7.21: Initial probe guesses for the ePIE reconstruction algorithm, with non-penalizing phase profiles.

of the number of iterations. The plot indicates that the ellipsoidal configuration and the z-fold with 45° yaw converge fast (in terms of iteration) with a monotonic trend, both reaching a residual error of approximately 0.31 after 400 iterations, mutually differing from each other of approximately 1.6%. This configuration of the z-fold, despite its larger spot size and lower flux compared to the ellipsoid, reaches the same residual error in less time, spanning the field of view with fewer scan points. When the yaw is increased to 90°, the performances of the z-fold configuration improve, achieving the lowest residual value. The toroidal geometry underperforms in the error minimization and displays a slower convergence, with the residual error stabilizing above 0.36 and showing a characteristic shoulder in the early iterations, a signature of poor correction efficiency. Consequently, the toroidal mirror requires a larger number of iterations to reach reconstruction quality comparable to the other cases. This confirms that such geometry is not optimal for noisy datasets, and it is consistent with the lower photon flux due to operation with pinhole confinement, which demands longer exposure times. Considering reconstruction time, the ellipsoid reach full convergence slower than the z-fold, due to the larger data volume. The z-fold achieves the same residual error in less time and, when yaw is used to exploit the height error profile of the mirror, lower residual errors can be reached in less time. Ptychographic performance was assessed in terms of resolution using the single-image Fourier Ring Correlation (FRC) with random splitting [153, 154] to provide a robust

spatial resolution metric to all the focusing geometries. This is defined as defined as the correlation between the Fourier amplitudes of two independent datasets $o_1(k)$ and $o_2(k)$:

$$FRC(k) = \frac{\sum_{k_j \in k} o_1(k_i) o_2^*(k_i)}{\sqrt{\sum_{k_j \in k} |o_1(k)|^2 \sum_{k_j \in k} |o_2(k)|^2}}, \tag{7.17}$$

where k is the frequency-space coordinate. The FRC expresses the spatial frequency content that is retrieved in the reconstruction, providing a criterion for estimating the achievable spatial resolution, which is evaluated through the standard 1-bit and $1/2$-bit thresholds. The results are displayed in Fig. 7.22b: the reconstructed image for each configuration is evaluated at three different termination criteria. These criteria are defined as follows: (i) 300 iterations for approximate convergence, that is when convergence is fairly reached for all probes, avoiding high computational load; (ii) 800 iterations for extended convergence, chosen when the computational resources are sufficient to drive the full reconstruction to full convergence; (iii) a criterion based on the stabilization of the DRMS error below $\epsilon = 3e^{-3}$ over five consecutive iterations, set according to the available time or computational power of the operator driving the reconstruction. The results indicate that similar resolution performances, measured as the highest spatial frequency captured at 1-bit and $1/2$-bit thresholds, are reached. The resolution is indeed ultimately limited by the signal-to-noise ratio (SNR), which is identical. A closer inspection reveals that the z-fold 45° configuration reaches a slightly higher cut-off, corresponding to a spatial frequency around $0.2 \times 10^7 m^{-1}$, i.e. a resolution of $0.5\mu m$. However, this difference remains within the intrinsic uncertainty of the adopted FRC method. Moreover, despite the toroid underperforms in the error minimization, yet it does not lose the recoverable spatial frequency content in the final reconstructed image. Despite the equivalence in the final resolution results, it shall be noted that for all criteria, the computational demand of each probe configuration differs. In fact, during a ptychographic reconstruction, the computational demand is proportional to the total number of processed patterns (P), which is the product of the number of iterations (M_{iter}) and the number of diffraction patterns captured during the scan ($N_{patterns}$). Since the FOV is kept fixed with an overall diameter of $23\mu m$, probes with smaller spot sizes require a higher number of diffraction patterns to cover the same area. A higher number of diffraction patterns indeed requires more forward and backward FFTs, carried out at each scan position and resulting in a higher computational cost (see table 7.4). Focusing on the third convergence criterion only,

Probe	P @ $\epsilon < 3e^{-3}$	P @ $M_{iter} = 300$	P @ $M_{iter} = 800$
Ellipse	$280 \times 48 = 13440$	$280 \times 300 = 84000$	$280 \times 800 = 224000$
z-fold +45°	$49 \times 50 = 2450$	$49 \times 300 = 14700$	$49 \times 800 = 39200$
z-fold +90°	$149 \times 60 = 8940$	$149 \times 300 = 44700$	$149 \times 800 = 119200$
Pinholed Toroid	$52 \times 54 = 2808$	$52 \times 300 = 15600$	$52 \times 800 = 41600$

Table 7.4: Computational demand for each probe under the three convergence criteria.

the z-fold 45° shows the highest computational advantage with respect to the ellipsoidal counterpart, reducing the number of processed patterns by 81.8%, followed by the toroidal probe with a 79.1% reduction and then the z-fold 90° with a 33.5% reduction. A similar trend is observed for the other two criteria. This confirms that, the z-fold 45° results as the most computationally efficient configuration. As such, it represents a suitable choice for pump-probe measurements and real-time ptychography, provided that the output image quality remains similar to the other cases.

The Michelson contrast is another metric used to assess the quality of the reconstructed image and compare the performances of the different illumination functions. This method is shown in Fig. 7.22a: from the reconstructed image, a uniform portion with sharp features extracted. This section is shown in amplitude (top) and phase (bottom) at each convergence criterion (row) for each probe (column). To compute the contrast C, both amplitude or phase images may be used, however the amplitude one most clearly highlights the differences and therefore is chosen. To obtain C, a lineout is extracted and the following formula is used:

$$C = \frac{A_{max} - A_{min}}{A_{max} + A_{min}}. \tag{7.18}$$

Here A_{max} and A_{min} are the the local maxima and minima of the lineouts within the orange areas highlighted on the right side of Fig. 7.22a. This quantity expresses how efficiently the reconstruction reproduces the amplitude modulations in the sample, and was used it to capture the sample lines visibility and the overall information content recovered by the algorithm. Even though its definition derives from interferometric studies on optical coherence and is now widely used as the visibility parameter to characterize spatial and temporal coherence in illumination functions [115]. The summary of the results is expressed in Fig. 7.22c. Using the Michelson contrast formulation as a metric, the z-fold focusing scheme consistently provides the highest contrast across all configurations, for every convergence criterion, and regardless of the degree of yaw misalignment. Also in

this case, the yaw can be exploited as a degree of freedom to enhance the contrast of the image, especially when rapid convergence is adopted as a termination criterion. The z-fold outperforms the other geometries thanks to the structured profile, which increases variations in the diffraction patterns, supporting the deconvolution process. The toroidal geometry remains below the other solutions for the ϵ-based criterion as convergence is not reached. However it surpasses the ellipsoidal configuration when quick convergence is targeted. achieved. Indeed, the more heterogeneous profiles generate exit waves that differ more between scan positions. This diversity supports a more efficient redistribution of object and probe information across iterations, stabilizing contrast and preventing the drop observed with the ellipsoidal illumination. At long convergence instead, the algorithm tries to fine-tune the reconstruction which may already be stable. In some cases, such as the z-fold, this may lead to lower contrast compared to the quick convergence because of induced amplitude fluctuations.

To conclude, because the z-fold attains higher contrast in less time while maintaining the same resolution as other configurations, it provides structural information more rapidly. This architecture also provides the best trade-off of speed, robustness to misalignments, and reconstruction quality for ultrafast XUV ptychography. These results indeed support the choice of the z-fold layout as the preferred operational choice for time-resolved XUV ptychography in our beamline.

7.7 Improved Z-fold Design

Starting from the preliminary ray tracing simulations, which identified the z-fold as the most appropriate layout for the probe synthesis, the design of the microscope has been progressively refined in ShadowOui to optimize both throughput and resilience to various perturbative factors. These factors include variations in source size, angular divergence, and surface figure errors in the optical components.

7.7.1 Source and Updated Distances

As anticipated in section 7.5.2, the HHG source is not firmly defined in terms of size and angular aperture, but rather spans $30 - 50\mu m$ $1/e^2$ in intensity diameter and $0.5 - 2mrad$ FWHM divergence. Therefore, the ptychography beamline has been benchmarked against the worst-case scenario, that practically means satisfying the oversampling requirement at

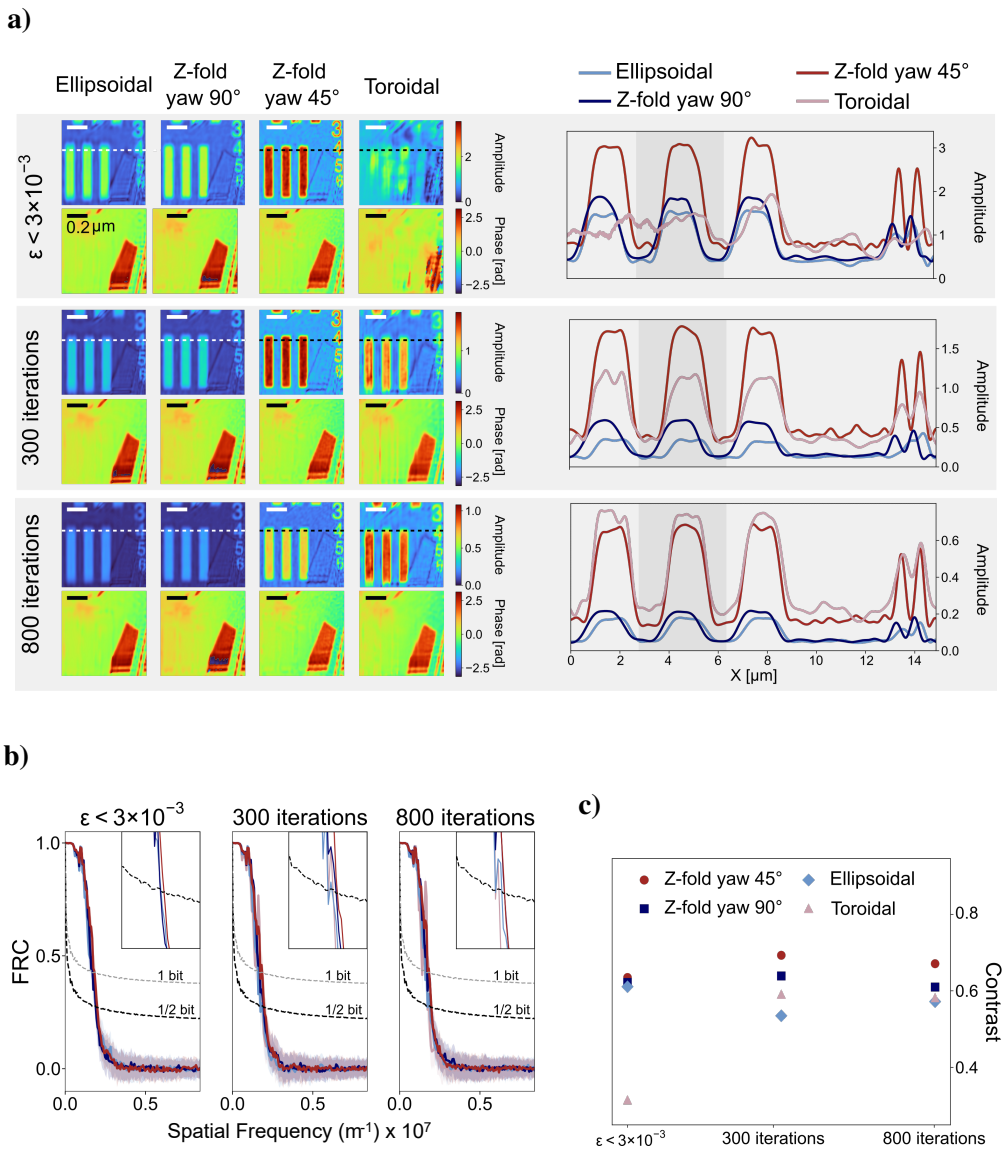


Figure 7.22: (a) Lineouts of the reconstructed amplitude image at different termination criteria for each focusing geometry scheme. (b) Results of FRC for the multiple geometries at different termination criteria. The resolution is measured at 1-bit and 1/2-bit thresholds. (c) The calculated contrast for each focusing geometry and termination criteria.

Optical Element 1	Optical Element 2	Distance [mm]
Source Plane	Rej 1	592.95
Rej 1	Rej 2	409.04
Rej 2	Filter	227
Filter	FMM	1432.76
FMM	SMM	200
SMM	Image Plane	~300

Table 7.5: Beam path in the z-fold delivery scheme simulated for the probe arm of the Ultrafast XUV beamline.

the sample plane when:

- the operating wavelength is $12.9nm$, which corresponds to the optimized emission in He atmosphere with the HHG driver at $785nm$ (see section 7.7.3);
- the sample-to-detector distance is fixed at $26mm$, that allows the maximum N.A., thereby the maximum resolution capability;
- the source size is defined as $50\mu m$ $1/e^2$ wide in diameter, with a FWHM divergence of $2mrad$, implemented in ShadowOui as a Gaussian source with $S_\sigma = 12.5\mu m$ and $Div_\sigma = 0.849mrad$.

This requires specific tailoring of the z-fold design in terms of distances, sizes, offsets and substrate features in order to guarantee a spot with diameter

$$D < \frac{\lambda z}{\sigma p} = 15.25\mu m, \tag{7.19}$$

where $\sigma = 2$ and the pixel size of the AXIS-SXR detector is equal to $p = 11\mu m$. In practice, however, an oversampling (> 4) is desired, to provide better reconstruction robustness under realistic conditions.

In this design phase, the simulation is conducted with 7 million rays to increase the statistics during propagation. The distances are implemented by averaging the values obtained using the 3D model of the beamline and with the measuring tape. The values are summarized in table 7.5. After generation, the rays travel towards the two rejectors at 6° grazing angle of incidence and subsequently to the filter. Due to the high divergence of the beam, the filter cuts approximately 6% of the input XUV photons. In the simulation

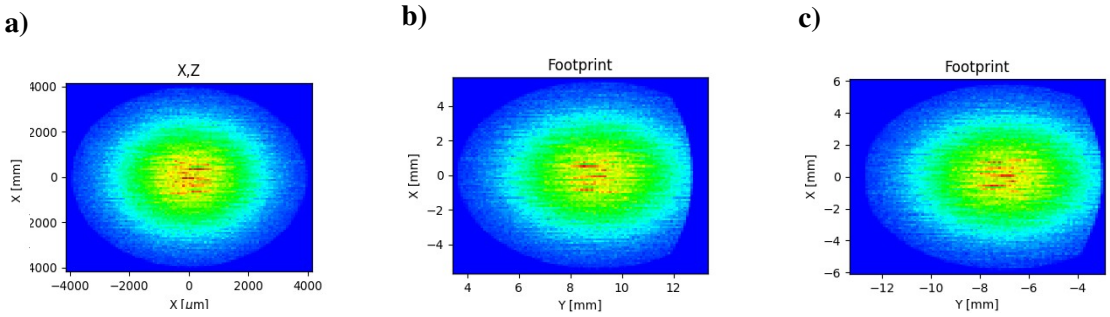


Figure 7.23: Beam appearance at (a) the intermediate plane between the filter and FMM, (b) at the FMM surface and (c) at SMM surface.

this is indicated by the sharp edge around the beam at the intermediate plane between the filter and FMM, shown in Fig. 7.23a. Upon propagation, the beam impinges on the FMM with a diameter of approximately $D_{XUV} \sim 9mm$ $1/e^2$. To simultaneously minimize coma aberrations in the focal point, prevent beam clipping at the SMM, and ensure practical feasibility of the setup, the off-axis geometry was slightly adjusted, as illustrated in Fig. 7.24. These adjustments are determined by satisfying the following geometrical condition, which ensures a proper balance of distances so that the SMM does not block the direct transmission of the beam toward the FMM, while maintaining a manageable offset of approximately $JOG \sim 4mm$:

$$JOG - (R_{SMM} - OFFSET_{SMM}) \cos\theta \leq d \sin(2\theta) - \frac{D_{XUV}}{2}. \tag{7.20}$$

Here, the angle of incidence on both mirrors is $\theta = 2°$, using the pole as a reference. The offset is set to $9mm$ and $7mm$ from the pole, respectively for the FMM and SMM. The separation distance between both optical elements is consistent with earlier simulations ($d = 200mm$) and the image plane is preliminary located at $\sim 300mm$ from the SMM. This configuration provides a geometric demagnification factor of 9.6, ensures a practical spacing between the FMM and the sample, and leaves sufficient room for the potential insertion of a pinhole to confine the illumination function. Considering the distance of the source, to obtain an image plane $300mm$-away from the SMM, a ROC of $\sim 540mm$ is required. This is calculated by ShadowOui when solving for the mirror equation. This value implies the optic to be customized, but it is not a particular issue since surface errors also require a particular fine-tuning (see section 7.7.2). Ultimately, the positions of the

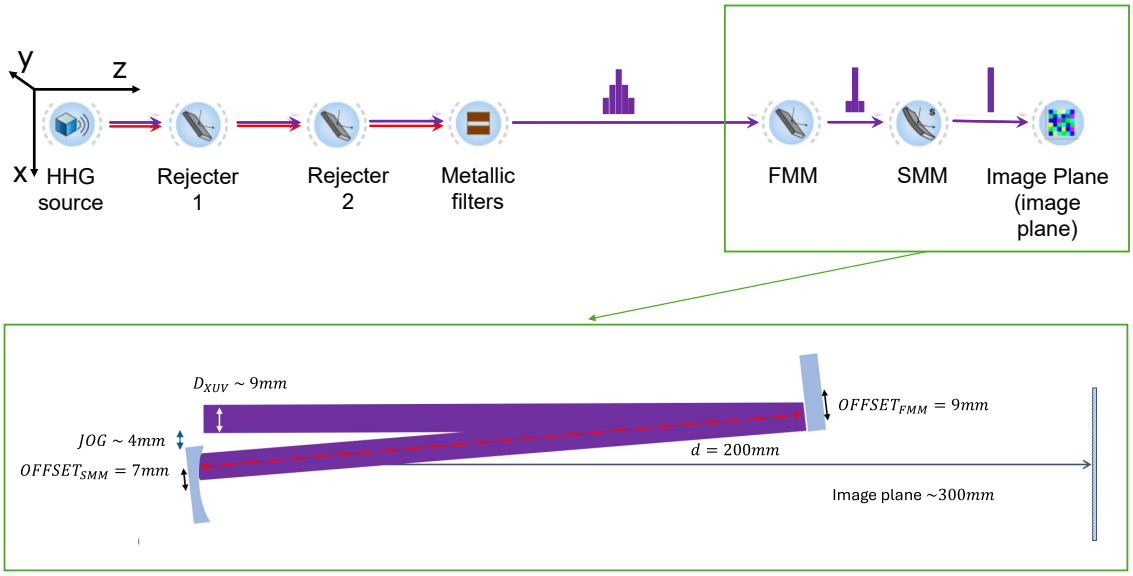


Figure 7.24: Sketch of the beam propagation with ShadowOui widgets and a detail on the specific z-fold scheme designed for the Ultrafast XUV Ptychographic microscope. The XUV beam is indicated in purple, and initially copropagates with the driver, which is later removed by the combination of rejectors and metallic filters, Consecutively, the remaining harmonic comb is filtered by the application of multilayers in the z-fold and finally reaches the sample plane. The z-fold layout presents different offsets for the spherical and flat multilayer mirrors, a distance and a jog which allow to avoid beam clipping while maintaining quasi-normal incidence.

FMM and SMM lead to an additional reduction of ~4% to the total number of transmitted rays, which can be considered negligible.

7.7.2 Substrate Specifications of XUV Mirrors

To ensure full compatibility with the stringent requirements of the focusing geometry, particular attention is devoted to the definition of the substrate specifications for both the FMM and SMM. All substrates are manufactured with circular cross sections with nominal diameter of 25.4mm and a standard thickness of 6.35 ± 0.25mm, with a usable optical aperture of at least 24mm (~ 96% of the clear aperture). These geometric parameters are necessary to maintain compatibility with the offset positions and maximize the effective area for the reflective multilayer coatings. For the spherical mirror, the substrate requires a nominal radius of curvature of 540mm, with maximum fabrication error of ±2%. The angle of incidence at the beam interaction point must be in the range 2.74° ± 1°, which

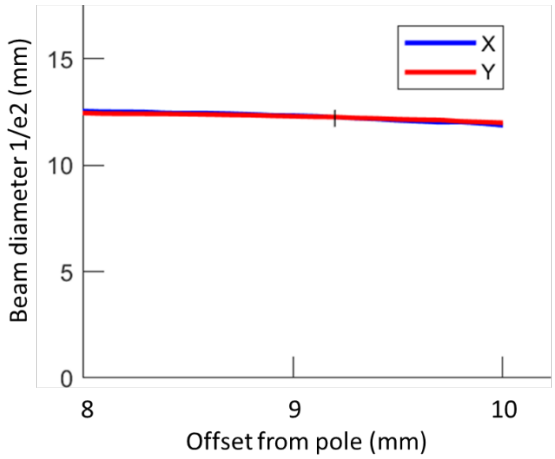


Figure 7.25: Beam diameter as a function of FMM offset. A continuous reduction of the diameter is observed in both transverse beam directions, due to the semicircular clipping induced by the mirror's substrate.

was evaluated considering the curvature of the surface and the lateral offset of $7mm$ from the center of the optics. The flat mirror substrate does not imply an ideal plane, but rather a finite spherical curvature, modeled in ray tracing simulations using a "Spherical Mirror" widget instead of a "Plane Mirror" one. In this framework, a value of $2km$ is defined as the nominal radius of curvature for the flat mirrors, with an asymmetric tolerance of $[-1km, +\infty]$. It was indeed observed that for values of curvature ranging from $1km$ to infinity, the focal shift introduced at the sample plane remained sub-millimetric and did not significantly affect the size of the beam or the quality of the wavefront. Therefore, specifying a large but finite radius ensures the manufacturability without compromising optical performance. The FMM is operated at a nominal incidence angle of $2° \pm 1°$, with the beam impinging on a position $9mm$-away from the pole, as shown in Fig. 7.24. As anticipated in section 7.7.1, the offset positions provide a certain flexibility to the z-fold when the source is in the worst possible conditions. However they have an impact on the delivery of the beam at the sample plane. Considering the flat mirror, an increase in the offset from $8mm$ to $10mm$, as shown in Fig. 7.25, leads to a progressive clipping of the beam at the edges, resulting in a reduction of its diameter at the sample plane of no more than $1\mu m$, with no significant reduction in flux. For the spherical mirror, variations in the offset between $6.5mm$ and $7.5mm$ induced negligible changes in the resulting diameter, confirming that the entire footprint of the beam hits the surface of the mirror. Even though

these results, especially for the flat mirror, suggest that a smaller offset is beneficial,it is less suitable for the tight z-fold geometry employed.

7.7.3 Multilayer Coating Specifications

The quasi-normal incidence design of the z-fold requires multilayers (see section 1.3.3) to be applied on the surface of the mirrors. To define the specifications of the multilayer coatings, the emission characteristics of the harmonic source were taken into account. The multilayer was designed to operate with s-polarized light, as required by the geometry of the rejectors. In fact, to efficiently suppress the fundamental radiation, the polarization of the light emerging from the XUUS^{TM} system is oriented parallel to the normal of the optical table and consequently, the coherently upconverted harmonics share the same polarization state. In the frequency domain, the HHG spectrum is composed by discrete lines referenced to the central wavelength of the driver. In the case of RAEA^{TM}, a consistently observed spectral figure is shown in Fig. 6.8, and the corresponding XUV spectra from the XUUS^{TM} are shown in Fig. 6.9. For a central wavelength of $\lambda = 785nm$, the emission with the highest photon-efficiency was calculated to be at $12.9nm$ $(96.5eV)$ and $29.1nm$ $(42.6eV)$, respectively the 61^{st} and 27^{th} harmonics in He and Ar atmospheres. The calculation took into account the characterization carried out by the supplier using the driver at $790nm$ and assumed a linear shift of the harmonic frequencies upon a slight change of the input wavelength, according to

$$\lambda_q = \lambda_0/q. \tag{7.21}$$

Here q is the harmonic order and λ_0 the wavelength of the fundamental light. Therefore, two types of multilayers, centered at $12.9nm$ $(96.5eV)$ and $29.1nm$ $(42.6eV)$ are required to be compatible with the different emission spectra in the two gases.

In addition to the "exact" central wavelength (or energy) of the multilayers, particular attention was given to the definition of the peak energy tolerance. The RAEA^{TM} can, in principle, provide sufficient power for HHG when emitting in the range $770-800nm$, with a consecutive shifting of the most prominent peak of the harmonic comb. Applying the aforementioned equation, this corresponds to maximum values of $0.55nm$ (or $0.8eV$) and $0.25nm$ (or $1.8eV$) shifts for Ar and He combs, respectively, as indicated in Fig. 7.26. These values have been considered preliminary for peak energy tolerances. However, it must be noted that the natural drift of the wavelength of the central driver rarely exceeds the $\pm 5nm$ range in our build, therefore the realistic shift of the XUV comb can be essentially confined

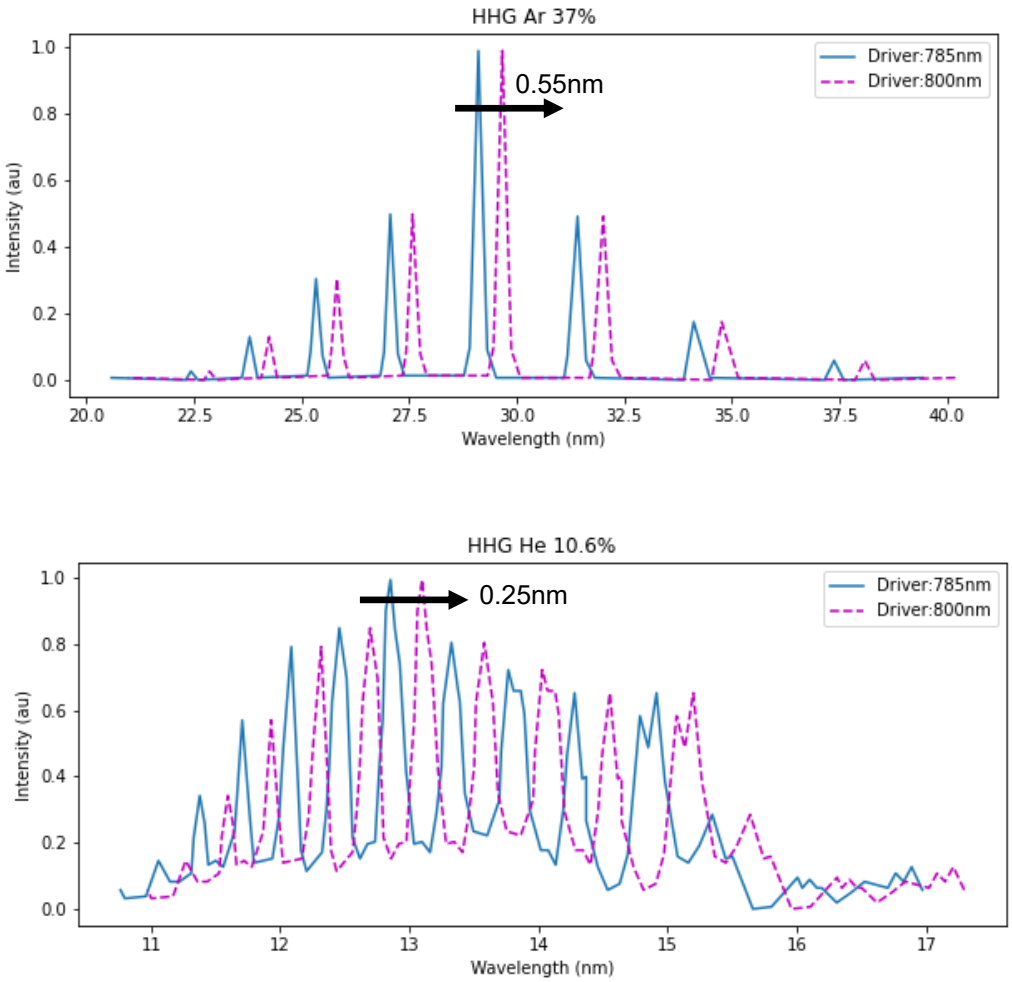


Figure 7.26: Maximum linear wavelength shifts acquired by the (top) Ar generated comb when the driver is changed from 785nm to 800nm and (bottom) He generated comb when the driver is changed from 785nm to 800nm.

to 0.2nm (or 0.3eV) and 0.1nm (or 0.6eV) for Ar and He atmospheres, respectively.

To define the passband of the two multilayer coatings, the linewidth of the harmonics was considered in first instance. The most intense energy peaks in Ar atmosphere has a linewidth of 0.22nm (0.3eV) FWHM, while in He this is approximately 0.18nm (1.3eV) FWHM. These values pose a lower limit to the passband required for the entire multilayer stacks. The higher limit is instead set by the separation between the harmonic teeth. Indeed, even if nowadays iterative ptychographic algorithms can resolve multi-energetic beams using multi-mode decomposition, for a more robust and quick reconstruction a single mode is highly preferred. Therefore, by setting the desired bandwidth equal to the

frequency separation, the spectral purity is preserved. The specified passband is indicated by the red lines in Fig. 6.9 and corresponds to $2.3nm$ ($3.1eV$) at $12.9nm$ ($42.6eV$) and $0.4nm$ ($3.04eV$) at $29.1nm$ ($96.5eV$). As for the peak energy, the tolerances on the passband of the coatings have been defined as well. However, the estimation of the final values have been carried out upon exchanging information and receiving preliminary reflectivity profiles from world leading manufacturers NTT-AT and SESO Thales. The passband tolerance shall, in principle, be as small as possible. If excessive broadening or narrowing of the bandwidth of the multilayers is combined either with inaccuracies in the position of the main energy peak or shifts in the frequency of the driving laser, inefficient filtering or relevant flux reduction can take place. Additionally, due to the implementation of two multilayer mirrors in the z-fold, any narrowing in the bandpass of each mirror leads to a cumulative reduction of the total spectral bandwidth.

NTT-AT proposed bilayer coatings based on SiC/Mg and Mo/Si respectively for the lowest and highest energy required in our experimental setup. The SiC/Mg coating provides a peak reflectivity of 49% and is identically designed for the flat and the spherical mirrors, because their AOI difference (2° vs 2.74°) is negligible. The multilayer period is nominally $14.6nm$-thick and the bandwidth equals $2.1eV$ FWHM, and is therefore narrower than the peak-to-peak distance in the Ar spectrum. For this reason, in order to avoid the passband of the multilayer to fall within two comb lines the supplier agreed to manufacture the coating with a tolerance of $\pm 0.3eV$ — corresponding to a bilayer variation of only ±0.7% — in the position of the highest reflectivity value. This guarantees operations for limited but realistic changes in the driver up to $790nm$, and avoids high flux reductions. From previous coating runs, the supplier expected a bandwidth tolerance of approximately $\pm 0.2eV$, which is well suited for our purposes as shown in the worst-case scenario simulated in Fig. 7.27b. Here, the harmonic spectrum at $790nm$ was overlayed with the cumulative reflectivity curve of the multilayers, possessing both a $\pm 0.3eV$ shift and a FWHM of $1.9eV$. The desired operative condition is instead shown in Fig. 7.27a.

The Mo/Si coatings used to reflect and filter $96.5eV$ s-polarized XUV radiation imply identical considerations. The reflectivity of the multilayer is estimated ab-initio to 56%, with a peak energy accuracy of $\pm 0.3eV$, corresponding to a ±0.3% accuracy of the d-period. Despite the reflectivity profile has a bandwidth of $2.5eV$, thus lower than the separation between the odd harmonics in the HHG spectrum, the simulations suggest proper filtering and flux reduction of $\sim$ 50% even in shifted driver conditions, as illustrated in Fig. 7.28b.

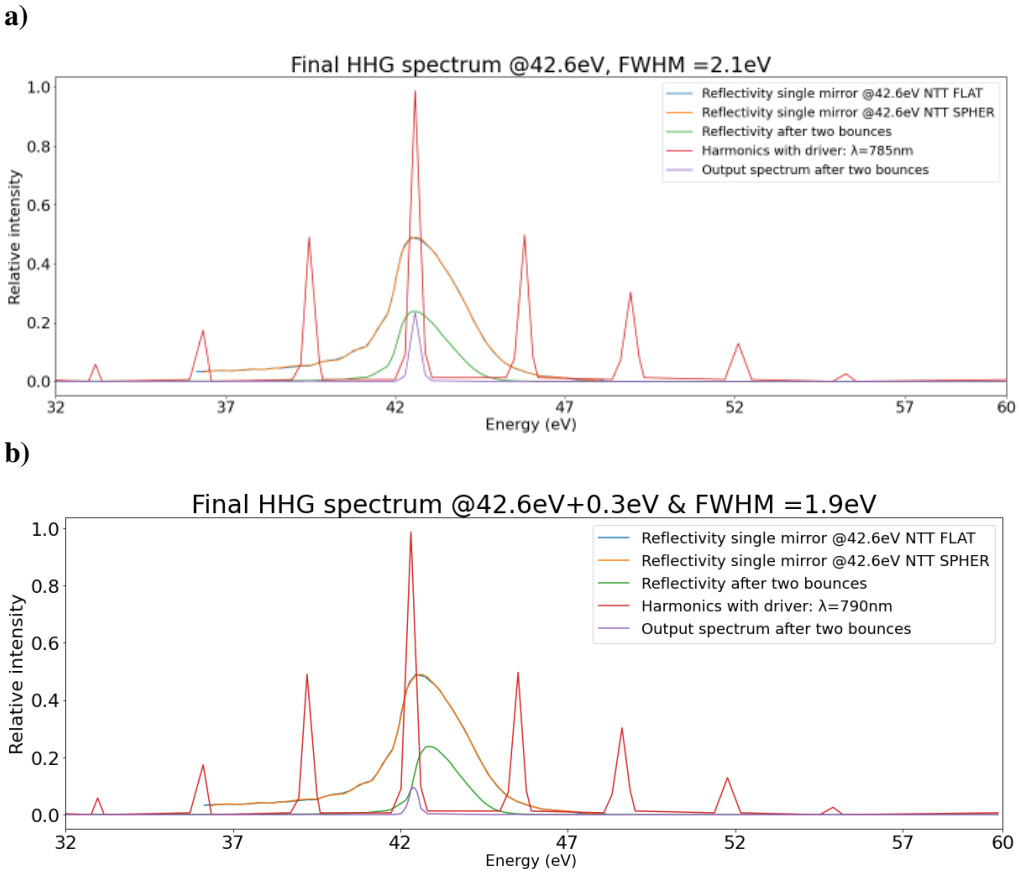


Figure 7.27: Spectral content of the low energy XUV beam after the bouncing off the NTT-AT multilayer mirrors couple. (a) The XUUS spectrum at $42.6eV$ is overlayed with the resulting green reflectivity curve from the two SiC/Mg coatings with $2.3eV$ bandpass. The resulting curve is shown in purple. (b) The spectrum shifted by $0.3eV$, corresponding to a driver at $790nm$ is overlayed with a narrower cumulative reflectivity curve, due to the passband of the multilayers being $1.9eV$ wide. The result is highlighted in purple.

SESO Thales proposed trilayer coatings based on Al/Mo/SiC for low energy, and bilayer stacks of Mo/Si for higher one. Compared to NTT-AT, the specifications were provided in wavelength units rather than energies. For filtering at $29.1nm$, the estimated reflectivity for a single multilayer exceeded 43% and is minimally affected by a $\pm 1°$ variation of the angle of incidence, compatible for both flat and spherical mirrors in the z-fold scheme. With respect to the reflectivity profile proposed by NTT-AT, the bandwidth is larger and can be manufactured to cope with with the requirement of $2.3nm$ ($\sim 3eV$ at $42.6eV$) of interharmonic distance, allowing for less critical operations even in case of shifted frequency of the driver. A $\pm 0.55nm$ tolerance in the peak energy was estimated

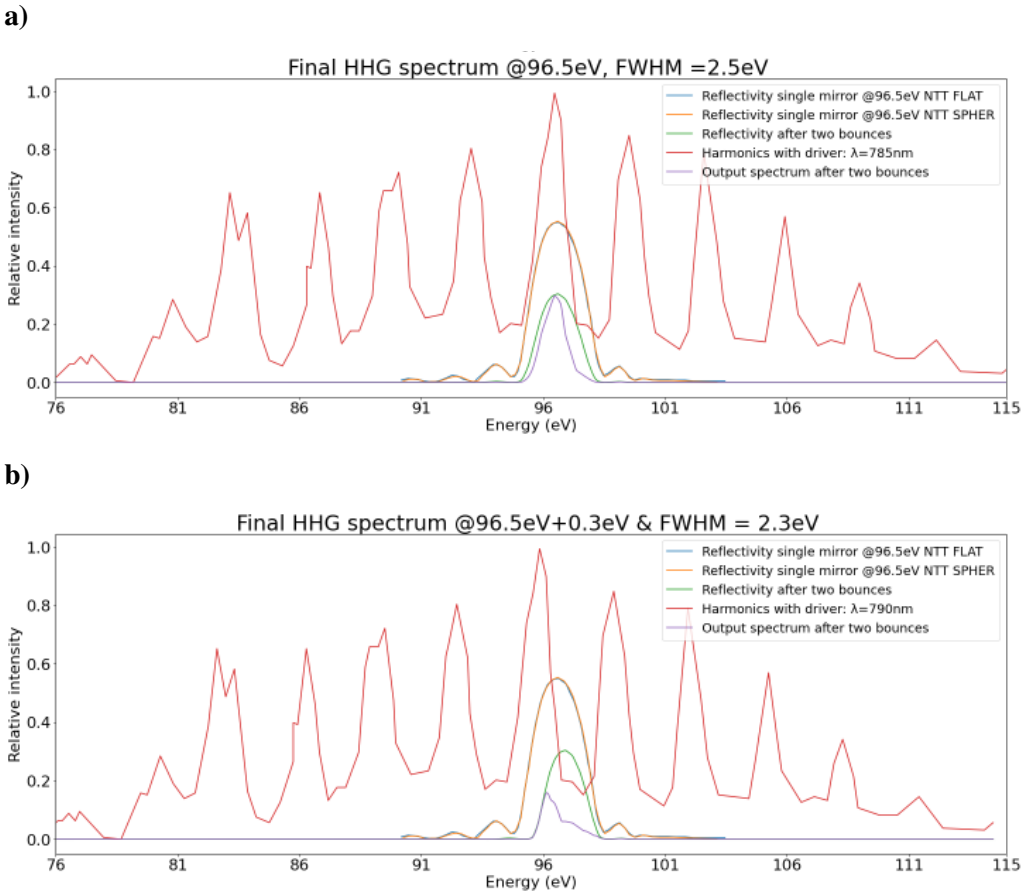


Figure 7.28: Spectral content of the highly energetic XUV beam after the bouncing off bouncing off the NTT-AT multilayer mirrors couple. (a) The XUUS spectrum at $96.5V$ is overlayed with the resulting reflectivity curve from the two Mo/Si coatings with $2.7eV$ bandpass. The resulting curve is shown in output is shown in purple. (b) The spectrum shifted by $0.3eV$, corresponding to a driver at $790nm$ is overlayed with a narrower cumulative reflectivity curve, with a passband $1.9eV$ wide. The result is highlighted in purple.

to be feasible to manufacture, however, building upon the experience of NTT-AT, this was agreed to $\pm 0.2nm$ ($\pm 0.3eV$). The same value have was considered for bandwidth tolerance, which allows, also in the worst-case scenario, to be operative and select the single frequency with enough flux. A similar scenario is valid for $12.9nm$ radiation: both the accuracy of the reflectivity peak position and the passband were defined to be in the $\pm 0.3eV$ ($0.1nm$) range, at the current central wavelength. The expected reflectivity curves, for low and high energy emission are plotted in Fig. 7.30 and Fig. 7.29 in the nominal and worst case scenarios.

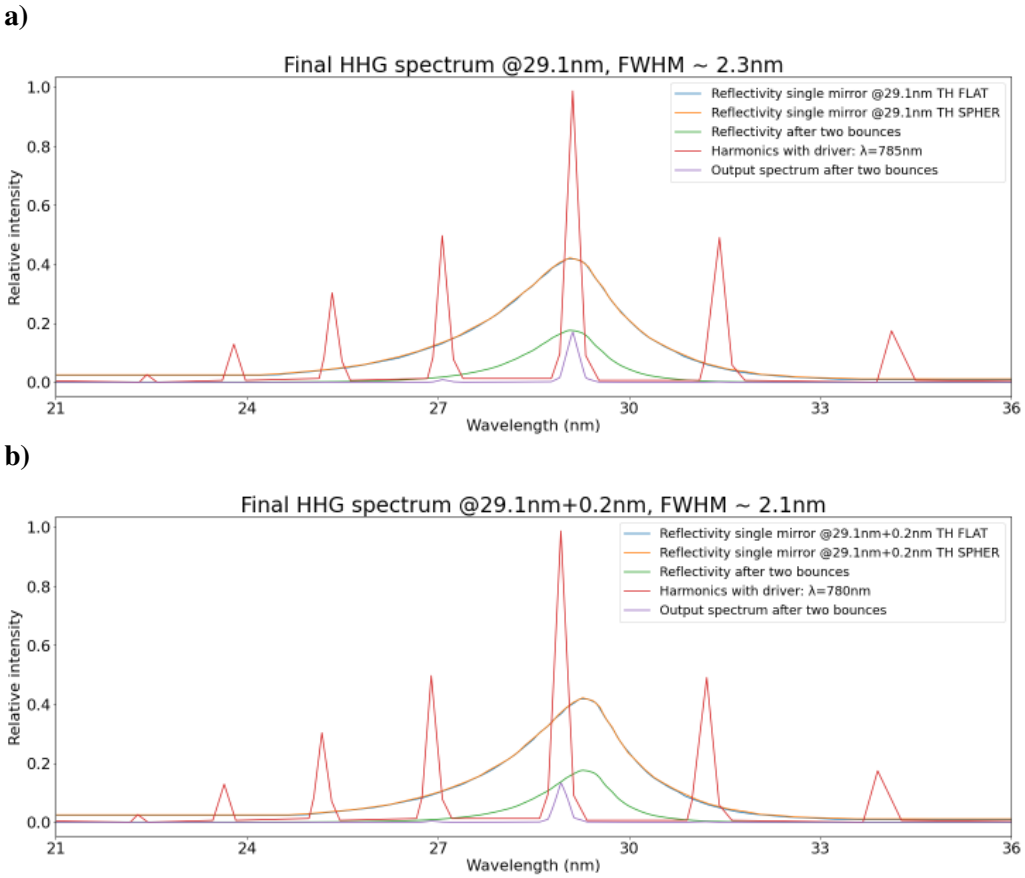
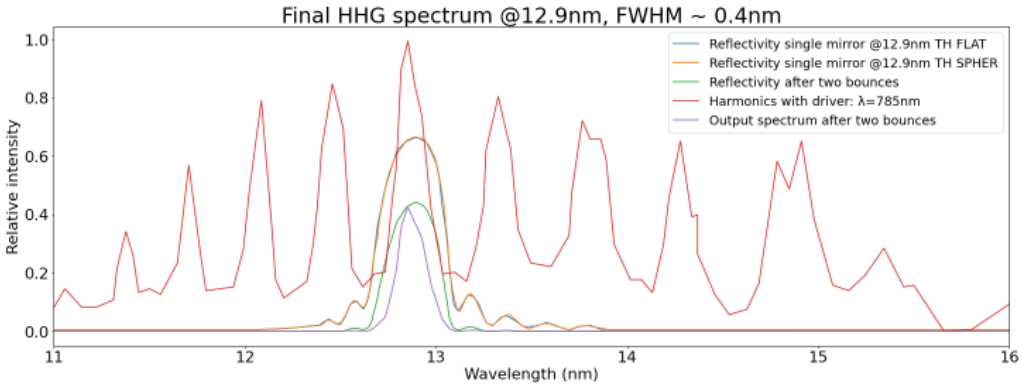


Figure 7.29: Spectral content of the XUV beam after bouncing off the SESO multilayer mirrors couple compatible with Ar-based emission. (a) The XUUS spectrum at 29.1nm is overlayed with the resulting green reflectivity curve from the two Al/Mo/Si coatings with 2.3nm bandpass. The resulting curve is shown in purple. (b) The spectrum shifted by 0.2nm, corresponding to a driver at 790nm is overlayed with a narrower cumulative reflectivity curve of the multilayer. The result is highlighted in purple.

Once the harmonic frequency is isolated, it is worth investigating the effect that multilayer mirrors have on the temporal duration of the pulse. In such a configuration, the temporal properties of the filtered radiation are determined by the interplay between the global temporal envelope of the pulse and the GDD of the multilayer mirrors. Given a driving laser pulse duration of $\tau_{\text{driver}} \simeq 35.6fs$, the HHG emission process is inherently confined within this temporal window. Consequently, the temporal envelope of the selected radiation remains essentially governed by the driver ($\tau_{\text{env}} \approx 35.6fs$), regardless of the specific harmonic isolated by the multilayer pairs (centered at 42.6eV and 96.5eV, respectively). The potential temporal broadening induced by the optics is quantified

a)



b)

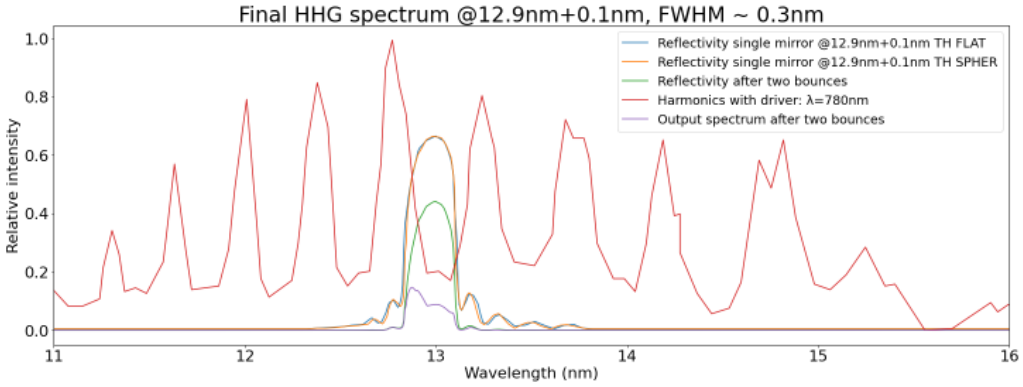


Figure 7.30: Spectral content of the XUV beam after bouncing off the SESO multilayer mirrors couple compatible with He-based emission. (a) The XUUS spectrum at 12.9nm is overlayed with the resulting reflectivity curve from the two Mo/Si coatings with 0.4nm bandpass. The resulting curve is shown in output is shown in purple. (b) The spectrum shifted by 0.1nm, corresponding to a driver at 790nm is overlayed with a narrower cumulative reflectivity curve, due to the multilayers' passband being 0.3nm wide. The result is highlighted in purple.

through their GDD, which can be defined as the delay suffered by each frequency while while passing through the multilayer stack. Considering the effective penetration depth $L_{eff} = Nd\cos\theta$ of the multilayer (according to Bragg's Law), the GDD can be calculated as

$$GDD = \frac{d\tau_g}{d\omega} \approx \frac{\Delta\tau_g}{\Delta\omega} = \frac{2L_{eff}}{c\Delta\omega} = \frac{2Nd\ \cos\theta}{c\Delta\omega} \approx 0.44\ fs^2, \tag{7.22}$$

where the multiplicative factor of 2 is due to the double pass through the multilayer stack. In the formula $\theta = 2°$ is the AOI, $N \approx 20$ is the number of layers, $d \approx 15nm$

is the multilayer period, c the speed of light and $\Delta\omega$ is the reflected frequency spectrum compatible to the multilayer bandwidth of $3eV$. Since each energy is selected through a mirror pair, two consecutive reflections lead to ($GDD \approx 1\ fs^2$, which remains several orders of magnitude smaller than the square of the temporal envelope:

$$\frac{GDD}{\tau_{\text{env}}^2} \approx \frac{1fs^2}{(35.6fs)^2} \approx 0.0008 \ll 1. \tag{7.23}$$

Since the induced broadening scales with the factor $\sqrt{1 + (GDD/\tau_{\text{env}}^2)^2}$ (an alternative form of eq. (6.1)), the modification to the pulse duration is well below the 1% level. Therefore it is possible to conclude that the temporal structure of the field remains essentially determined by the driving pulse for both energy regimes. This confirms that the temporal resolution required for pump-probe applications is not compromised by the multilayer spectral selection, regardless of whether the low-energy or high-energy mirror pair is employed. According to the current design, the mirror coatings are compatible with realistic beamline operating conditions under various HHG scenarios. The design accounts for potential shifts in the driving laser wavelength, possible misalignments of the XUV mirrors, the variability of the multilayer deposition process on the substrates and the preservation of the pulse temporal duration.

7.7.4 Representative Surface Error Profiles of XUV mirrors

The ray tracing simulation has been carried out implementing realistic surface error profiles and, when available, measured ones. Referencing to the complete beam path shown in Fig. 7.24, the first optical elements that intercept the harmonic comb are the rejector mirrors. The surface error profile implemented into the simulation is identical to the one presented in 7.5.3 and reported again in Fig. 7.31a. In this occurrence, the figure error profiles of the FMM and SMM have been generated starting from real mirror profiles present in the DABAM. In particular for FMM, using the "DABAM Height Profile" widget, the tangential profile of the smallest plane mirror was reshaped in size to be compatible with a $1''$ diameter and was then normalized to obtain an average slope error of $0.5\mu rad$. It was finally combined with a sagittal profile obtained via Monte-Carlo generation using a correlation length close to the size of the mirror itself ($25mm$). The same approach is used for the SMM to obtain a variable slope error in the range $1 - 5\mu rad$, with the specific purpose of assessing the dimension of the spot, and therefore the oversampling, as

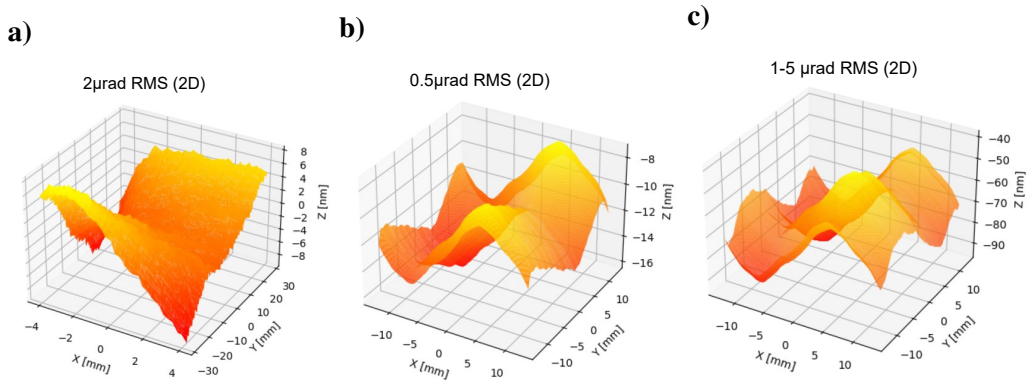


Figure 7.31: Figure errors and relative 2D RMS slope error values for (a) the measured rejector mirror, (b) FMM and (c) SMM.

a function of the RMS value of the slope error. The profiles can be observed in Fig. 7.31b and Fig. 7.31c. For each slope error curve of SMM, caustic scans are conducted to extract the spot size at the location of the circle of least confusion (COLC) that is, by definition, the $x-z$ plane at which the probe diameter is equal along both transversal directions. This is obtained by recording the intensity distribution of the beam as a function of position along the optical axis, which is moved with the "Scanning Variable Loop Point" widget. An example with SMM possessing 2D RMS slope error of $3\mu rad$ is shown in Fig. 7.32a: each scan spans a $2mm$ range, from $297mm$ to $299mm$, with a $0.01mm$ step size, and allows the collection of 200 images of the beam propagating through the focus. The red and blue curves follow the evolution of the $1/e^2$ beam diameters, extracted through a gaussian fit, on the two transversal axes. However, one shall notice that, because the beam does not overfill the surface of the mirror, the rays experience different local error profiles as the yaw changes, and therefore give rise to different intensity distribution at the circle of least confusion. The inset shows the appearance of the beam at the COLC observed through the "Plot XY widget at the specific angle of 97.2° with respect to the initialized random yaw angle. However, rotating the optics to 180°, as depicted in Fig. 7.32b, the diameter of the beam on one particular dimension almost doubles, exceeding $15.25\mu m$ and therefore violating the oversampling requirement. In this case, the aberrations become so relevant that gaussian fitting is not reliable for addressing the diameter of the spot, hence the FWHM is manually extracted and converted to an equivalent $1/e^2$ Gaussian-like diameter.

To find a threshold value for the acceptable slope error magnitude and commission the manufacturing to the fabrication companies, the spot figures at the COLC were acquired as a function of the azimuthal yaw angle and averaged. Each scan collects 200 images where

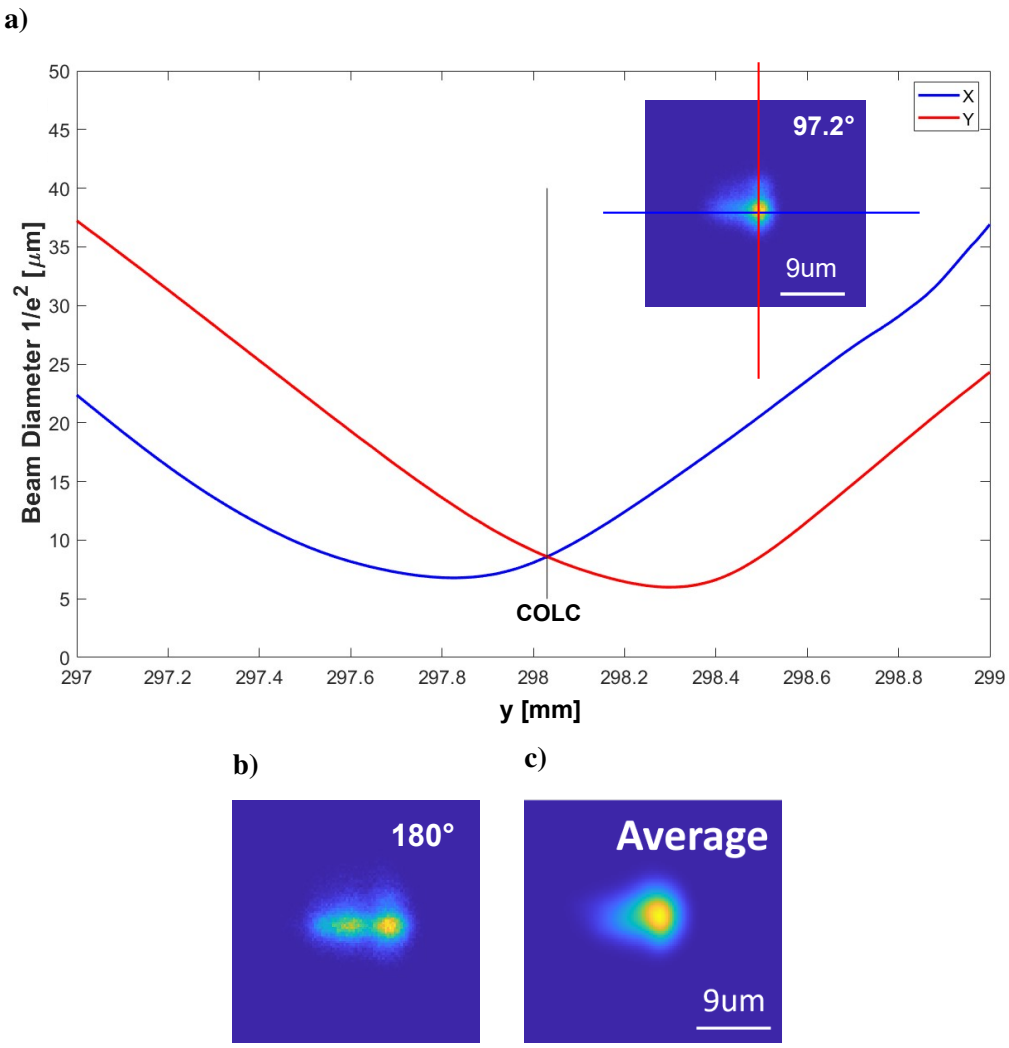


Figure 7.32: Caustic curve and spot size as a function of the yaw angle. (a) The caustic curve acquired for the localization of the COLC after the off-axis z-fold when the yaw angle is casually chosen at 97.2°. The inset shows the corresponding spot. (b) Spot size variation when the yaw angle is set to 180°, with strong aberrations occurring due to the local slope error profile. (c) Probe appearance upon azimuthal averaging.

the yaw angle is rotated from 0° to 360° via the "Scanning Variable Loop Point" widget and, at each point, the maximum beam diameter in x or z direction is saved. Each of the 200 diameters is finally averaged (see Fig. 7.32c) to provide an indication of the beam size at all possible yaw angles. Under this idea, if the average beam diameter is compatible with $\sigma > 2$, more than 50% of the positions are considered suitable for ptychography. Simulations performed for 2D RMS slope errors normalized at $1, 3, 5 \mu rad$ applied to

the SMM yield σ_{AVG} values of approximately 2.7, 2 and 1.8, respectively. These results guided the identification of $3\mu rad$ as the acceptable fabrication threshold. However, a slope error equal to $1\mu rad$ RMS is required to ensure maximum robustness of the z-fold configuration in worst-case source conditions.

In addition to figure accuracy, the surface roughness of the mirror substrates is a critical parameter due to its direct impact on the reflectivity and coherence preservation in the XUV spectral range. Taking into account eq. (7.7) with $R_0 = 1$, the total reflection loss can be calculated as $R_{loss} = 1 - R^2$ since two almost identical reflection events take place within the z-fold. A demanding yet feasible RMS surface roughness $\sigma \leq 0.25nm$ was required to the manufacturers. This value provides a total reduction of specular reflectivity of only $\sim 2.9\%$ at $12.9nm$ and about $\sim 0.6\%$ at $29.1nm$, in such a way that losses from diffuse scattering are minimized and the precise application of reflective multilayer coatings is favored.

To ensure a representative sampling of the optical surface on the effectively used areas, we requested the manufacturers to inspect figure errors, slope errors, and roughness across five $6mm$-wide positions. These positions included the center and the four offset regions (with a tolerance of $\pm 1mm$).

7.7.5 Real Mirror Profiles

The production of the XUV optics at $12.9nm$ $(96.5eV)$ and $29.1nm$ $(42.6eV)$ was commissioned to NTT-AT and SESO Thales, two world-leading companies in the manufacture of superpolished mirrors.

The initial metrological data provided by NTT for both the flat and spherical multilayer-coated mirrors presented excessive filtering at spatial frequencies ($< 1mm^{-1}$) (see Fig. 7.33a). Therefore, a dedicated metrology campaign was conducted at the ELETTRA synchrotron facility in Trieste, using both a high-resolution Fizeau interferometer (Zygo Dynafiz) and a contact profilometer (Zygo Nexview). As part of this effort, surface error profiles were measured and analyzed. The same operation was carried out on one rejector in our build, in order to cross-validate the quality of data from KMLabs. The surface profiles of the rejector were obtained by averaging four interferometric acquisitions at $632nm$, with a reference plane ($\lambda/40$) subtracted. Each measurement was adjusted to minimize the distortion of fringes in the interferometer. The resulting files, in the original Zygo format, were later processed to extract usable height maps with real physical dimensions. Regions

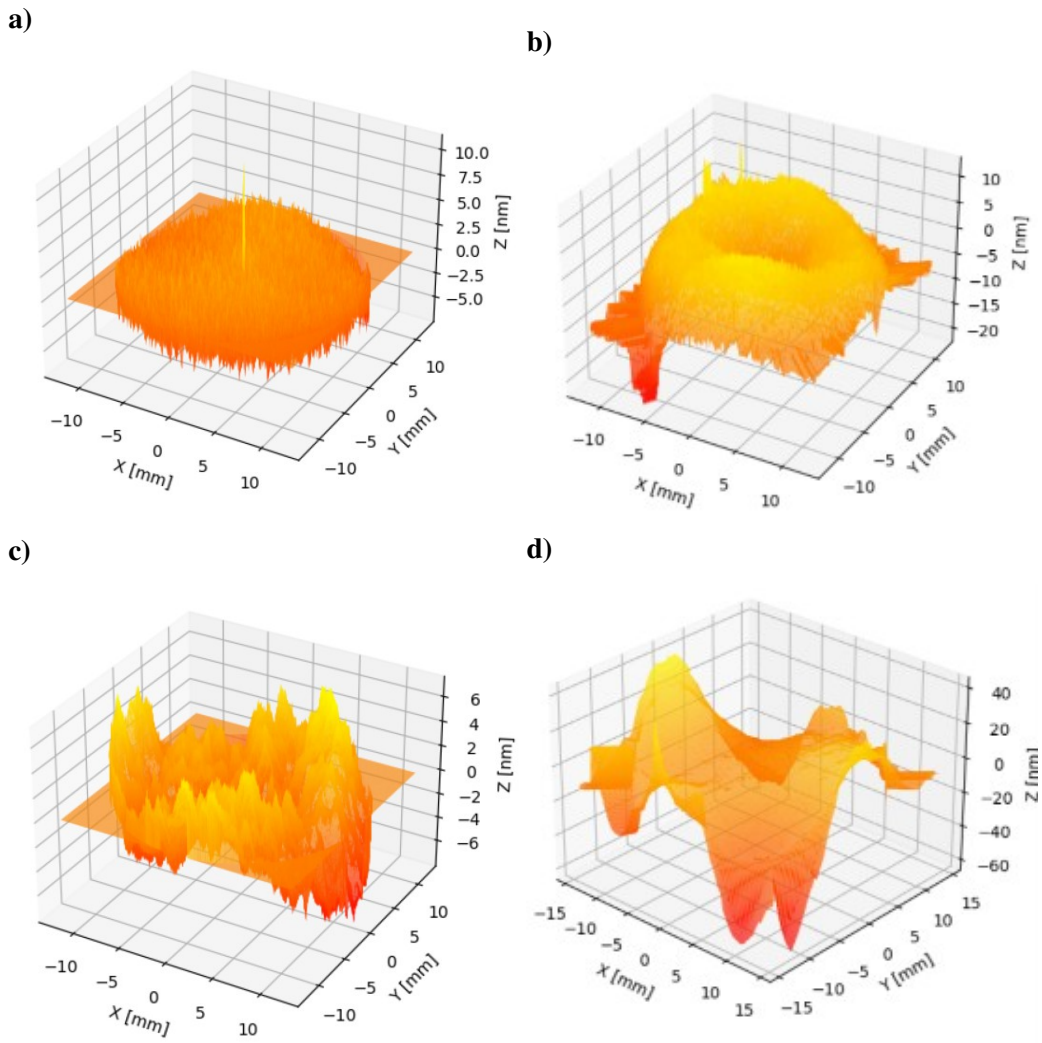


Figure 7.33: Figure error profiles from metrology measurements carried out by NTT-AT and the LUXEM Group at ELETTRA – Sincrotrone Trieste. (a) Substrate of the Flat Multilayer Mirror at 13*nm* measured by NTT, with excessive low frequency filtering. (b) Same mirror measured at ELETTRA with the Zygo Dynafiz. (c) Substrate of the Spherical Multilayer Mirror at 13*nm* measured by NTT and (d) the same surface profiled with the Zygo Nexview at ELETTRA.

outside the mirror aperture, resulting from raster scans larger than the optical surface, were interpolated using a nearest-neighbor algorithm. This step was essential to produce rectangular, uniformly sampled arrays compatible with the input format required by ShadowOui. The final interferometric datasets were ultimately aligned to the coordinate axes and downsampled by a factor of 2, reducing the size of the matrix while preserving surface shape and high-frequency content. This procedure enabled direct incorporation

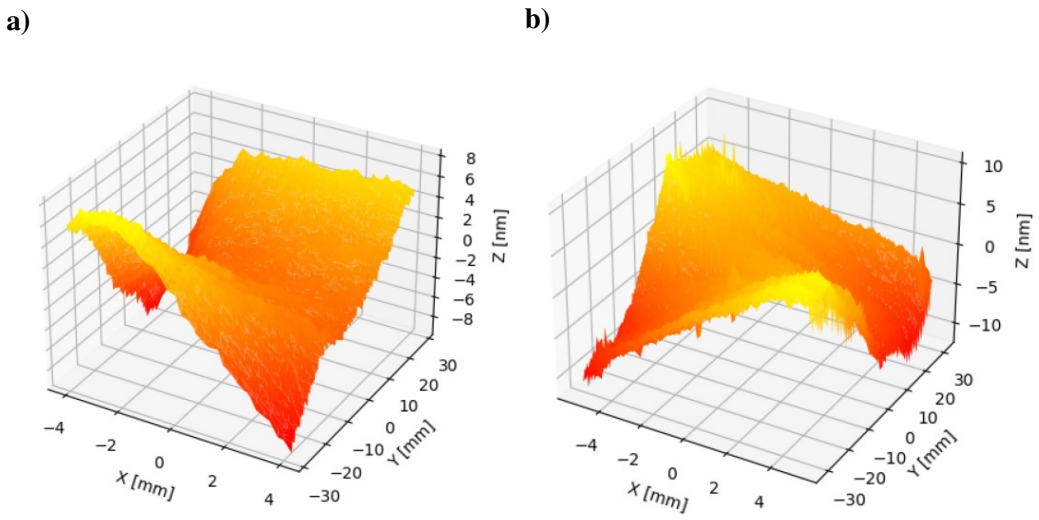


Figure 7.34: Metrological investigation of the rejector's surface. (a) Representative and (b) measured rejector profiles visualized in Oasys-ShadowOui. The measured figure error looks consisted with respect to the supplier, while differences in the RMS slope error values can be attributed to the almost double sampling resolution used at ELETTRA.

of the measured slope error profiles into the beamline simulation framework. The measurements show a close match between the representative rejector profile from KMLabs, shown in Fig. 7.34a, and the real rejector profile measured using the Fizeu interferometer at ELETTRA (Fig. 7.34b). Despite looking flipped, the figure error shows similar surface features and RMS values. The highest slope error RMS value is attributed to higher sampling (68×398 with $\sim 157\mu m$ resolution). Furthermore, the measurement provides a peak-valley value of $\sim 30nm$ along the tangential direction, which translates to a 1D ROC of

$$ROC \approx \frac{L^2}{8PV} = 20km, \tag{7.24}$$

obtained using $L = 68mm$ as the major side of the total measured area. The mirror has therefore very high planarity and the use of the "Plane Mirror" widget for its implementation in ShadowOui simulations is justified.

Following the characterization of the rejector optics, detailed analysis was performed on the flat and spherical multilayer-coated mirrors at $12.9nm$ supplied by NTT. The profiles of these mirrors were acquired at ELETTRA using the same methodology employed for the rejector, and were processed analogously. For the flat mirror, a total of eight usable interferometric datasets (each consisting of 4 averaged measurements) were selected and

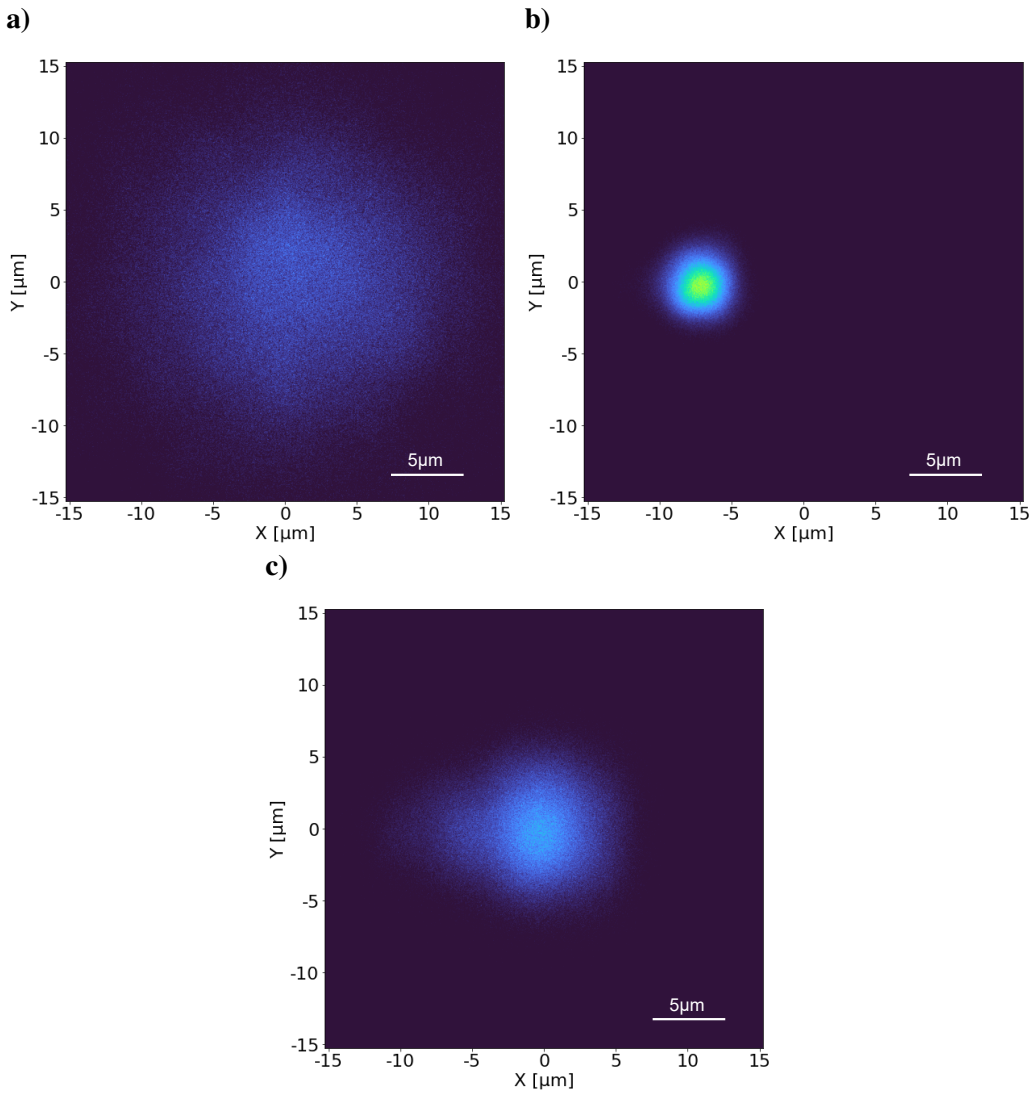


Figure 7.35: Multiple spot size intensity distributions. (a) Illumination function at the COLC using the best source conditions and the measured NTT-AT mirrors profiles. (b) Illumination function at the COLC using the best source conditions and the measured SESO Thales mirrors profiles. (c) Illumination function at the COLC using the worst source conditions and the measured SESO Thales mirrors profiles.

averaged to produce the final height profile, shown in Fig. 7.33b. The result was binned by a factor of 2 to match the input requirements of ShadowOui, as done for the rejector. The curvature of the mirror is derived from eq. (7.24) using $L = 24.4mm$ (the measured diameter) and $PV = 46.5nm$. The result corresponds to approximately $1.63km$, which is within the tolerance range requested to the supplier.

The spherical mirror supplied by NTT was treated analogously. Two measurements were acquired with the Zygo Nexview profilometer, cleaned, and averaged. These were binned by a factor of 4 to accommodate the higher native resolution of the profilometer. The average profile, shown in Fig. 7.33d, presents several general deviation from its nominal ROC of $545mm$, and significantly differ from the measured profile by the supplier (see Fig. 7.33c), which possess more limited height variations. The impact of the slope error from the measured NTT mirror profiles on the propagation of the beam was evaluated via ray tracing. The simulation makes use of both representative and measured rejector profiles, to avoid the amplification of slope error effects due to the same figure error on both plane mirrors. The flat and spherical mirrors composing the z-fold are both modeled with the "Spherical Mirror" widget, to specify the exact ROC. Fig. 7.35a shows that, even in with the best conditions of the source ($S = 30\mu m$ and $Div = 0.7mrad$), the intensity distribution at the image plane located $301.4mm$ away from the spherical mirror, has diameter $\sim 25\mu m$ $1/e^2$ and $\sigma = 1.21$. Therefore, it exceeds the limit of $15.25\mu m$ in our high-resolution configuration and violates the $\sigma > 2$ requirement. The results is nevertheless consistent with our previous analysis: being the slope error higher than $3\mu rad$ RMS, the probe becomes severely affected and an optical confining element, such as a pinhole, shall be adopted to recover an acceptable spot size for ptychography.

The interferometric measurements of the optics supplied by SESO Thales were acquired using a Zygo interferometer, employed to characterize both flat and spherical mirrors. Due to the small aperture of the optical elements and the very narrow chamfer required ($< 1mm$), dedicated optical setups were set up for the acquisition of metrology data (see Fig. 7.36). For the assessment of flat mirrors, a highly stable and precisely calibrated Transmission Flat (TF) served as the fundamental reference optic within the configuration of the interferometer. The physical dimensions of the mirrors often exceeded the inherent field of view of the interferometer, therefore stitching was systematically implemented. This process involved the precise mechanical translation of the mirror under test across the interferometer aperture, allowing for the sequential capture of numerous overlapping sub-aperture measurements. Subsequently, a highly advanced computational algorithm was employed for meticulously piecing together these individual interferograms. This algorithm rigorously accounted for any relative displacement, tip and tilt between adjacent measurements, thereby enabling the accurate reconstruction of a comprehensive, full-aperture surface map of the mirror. For the characterization of spherical mirrors, a specialized Transmission Sphere (TS) was carefully selected and integrated into the

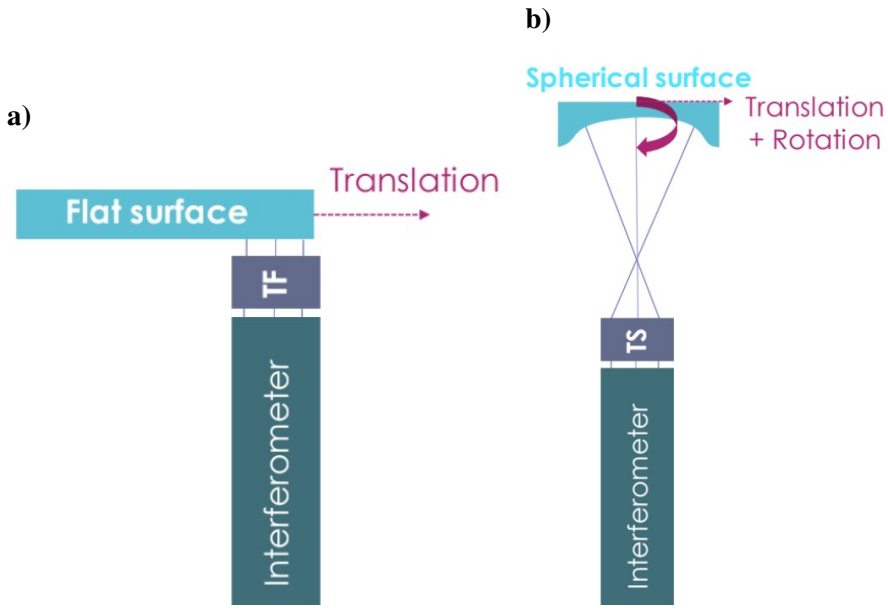


Figure 7.36: Surface error profiles acquisition methods. In (a) the measurement approach used for the flat substrates, with a transmission flat used as reference. (b) Measurement approach used for the spherical substrates, with a transmission sphere used as reference. acquisition for flat and spherical mirrors.

interferometric setup instead of the TF. This optical element served the crucial function of transforming the collimated output beam of the interferometer into a perfectly converging or diverging spherical wavefront, that precisely matched the nominal curvature of the mirror under examination. This arrangement established a highly desirable "null test" configuration, where, for an ideal spherical surface, the recombined wavefronts would produce a uniform field of illumination rather than interference fringes. Consequently, any observed deviations in the resulting interferogram directly indicated departures from the specified ideal spherical form. Analogous to the flat mirror process, principles of precise translation and rotation of the spherical mirror were applied when necessary to acquire multiple sub-aperture measurements that were subsequently integrated using the aforementioned stitching algorithms. The culmination of this process was the generation of the Stitching Map, which represented the global, reconstructed surface figure of the mirror. Beyond the raw surface reconstruction, the process also yielded an Error Map. This particular map was generated through the subtraction of the sub-pupil maps after their positional adjustments during the stitching process. Its purpose was to quantify and visualize the measurement accuracy on the global map, essentially revealing the residual

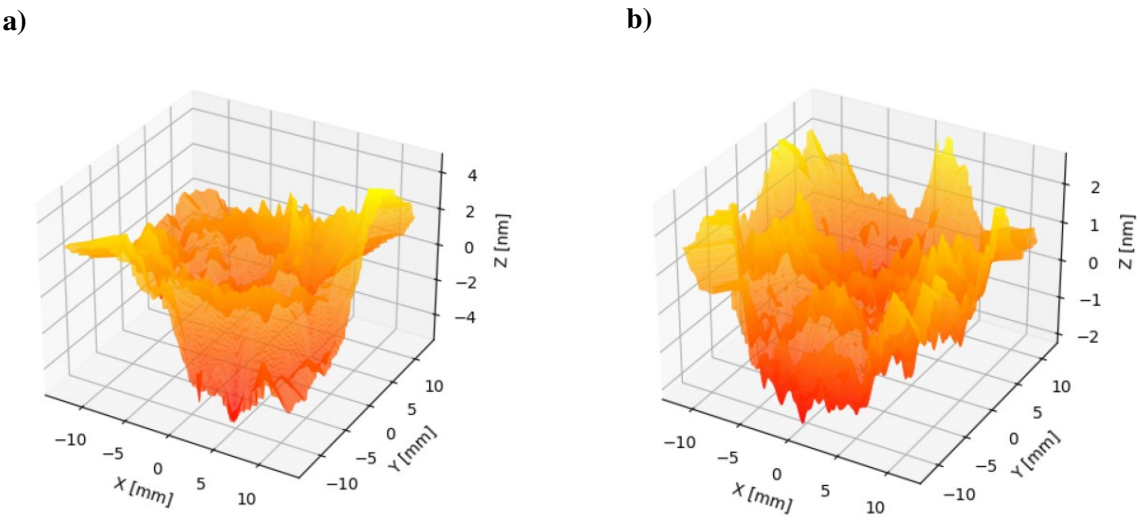


Figure 7.37: Figure error profiles of the SESO Thales z-fold mirrors destined to the Mo/Si coating for high energy XUV light. (a) Flat mirror profile and (b) Spherical mirror profile.

discrepancies or uncertainties inherent in the stitching process itself. This map served as an indicator of how well the overlapping sub-pupil measurements consistently aligned and integrated. Importantly, the inherent imperfections of the measuring optics themselves posed a challenge. The initial Stitching Map implicitly contained contributions from the errors of the reference optical element (the TF or TS). To meticulously deconvolute and isolate the true mirror errors from these systematic biases, a dedicated and rigorous calibration method called "Cavity Mapping" was executed. This procedure consisted in applying an iterative algorithm to progressively refine the estimation of the true surface figure of the reference optic, by analyzing the individual sub-apertures and taking into account the inherent redundancy of the stitching process. This process allowed for the accurate characterization and subsequent reconstruction of the Cavity Map, which precisely represented the systematic error profile of the reference optical component. Ultimately, to yield the definitive and highly accurate surface figure of the mirror, the determined Cavity Map was mathematically subtracted from the raw Stitching Map, eliminating the systematic influence of the measurement apparatus.

The SESO maps were processed using the same procedure applied to the ELETTRA data: the axes were centered, "no data" entries interpolated via nearest-neighbor methods, and the matrices binned to reduce resolution while preserving curvature and slope information. The final surface profiles imported into the simulations at $12.9nm$ are shown in Fig. 7.37a and Fig. 7.37b, for the flat and spherical mirror, respectively. It is important to

point out that, compared to the NTT mirrors, we have actively liaised with SESO in order to define, after polishing, the substrates to be coated at each central wavelength. Therefore, the best substrates have been assigned for Mo/Si coating, due to the most stringent requirements in beam size and oversampling at higher energies. In this framework, the ray tracing simulations turned out to be an essential tool for both design and manufacturing validation processes. The flat mirror profile is extracted from an average of 41 measurements, with a squared pixel resolution of $\sim 95\mu m$ and a total measured area of $25mm \times 25mm$. The ROC of the flat mirror is provided by the best fitting sphere subtracted to obtain the figure error and corresponds to $2.43km$, so above the $2km$ requirement. The remaining figure error shows extremely low slopes in the two perpendicular directions, with 1D RMS values $\leq 1\mu rad$. The 2D RMS value, calculated through the Pythagorean theorem, is instead slightly higher than unity but well below the threshold limit at $3\mu rad$. The spherical mirror substrate is obtained by averaging 44 independent measurements, each with a pixel size resolution of $\sim 74\mu m$ for a total covered area of $23mm \times 23mm$. Its ROC is calculated by the removal of the best fitting sphere as for the flat substrate and is estimated to $540.4mm$, in agreement with the design directives. The figure error profiles obtained after polishing exhibit low slopes, below $1\mu rad$ RMS in both 1D and in 2D. Finally, for both substrates, the roughness was measured on the five $6mm$-wide apertures. The analysis led to $0.21nm$ RMS and $0.28nm$ RMS for both flat and spherical optics, thus compatible with the coating stage. The height error profiles for each mirror is shown in Fig. 7.37.

Inside the ray tracing simulator, using the same profiles for the rejectors, the mirrors from SESO perform better than the counterparts from NTT, producing, as shown in Fig. 7.35, high quality beam at the sample plane both at worst- and best-case source scenarios. In the same case presented previously ($S = 30\mu m$ and $Div = 0.7mrad$), the spot size at the image plane, found by caustic scans at $298.24mm$ (see Fig. 7.38a) from the SMM, appears highly confined with a minimal beam waist of approximately $5.1\mu m$. This value corresponds to an oversampling factor ~ 6 and meets the Nyquist sampling requirement for ptychography. The simulation shows clean Gaussian-like focal minimum with negligible coma aberrations from the off-axis geometry. Even under a worst-case source scenario (see Fig. 7.35c), the surface features of the mirrors guarantee only minimal distortion in the beam and a diameter $\sim 10.5\mu m$, corresponding to a $\sigma = 2.89$. Ultimately, no significant beam asymmetry or degradation was observed when rotating the mirror around its optical axis (see Fig. 7.38b and Fig. 7.38c), with $\sigma > 2.35$, confirming the overall uniformity of the surface. This demonstrates that the mirrors from SESO are

both within the specifications but also provide operational robustness across a wide range of illumination conditions. These results indicate that the mirrors fabricated by SESO Thales meet the performance requirements for high-resolution XUV ptychography. The beam profiles are clean, symmetric, and exhibit minimal sensitivity to alignment errors, making these optics suitable for long-term use in time-resolved or scanning applications without the need for additional spatial filtering. In contrast to the NTT mirrors, the SESO substrates do not require post-conditioning via apertures or pinholes to achieve an acceptable quality. A pair of flat and spherical mirrors of comparable quality was assigned for the multilayer deposition in Al/Mo/Si optimized at $42.6eV$. The ROC of both optical elements is lightly worse than the previous pair, corresponding to a $1.11km$ for the flat substrate and a $541.7mm$ for the spherical one, but nonetheless inside the range defined during the design phase. After the removal of the best fitting sphere, the figure error is left and characterized with interferometric measurements. The flat substrate, whose measured area is $\sim 25mm \times 25mm$ wide, is characterized by a 2D slope error profile of $\sim 1.8\mu rad$ RMS, therefore higher than the intended purpose of $0.5\mu rad$. The spherical substrate displays a 2D RMS slope error of $\sim 1.5\mu rad$ on a $\sim 23mm \times 23mm$ area, slightly higher than the previously presented couple but nevertheless consistent with the threshold of $3\mu rad$. However, it is important to take into account that this limit value is not strictly required for $29.1nm$ light, since the oversampling condition is relaxed due to the higher wavelength, which approximately set the limit of the probe diameter to $D = 34\mu m$ $1/e^2$. The surface profiles are shown in Fig. 7.39 and possess 1D slope errors in the order of $1.1\mu rad$. In the same source conditions as the previous simulation, the combination of new height errors and ROCs produce a slightly aberrated probe at $298.63mm$, the new position of the the circle of least confusion. The image of the probe, in this scenario is displayed in Fig. 7.40, where, due to the different illumination wavelength, the projected pixel size and detector's area at the sample plane ($26mm$ away from the detector) is almost doubled, leading to extremely high oversampled probe.

7.7.6 Future Perspectives of Ray Tracing Simulations

ShadowOui has been a crucial tool in guiding the precise modeling of each optical element, from the source to the experimental chamber, taking into account mechanical tolerances and physical constraints. The detailed simulations have provided essential inputs for the design and validation of the custom mirrors (both flat and spherical) within the experi-

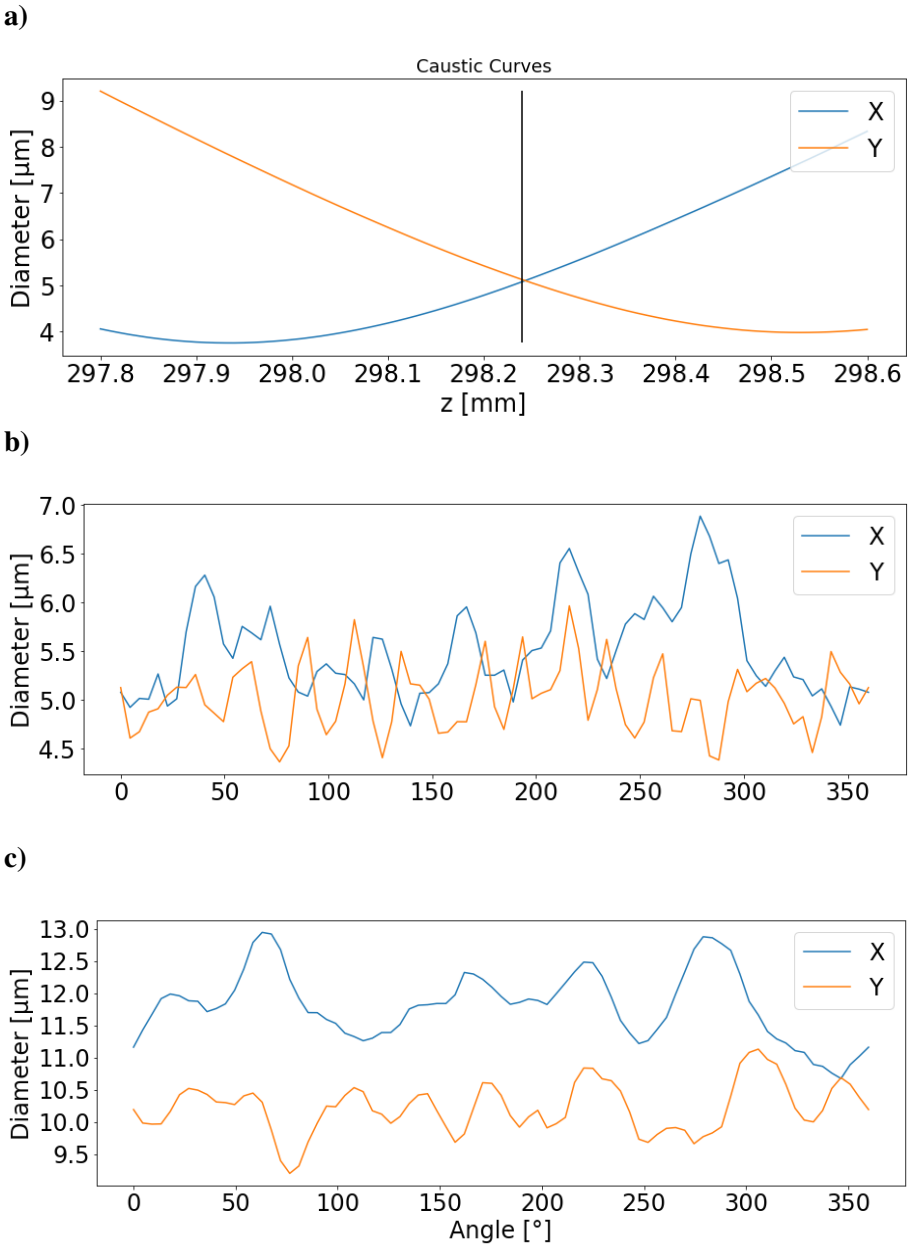


Figure 7.38: Beam diameter dependence as a function z and yaw angle in different source conditions. (a) Beam diameter as a function of the optical axis position z in the best case scenario, indicating a COLC at 298.24mm from the spherical mirror. The step size is 0.01mm. (b) Beam diameter as a function of the yaw angle in the best case scenario with 4.5° steps, suggesting high beam confinement within 7μm $1/e^2$. (c) Beam diameter as a function of the yaw angle in the worst source scenario with 4.5° steps, suggesting a suitable beam confinement within 13μm $1/e^2$.

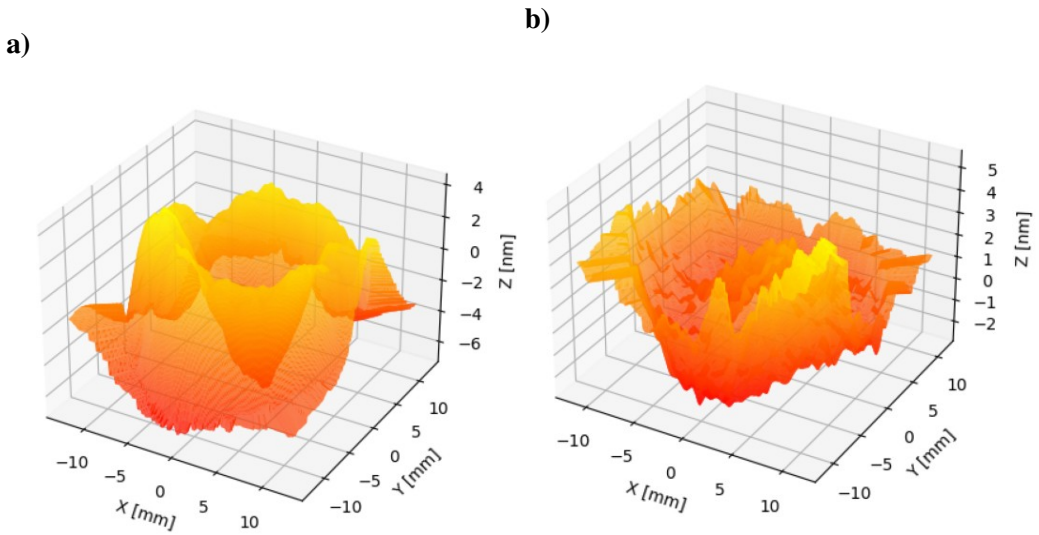


Figure 7.39: Figure error profiles of the SESO Thales z-fold mirrors destined to the Al/Mo/Si coatings at low energy. (a) Flat mirror profile and (b) Spherical mirror profile.

mental chamber, translating the theoretical expectations into manufacturing requirements.

Beyond its value as a design and validation tool, this ray tracing approach offers two additional advantages for the ptychographic workflow. First, it enables a predictive estimation of the illumination function at the sample plane, neglecting only diffraction effects. This allows systematic evaluation of misalignments and optical imperfections without breaking vacuum for direct optical access. By leveraging this capability, one can adjust experimental parameters into the simulation first and, in a second stage, correct for the misalignment by means of remotely actuated devices, enhancing operational efficiency and minimizing experimental downtime. Second, ray tracing allows using its output data to inform the initial guess for the probe function in the ptychographic reconstruction algorithm to significantly accelerate the convergence rate. By incorporating physically derived information into the reconstruction process, the dimensionality of the optimization problem is reduced, allowing the iterative algorithm such as ePIE to reach a stable solution in fewer iterations. In summary, ray tracing simulations shall not be considered as a static design tool but function as a true digital twin of the beamline. Therefore, the simulations enable predictive adaptation of the microscope design, facilitate high-throughput operation by minimizing maintenance-related interruptions, and improve the overall reliability and efficiency of the experimental workflow. This integrated approach to optical modeling and system design represents a critical enabling factor for the routine use of ptychography,

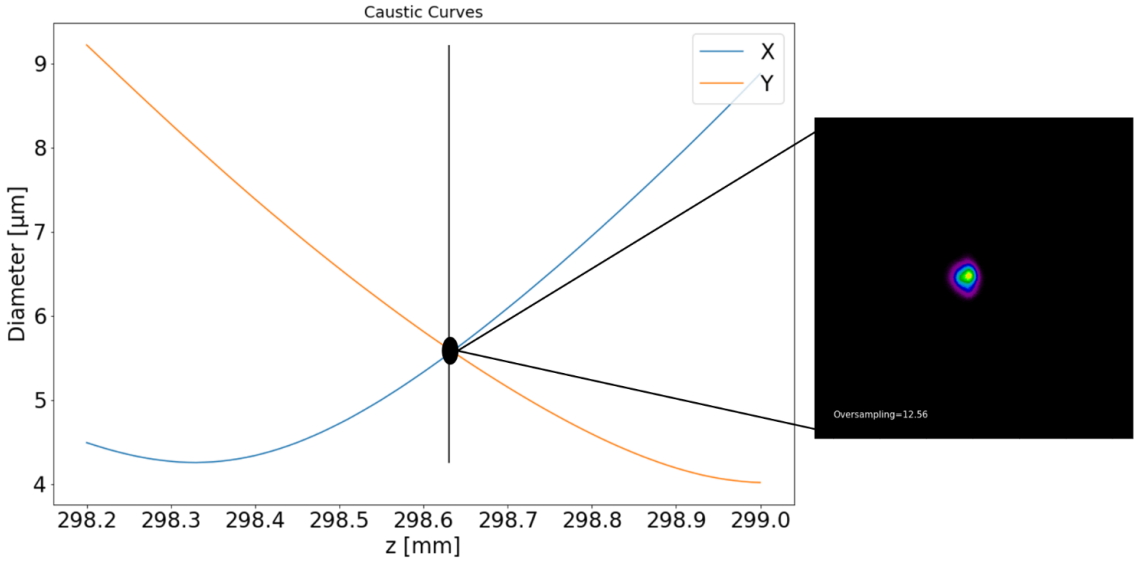


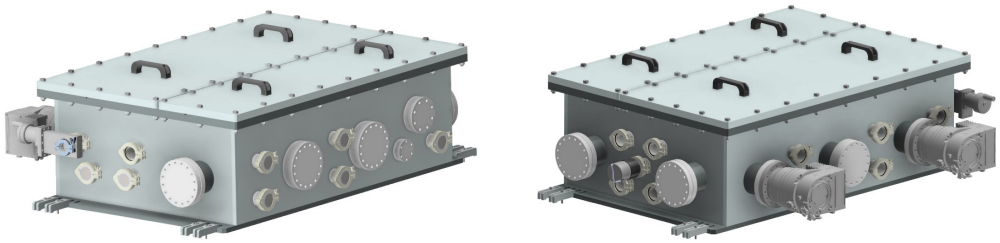
Figure 7.40: Caustic scan relative to the beam propagation from the spherical mirror using the SESO Thales mirror profiles for $29.1nm$ XUV light. At the COLC the spot size is observed being compatible with a size of $\sim 6\mu m$ $1/e^2$. The window size is reshaped considering the detector size and the operational wavelength, therefore high oversampling values are reached.

especially in time-resolved scenarios where system availability and stability are paramount.

7.8 Experimental Chamber Design

Based on the feasibility study conducted through ShadowOui, and considering the constraints discussed in section 7.1, the experimental chamber was designed and manufactured to accommodate the z-fold-based microscope layout. The custom design of the experimental chamber was generated through 3D modeling, in collaboration with the manufacturer (ALCA Technology). Fig. 7.41a and Fig. 7.41 show both sides of the 3D rendering of the experimental chamber, while in Fig. 7.41c the final product on the optical table can be observed. The chamber occupies an internal footprint of $670mm \times 1000mm$, a size determined by carefully considering the spatial requirements for in-vacuum optical elements, detectors, and motion stages. To accommodate those, the chamber supports up to $20kg$ of equipment installed on the upper internal surface. It is fabricated in AISI 304L stainless steel for mechanical robustness under vacuum, with $15mm$-thick walls to balance strength and compactness. The walls are $330mm$ high from the base of the chamber, allowing

a)



b)

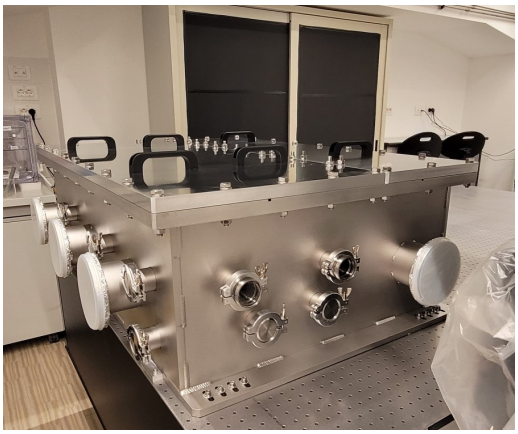


Figure 7.41: The experimental chamber. In (a) the 3D rendering showing the four sides of the mechanical body, in (b) the deployment on the optical table.

access to users of average height. The lid is composed of two parts, a larger and a smaller section, to simplify maintenance or major changes in the configuration of the microscope. Fig. 7.42 shows the interior of the experimental chamber. It houses a 5083 Al breadboard with M6 tapped holes spaced at 25mm intervals, which is mechanically isolated from the base via spacers to mitigate deformation during pump-down. The breadboard and chamber base form a 54mm-high mechanical stack, which was specifically defined to obtain the center of rotation of the mirrors at the desired height, as described in the following lines.

To implement the z-fold geometry, the experimental setup requires high precision to guide the position of the flat and spherical mirrors. This necessitates the integration of multi-axis vacuum-compatible motion stages capable of full angular and translational control. The adopted solution consists of two vertical SmarAct towers, referred to as T1 and T2, which guide the alignment of the z-fold. The tower footprint is compact, ($52 \times 52mm$) and is mounted on a 6mm thick aluminum baseplates designed to position

the mirrors such that their rotational center is located precisely 147.5mm above the surface of the breadboard. This value, summed with the 54mm described before, leads to a beam height of 201.5mm from the surface of the optical table, and matching the beam height out from the rejectors. The T1 and T2 towers are each composed of two linear CLS-5252-S-HV stages for motion along the X and Y directions, a central SR-5014-S-HV rotary stage (angular resolution $< 2\mu^\circ$) for azimuthal control, and two CGO goniometers with center of rotations at 60.5mm and 77.5mm above their surface. These stages have a closed loop angular resolution $< 2\mu^\circ$ and are mounted one above each other for fine angular adjustments. Therefore, each tower provides the degrees of freedom required for precise angular and translational fine-tuning down to pressures in the order of $10^{-7}\ mbar$. The mirrors are mounted on vacuum-compatible custom pedestals and equipped with Newport 8821-L-UHV motorized mounts, to provide an additional tip and tilt. All stages can operate both in open- and closed-loop with the electronics, and can guarantee nanometric resolution.

The sample manipulator is similarly engineered to bring the center of the sample to the same internal elevation of 147.5mm. This manipulator integrates a vertical stack of CLS, SLC, and SR SmarAct stages, enabling seven degrees of freedom including fine and coarse rotational motion, with closed loop resolutions $< 2\mu^\circ$ and $< 4\mu^\circ$ respectively.

An additional stack of stages is implemented to actuate a set of pinhole apertures, used to spatially confine the probe illumination as a derisking option. This stack incorporates three SLC-1730-S-HV stages mounted on a custom aluminum riser block and terminates with a plate accommodating interchangeable Hitachi Strip Apertures. The strip is made in platinum-iridium, and offers multiple apertures of different sizes ($10 - 400\mu m$), selected based on dimension of the beam as it propagates towards the image plane.

All motion stages are controlled through a dedicated automation infrastructure composed of two 19″ rack enclosures. The first rack governs the optical towers T1 and T2, while the second manages the sample and pinhole manipulators. Each rack contains one MCS2-MOD-0003 master module and three MCS2-MOD-0001 controller modules, each one capable of addressing three linear stages. Sensor readout is handled by MCS2-S-0005 modules placed outside the vacuum, with connectivity to the internal stages provided by twenty 11-pin Fischer vacuum feedthroughs.

The pump beam is steered with two 1″ dielectric ultrafast mirrors in a loose z-fold configuration, with the angle of incidence manually found to directly send the pump as collinear as possible to the probe. The mirrors are mounted on two clear-edge Newport

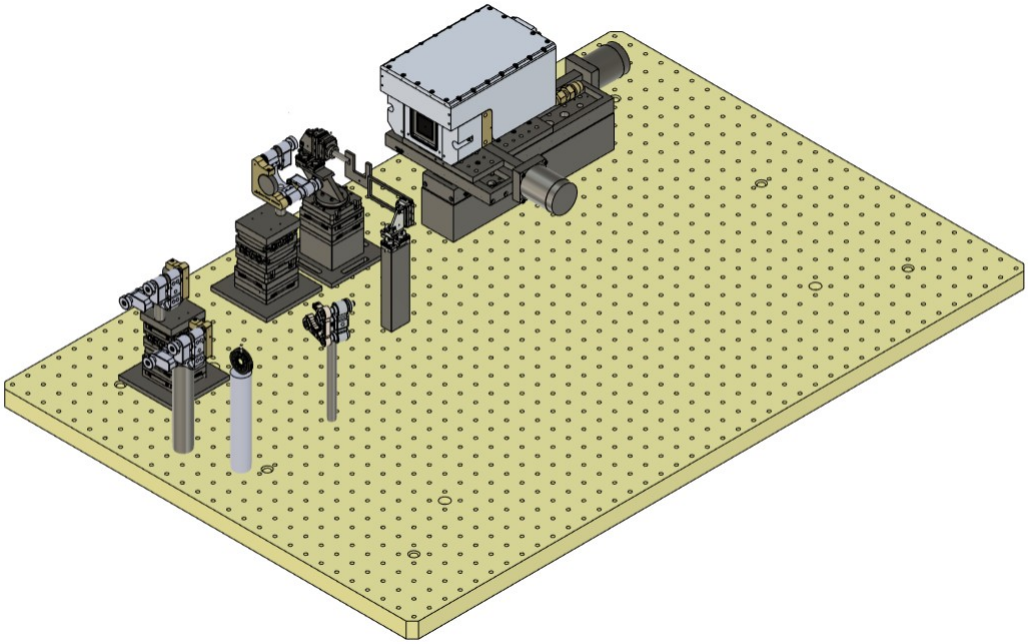


Figure 7.42: Internal rendering of the experimental chamber. On the left side two piezo actuated mirrors on SmarAct stages stacks are oriented in a z-fold configuration for probe focusing the sample plane. Other two sophisticated stages stacks pilot the sample and pinhole positions. An aperture and two additional mirrors on simple posts, with one being piezo actuated, are used for guiding the pump beam to the sample and induce the ultrafast dynamics. The detector stands on two orthogonal Standa linear stages for a variable position and numerical aperture.

mounts (SN100C-F2H and 8821-L-UHV), with the second one possessing tip and tilt remote control via piezo-actuators.

The detector is positioned such that its active area is centered at 147.5mm above the breadboard, thereby aligning it with the optical axis defined by the mirror system, as shown in Fig. 7.43. It must be able to move along the x and z axes to allow for changes in sample-detector distance, field of view and resolution. This requirement is fulfilled using two orthogonally mounted Standa linear stages (MT175V-50-VSS42-VC15F-FT and 8MT175V-150-VSS42-VC15F-FT). The height offset is achieved via mechanical adapters mounted beneath the stages, that ensure the exact placement of the chip center to the optical axis. The stages are driven by two-phase stepper motors and offer travel ranges of 150mm along the beam propagation axis (allowing for a N.A. in the range $0.43 - 0.06$) and 50mm on the transverse direction. This latter translational degree of freedom is particular important to obtain an image of the direct beam from the source, moving the flat mirror out

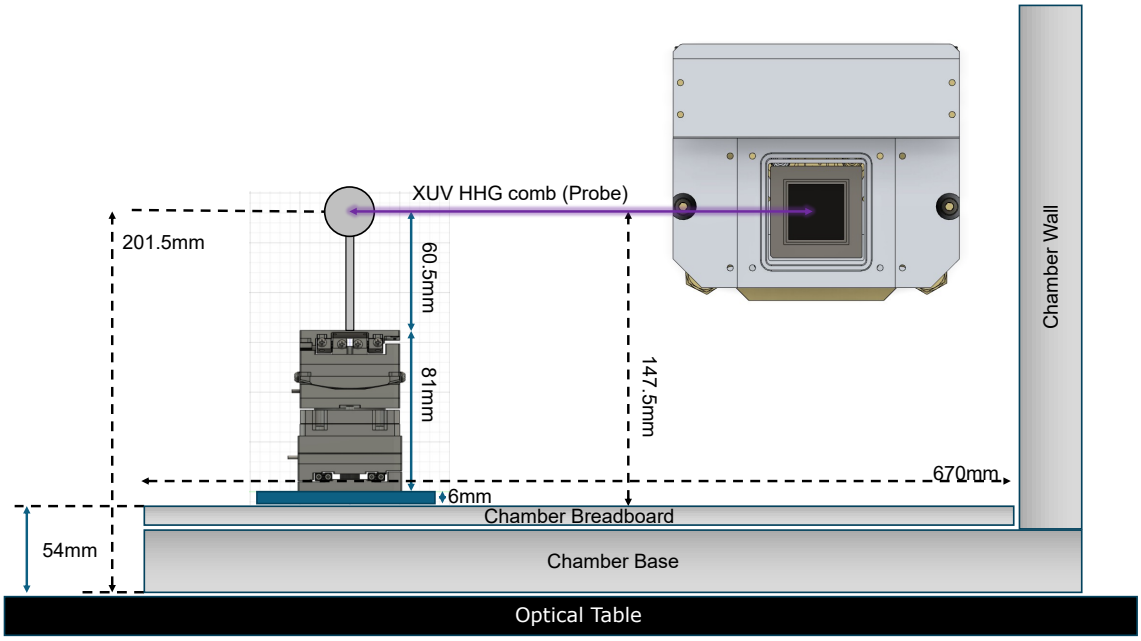


Figure 7.43: Sketch of the detector's vertical position compared to the mirror's pole located at the circle of least confusion. The sum of chamber base and breadboard is $54mm$ which, added to the $6mm$ base of the stages' stack and the $147.5mm$ of the stages' center of rotation, gives a total height of $201.5mm$ from the table's surface. A the same height, the center of the detector's chip shall be positioned.

of the beam path and bypassing the z-fold. Both stages offer sub-millimetric resolution, an accuracy lower than $100\mu m$, and bidirectional repeatability under $10\mu m$.

To accommodate all these mechanical and optical systems, the chamber integrates a variety of flanges. Four CF100 ports are installed laterally for connection to the turbo-molecular pumps, designed as pass-throughs to allow rear mounting. CF40 and CF63 flanges are used for the water feedthroughs and the electrical connectors of the detector. KF40 flanges are primarily assigned to the connectors of the motion stages and are spaced sufficiently to allow easy access for metallic clamps. The beam gets inside the chamber passing through one out of four sapphire windows mounted on CF flanges. They are aligned with the grid of holes of both the internal breadboard and the external optical table, to facilitate the beam alignment. Additional flanges are available for a future expansion of the microscope layout.

In summary, the experimental chamber integrates mechanical robustness, vacuum compatibility, and nanometric positioning precision of its main elements, ensuring stable optical alignment for the z-fold but also opening the possibility for future expansions and

modifications to evolving experimental needs.

7.9 Data Management System

To manage, process and store the data gathered during experimental campaigns, the entire system was equipped with an architecture based on two-levels.

The beamline is controlled by a dedicated Acquisition Workstation (Intel Xeon 12C/24T, 128 GB RAM), which handles real-time communication with detectors (AXIS-SXR from Axis Photonique Inc, beam profilers, photodiodes) and motion controllers via USB 3.0 and Ethernet. To manage the high data throughput, this station is equipped with high-speed NVMe storage for temporary local storage.

For long-term storage and intensive processing, the workstation is integrated into a private 10 Gbps VLAN connected to the Blade, a high-performance Lambda Server (AMD EPYC 32 cores, 256 GB RAM, dual NVIDIA RTX A6000 GPUs). This server provides a multi-terabyte redundant storage (MDRAID1 NVMe and SATA SSDs) and hosts the software where the ptychographic reconstruction engines are executed. This setup ensures efficient data transfer and sufficient computational power for near real-time image reconstruction.

7.10 Preliminary Microscopy Reconstructions with Ray-traced Probes

Preliminary microscopy reconstructions are performed with a ray-traced probe generated using the height profiles in Fig. 7.37. However, the reconstruction shown in this paragraph is distinguished by the use of real source parameters characterized after the implementation of the experimental chamber described in section 7.8. The direct beam from the XUUS was imaged onto the detector by removing the z-fold assembly. Knowing the M^2 of the beam from the supplier and systematically moving the position of the detector along the optical axis, the size and divergence of the beam source were estimated to $S_\sigma = 3.582\mu m$ and $Div_\sigma = 0.75mrad$. Noticeably, the size of the source is much smaller than the value initially considered during the design stage. However, this does not provide significant differences since, for propagation distances of the order of our beamline, the divergence is the main factor that determines the final spot size. These parameters were imported in

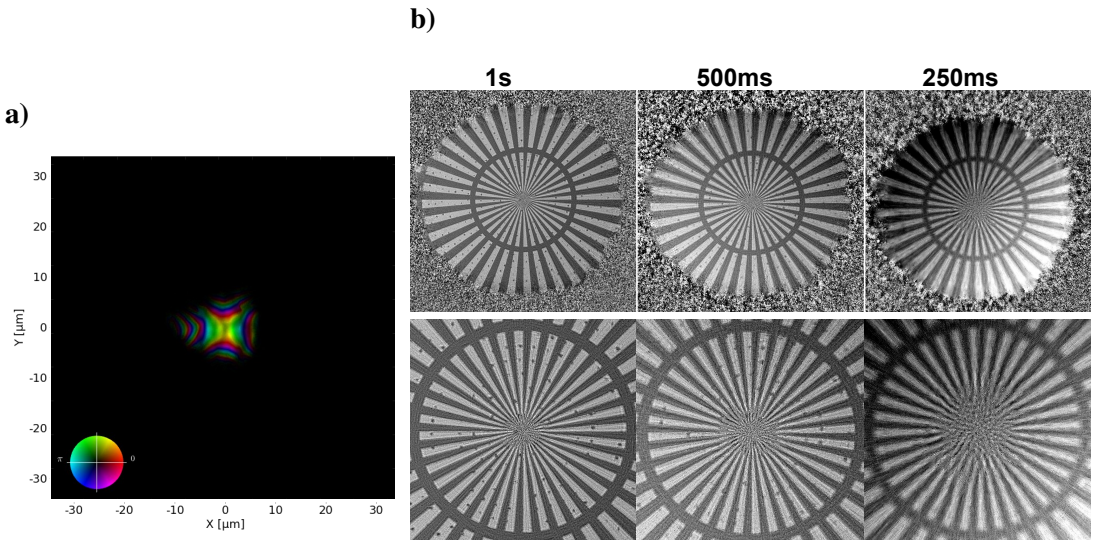


Figure 7.44: (a) Ground truth probe obtained combining ray tracing and GS algorithm and (b) reconstructed images as a function of the simulated exposure time and the refined result by imaging the 30 reconstruction showing the least error (bottom row).

ShadowOui and an updated ray tracing simulation was carried out. Caustic scans indicate the position of the COLC 298.16mm away from the spherical mirror, with a spot size equal to $D_{XUV} = 6.17\mu m\ 1/e^2$. The complex profile of the probe is displayed in Fig. 7.44a and was retrieved by means of the GS algorithm, using the same procedure described in section 7.6. In an initial simulation, the 2048×2048 probe was used as a ground truth to generate multiple diffraction patterns from a $20nm$-thick Siemens Star patterned onto a $200nm$ Silicon membrane. The patterns were obtained following a Fermat spiral scanning scheme and taking into account the real characteristics of the AXIS detector as in section 7.6.

Reconstructions were performed using a code based on difference map and maximum likelihood and show an increase in contrast as a function of the exposure time as indicated in Fig. 7.44b. High quality images are retrieved by optimizing the step size of the scanning grid, with the highest overlapping value equal to $3\mu m$. The final object image results from 100 independent reconstructions, of which the 30 exhibiting the smallest reconstruction error were selected and averaged. In the following step, the microscope capability was benchmarked on a simulated monodispersed thin film of textured core-shell nanoparticles ($300nm \pm 10nm$ Au core and $50nm \pm 4nm$ ligand shell) on a $30nm$ Si_3N_4 substrate with a realistic roughness of 3%. To demonstrate the microscope throughput and resolve the ligand structure of the nanoparticles, the algorithm was initialized using

the probe recostructed in the Siemens Star case as a guess function. In fact, this leads to an increase in the convergence rate of the iterative process and to more accurate results. Specifically, the initial probe is deconvolved from the siemens star reconstructed at $500ms$ exposure time and $1\mu m$ step size, which are the operative parameters more suitable for the reconstruction of the observed NP-based sample. The results of the iterative algorithm are shown in Fig. 7.45: the amplitude image of the complete sample is first shown without reuse applied, with the onset indicating the sharpness of the nanoparticles on a portion of the image. The effect of reusing the previously reconstructed probe is clearly visible in terms of image sharpness in Fig. 7.45b. Even more pronounced is the application of averaging, which allows to retrieve a smooth distribution of NPs (Fig. 7.45c) both in amplitude and phase. A lineout of the phase image across three joint nanoparticles displays a modulation of the gray value, indicating the capability to resolve the refractive index of the ligand shell, which is theoretically possible with $29.1nm$ light.

Performing this virtual experiment using real measured parameters, promising results are obtained. This indicates that studying the nanoscale heterogeneity at high resolution is possible with the developed ptychography setup. By extending the scenario to time-resolved measurements, this preliminary study suggests the feasibility of visualizing the associated light-activated functions, an aspect that plays a pivotal role in the foundational development of next-generation smart nanomaterials and their characterization.

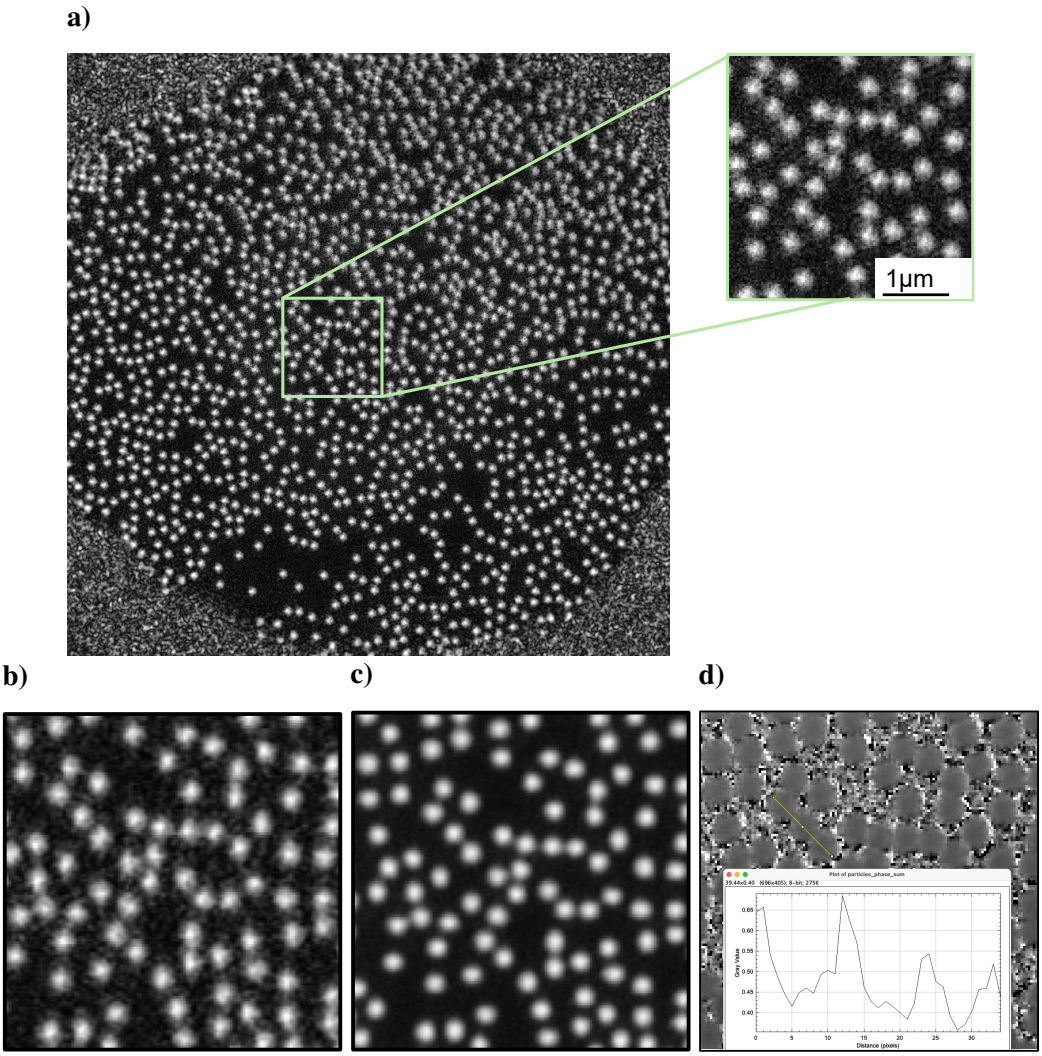


Figure 7.45: Reconstructed amplitude and phase images of monodispersed core-shell nanoparticles. (a) Wide field of view of the reconstructed sample, with inset showing the nanoparticles detail. (b) The same area by reusing the probe from the siemens star as a ground truth for the blind deconvolution in ptychography. (c) The same area by applying the averaging of the 30 best reconstructions, all carried out with the probe's reuse. (d) Corresponding phase image, with lineout on three consecutive particles highlighting greyscale modulation with a periodicity corresponding to the shell thickness.

Chapter 8

Conclusions and Future Perspectives

This chapter provides the concluding remarks of this dissertation. It synthesizes the main outcomes of the doctoral work, discusses possible improvements to the beamline and highlights prospective applications that may be pursued in both the near and long term.

8.1 Conclusions

The central objective of this doctoral project was the development of a microscope capable of combining high spatial and temporal resolution to investigate the transient dynamics of photoexcited samples. Achieving such dual resolution requires the integration of a high-energy source with pump-probe methodology, enabling the simultaneous capture of structural and temporal evolution of a sample at the femtosecond-nanometer scale.

To accomplish the spatial resolution requirement, the microscope was designed around a HHG source, which provides access to the soft X-ray and XUV regime by upconverting femtosecond infrared laser pulses. This configuration offers the ability to reach short wavelengths and thus higher spatial resolution, while also producing stable, coherent, and high-flux radiation. These properties enable the use of CDI, a computational microscopy technique in which the images are reconstructed from diffraction patterns rather than directly generated by image forming optics. The specific CDI approach employed here is ptychography, in which the sample is scanned through a tailored illumination function derived from the HHG source. By acquiring diffraction patterns from partially overlapping regions, iterative algorithms can solve for the phase-problem and reconstruct both the object and the probe functions as complex images, thus achieving fully quantitative imaging.

In this framework, the ultimate spatial resolution depends primarily on the detector sensor and the wavelength of the illumination rather than on the image-forming optics.

To address the temporal resolution requirement, the microscope was designed as a pump-probe system. Both pump and probe pulses originate from a single mode-locked oscillator (KMLabs Griffin^{TM}) feeding a chirped-pulse amplifier system (RAEA^{TM}), emitting $35fs$-long pulses at $5KHz$ repetition rate, with an energy of $3mJ$. After a series of beamsplitter for diagnostics and ancillary setups, the output is split: 10% of the output serves as the pump, exciting the sample and triggering a transient dynamical response. The remaining 90% of the power is directed to the HHG source (XUUS$^{TM)}$, which converts the input near-infrared radiation into the XUV domain. A translation stage in the pump arm controls the relative delay, allowing the sample to be probed at successive instants of its evolution. For systems with reproducible dynamics, repeating the measurement over multiple time delays enables the reconstruction of the full transient dynamics.

The realization of such an instrument required overcoming significant technical challenges in both pump and probe arms. Careful optical design, mechanical implementation, and diagnostic validation were essential to ensure that the system met the stringent requirements of ultrafast ptychography. In a HHG-based ultrafast system, the ultimate performances are directly linked to the quality of the primary light source. For this reason, significant effort was devoted to the characterization and optimization of the primary laser system. The optimization process was enabled by a dedicated diagnostic section, which included both a beam profiler and a FROG device. The beam profiler provided detailed information on the spatial characteristics of the beam and allowed correction of astigmatism, while the FROG retrieved the temporal and spectral profiles. Final measurements indicated a pulse duration of $35.6fs$ (FWHM) and a spectral bandwidth of $25.5nm$, corresponding to near-transform-limited pulsed operation.

Following the primary source, the HHG stage was customized to enable stable delivery of XUV radiation into the experimental chamber. Mechanical modifications, realized in collaboration with the workshop of the University of Pavia, included a mechanism to vertically mount the rejectors to raise the beam height, and custom flanges for improved cooling and alignment.

The design of the probe branch and microscope was constrained by the physically available space on the optical table and the aim to reach a resolution comparable to the XUV wavelength at the sample plane. A target resolution of $15nm$ was defined based on harmonic generation in He, optimized for emission near $13nm$. This dictated both

the specifications of the detector and the size of illumination at the sample plane. The AXIS detector, with its small pixel size, large active area, and sCMOS technology, was selected to meet these needs while providing a frame rate of $24Hz$ compared to CCD technologies. The demagnification of the probe beam was carefully derived and, through extensive ray-tracing performed with ShadowOui, realized by exploring different focusing optics schemes.

Three geometries, ellipsoidal, toroidal, and z-fold, were compared under equivalent source-to-sample distances, incorporating realistic slope errors and misalignments. Ray-tracing and ptychographic simulations demonstrated that, despite a slightly aberrated probe profile, an off-axis z-fold offered the most robust performance, balancing stability against substrate errors, ease of alignment, and cost-effectiveness. This design was further refined using the detailed distances from the source to the experimental chamber, focusing on operation at $12.9nm$, corresponding to the shorter yet most demanding wavelength produced by the XUUS^{TM}. Source sizes of $30 - 50\mu m$ $1/e^2$ were considered, consistent with supplier data, and realistic slope errors were introduced to test the resilience of the system. Final simulations defined the incidence angles, radii of curvature, mirror dimensions, and offsets. Parallel to the optical design, the properties of the coatings applied to the mirrors in the z-fold were studied. Multilayer coatings were optimized to achieve high reflectivity while accounting for potential spectral fluctuations of the source and uncertainties in the coating deposition processes. The resulting specifications ensure beamline functionality even under suboptimal conditions. The mirrors were manufactured by NTT-AT and SESO Thales, and their surface quality was verified through independent metrology at ELETTRA and supplier-provided measurements, respectively. While the NTT-AT mirrors did not completely meet the design requirements, the SESO Thales optics demonstrated compliance, confirming their suitability for the microscope.

The robustness of the optical design was further validated through ptychographic reconstructions using simulated datasets. The outputs from ShadowOUI, supplemented with phase information obtained via the Gerchberg-Saxton algorithm, were used to generate diffraction patterns from Siemens stars and distributions of core-shell nanoparticles. Reconstructions demonstrated that calibration with the Siemens star enabled reliable recovery of nanoparticle structures, clearly resolving both core and shell. These results confirmed the adequacy of the z-fold geometry and the feasibility of quantitative imaging at the targeted resolution.

The experimental chamber housing the microscope was designed and fabricated in

collaboration with ALCA Technology. A complete 3D model was constructed to anticipate alignment constraints with the rest of the beamline. The chamber was engineered to support operations both in transmission and reflection geometries. Multiple motorized stages allow alignment of optics, samples, and apertures, while the AXIS detector is mounted on stages providing both transverse and longitudinal motion, enabling tuning of the numerical aperture and direct beam imaging. Ultimately, the chamber is suitable for high-vacuum environments and incorporates low-permeability materials, custom flange layouts and other key engineering features.

The pump branch was built to preserve pulse quality while providing tunable fluence and polarization at the sample. Low-GDD reflective optics were prioritized, transmissive elements were minimized, and thin polarizers and waveplates were integrated to control power and polarization. Telescopes were introduced when required, and a delay-stage provides precise pump-probe timing with fs accuracy. The careful matching of pump and probe arms ensured time-zero determination with sub-$3ps$ uncertainty and reliable implementation of ultrafast pump-probe experiments.

From design to commissioning, this step-by-step approach ultimately led to the realization of an instrument capable of fulfilling the stringent requirements of ultrafast ptychography. The probe arm can operate with two distinct harmonic combs (from Ar or He), while multilayer-coated mirrors allow the selection of a single harmonic order, yielding quasi-monochromatic conditions that favouts ptychography reconstructions. The HHG source, operated in argon at $74Torr$, was estimated to have a source size of $3.582\mu m$, a divergence of $0.75mrad$ in units of σ, and a flux of approximately $10^{11}\ ph/s$ (measured with an in-line photodiode). This ensures sufficient signal-to-noise ratios to populate the full dynamic range of the detector, a prerequisite for successful reconstructions at nominal spatial resolution. The spatial resolution of the microscope is theoretically limited at $15nm$ with a field of view extending to tens or hundreds of micrometers, depending on the parameters of the scanning ptychography acquisition algorithm. Reconstructions performed on simulated datasets implementing the real source characteristics and the detector specifications demonstrated the capability to resolve not only the overall morphology of test objects such as Siemens Stars, but also fine structural features of core-shell nanoparticles. The flexibility of the system was further enhanced by the pump branch. By adjusting polarization, fluence (up to $42.6mJ/cm^2$ by construction), and delay, the instrument can access different excitation regimes in the sample, ranging from weak perturbations to strong photoexcitation. The beamline thus constitutes a laboratory-scale platform for

time-resolved coherent imaging. While modern free-electron lasers can achieve temporal resolutions in the tens-of-femtoseconds regime using dedicated timing diagnostics, these measurements typically require shot-to-shot timing correction due to intrinsic arrival-time jitter. In contrast, HHG-based sources inherit the timing stability of the driving laser, enabling intrinsically synchronized pump–probe measurements in a compact laboratory environment.

Beyond the technical milestones achieved, the originality of this work lies in the conception and realization of a beamline designed exclusively for time-resolved ptychography at the laboratory scale. Unlike beamlines adapted for multi-purpose operation, every design choice presented in this dissertation was tailored for ultrafast ptychographic imaging. This optimization distinguishes the instrument from other laboratory-scale HHG beamlines. A particularly innovative aspect is the integration of advanced ray-tracing simulations with metrological data into a "digital twin" of the probe delivery system. By incorporating measured source characteristics and the actual surface profiles of the multilayer optics, the virtual model becomes a faithful replica of the physical beamline. This methodology brings three major advantages: first, it enables the development and testing of the beamline in a virtual environment, allowing design modifications to be evaluated before physical implementation; second, it provides a precise benchmark for the expected performance, guiding alignment and correction of astigmatism with quantitative confidence; and third, it offers an informed initial guess for the illumination function in ptychographic reconstructions, accelerating convergence and improving reconstruction fidelity compared to arbitrary initialization. Equally crucial was the rigorous approach to the selection and optimization of the XUV optics. The robustness of the microscope derives directly from minimizing aberrations and ensuring stable alignment, both reducing downtime and maximizing throughput during experimental campaigns. The careful definition of slope-error tolerances, coating specifications, and mirror geometries provided a beam delivery system that remains resilient to realistic imperfections in manufacturing and alignment. Additionally, the careful choice of multilayer coatings ensures both spectral selectivity and high reflectivity across the desired operating range, allowing the probe arm to deliver a photon flux sufficient to exploit the full dynamic range of the detector. This capability is essential to reach the nominal resolution of the experiment, as it guarantees the presence of scattering signals at high detection angles.

In conclusion, the contributions of this dissertation can be identified on both a conceptual and an implementation level. Conceptually, this work establishes a design strategy for

laboratory-scale instruments dedicated to ultrafast ptychography. Practically, it introduces a digital twin methodology and a systematic optical optimization workflow that together form a reproducible framework for future XUV beamlines dedicated to coherent imaging.

8.2 Future Perspectives

The most immediate developments will focus on completing the commissioning of the microscope using $\sim 30nm$ light. This will involve testing benchmark samples, such as a Siemens Star, in static conditions and applying the reconstruction methodology validated on synthetic samples to experimental data. Once the robustness of the acquisition and reconstruction protocols is established, they will be applied to image core-shell nanoparticles. Following the validation in static conditions, the following steps will involve the introduction of the pump-probe detection scheme on functionalized materials.

A particular compelling case is the study of nanoparticle (NP) superlattices, which represent typical self-assembled functional materials [1]. The methodology developed here will enable systematic investigations of changes in electron–phonon coupling mediated by end-group chemistry and ligand-ligand interactions, which serve as control parameters for tuning band structure and lattice stiffness [18]. In thiolated-NP systems, ligand length is known to drive transitions from crystalline to liquid-like phases via an intermediate hexatic state, with thermal and optical responses reminiscent of liquid crystals. Ultrafast diffraction studies have already shown that in such supracrystals, van der Waals interactions can generate stiffness levels comparable to covalently bonded crystals by tuning the length of the ligands and their interdigitation [155]. Ultrafast ptychography, by combining femtosecond temporal resolution with nanometric spatial contrast, is ideally suited to probe the role of grain boundaries, discontinuities, and heterogeneity in the supramolecular photo-response, phenomena which require both spatial and temporal resolution to be understood. The full potential of the microscope will then be explored by extending these measurements to shorter wavelengths, targeting $13nm$ operation. At this regime, the system is expected to achieve its ultimate spatial resolution of $\sim 15nm$, allowing the observation of structural dynamics at smaller scales.

Looking on a medium-term perspective, the beamline can be equipped with a dedicated spectrometer, whose development at design level is already in progress. This will allow time-resolved multispectral imaging experiments to be carried out quantitatively, enabling chemically resolved imaging, elemental identification, and the precise mapping

of elemental distributions within samples [14]. As a benchmark case, the study will be extended to binary NP superlattices composed of elements such as Si and Ge. These systems are of particular interest because of size-dependent strain effects on their band structure, which can be activated by light pulses. Given the multibeam nature of the setup, spectrally resolved ultrafast microscopy will be performed in the time domain, exploiting contrast at the Si L-edge and the Ge M-edge. This will allow selective probing of the contributions from the two sublattices, while simultaneously monitoring light-induced band-gap modulation.

Since the photon energies available from HHG sources cover the M-edges of key transition metals such as Fe, Co, and Ni, ultrafast soft X-ray magnetic imaging is another promising opportunity for future studies. Potentially, this will open the possibility to study ultrafast magnetic dynamics, including the formation and evolution of topological spin textures such as skyrmions [21–23]. For the same reason, by extending operation into the water window, the same approach can be applied to investigate biological samples, exploiting the natural contrast provided by soft X-rays between carbon-based materials and water [90, 136, 138].

The methodological framework established in this work also opens the possibility of extending ultrafast imaging to OAM beams [82, 83, 100]. By incorporating spiral zone plates into the current simulative environment in ShadowOUI, it becomes feasible to evaluate the generation of structured XUV beams specifically designed to interrogate and visualize chirally active materials, paving the way for future experimental implementations.

Bibliography

[1] "Nanoparticles: From Theory to Application". en. In: ed. by Günter Schmid. Edition: 1. Wiley, Aug. 2010. ISBN: 978-3-527-32589-4 978-3-527-63154-4. DOI: 10.1002/9783527631544. URL: https://onlinelibrary.wiley.com/doi/book/10.1002/9783527631544 (visited on 09/08/2025).

[2] M.-P. Pileni. "Self-assembly of inorganic nanocrystals: fabrication and collective intrinsic properties". eng. In: *Acc Chem Res* 40.8 (Aug. 2007), pp. 685–693. ISSN: 0001-4842. DOI: 10.1021/ar6000582.

[3] Hideyuki Nakanishi et al. "Dynamic internal gradients control and direct electric currents within nanostructured materials". eng. In: *Nat Nanotechnol* 6.11 (Oct. 2011), pp. 740–746. ISSN: 1748-3395. DOI: 10.1038/nnano.2011.165.

[4] Mrinmoy De, Partha S. Ghosh, and Vincent M. Rotello. "Applications of Nanoparticles in Biology". en. In: *Advanced Materials* 20.22 (2008). _eprint: https://advanced.onlinelibrary.wiley.com/doi/pdf/10.1002/adma.200703183, pp. 4225–4241. ISSN: 1521-4095. DOI: 10.1002/adma.200703183. URL: https://onlinelibrary.wiley.com/doi/abs/10.1002/adma.200703183 (visited on 03/16/2026).

[5] B.D. Patterson et al. "Ultrafast phenomena at the nanoscale: Novel science opportunities at the swissfel X-ray laser". en. In: *Europhysics News* 41.5 (Sept. 2010), pp. 28–32. ISSN: 0531-7479, 1432-1092. DOI: 10.1051/epn/2010503. URL: http://www.europhysicsnews.org/10.1051/epn/2010503 (visited on 05/15/2025).

[6] Peter W. Hawkes and John C. H. Spence, eds. *Springer Handbook of Microscopy*. en. Springer Handbooks. Cham: Springer International Publishing, 2019. ISBN: 978-3-030-00068-4 978-3-030-00069-1. DOI: 10.1007/978-3-030-00069-1. URL: http://link.springer.com/10.1007/978-3-030-00069-1 (visited on 05/13/2025).

[7] Chunli Bai. *Scanning Tunneling Microscopy and Its Application*. en. Google-Books-ID: 3Q08jRmmtrkC. Springer Science & Business Media, Aug. 2000. ISBN: 978-3-540-65715-6.

[8] Majed Chergui and Ahmed H. Zewail. "Electron and X-Ray Methods of Ultrafast Structural Dynamics: Advances and Applications". en. In: *ChemPhysChem* 10.1 (2009). _eprint: https://onlinelibrary.wiley.com/doi/pdf/10.1002/cphc.200800667, pp. 28–43. ISSN: 1439-7641. DOI: 10.1002/cphc.200800667. URL: https://onlinelibrary.wiley.com/doi/abs/10.1002/cphc.200800667 (visited on 05/18/2025).

[9] Peng Li et al. "4th generation synchrotron source boosts crystalline imaging at the nanoscale". en. In: *Light Sci Appl* 11.1 (Mar. 2022), p. 73. ISSN: 2047-7538. DOI: 10.1038/s41377-022-00758-z. URL: https://www.nature.com/articles/s41377-022-00758-z (visited on 03/16/2026).

[10] Brian W. J. McNeil and Neil R. Thompson. "X-ray free-electron lasers". en. In: *Nature Photon* 4.12 (Dec. 2010). Publisher: Nature Publishing Group, pp. 814–821. ISSN: 1749-4893. DOI: 10.1038/nphoton.2010.239. URL: https://www.nature.com/articles/nphoton.2010.239 (visited on 05/13/2025).

[11] John Rodenburg and Andrew Maiden. "Ptychography". en. In: *Springer Handbook of Microscopy*. Ed. by Peter W. Hawkes and John C. H. Spence. Series Title: Springer Handbooks. Cham: Springer International Publishing, 2019, pp. 819–904. ISBN: 978-3-030-00068-4 978-3-030-00069-1. DOI: 10.1007/978-3-030-00069-1_17. URL: http://link.springer.com/10.1007/978-3-030-00069-1_17 (visited on 01/11/2025).

[12] Pierre Thibault et al. “High-Resolution Scanning X-ray Diffraction Microscopy”. In: *Science* 321.5887 (July 2008). Publisher: American Association for the Advancement of Science, pp. 379–382. DOI: 10.1126/science.1158573. URL: https://www.science.org/doi/abs/10.1126/science.1158573 (visited on 05/15/2025).

[13] A. M. Maiden, M. J. Humphry, and J. M. Rodenburg. “Ptychographic transmission microscopy in three dimensions using a multi-slice approach”. EN. In: *J. Opt. Soc. Am. A, JOSAA* 29.8 (Aug. 2012). Publisher: Optica Publishing Group, pp. 1606–1614. ISSN: 1520-8532. DOI: 10.1364/JOSAA.29.001606. URL: https://opg.optica.org/josaa/abstract.cfm?uri=josaa-29-8-1606 (visited on 05/17/2025).

[14] Bosheng Zhang et al. “Ptychographic hyperspectral spectromicroscopy with an extreme ultraviolet high harmonic comb”. EN. In: *Opt. Express, OE* 24.16 (Aug. 2016). Publisher: Optica Publishing Group, pp. 18745–18754. ISSN: 1094-4087. DOI: 10.1364/OE.24.018745. URL: https://opg.optica.org/oe/abstract.cfm?uri=oe-24-16-18745 (visited on 09/08/2025).

[15] Robert M. Karl et al. “Full-field imaging of thermal and acoustic dynamics in an individual nanostructure using tabletop high harmonic beams”. In: *Science Advances* 4.10 (Oct. 2018). Publisher: American Association for the Advancement of Science, eaau4295. DOI: 10.1126/sciadv.aau4295. URL: https://www.science.org/doi/10.1126/sciadv.aau4295 (visited on 05/17/2025).

[16] Dennis F. Gardner et al. “Subwavelength coherent imaging of periodic samples using a 13.5 nm tabletop high-harmonic light source”. en. In: *Nature Photon* 11.4 (Apr. 2017). Publisher: Nature Publishing Group, pp. 259–263. ISSN: 1749-4893. DOI: 10.1038/nphoton.2017.33. URL: https://www.nature.com/articles/nphoton.2017.33 (visited on 05/17/2025).

[17] Elisabeth R. Shanblatt et al. “Quantitative Chemically Specific Coherent Diffractive Imaging of Reactions at Buried Interfaces with Few Nanometer Precision”. In: *Nano Lett.* 16.9 (Sept. 2016). Publisher: American Chemical

Society, pp. 5444–5450. ISSN: 1530-6984. DOI: 10.1021/acs.nanolett.6b01864. URL: https://doi.org/10.1021/acs.nanolett.6b01864 (visited on 05/17/2025).

[18] Yoonseob Kim et al. "Stretchable nanoparticle conductors with self-organized conductive pathways". eng. In: *Nature* 500.7460 (Aug. 2013), pp. 59–63. ISSN: 1476-4687. DOI: 10.1038/nature12401.

[19] Elena V. Shevchenko et al. "Structural diversity in binary nanoparticle superlattices". eng. In: *Nature* 439.7072 (Jan. 2006), pp. 55–59. ISSN: 1476-4687. DOI: 10.1038/nature04414.

[20] Jennifer L. Russell et al. "Binary Colloidal Crystal Films Grown by Vertical Evaporation of Silica Nanoparticle Suspensions". eng. In: *Langmuir* 33.39 (Oct. 2017), pp. 10366–10373. ISSN: 1520-5827. DOI: 10.1021/acs.langmuir.7b02553.

[21] Sergey Zayko et al. "Ultrafast high-harmonic nanoscopy of magnetization dynamics". en. In: *Nat Commun* 12.1 (Nov. 2021), p. 6337. ISSN: 2041-1723. DOI: 10.1038/s41467-021-26594-0. URL: https://www.nature.com/articles/s41467-021-26594-0 (visited on 03/30/2025).

[22] Chan La-O-Vorakiat et al. "Ultrafast Demagnetization Dynamics at the M Edges of Magnetic Elements Observed Using a Tabletop High-Harmonic Soft X-Ray Source". In: *Phys. Rev. Lett.* 103.25 (Dec. 2009). Publisher: American Physical Society, p. 257402. DOI: 10.1103/PhysRevLett.103.257402. URL: https://link.aps.org/doi/10.1103/PhysRevLett.103.257402 (visited on 09/08/2025).

[23] Stefan Mathias et al. "Ultrafast element-specific magnetization dynamics of complex magnetic materials on a table-top". In: *Journal of Electron Spectroscopy and Related Phenomena* 189 (Aug. 2013), pp. 164–170. ISSN: 0368-2048. DOI: 10.1016/j.elspec.2012.11.013. URL: https://www.sciencedirect.com/science/article/pii/S0368204812001648 (visited on 09/08/2025).

[24] Robert Hooke. *Micrographia Or Some Physiological Descriptions of Minute Bodies*. en. Google-Books-ID: K5gBDJhvSMQC. Cosimo, Inc., Nov. 2007. ISBN: 978-1-60206-963-3.

[25] Yves F. Dufrêne et al. "Imaging modes of atomic force microscopy for application in molecular and cell biology". en. In: *Nature Nanotech* 12.4 (Apr. 2017). Publisher: Nature Publishing Group, pp. 295–307. ISSN: 1748-3395. DOI: 10.1038/nnano.2017.45. URL: https://www.nature.com/articles/nnano.2017.45.

[26] P. K. Hansma et al. "Scanning Tunneling Microscopy and Atomic Force Microscopy: Application to Biology and Technology". In: *Science* 242.4876 (1988), pp. 209–216. DOI: 10.1126/science.3051380. eprint: https://www.science.org/doi/pdf/10.1126/science.3051380. URL: https://www.science.org/doi/abs/10.1126/science.3051380.

[27] Ahmed H. Zewail. "Micrographia of the twenty-first century: from camera obscura to 4D microscopy". In: *Philosophical Transactions of the Royal Society A: Mathematical, Physical and Engineering Sciences* 368.1914 (Mar. 2010). Publisher: Royal Society, pp. 1191–1204. DOI: 10.1098/rsta.2009.0265. URL: https://royalsocietypublishing.org/doi/full/10.1098/rsta.2009.0265 (visited on 10/12/2025).

[28] E. Abbe. "Beiträge zur Theorie des Mikroskops und der mikroskopischen Wahrnehmung". de. In: *Archiv f. mikrosk. Anatomie* 9.1 (Dec. 1873), pp. 413–468. ISSN: 0176-7364. DOI: 10.1007/BF02956173. URL: https://doi.org/10.1007/BF02956173 (visited on 05/13/2025).

[29] Adam M. Larson. "Multiphoton microscopy". en. In: *Nature Photon* 5.1 (Jan. 2011). Publisher: Nature Publishing Group, pp. 1–1. ISSN: 1749-4893. DOI: 10.1038/nphoton.an.2010.2. URL: https://www.nature.com/articles/nphoton.an.2010.2 (visited on 05/13/2025).

[30] G. Binnig, C. F. Quate, and Ch. Gerber. "Atomic Force Microscope". In: *Phys. Rev. Lett.* 56.9 (Mar. 1986). Publisher: American Physical Society, pp. 930–933. DOI: 10.1103/PhysRevLett.56.930. URL:

https://link.aps.org/doi/10.1103/PhysRevLett.56.930 (visited on 05/13/2025).

[31] Louis de Broglie. "XXXV. A tentative theory of light quanta". In: *The London, Edinburgh, and Dublin Philosophical Magazine and Journal of Science* 47.278 (Feb. 1924). Publisher: Taylor & Francis _eprint: https://doi.org/10.1080/14786442408634378, pp. 446–458. ISSN: 1941-5982. DOI: 10.1080/14786442408634378. URL: https://doi.org/10.1080/14786442408634378 (visited on 05/13/2025).

[32] E. Schrödinger. "An Undulatory Theory of the Mechanics of Atoms and Molecules". In: *Phys. Rev.* 28.6 (Dec. 1926). Publisher: American Physical Society, pp. 1049–1070. DOI: 10.1103/PhysRev.28.1049. URL: https://link.aps.org/doi/10.1103/PhysRev.28.1049 (visited on 05/13/2025).

[33] C. Davisson and L. H. Germer. "Diffraction of Electrons by a Crystal of Nickel". In: *Phys. Rev.* 30.6 (Dec. 1927). Publisher: American Physical Society, pp. 705–740. DOI: 10.1103/PhysRev.30.705. URL: https://link.aps.org/doi/10.1103/PhysRev.30.705 (visited on 05/13/2025).

[34] M. Knoll and E. Ruska. "Das Elektronenmikroskop". de. In: *Z. Physik* 78.5 (May 1932), pp. 318–339. ISSN: 0044-3328. DOI: 10.1007/BF01342199. URL: https://doi.org/10.1007/BF01342199 (visited on 05/13/2025).

[35] Jacques Dubochet et al. "Cryo-electron microscopy of vitrified specimens". en. In: *Quarterly Reviews of Biophysics* 21.2 (May 1988), pp. 129–228. ISSN: 1469-8994, 0033-5835. DOI: 10.1017/S0033583500004297. URL: https://www.cambridge.org/core/journals/quarterly-reviews-of-biophysics/article/abs/cryoelectron-microscopy-of-vitrified-specimens/471BB7106E820E9B88F1FAED9875C277# (visited on 05/13/2025).

[36] Rafael Fernandez-Leiro and Sjors H. W. Scheres. "Unravelling biological macromolecules with cryo-electron microscopy". en. In: *Nature* 537.7620 (Sept. 2016). Publisher: Nature Publishing Group, pp. 339–346. ISSN: 1476-4687. DOI: 10.1038/nature19948. URL: https://www.nature.com/articles/nature19948 (visited on 05/13/2025).

[37] Wayne E. King et al. “Ultrafast electron microscopy in materials science, biology, and chemistry”. In: *Journal of Applied Physics* 97.11 (June 2005), p. 111101. ISSN: 0021-8979. DOI: 10.1063/1.1927699. URL: https://doi.org/10.1063/1.1927699 (visited on 05/13/2025).

[38] Zhensheng Tao et al. “Space charge effects in ultrafast electron diffraction and imaging”. In: *Journal of Applied Physics* 111.4 (Feb. 2012), p. 044316. ISSN: 0021-8979. DOI: 10.1063/1.3685747. URL: https://doi.org/10.1063/1.3685747 (visited on 05/13/2025).

[39] Wilhelm Conrad Röntgen. *Eine neue Art von Strahlen*. ger. Würzburg : Verlag und Druck der Stahel’schen K. Hof- und Universitäts-Buch- und Kunsthandlung, 1896. URL: http://archive.org/details/eineneueartvonst00rntg (visited on 05/13/2025).

[40] P. K. Spiegel. “The first clinical X-ray made in America–100 years”. eng. In: *AJR Am J Roentgenol* 164.1 (Jan. 1995), pp. 241–243. ISSN: 0361-803X. DOI: 10.2214/ajr.164.1.7998549.

[41] F. R. Elder et al. “Radiation from Electrons in a Synchrotron”. In: *Phys. Rev.* 71.11 (June 1947). Publisher: American Physical Society, pp. 829–830. DOI: 10.1103/PhysRev.71.829.5. URL: https://link.aps.org/doi/10.1103/PhysRev.71.829.5 (visited on 05/13/2025).

[42] Edwin M. McMillan. “The Synchrotron—A Proposed High Energy Particle Accelerator”. In: *Phys. Rev.* 68.5-6 (Sept. 1945). Publisher: American Physical Society, pp. 143–144. DOI: 10.1103/PhysRev.68.143. URL: https://link.aps.org/doi/10.1103/PhysRev.68.143 (visited on 05/13/2025).

[43] Klaus Wille (prof.) *The Physics of Particle Accelerators: An Introduction*. en. Google-Books-ID: k1STXLP4lkgC. Oxford University Press, 2000. ISBN: 978-0-19-850549-5.

[44] C. Pellegrini, A. Marinelli, and S. Reiche. “The physics of x-ray free-electron lasers”. In: *Rev. Mod. Phys.* 88.1 (Mar. 2016). Publisher: American Physical Society, p. 015006. DOI: 10.1103/RevModPhys.88.015006. URL:

https://link.aps.org/doi/10.1103/RevModPhys.88.015006 (visited on 05/13/2025).

[45] Daniel Nilsson. "Zone Plates for Hard X-Ray Free-Electron Lasers". eng. In: (2013). Publisher: KTH Royal Institute of Technology. URL: https://urn.kb.se/resolve?urn=urn:nbn:se:kth:diva-122161 (visited on 05/13/2025).

[46] E. Allaria et al. "Highly coherent and stable pulses from the FERMI seeded free-electron laser in the extreme ultraviolet". en. In: *Nature Photon* 6.10 (Oct. 2012). Publisher: Nature Publishing Group, pp. 699–704. ISSN: 1749-4893. DOI: 10.1038/nphoton.2012.233. URL: https://www.nature.com/articles/nphoton.2012.233 (visited on 05/13/2025).

[47] M. Lewenstein et al. "Theory of high-harmonic generation by low-frequency laser fields". In: *Phys. Rev. A* 49.3 (Mar. 1994). Publisher: American Physical Society, pp. 2117–2132. DOI: 10.1103/PhysRevA.49.2117. URL: https://link.aps.org/doi/10.1103/PhysRevA.49.2117 (visited on 05/13/2025).

[48] A. McPherson et al. "Studies of multiphoton production of vacuum-ultraviolet radiation in the rare gases". EN. In: *J. Opt. Soc. Am. B, JOSAB* 4.4 (Apr. 1987). Publisher: Optica Publishing Group, pp. 595–601. ISSN: 1520-8540. DOI: 10.1364/JOSAB.4.000595. URL: https://opg.optica.org/josab/abstract.cfm?uri=josab-4-4-595 (visited on 05/13/2025).

[49] Francesca Calegari et al. "Advances in attosecond science". en. In: *J. Phys. B: At. Mol. Opt. Phys.* 49.6 (Feb. 2016). Publisher: IOP Publishing, p. 062001. ISSN: 0953-4075. DOI: 10.1088/0953-4075/49/6/062001. URL: https://dx.doi.org/10.1088/0953-4075/49/6/062001 (visited on 05/13/2025).

[50] Tenio Popmintchev et al. "Bright Coherent Ultrahigh Harmonics in the keV X-ray Regime from Mid-Infrared Femtosecond Lasers". en. In: 336 (2012).

[51] Anne L'Huillier. "Nobel Lecture: The route to attosecond pulses". en. In: *Rev. Mod. Phys.* 96.3 (Aug. 2024), p. 030503. ISSN: 0034-6861, 1539-0756. DOI: 10.1103/RevModPhys.96.030503. URL: https://link.aps.org/doi/10.1103/RevModPhys.96.030503 (visited on 06/24/2025).

[52] David T. Attwood and Anne Sakdinawat. *X-rays and extreme ultraviolet radiation: principles and applications*. en. 2nd ed. Cambridge: Cambridge university press, 2016. ISBN: 978-1-107-06289-4.

[53] Rei Kitamura, Laurent Pilon, and Miroslaw Jonasz. "Optical constants of silica glass from extreme ultraviolet to far infrared at near room temperature". EN. In: *Appl. Opt., AO* 46.33 (Nov. 2007). Publisher: Optica Publishing Group, pp. 8118–8133. ISSN: 2155-3165. DOI: 10.1364/AO.46.008118. URL: https://opg.optica.org/ao/abstract.cfm?uri=ao-46-33-8118 (visited on 05/14/2025).

[54] A. Snigirev et al. "A compound refractive lens for focusing high-energy X-rays". In: *Nature* 384.6604 (Nov. 1996), pp. 49–51. ISSN: 1476-4687. DOI: 10.1038/384049a0. URL: https://doi.org/10.1038/384049a0.

[55] Andreas Schropp et al. "Full spatial characterization of a nanofocused x-ray free-electron laser beam by ptychographic imaging". en. In: *Sci Rep* 3.1 (Apr. 2013). Publisher: Nature Publishing Group, p. 1633. ISSN: 2045-2322. DOI: 10.1038/srep01633. URL: https://www.nature.com/articles/srep01633 (visited on 05/15/2025).

[56] Albert V. Baez. "Fresnel Zone Plate for Optical Image Formation Using Extreme Ultraviolet and Soft X Radiation". EN. In: *J. Opt. Soc. Am., JOSA* 51.4 (Apr. 1961). Publisher: Optica Publishing Group, pp. 405–412. DOI: 10.1364/JOSA.51.000405. URL: https://opg.optica.org/josa/abstract.cfm?uri=josa-51-4-405 (visited on 05/14/2025).

[57] Cameron M. Kewish et al. "Optimum design of aspect ratio limited x-ray zone plates". en. In: *Optica* 11.2 (Feb. 2024), p. 251. ISSN: 2334-2536. DOI: 10.1364/OPTICA.505082. URL: https://opg.optica.org/abstract.cfm?URI=optica-11-2-251 (visited on 05/14/2025).

[58] A. Sorrentino et al. "MISTRAL: a transmission soft X-ray microscopy beamline for cryo nano-tomography of biological samples and magnetic domains imaging". en. In: *J Synchrotron Rad* 22.4 (July 2015). Publisher: International Union of Crystallography, pp. 1112–1117. ISSN: 1600-5775. DOI: 10.1107/S1600577515008632. URL: https://journals.iucr.org/s/issues/2015/04/00/vv5105/ (visited on 03/22/2026).

[59] A. Gianoncelli et al. "Current status of the TwinMic beamline at Elettra: a soft X-ray transmission and emission microscopy station". en. In: *J Synchrotron Rad* 23.6 (Nov. 2016). Publisher: International Union of Crystallography, pp. 1526–1537. ISSN: 1600-5775. DOI: 10.1107/S1600577516014405. URL: https://journals.iucr.org/s/issues/2016/06/00/ig5036/ (visited on 03/22/2026).

[60] Ray Conley et al. "Wedged multilayer Laue lens". eng. In: *Rev Sci Instrum* 79.5 (May 2008), p. 053104. ISSN: 0034-6748. DOI: 10.1063/1.2924209.

[61] B. L. Henke, E. M. Gullikson, and J. C. Davis. "X-Ray Interactions: Photoabsorption, Scattering, Transmission, and Reflection at E = 50-30,000 eV, Z = 1-92". In: *Atomic Data and Nuclear Data Tables* 54.2 (July 1993), pp. 181–342. ISSN: 0092-640X. DOI: 10.1006/adnd.1993.1013. URL: https://www.sciencedirect.com/science/article/pii/S0092640X83710132 (visited on 03/21/2026).

[62] Paul Kirkpatrick and A. V. Baez. "Formation of Optical Images by X-Rays". EN. In: *JOSA, Vol. 38, Issue 9, pp. 766-774* (Sept. 1948). Publisher: Optica Publishing Group. DOI: 10.1364/JOSA.38.000766. URL: https://opg.optica.org/josa/abstract.cfm?uri=josa-38-9-766 (visited on 05/14/2025).

[63] Julio Cesar da Silva et al. "Efficient concentration of high-energy x-rays for diffraction-limited imaging resolution". EN. In: *Optica, OPTICA* 4.5 (May 2017). Publisher: Optica Publishing Group, pp. 492–495. ISSN: 2334-2536. DOI: 10.1364/OPTICA.4.000492. URL: https://opg.optica.org/optica/abstract.cfm?uri=optica-4-5-492 (visited on 05/14/2025).

[64] Saša Bajt et al. “Design and performance of capping layers for extreme-ultraviolet multilayer mirrors”. EN. In: *Appl. Opt., AO* 42.28 (Oct. 2003). Publisher: Optica Publishing Group, pp. 5750–5758. ISSN: 2155-3165. DOI: 10.1364/AO.42.005750. URL: https://opg.optica.org/ao/abstract.cfm?uri=ao-42-28-5750 (visited on 05/14/2025).

[65] Sasa Bajt et al. “Improved reflectance and stability of Mo/Si multilayers”. In: *OE* 41.8 (Aug. 2002). Publisher: SPIE, pp. 1797–1804. ISSN: 0091-3286, 1560-2303. DOI: 10.1117/1.1489426. URL: https://www.spiedigitallibrary.org/journals/optical-engineering/volume-41/issue-8/0000/Improved-reflectance-and-stability-of-MoSi-multilayers/10.1117/1.1489426.full (visited on 03/22/2026).

[66] *Diffraction-limited imaging in a scanning transmission x-ray microscope - ScienceDirect*. URL: https://www.sciencedirect.com/science/article/abs/pii/0030401891900167 (visited on 05/15/2025).

[67] Jianwei Miao. “Computational microscopy with coherent diffractive imaging and ptychography”. en. In: *Nature* 637.8045 (Jan. 2025), pp. 281–295. ISSN: 0028-0836, 1476-4687. DOI: 10.1038/s41586-024-08278-z. URL: https://www.nature.com/articles/s41586-024-08278-z (visited on 03/30/2025).

[68] D. Sayre. “Some implications of a theorem due to Shannon”. en. In: *Acta Cryst* 5.6 (Nov. 1952). Publisher: International Union of Crystallography, pp. 843–843. ISSN: 0365-110X. DOI: 10.1107/S0365110X52002276. URL: https://journals.iucr.org/q/issues/1952/06/00/a00763/ (visited on 05/15/2025).

[69] R. Gerchberg. “A practical algorithm for the determination of phase from image and diffraction plane pictures”. In: *Optik* (1972). URL: https://www.semanticscholar.org/paper/A-practical-algorithm-for-the-determination-of-from-Gerchberg/5a114d3050a0a33f8cc6d28d55fa048a5a7ab6f2 (visited on 05/15/2025).

[70] J. R. Fienup. “Reconstruction of an object from the modulus of its Fourier transform”. EN. In: *Opt. Lett., OL* 3.1 (July 1978). Publisher: Optica Publishing Group, pp. 27–29. ISSN: 1539-4794. DOI: 10.1364/OL.3.000027. URL: https://opg.optica.org/ol/abstract.cfm?uri=ol-3-1-27 (visited on 05/15/2025).

[71] J. N. Cederquist et al. “Phase retrieval from experimental far-field speckle data”. EN. In: *Opt. Lett., OL* 13.8 (Aug. 1988). Publisher: Optica Publishing Group, pp. 619–621. ISSN: 1539-4794. DOI: 10.1364/OL.13.000619. URL: https://opg.optica.org/ol/abstract.cfm?uri=ol-13-8-619 (visited on 05/15/2025).

[72] M. J. Pérez-Ilzarbe, M. Nieto-Vesperinas, and R. Navarro. “Phase retrieval from experimental far-field intensity data”. EN. In: *J. Opt. Soc. Am. A, JOSAA* 7.3 (Mar. 1990). Publisher: Optica Publishing Group, pp. 434–440. ISSN: 1520-8532. DOI: 10.1364/JOSAA.7.000434. URL: https://opg.optica.org/josaa/abstract.cfm?uri=josaa-7-3-434 (visited on 05/15/2025).

[73] Jianwei Miao et al. “Extending the methodology of X-ray crystallography to allow imaging of micrometre-sized non-crystalline specimens”. en. In: *Nature* 400.6742 (July 1999). Publisher: Nature Publishing Group, pp. 342–344. ISSN: 1476-4687. DOI: 10.1038/22498. URL: https://www.nature.com/articles/22498 (visited on 05/15/2025).

[74] Friso van der Veen and Franz Pfeiffer. “Coherent x-ray scattering”. en. In: *J. Phys.: Condens. Matter* 16.28 (July 2004), p. 5003. ISSN: 0953-8984. DOI: 10.1088/0953-8984/16/28/020. URL: https://dx.doi.org/10.1088/0953-8984/16/28/020 (visited on 05/15/2025).

[75] R. Hegerl and W. Hoppe. “Dynamische Theorie der Kristallstrukturanalyse durch Elektronenbeugung im inhomogenen Primärstrahlwellenfeld”. de. In: *Berichte der Bunsengesellschaft für physikalische Chemie* 74.11 (1970). _eprint: https://onlinelibrary.wiley.com/doi/pdf/10.1002/bbpc.19700741112, pp. 1148–1154. ISSN: 0005-9021. DOI: 10.1002/bbpc.19700741112. URL: https:

//onlinelibrary.wiley.com/doi/abs/10.1002/bbpc.19700741112 (visited on 05/15/2025).

[76] J. M. Rodenburg and R. H. T. Bates. "The theory of super-resolution electron microscopy via Wigner-distribution deconvolution". In: *Philosophical Transactions of the Royal Society of London. Series A: Physical and Engineering Sciences* 339.1655 (Jan. 1997). Publisher: Royal Society, pp. 521–553. DOI: 10.1098/rsta.1992.0050. URL: https://royalsocietypublishing.org/doi/abs/10.1098/rsta.1992.0050 (visited on 05/15/2025).

[77] P. D. Nellist, B. C. McCallum, and J. M. Rodenburg. "Resolution beyond the 'information limit' in transmission electron microscopy". en. In: *Nature* 374.6523 (Apr. 1995). Publisher: Nature Publishing Group, pp. 630–632. ISSN: 1476-4687. DOI: 10.1038/374630a0. URL: https://www.nature.com/articles/374630a0 (visited on 05/15/2025).

[78] Henry N. Chapman. "Phase-retrieval X-ray microscopy by Wigner-distribution deconvolution". In: *Ultramicroscopy* 66.3 (Dec. 1996), pp. 153–172. ISSN: 0304-3991. DOI: 10.1016/S0304-3991(96)00084-8. URL: https://www.sciencedirect.com/science/article/pii/S0304399196000848 (visited on 05/15/2025).

[79] J. M. Rodenburg et al. "Hard-X-Ray Lensless Imaging of Extended Objects". In: *Phys. Rev. Lett.* 98.3 (Jan. 2007). Publisher: American Physical Society, p. 034801. DOI: 10.1103/PhysRevLett.98.034801. URL: https://link.aps.org/doi/10.1103/PhysRevLett.98.034801 (visited on 05/15/2025).

[80] J. M. Rodenburg and H. M. L. Faulkner. "A phase retrieval algorithm for shifting illumination". In: *Applied Physics Letters* 85.20 (Nov. 2004), pp. 4795–4797. ISSN: 0003-6951. DOI: 10.1063/1.1823034. URL: https://doi.org/10.1063/1.1823034 (visited on 05/17/2025).

[81] Joan Vila-Comamala et al. "Characterization of high-resolution diffractive X-ray optics by ptychographic coherent diffractive imaging". en. In: *Opt. Express* 19.22 (Oct. 2011), p. 21333. ISSN: 1094-4087. DOI: 10.1364/OE.19.021333. URL: https://opg.optica.org/oe/abstract.cfm?uri=oe-19-22-21333 (visited on 05/15/2025).

[82] J. Vila-Comamala, A. Sakdinawat, and M. Guizar-Sicairos. "Characterization of x-ray phase vortices by ptychographic coherent diffractive imaging". EN. In: *Opt. Lett., OL* 39.18 (Sept. 2014). Publisher: Optica Publishing Group, pp. 5281–5284. ISSN: 1539-4794. DOI: 10.1364/OL.39.005281. URL: https://opg.optica.org/ol/abstract.cfm?uri=ol-39-18-5281 (visited on 05/15/2025).

[83] Matteo Pancaldi et al. "High-resolution ptychographic imaging at a seeded free-electron laser source using OAM beams". en. In: *Optica* 11.3 (Mar. 2024), p. 403. ISSN: 2334-2536. DOI: 10.1364/OPTICA.509745. URL: https://opg.optica.org/abstract.cfm?URI=optica-11-3-403 (visited on 04/10/2025).

[84] Giulia F. Mancini et al. "Colloidal crystal order and structure revealed by tabletop extreme ultraviolet scattering and coherent diffractive imaging". en. In: *Opt. Express* 26.9 (Apr. 2018), p. 11393. ISSN: 1094-4087. DOI: 10.1364/OE.26.011393. URL: https://opg.optica.org/abstract.cfm?URI=oe-26-9-11393 (visited on 05/17/2025).

[85] Christina L. Porter et al. "General-purpose, wide field-of-view reflection imaging with a tabletop 13 nm light source". en. In: *Optica* 4.12 (Dec. 2017), p. 1552. ISSN: 2334-2536. DOI: 10.1364/OPTICA.4.001552. URL: https://opg.optica.org/abstract.cfm?URI=optica-4-12-1552 (visited on 05/17/2025).

[86] Matthew D. Seaberg et al. "Tabletop nanometer extreme ultraviolet imaging in an extended reflection mode using coherent Fresnel ptychography". en. In: *Optica* 1.1 (July 2014), p. 39. ISSN: 2334-2536. DOI: 10.1364/OPTICA.1.000039. URL: https://opg.optica.org/abstract.cfm?URI=optica-1-1-39 (visited on 04/05/2025).

[87] Wilhelm Eschen et al. "High-speed and wide-field nanoscale table-top ptychographic EUV imaging and beam characterization with a sCMOS detector". en. In: *Opt. Express* 31.9 (Apr. 2023), p. 14212. ISSN: 1094-4087. DOI: 10.1364/OE.485779. URL: https://opg.optica.org/abstract.cfm?URI=oe-31-9-14212 (visited on 05/17/2025).

[88] Yutaka Nagata et al. “At wavelength coherent scatterometry microscope using high-order harmonics for EUV mask inspection”. en. In: *Int. J. Extrem. Manuf.* 1.3 (Sept. 2019). Publisher: IOP Publishing, p. 032001. ISSN: 2631-7990. DOI: 10.1088/2631-7990/ab3b4e. URL: https://dx.doi.org/10.1088/2631-7990/ab3b4e (visited on 05/17/2025).

[89] Peter D. Baksh et al. “Quantitative and correlative extreme ultraviolet coherent imaging of mouse hippocampal neurons at high resolution”. en. In: *Sci. Adv.* 6.18 (May 2020), eaaz3025. ISSN: 2375-2548. DOI: 10.1126/sciadv.aaz3025. URL: https://www.science.org/doi/10.1126/sciadv.aaz3025 (visited on 04/16/2025).

[90] K. Giewekemeyer et al. “Ptychographic coherent x-ray diffractive imaging in the water window”. en. In: *Opt. Express* 19.2 (Jan. 2011), p. 1037. ISSN: 1094-4087. DOI: 10.1364/OE.19.001037. URL: https://opg.optica.org/oe/abstract.cfm?uri=oe-19-2-1037 (visited on 05/17/2025).

[91] Junjing Deng et al. “Correlative 3D x-ray fluorescence and ptychographic tomography of frozen-hydrated green algae”. In: *Science Advances* 4.11 (Nov. 2018). Publisher: American Association for the Advancement of Science, eaau4548. DOI: 10.1126/sciadv.aau4548. URL: https://www.science.org/doi/10.1126/sciadv.aau4548 (visited on 05/17/2025).

[92] Mirko Holler et al. “High-resolution non-destructive three-dimensional imaging of integrated circuits”. en. In: *Nature* 543.7645 (Mar. 2017). Publisher: Nature Publishing Group, pp. 402–406. ISSN: 1476-4687. DOI: 10.1038/nature21698. URL: https://www.nature.com/articles/nature21698 (visited on 05/17/2025).

[93] Martin Dierolf et al. “Ptychographic X-ray computed tomography at the nanoscale”. en. In: *Nature* 467.7314 (Sept. 2010). Publisher: Nature Publishing Group, pp. 436–439. ISSN: 1476-4687. DOI: 10.1038/nature09419. URL: https://www.nature.com/articles/nature09419 (visited on 05/17/2025).

[94] M. Holler et al. “X-ray ptychographic computed tomography at 16 nm isotropic 3D resolution”. en. In: *Sci Rep* 4.1 (Jan. 2014). Publisher: Nature Publishing

Group, p. 3857. ISSN: 2045-2322. DOI: 10.1038/srep03857. URL: https://www.nature.com/articles/srep03857 (visited on 05/17/2025).

[95] Aaron Michelson et al. "Three-dimensional visualization of nanoparticle lattices and multimaterial frameworks". en. In: *Science* 376.6589 (Apr. 2022), pp. 203–207. ISSN: 0036-8075, 1095-9203. DOI: 10.1126/science.abk0463. URL: https://www.science.org/doi/10.1126/science.abk0463 (visited on 04/03/2025).

[96] Silvio Fuchs et al. "Optical coherence tomography with nanoscale axial resolution using a laser-driven high-harmonic source". EN. In: *Optica, OPTICA* 4.8 (Aug. 2017). Publisher: Optica Publishing Group, pp. 903–906. ISSN: 2334-2536. DOI: 10.1364/OPTICA.4.000903. URL: https://opg.optica.org/optica/abstract.cfm?uri=optica-4-8-903 (visited on 05/17/2025).

[97] Pascal Mercère et al. "Hartmann wave-front measurement at 13.4 nm with EUV/120 accuracy". EN. In: *Opt. Lett., OL* 28.17 (Sept. 2003). Publisher: Optica Publishing Group, pp. 1534–1536. ISSN: 1539-4794. DOI: 10.1364/OL.28.001534. URL: https://opg.optica.org/ol/abstract.cfm?uri=ol-28-17-1534 (visited on 05/17/2025).

[98] H. Medecki et al. "Phase-shifting point diffraction interferometer". EN. In: *Opt. Lett., OL* 21.19 (Oct. 1996). Publisher: Optica Publishing Group, pp. 1526–1528. ISSN: 1539-4794. DOI: 10.1364/OL.21.001526. URL: https://opg.optica.org/ol/abstract.cfm?uri=ol-21-19-1526 (visited on 05/17/2025).

[99] M. Odstrcil et al. "Ptychographic coherent diffractive imaging with orthogonal probe relaxation". en. In: *Opt. Express* 24.8 (Apr. 2016), p. 8360. ISSN: 1094-4087. DOI: 10.1364/OE.24.008360. URL: https://opg.optica.org/abstract.cfm?URI=oe-24-8-8360 (visited on 05/17/2025).

[100] Antonios Pelekanidis et al. "Generation Dynamics of Broadband Extreme Ultraviolet Vortex Beams". en. In: *ACS Photonics* 12.3 (Mar. 2025), pp. 1638–1649. ISSN: 2330-4022, 2330-4022. DOI:

10.1021/acsphotonics.4c02516. URL: https://pubs.acs.org/doi/10.1021/acsphotonics.4c02516 (visited on 04/17/2025).

[101] Jérémy R. Rouxel et al. "Hard X-ray helical dichroism of disordered molecular media". In: *Nat. Photon.* 16.8 (Aug. 2022), pp. 570–574. ISSN: 1749-4885, 1749-4893. DOI: 10.1038/s41566-022-01022-x. URL: https://www.nature.com/articles/s41566-022-01022-x (visited on 06/18/2023).

[102] Joseph W. Goodman. *Introduction to Fourier Optics*. en. Google-Books-ID: ow5xs_Rtt9AC. Roberts and Company Publishers, 2005. ISBN: 978-0-9747077-2-3.

[103] David Paganin and David Paganin. *Coherent X-Ray Optics*. Oxford Series on Synchrotron Radiation. Oxford, New York: Oxford University Press, Jan. 2006. ISBN: 978-0-19-856728-8.

[104] Max Born and Emil Wolf. *Principles of Optics: Electromagnetic Theory of Propagation, Interference and Diffraction of Light*. 7th ed. Cambridge: Cambridge University Press, 1999. DOI: 10.1017/CBO9781139644181. URL: https://www.cambridge.org/core/books/principles-of-optics/D12868B8AE26B83D6D3C2193E94FFC32 (visited on 05/17/2025).

[105] *Coherence (physics)*. en. Page Version ID: 1290023589. May 2025. URL: https://en.wikipedia.org/w/index.php?title=Coherence_(physics)&oldid=1290023589 (visited on 05/17/2025).

[106] J. Miao, D. Sayre, and H. N. Chapman. "Phase retrieval from the magnitude of the Fourier transforms of nonperiodic objects". EN. In: *J. Opt. Soc. Am. A, JOSAA* 15.6 (June 1998). Publisher: Optica Publishing Group, pp. 1662–1669. ISSN: 1520-8532. DOI: 10.1364/JOSAA.15.001662. URL: https://opg.optica.org/josaa/abstract.cfm?uri=josaa-15-6-1662 (visited on 05/17/2025).

[107] J. Miao and D. Sayre. "On possible extensions of X-ray crystallography through diffraction-pattern oversampling". en. In: *Acta Cryst A* 56.6 (Nov. 2000). Publisher: International Union of Crystallography, pp. 596–605. ISSN: 0108-7673. DOI: 10.1107/S010876730001031X. URL:

https://journals.iucr.org/a/issues/2000/06/00/bk0084/ (visited on 05/17/2025).

[108] T. B. Edo et al. "Sampling in x-ray ptychography". en. In: *Phys. Rev. A* 87.5 (May 2013), p. 053850. ISSN: 1050-2947, 1094-1622. DOI: 10.1103/PhysRevA.87.053850. URL: https://link.aps.org/doi/10.1103/PhysRevA.87.053850 (visited on 05/10/2025).

[109] Dennis Floyd Gardner Jr. "Coherent Diffractive Imaging Near the Spatio-Temporal Limit with High-Harmonic Sources". PhD thesis. University of Colorado at Boulder, 2017.

[110] Andrew M. Maiden and John M. Rodenburg. "An improved ptychographical phase retrieval algorithm for diffractive imaging". In: *Ultramicroscopy* 109.10 (Sept. 2009), pp. 1256–1262. ISSN: 0304-3991. DOI: 10.1016/j.ultramic.2009.05.012. URL: https://www.sciencedirect.com/science/article/pii/S0304399109001284 (visited on 05/18/2025).

[111] D. Russell Luke. "Relaxed averaged alternating reflections for diffraction imaging". en. In: *Inverse Problems* 21.1 (Nov. 2004), p. 37. ISSN: 0266-5611. DOI: 10.1088/0266-5611/21/1/004. URL: https://dx.doi.org/10.1088/0266-5611/21/1/004 (visited on 05/18/2025).

[112] Franz Pfeiffer. "X-ray ptychography". en. In: *Nature Photon* 12.1 (Jan. 2018), pp. 9–17. ISSN: 1749-4893. DOI: 10.1038/s41566-017-0072-5. URL: https://doi.org/10.1038/s41566-017-0072-5 (visited on 05/17/2025).

[113] Pierre Thibault and Andreas Menzel. "Reconstructing state mixtures from diffraction measurements". en. In: *Nature* 494.7435 (Feb. 2013), pp. 68–71. ISSN: 0028-0836, 1476-4687. DOI: 10.1038/nature11806. URL: https://www.nature.com/articles/nature11806 (visited on 04/10/2025).

[114] Robert Maurice Karl Jr. "Ultrafast Coherent Diffractive Imaging of Nano-scale Dynamics Using High Harmonic Sources". PhD thesis. University of Colorado at Boulder, 2019.

[115] Orazio Svelto. *Principles of Lasers*. en. Boston, MA: Springer US, 2010. ISBN: 978-1-4419-1301-2 978-1-4419-1302-9. DOI: 10.1007/978-1-4419-1302-9. URL: http://link.springer.com/10.1007/978-1-4419-1302-9 (visited on 05/31/2025).

[116] Ursula Keller. *Ultrafast Lasers: A Comprehensive Introduction to Fundamental Principles with Practical Applications*. en. Graduate Texts in Physics. Cham: Springer International Publishing, 2021. ISBN: 978-3-030-82531-7 978-3-030-82532-4. DOI: 10.1007/978-3-030-82532-4. URL: https://link.springer.com/10.1007/978-3-030-82532-4 (visited on 05/31/2025).

[117] Donna Strickland and Gerard Mourou. "Compression of amplified chirped optical pulses". In: *Optics Communications* 55.6 (Oct. 1985), pp. 447–449. ISSN: 0030-4018. DOI: 10.1016/0030-4018(85)90151-8. URL: https://www.sciencedirect.com/science/article/pii/0030401885901518 (visited on 06/07/2025).

[118] Sterling Backus et al. "High power ultrafast lasers". In: *Review of Scientific Instruments* 69.3 (1998), pp. 1207–1223. DOI: 10.1063/1.1148795. URL: http://aip.scitation.org/doi/10.1063/1.1148795.

[119] O. Martinez. "3000 times grating compressor with positive group velocity dispersion: Application to fiber compensation in 1.3-1.6 μm region". In: *IEEE Journal of Quantum Electronics* 23.1 (Jan. 1987), pp. 59–64. ISSN: 1558-1713. DOI: 10.1109/JQE.1987.1073201. URL: https://ieeexplore.ieee.org/abstract/document/1073201 (visited on 06/06/2025).

[120] E. Treacy. "Optical pulse compression with diffraction gratings". In: *IEEE Journal of Quantum Electronics* 5.9 (Sept. 1969), pp. 454–458. ISSN: 1558-1713. DOI: 10.1109/JQE.1969.1076303. URL: https://ieeexplore.ieee.org/document/1076303 (visited on 06/06/2025).

[121] *Learn Chirped pulse amplification facts for kids*. en. URL: https://kids.kiddle.co/Chirped_pulse_amplification (visited on 06/07/2025).

[122] H. P. Weber. “Method for Pulsewidth Measurement of Ultrashort Light Pulses Generated by Phase-Locked Lasers using Nonlinear Optics”. In: *Journal of Applied Physics* 38.5 (Apr. 1967), pp. 2231–2234. ISSN: 0021-8979. DOI: 10.1063/1.1709859. URL: https://doi.org/10.1063/1.1709859 (visited on 06/12/2025).

[123] C. Iaconis and I.A. Walmsley. “Self-referencing spectral interferometry for measuring ultrashort optical pulses”. In: *IEEE Journal of Quantum Electronics* 35.4 (Apr. 1999), pp. 501–509. ISSN: 1558-1713. DOI: 10.1109/3.753654. URL: https://ieeexplore.ieee.org/document/753654 (visited on 06/16/2025).

[124] C. Iaconis and I. A. Walmsley. “Spectral phase interferometry for direct electric-field reconstruction of ultrashort optical pulses”. EN. In: *Opt. Lett., OL* 23.10 (May 1998). Publisher: Optica Publishing Group, pp. 792–794. ISSN: 1539-4794. DOI: 10.1364/OL.23.000792. URL: https://opg.optica.org/ol/abstract.cfm?uri=ol-23-10-792 (visited on 06/16/2025).

[125] D.J. Kane. “Recent progress toward real-time measurement of ultrashort laser pulses”. In: *IEEE Journal of Quantum Electronics* 35.4 (Apr. 1999), pp. 421–431. ISSN: 1558-1713. DOI: 10.1109/3.753647. URL: https://ieeexplore.ieee.org/abstract/document/753647 (visited on 06/14/2025).

[126] Rick Trebino et al. “Measuring ultrashort laser pulses in the time-frequency domain using frequency-resolved optical gating”. en. In: *Review of Scientific Instruments* 68.9 (Sept. 1997), pp. 3277–3295. ISSN: 0034-6748, 1089-7623. DOI: 10.1063/1.1148286. URL: https://pubs.aip.org/rsi/article/68/9/3277/322634/Measuring-ultrashort-laser-pulses-in-the-time (visited on 06/14/2025).

[127] Daniel J. Kane and Rick Trebino. “Single-shot measurement of the intensity and phase of an arbitrary ultrashort pulse by using frequency-resolved optical gating”. EN. In: *Opt. Lett., OL* 18.10 (May 1993). Publisher: Optica Publishing Group, pp. 823–825. ISSN: 1539-4794. DOI: 10.1364/OL.18.000823. URL: https://opg.optica.org/ol/abstract.cfm?uri=ol-18-10-823 (visited on 06/14/2025).

[128] Rick Trebino and Daniel J. Kane. "Using phase retrieval to measure the intensity and phase of ultrashort pulses: frequency-resolved optical gating". EN. In: *J. Opt. Soc. Am. A, JOSAA* 10.5 (May 1993). Publisher: Optica Publishing Group, pp. 1101–1111. ISSN: 1520-8532. DOI: 10.1364/JOSAA.10.001101. URL: https://opg.optica.org/josaa/abstract.cfm?uri=josaa-10-5-1101 (visited on 06/14/2025).

[129] K. W. DeLong et al. "Frequency-resolved optical gating with the use of second-harmonic generation". EN. In: *JOSA B, Vol. 11, Issue 11, pp. 2206-2215* (Nov. 1994). Publisher: Optica Publishing Group. DOI: 10.1364/JOSAB.11.002206. URL: https://opg.optica.org/josab/abstract.cfm?uri=josab-11-11-2206 (visited on 06/14/2025).

[130] *Advanced Femto Technology- SHG FROG products, TG FROG, pulse measurement products, single shot FROG*. URL: http://advancedfemtotech.com/Tutorial_SHG_FROG.html (visited on 06/14/2025).

[131] *GRENOUILLE*. URL: https://www.swampoptics.com/grenouille.html (visited on 06/14/2025).

[132] Tenio Popmintchev. "Tunable ultrafast coherent light in the soft and hard X-ray regions of the spectrum: Phase matching of extreme high-order harmonic generation". PhD thesis. 2009.

[133] Kenichi L. Ishikawa. "High-Harmonic Generation". en. In: *Advances in Solid State Lasers Development and Applications*. IntechOpen, Feb. 2010. ISBN: 978-953-7619-80-0. DOI: 10.5772/7961. URL: https://www.intechopen.com/chapters/8418 (visited on 06/28/2025).

[134] Tenio Popmintchev. "The attosecond nonlinear optics of bright coherent X-ray generation". en. In: *nature photonics* 4 (2010).

[135] P B Corkum. "Plasma perspective on strong field multiphoton ionization". en. In: *PHYSICAL REVIEW LETTERS* 71.13 (1993).

[136] Eiji J. Takahashi et al. “Coherent Water Window X Ray by Phase-Matched High-Order Harmonic Generation in Neutral Media”. In: *Phys. Rev. Lett.* 101.25 (Dec. 2008). Publisher: American Physical Society, p. 253901. DOI: 10.1103/PhysRevLett.101.253901. URL: https://link.aps.org/doi/10.1103/PhysRevLett.101.253901 (visited on 06/28/2025).

[137] Ch. Spielmann et al. “Generation of Coherent X-rays in the Water Window Using 5-Femtosecond Laser Pulses”. In: *Science* 278.5338 (Oct. 1997). Publisher: American Association for the Advancement of Science, pp. 661–664. DOI: 10.1126/science.278.5338.661. URL: https://www.science.org/doi/abs/10.1126/science.278.5338.661 (visited on 06/24/2025).

[138] M.-C. Chen et al. “Bright, Coherent, Ultrafast Soft X-Ray Harmonics Spanning the Water Window from a Tabletop Light Source”. In: *Phys. Rev. Lett.* 105.17 (Oct. 2010). Publisher: American Physical Society, p. 173901. DOI: 10.1103/PhysRevLett.105.173901. URL: https://link.aps.org/doi/10.1103/PhysRevLett.105.173901 (visited on 06/28/2025).

[139] Zenghu Chang. *Fundamentals of Attosecond Optics*. Boca Raton: CRC Press, Apr. 2016. ISBN: 978-0-429-19302-6. DOI: 10.1201/b10402.

[140] Charles G Durfee Iii et al. “Phase Matching of High-Order Harmonics in Hollow Waveguides”. en. In: *PHYSICAL REVIEW LETTERS* 83.11 (1999).

[141] Randy A. Bartels et al. “Generation of Spatially Coherent Light at Extreme Ultraviolet Wavelengths”. en. In: *Science* 297.5580 (July 2002), pp. 376–378. ISSN: 0036-8075, 1095-9203. DOI: 10.1126/science.1071718. URL: https://www.science.org/doi/10.1126/science.1071718 (visited on 01/30/2025).

[142] Robert W. Boyd. *Nonlinear Optics*. en. Google-Books-ID: uoRUi1Yb7ooC. Elsevier, May 2008. ISBN: 978-0-08-048596-6.

[143] D. Cocco et al. “Wavefront preserving X-ray optics for Synchrotron and Free Electron Laser photon beam transport systems”. en. In: *Physics Reports* 974 (Aug. 2022). Publisher: Elsevier BV, pp. 1–40. ISSN: 0370-1573. DOI:

10.1016/j.physrep.2022.05.001. URL: https://linkinghub.elsevier.com/retrieve/pii/S0370157322001478 (visited on 07/16/2025).

[144] Manuel Sanchez Del Rio et al. "*SHADOW3*: a new version of the synchrotron X-ray optics modelling package". en. In: *J Synchrotron Rad* 18.5 (Sept. 2011). Publisher: International Union of Crystallography (IUCr), pp. 708–716. ISSN: 0909-0495, 1600-5775. DOI: 10.1107/s0909049511026306. URL: https://journals.iucr.org/paper?S0909049511026306 (visited on 07/16/2025).

[145] Luca Rebuffi and Manuel Sánchez Del Río. "*ShadowOui* : a new visual environment for X-ray optics and synchrotron beamline simulations". en. In: *J Synchrotron Rad* 23.6 (Nov. 2016), pp. 1357–1367. ISSN: 1600-5775. DOI: 10.1107/S1600577516013837. URL: https://scripts.iucr.org/cgi-bin/paper?S1600577516013837 (visited on 01/11/2025).

[146] W. B. Peatman. "Gratings, Mirrors and Slits: Beamline Design for Soft X-Ray Synchrotron Radiation Sources". In: (Oct. 2018). DOI: 10.1201/9780203719909.

[147] Franco Cerrina. "Ray Tracing Of X-Ray Optical Systems: Source Models." In: *X-Ray Instrumentation in Medicine and Biology, Plasma Physics, Astrophysics, and Synchrotron Radiation*. Vol. 1140. SPIE, Nov. 1989, pp. 330–336. DOI: 10.1117/12.961842. URL: https://www.spiedigitallibrary.org/conference-proceedings-of-spie/1140/0000/Ray-Tracing-Of-X-Ray-Optical-Systems-Source-Models/10.1117/12.961842.full (visited on 07/15/2025).

[148] Xianbo Shi et al. "A hybrid method for X-ray optics simulation: combining geometric ray-tracing and wavefront propagation". en. In: *J Synchrotron Rad* 21.4 (July 2014). Publisher: International Union of Crystallography (IUCr), pp. 669–678. ISSN: 1600-5775. DOI: 10.1107/s160057751400650x. URL: https://journals.iucr.org/paper?S160057751400650X (visited on 07/16/2025).

[149] D. Cocco et al. “Wavefront preserving X-ray optics for Synchrotron and Free Electron Laser photon beam transport systems”. en. In: *Physics Reports* 974 (Aug. 2022). Publisher: Elsevier BV, pp. 1–40. ISSN: 0370-1573. DOI: 10.1016/j.physrep.2022.05.001. URL: https://linkinghub.elsevier.com/retrieve/pii/S0370157322001478 (visited on 07/15/2025).

[150] Yonghong Deng et al. “Review on mid-spatial frequency error suppression in optical components manufacturing”. en. In: *Int J Adv Manuf Technol* 126.11 (June 2023), pp. 4827–4847. ISSN: 1433-3015. DOI: 10.1007/s00170-023-11408-y. URL: https://doi.org/10.1007/s00170-023-11408-y (visited on 03/26/2026).

[151] Manuel Sanchez Del Rio et al. “DABAM: an open-source database of X-ray mirrors metrology”. en. In: *J Synchrotron Rad* 23.3 (May 2016). Publisher: International Union of Crystallography (IUCr), pp. 665–678. ISSN: 1600-5775. DOI: 10.1107/s1600577516005014. URL: https://journals.iucr.org/paper?S1600577516005014 (visited on 07/16/2025).

[152] L. Poletto et al. “Micro-focusing of attosecond pulses by grazing-incidence toroidal mirrors”. en. In: *Opt. Express* 21.11 (June 2013), p. 13040. ISSN: 1094-4087. DOI: 10.1364/OE.21.013040. URL: https://opg.optica.org/oe/abstract.cfm?uri=oe-21-11-13040 (visited on 08/04/2025).

[153] Marin van Heel and Michael Schatz. “Fourier shell correlation threshold criteria”. In: *Journal of Structural Biology* 151.3 (Sept. 2005), pp. 250–262. ISSN: 1047-8477. DOI: 10.1016/j.jsb.2005.05.009. URL: https://www.sciencedirect.com/science/article/pii/S1047847705001292 (visited on 08/04/2025).

[154] Sami Koho et al. “Fourier ring correlation simplifies image restoration in fluorescence microscopy”. en. In: *Nat Commun* 10.1 (July 2019). Publisher: Nature Publishing Group, p. 3103. ISSN: 2041-1723. DOI: 10.1038/s41467-019-11024-z. URL: https://www.nature.com/articles/s41467-019-11024-z (visited on 12/19/2025).

[155] Giulia Fulvia Mancini et al. “Local photo-mechanical stiffness revealed in gold nanoparticles supracrystals by ultrafast small-angle electron diffraction”. en. In: *Structural Dynamics* 6.2 (Mar. 2019), p. 024304. ISSN: 2329-7778. DOI: 10.1063/1.5091858. URL: https://pubs.aip.org/sdy/article/6/2/024304/366453/Local-photo-mechanical-stiffness-revealed-in-gold (visited on 09/08/2025).